Cosmological observations as a probe of fundamental physics and astrophysics

Simone Ferraro

A Dissertation
Presented to the Faculty
of Princeton University
in Candidacy for the Degree
of Doctor of Philosophy

Recommended for Acceptance
by the Department of
Astrophysical Sciences
Adviser: Prof. David N. Spergel

September 2015

Abstract

The unifying theme of this dissertation is using cosmological observations as a tool to discover new physics and astrophysics.

The first part focuses on the effects of primordial non-Gaussianity on the large-scale distribution of dark matter halos. The statistical properties of the primordial fluctuation contain a wealth of information about the Universe's early moments, and these properties are imprinted on the late-time distribution of matter. The first chapter serves as an introduction to the effects of non-Gaussianity on halo bias, summarizing previous work and extending it to the cubic local model (the $g_{\rm NL}$ model). Chapter 2 generalizes some of the techniques of Chapter 1, allowing for the calculation of halo bias with arbitrary initial conditions, while Chapter 3 shows the relationship between the seemingly different techniques existing in the literature. Detailed forecasts for upcoming surveys are presented in Chapter 4, including the effect of marginalization over shot-noise and Gaussian part of the bias, photometric redshifts uncertainties and multi-tracer analysis to reduce the effect of cosmic variance.

The second part contains work on two secondary anisotropies of the Cosmic Microwave Background radiation (CMB), namely the Integrated Sachs-Wolfe (ISW) effect and the kinetic Sunyaev-Zel'dovich (kSZ) effect. The late-time ISW effect arises because of decay of the large-scale gravitational potential due to the accelerated expansion and is therefore a powerful probe of dark energy. Chapter 5 presents a new detection of the ISW effect, using WISE galaxies and AGN as tracers of the gravitational potential, whose bias is measured in cross-correlation with CMB lensing maps. An appendix discusses the contamination of this measurement due to the linear part of the kSZ effect, the Doppler shift of photon energy due to scattering off coherently moving electrons. The last chapter explores the prospects of detecting the kSZ signal from sources for which accurate redshift information is not available (such as the WISE catalog). Forecasts are presented, as well as comparison with simulations and a discussion of the main sources of contamination.

Acknowledgements

First, I would like to thank my advisor, David Spergel, who has been a constant source of inspiration and support. I have learned so much from him, both about science and how to choose good projects. During my time at Princeton I have been exposed to so many good ideas to keep me busy in the years to come. His continuos encouragement during hard times is especially appreciated.

A great thanks goes to all of my great collaborators over the years. In particular, I wish to thank Kendrick Smith, who has been a 'second advisor', for years of productive and enjoyable collaboration. It has also been a great pleasure to collaborate with Daniel Baumann, Cora Dvorkin, Daniel Green, Brandon Hensley, Colin Hill, Wayne Hu, Marilena LoVerde, Emmanuel Schaan, Fabian Schmidt and Blake Sherwin.

I have also benefitted from many discussion with the faculty at Princeton, and in particular with Matias Zaldarriaga, Michael Strauss, Neta Bahcall, Bruce Draine and Jerry Ostriker, as well as several members of the ACTPol collaboration. Also, I would like to thank Jill Knapp, Jenny Greene and Charlotte Zanidakis for their support regarding the graduate program.

A special thank to Emmanuel Schaan, a great friend and a great collaborator. Much of my understanding of physics has been shaped by the many discussions with him and with Hao Zhang of MIT.

I have been very lucky to have had so many great friends in Princeton that have made my stay here enjoyable. The list is too long to be included here, but you know who you are and will be thanked in person.

A big thank you to all of my teachers, from primary school to graduate classes who got me excited about science and encouraged me to pursue it at a professional level.

Finally, I would like to thank my family. Without their support, nothing that I have achieved would have been possible. They encouraged me to think independently and to

pursue my interests, even when that meant moving far from home and that they would rarely see me. I dedicate this thesis to them.

During my time at Princeton I have been supported financially by a combination of fellowships, including the Martin Schwarzschild fellowship in Astronomy and a number of research grants. Detailed funding information for each chapter can be found in the acknowledgements section at the end of the chapter.

For my parents.

Relation to Published Work

This dissertation divided into two main sections and comprises six chapters. The first section includes four chapters and explores the effect of primordial non-Gaussianity on the halo bias at late times. The topics of the second section are the *Integrated Sachs-Wolfe* (ISW) effect and the *kinetic Sunyaev-Zel'dovich* (kSZ) effect.

Chapter 1 provides an introduction to the effect of primordial non-Gaussianity on halo bias, explains the peak-background split formalism and extends it to the cubic form of local non-Gaussianity. Detailed comparison with N-body simulations is presented. This chapter is based on work done in collaboration with Kendrick Smith and Marilena LoVerde, and has been published in Smith, Ferraro and LoVerde, "Halo clustering and $g_{\rm NL}$-type primordial non-Gaussianity" in the *Journal of Cosmology and Astroparticle Physics* 03 (2012) 032. I co-developed the theoretical predictions and the comparison with previous work (with discussions and help from the other co-authors). Kendrick Smith and Marilena LoVerde performed and analyzed the simulations.

Part of the work presented in this chapter is also present in the Proceedings of the DPF-2011 Conference, Providence, RI, August 8-13, 2011.

Chapter 2 derives the halo-halo and halo-matter correlations for arbitrary (non-Gaussian) initial conditions. The concept of *stochastic bias* is explored and the conditions under which it arises are discussed, together with several examples. This chapter is based on work done in collaboration with Daniel Baumann, Daniel Green and Kendrick Smith, and has been published in Baumann, Ferraro, Green, Smith, *Journal of Cosmology and*

Astroparticle Physics 1305 (2013) 001 with the title "Stochastic Bias from Non-Gaussian Initial Conditions". I co-lead this work together with Daniel Baumann. All of the calculations were derived independently in two different sets of notes (one written by me) that were then merged to create a single paper.

Chapter 3 explores the relationship between different techniques to compute halo bias (such as barrier crossing, peak-background spit and local biasing) and show that they are equivalent under certain conditions, which are specified in the text. This chapter is based on work done in collaboration with Daniel Baumann, Daniel Green and Kendrick Smith, and has been published in Ferraro, Smith, Green, Baumann, *Monthly Notices of the Royal Astronomical Society* 435 934 (2013) with the title "On the correspondence between barrier crossing, peak-background split and local biasing". I co-lead this work together with Kendrick Smith. I have written most of the paper (with the exception of section 3.4.2) with input from the co-authors.

Chapter 4 provides forecast for primordial non-Gaussianity with halo bias with upcoming galaxy surveys. The effects of photometric redshift errors and cancellation of sample variance with multi-tracer analysis is also discussed. This chapter is based on work done in collaboration with Kendrick Smith and has been published in Ferraro and Smith, "Using large scale structure to measure $f_{\rm NL}$, $g_{\rm NL}$ and $\tau_{\rm NL}$", *Physical Review D* 91, 043506 (2015). I lead this work, having written most of the text, all of the code and made all of the figures.

Chapter 5 presents a new detection of the ISW effect with WISE galaxies and AGN. The galaxy/AGN bias is calibrated using CMB lensing, thus avoiding possible systematics that can arise when using the auto-correlation function. This work has been done in collaboration with Blake Sherwin and David Spergel and has been published in Ferraro, Sherwin and Spergel, *Physical Review D* 91, 083533 (2015) with the title "A WISE measurement of the ISW effect". I lead this work, and I have analyzed the data, written all of the code and most of the text, with frequent discussion with the co-authors.

Appendix 2 explores the contamination to the ISW signal due the Doppler effect (linear kSZ). This appendix is the result of currently unpublished work in collaboration with David Spergel. I lead this work, with advice from David Spergel.

Chapter 6 explores the prospects of detecting kSZ in absence of reliable redshift estimates for the tracer populations. The main sources of contaminations are discussed and forecasts are presented. This chapter builds on work in progress in collaboration with Colin Hill and David Spergel. The computation of the expected signal follows and confirms previously published results (see text for details). The calculation of the lensing leakage, cosmic variance and forecasts are my own, as well as all of the numerical computations. The hydrodynamical simulations were analyzed by Colin Hill and Nick Battaglia, while the theory curves are my work.

Contents

List of Tables

List of Figures

Chapter 1

Halo clustering and $g_{\rm NL}$-type primordial non-Gaussianity

1.1 Abstract

A wide range of multifield inflationary models generate non-Gaussian initial conditions in which the initial adiabatic fluctuation is of the form $(\zeta_G + g_{\rm NL}\zeta_G^3)$. We study halo clustering in these models using two different analytic methods: the peak-background split framework, and brute force calculation in a barrier crossing model, obtaining agreement between the two. We find a simple, theoretically motivated expression for halo bias which agrees with N-body simulations and can be used to constrain $g_{\rm NL}$ from observations. We discuss practical caveats to constraining $g_{\rm NL}$ using only observable properties of a tracer population, and argue that constraints obtained from populations whose observed bias is $\lesssim 2.5$ are generally not robust to uncertainties in modeling the halo occupation distribution of the population.

1.2 Introduction

In the last few decades, increasingly precise observations (e.g. [36, 53, 56, 58, 34, 66]) have led to a standard cosmological model in which small initial fluctuations evolve in a ΛCDM

background to give rise to the observed universe. Current data are consistent with initial fluctuations which are adiabatic, scalar, Gaussian, with weak deviations from scale invariance ($n_s < 1$ at 3σ).

The statistics of the initial fluctuations, i.e. deviations from Gaussian initial conditions, provide a powerful probe of the physics of the early universe. In the context of inflation [27, 41, 1, 28, 30, 65, 2], the simplest models (single-field, minimally coupled slow-roll) predict initial curvature perturbations with negligible deviations from Gaussianity. However, there is a rich phenomenology of non-Gaussian initial conditions in models with multiple fields, self-interactions near horizon crossing, or speed of sound $c_s \ll 1$ during inflation. In this paper, we will focus on non-Gaussianity of the so-called local type [59, 24, 37, 52], in which the primordial potential[1] is of the form

$$\Phi(\boldsymbol{x}) = \Phi_G(\boldsymbol{x}) + f_{\rm NL}(\Phi_G(\boldsymbol{x})^2 - \langle\Phi_G^2\rangle) + g_{\rm NL}(\Phi_G(\boldsymbol{x})^3 - 3\langle\Phi_G^2\rangle\Phi_G(\boldsymbol{x})) \qquad (1.1)$$

where Φ_G is a Gaussian field and $f_{\rm NL}$, $g_{\rm NL}$ are free parameters.[2]

Local non-Gaussianity can be generated by physical mechanisms involving multiple fields, such as light spectator fields during inflation which evolve to generate the initial adiabatic fluctuations (the curvaton scenario) [42, 46, 45], or models where the inflaton decay rate is modulated by a second field [19, 35]. Non-Gaussianity of local type is also naturally generated in non-inflationary models of the early universe such as the new ekpyrotic/cyclic scenario [3, 8, 39]. There is a theorem [48, 9] which states that any single-field model of inflation cannot generate detectable levels of local non-Gaussianity without violating observed limits on deviation from a scale-invariant power spectrum. Thus, detection of either $f_{\rm NL}$ or $g_{\rm NL}$ would rule out all single field models of inflation and place powerful constraints on the physics of the early universe. Current observational constraints on these parameters are consistent

[1] In studies of primordial non-Gaussianity, it is conventional to define a primordial potential $\Phi = \frac{3}{5}\zeta$, where ζ is the initial adiabatic curvature perturbation. Note that Φ is not the conformal Newtonian potential, which is given by $\frac{2}{3}\Phi$ deep in the radiation-dominated epoch where Eq. (1.1) applies.

[2] We define $g_{\rm NL}$-type non-Gaussianity including the term $-3\langle\Phi_G^2\rangle\Phi_G$; this term simply renormalizes Φ_G so that its power spectrum P_{Φ_G} is equal to the observed power spectrum P_Φ (to first order in $g_{\rm NL}$).

with zero [36, 62, 21, 17], but are expected to improve by an order of magnitude or more in the near future.

In models of inflation in which $|g_{\rm NL}| = \mathcal{O}(f_{\rm NL}^2)$, it is unlikely that observational constraints on $g_{\rm NL}$ will be competitive with constraints on $f_{\rm NL}$. However, there are a number of examples where $f_{\rm NL}^2 \ll |g_{\rm NL}|$, making the $g_{\rm NL}$ term in Eq. (1.1) the dominant source of primordial non-Gaussianity. This situation arises in curvaton models where non-quadratic terms in the potential are important [60, 33, 20, 31, 5] or in multifield models in which (ΔN) varies rapidly at the end of inflation [32, 4]. The existence of these scenarios makes searching for $g_{\rm NL}$ just as important as $f_{\rm NL}$ and measurements provide important constraints on the microphysical parameter space.

In a pioneering paper [12], Dalal et al showed that large-scale clustering of halos depends sensitively on $f_{\rm NL}$. More precisely, a sample of halos (or tracers such as galaxies or quasars) with constant bias b_1 in a Gaussian cosmology will have scale-dependent bias given by

$$b(k) \approx b_1 + 2\delta_c(b_1 - 1)\frac{f_{\rm NL}}{\alpha(k,z)} \tag{1.2}$$

in an $f_{\rm NL}$ cosmology. Here, δ_c is the spherical collapse threshold and $\alpha(k,z)$ is defined by

$$\alpha(k,z) = \frac{2k^2 T(k) D(z)}{3\Omega_m H_0^2} \tag{1.3}$$

so that the linear density field and the primordial potential are related by $\delta_{\rm lin}(k,z) = \alpha(k,z)\Phi(k)$. Large-scale structure constraints on $f_{\rm NL}$ from scale-dependent bias are currently competitive with the CMB (e.g. [62, 68]) and may ultimately provide constraints which are stronger (e.g. [11, 29]). The key identity (1.2) has been derived using several different analytic frameworks [50, 62, 25] and agrees with N-body simulations (e.g. [12, 26, 54, 17]).

In this paper we study the related issue of large-scale halo-clustering in a $g_{\rm NL}$ cosmology. We consider the large-scale halo bias in two analytic frameworks: the peak-background split (§1.4) and a barrier crossing model (§1.5). We find consistency between the two formalisms

(in disagreement with [15]) and obtain an expression analogous to Eq. (1.2) for the scale-dependent halo bias in a $g_{\rm NL}$ cosmology. Our main results are a universal relation between the scale-dependent halo bias in a $g_{\rm NL}$ cosmology and the mass function in an $f_{\rm NL}$ cosmology,

$$b(k) \approx b_1 + \frac{\beta_g g_{\rm NL}}{\alpha(k,z)} \quad \text{where} \quad \beta_g = 3(\partial \log n/\partial f_{\rm NL}) \tag{1.4}$$

and expressions for β_g (Eqs. (1.49), (1.50)) which can be used in practice to constrain $g_{\rm NL}$ from data. We also discuss caveats when estimating the $g_{\rm NL}$ bias from observable quantities (§1.6.4) and argue that constraints obtained from tracer populations which are not highly biased ($b_1 \gtrsim 2.5$) are generally not robust to uncertainties in HOD modeling.

Throughout this paper we use the WMAP5+BAO+SN fiducial cosmology [18], with baryon density $\Omega_b h^2 = 0.0226$, CDM density $\Omega_c h^2 = 0.114$, Hubble parameter $h = 0.70$, spectral index $n_s = 0.961$, optical depth $\tau = 0.080$, and power-law initial curvature power spectrum $k^3 P_\zeta(k)/2\pi^2 = \Delta^2_\zeta (k/k_{\rm piv})^{n_s-1}$ where $\Delta^2_\zeta = 2.42 \times 10^{-9}$ and $k_{\rm piv} = 0.002$ Mpc^{-1}. All power spectra and transfer functions have been computed using CAMB [40].

1.3 Definitions and notation

We will sometimes model halos of mass $\geq M$ with peaks in a smoothed density field δ_M defined as follows. Let $\delta_M(\boldsymbol{x})$ be the *linear* density field smoothed by a tophat filter with radius $R(M) = (3M/4\pi\rho_m)^{1/3}$, i.e.

$$\delta_M(\boldsymbol{x}) = \int \frac{d^3\boldsymbol{k}}{(2\pi)^3} e^{-i\boldsymbol{k}\cdot\boldsymbol{x}} \delta_{\rm lin}(\boldsymbol{k}) W_M(k) \tag{1.5}$$

where

$$W_M(k) = 3\,\frac{\sin(kR(M)) - kR(M)\cos(kR(M))}{(kR(M))^3} \tag{1.6}$$

Let $\sigma_M = \langle \delta_M^2 \rangle^{1/2}$ be the RMS amplitude of the smoothed density field, and let $\kappa_n(M)$ be its n-th non-Gaussian cumulant, defined by:

$$\kappa_n(M) = \frac{\langle \delta_M^n \rangle_{\rm conn}}{\sigma_M^n} \,. \tag{1.7}$$

Since δ_M and σ_M are defined via linear theory, $\kappa_n(M)$ is independent of redshift as implied by the notation. To first order in $f_{\rm NL}$ and $g_{\rm NL}$, we have

$$\kappa_3(M) = \kappa_3^{(1)}(M) f_{\rm NL} \tag{1.8}$$

$$\kappa_4(M) = \kappa_4^{(1)}(M) g_{\rm NL} \tag{1.9}$$

with higher cumulants equal to zero, where $\kappa_3^{(1)}(M), \kappa_4^{(1)}(M)$ are the values of the cumulants at $f_{\rm NL} = 1$ and $g_{\rm NL} = 1$ respectively. These values are given explicitly by:

$$\begin{aligned}
\kappa_3^{(1)}(M) &= \frac{6}{\sigma_M^3} \int \frac{d^3\boldsymbol{k}\, d^3\boldsymbol{k}'}{(2\pi)^6} W_M(k) W_M(k') W_M(|\boldsymbol{k}+\boldsymbol{k}'|) \frac{P_{mm}(k) P_{mm}(k') \alpha(|\boldsymbol{k}+\boldsymbol{k}'|)}{\alpha(k)\alpha(k')} \\
\kappa_4^{(1)}(M) &= \frac{24}{\sigma_M^4} \int \frac{d^3\boldsymbol{k}\, d^3\boldsymbol{k}'\, d^3\boldsymbol{k}''}{(2\pi)^9} W_M(k) W_M(k') W_M(k'') W_M(|\boldsymbol{k}+\boldsymbol{k}'+\boldsymbol{k}''|) \\
&\qquad \times \frac{P_{mm}(k) P_{mm}(k') P_{mm}(k'') \alpha(|\boldsymbol{k}+\boldsymbol{k}'+\boldsymbol{k}''|)}{\alpha(k)\alpha(k')\alpha(k'')}
\end{aligned} \tag{1.10}$$

where $\alpha(k)$ was defined previously in Eq. (1.3) and $P_{mm}(k)$ is the power spectrum of the linear density field, $\langle \delta_{\rm lin}(\boldsymbol{k}) \delta_{\rm lin}(\boldsymbol{k}') \rangle = (2\pi)^3 P_{mm}(k) \delta^{(3)}(\boldsymbol{k}+\boldsymbol{k}')$. For numerical calculation, the following fitting functions (from [44]) are convenient:

$$\kappa_3^{(1)}(M) = (6.6 \times 10^{-4}) \left(1 - 0.016 \log \left(\frac{M}{h^{-1} M_\odot} \right) \right) \tag{1.11}$$

$$\kappa_4^{(1)}(M) = (1.6 \times 10^{-7}) \left(1 - 0.021 \log \left(\frac{M}{h^{-1} M_\odot} \right) \right) . \tag{1.12}$$

This paper is mainly concerned with calculating halo bias $b(k) = P_{mh}(k)/P_{mm}(k)$ to first order in $f_{\rm NL}$ and $g_{\rm NL}$, so let us establish notation from the outset, by writing the large-scale

bias in the general form:

$$b(k) = b_1 + b_{1f} f_{\rm NL} + b_{1g} g_{\rm NL} + \frac{\beta_f f_{\rm NL} + \beta_g g_{\rm NL}}{\alpha(k)} \tag{1.13}$$

where unlike Eq. (1.2) and Eq. (1.4) we have allowed for scale-independent corrections b_{1f} and b_{1g} from $f_{\rm NL}$ and $g_{\rm NL}$ primordial non-Gaussianity. Equation (1.13) defines the coefficients $b_1, b_{1f}, b_{1g}, \beta_f, \beta_g$. This equation assumes that the k-dependence is of the functional form (constant) + (constant)/$\alpha(k)$, but we will derive this analytically (Eq. (1.34)) and show that it agrees with simulations (§1.6.1). In this notation, the Dalal et al formula (1.2) can be written as $\beta_f = 2\delta_c(b_1 - 1)$.

1.4 Peak-background split

The peak-background split formalism is a procedure for predicting halo clustering statistics on large scales. The basic idea is that a long-wavelength fluctuation in the initial curvature alters the local abundance of halos in a way which is equivalent to perturbing parameters of the background cosmology, e.g. the matter density ρ_m or the amplitude Δ_Φ of the initial fluctuations. The use of this formalism to study halo bias in non-Gaussian cosmologies was pioneered in [62]; we will review this calculation of the bias in an $f_{\rm NL}$ cosmology (§1.4.1) and then perform an analogous calculation in the $g_{\rm NL}$ case (§1.4.2).

1.4.1 $f_{\rm NL}$ cosmology

In an $f_{\rm NL}$ cosmology, the initial conditions are given by:

$$\Phi(\boldsymbol{x}) = \Phi_G(\boldsymbol{x}) + f_{\rm NL}(\Phi_G(\boldsymbol{x})^2 - \langle \Phi_G^2 \rangle) \tag{1.14}$$

To analyze the effect of a long-wavelength mode, let us decompose the *Gaussian* potential as a sum $\Phi_G = \Phi_l + \Phi_s$ of long-wavelength and short-wavelength contributions. The long/short-

wavelength decomposition of the non-Gaussian potential Φ is then

$$\Phi(\boldsymbol{x}) = \underbrace{\Phi_l(\boldsymbol{x}) + f_{\rm NL}\left(\Phi_l(\boldsymbol{x})^2 - \langle\Phi_l^2\rangle\right)}_{\rm long} + \underbrace{(1+2f_{\rm NL}\Phi_l(\boldsymbol{x}))\Phi_s(\boldsymbol{x}) + f_{\rm NL}(\Phi_s(\boldsymbol{x})^2 - \langle\Phi_s^2\rangle)}_{\rm short} \quad (1.15)$$

and contains explicit coupling between long and short wavelength modes of the Gaussian potential.

Let us consider how the term $(1+2f_{\rm NL}\Phi_l(\boldsymbol{x}))\Phi_s(\boldsymbol{x})$ in Eq. (1.15) affects $n_l(\boldsymbol{x})$, the long-wavelength part of the halo number density field. In a local region where the long-wavelength potential takes some value Φ_l, the amplitude Δ_Φ of the small-scale modes is perturbed: $\Delta_\Phi \to (1+2f_{\rm NL}\Phi_l)\Delta_\Phi$. This modifies the local halo abundance, in the same way that the global abundance would be modified if the cosmological parameter Δ_Φ were perturbed, i.e. we get a term in the long-wavelength halo density of the form $\Delta n(\boldsymbol{x}) = 2f_{\rm NL}\Phi_l(\boldsymbol{x})(\partial n/\partial\log\Delta_\Phi)$. In addition, even in a Gaussian cosmology, there is a perturbation to the local halo abundance which is proportional to the long-wavelength part $\delta_l(\boldsymbol{x})$ of the density fluctuation, i.e. a term of the form $\Delta n(\boldsymbol{x}) = \delta_l(\boldsymbol{x})(\partial n/\partial\delta_l)$. Putting this together, the long-wavelength part of the halo density is given by:[3]

$$\begin{aligned} n_l(\boldsymbol{x}) &= \bar{n} + \frac{\partial n}{\partial\delta_l}\delta_l(\boldsymbol{x}) + 2f_{\rm NL}\frac{\partial n}{\partial\log\Delta_\Phi}\Phi_l(\boldsymbol{x}) \\ &= \bar{n}(1 + b_1\delta_l(\boldsymbol{x}) + \beta_f f_{\rm NL}\Phi_l(\boldsymbol{x})) \end{aligned} \quad (1.16)$$

[3]In this derivation, we have swept two terms in Eq. (1.14) under the rug; let us now argue that these are indeed negligible. The term $f_{\rm NL}(\Phi_s(\boldsymbol{x})^2 - \langle\Phi_s^2\rangle)$ alters the statistics of the small scale modes; this does perturb the halo abundance (by generating skewness in the density field) but the perturbation is independent of the long-wavelength fluctuation Φ_l. Therefore, this term does not contibute to the large-scale halo bias. The term $f_{\rm NL}(\Phi_l(\boldsymbol{x})^2 - \langle\Phi_l^2\rangle)$ perturbs the long-wavelength modes and decorrelates them (to order $\mathcal{O}(f_{\rm NL})$) from both the linear density fluctuation $\delta(\boldsymbol{x})$ and the field $(2f_{\rm NL}\Phi_l)$ which modulates the local power spectrum amplitude Δ_Φ. In principle, this should generate stochastic bias at order $\mathcal{O}(f_{\rm NL}^2)$, but we will neglect this, since we are only calculating to order $\mathcal{O}(f_{\rm NL})$.

where

$$b_1 = \frac{\partial \log n}{\partial \delta_l} \tag{1.17}$$

$$\beta_f = 2\frac{\partial \log n}{\partial \log \Delta_\Phi}\,. \tag{1.18}$$

Intuitively, in an $f_{\rm NL}$ cosmology, the local power spectrum amplitude Δ_Φ is not spatially constant, but varies throughout the universe in a way which is proportional to the long-wavelength potential Φ_l.

Computing the halo bias $b(k) = P_{mh}(k)/P_{mm}(k)$ from Eq. (1.16) for $n_l(\boldsymbol{x})$, we get:

$$\begin{aligned} b(k) &= \frac{b_1 P_{mm}(k) + \beta_f P_{m\Phi}(k)}{P_{mm(k)}} \\ &= b_1 + \frac{\beta_f f_{\rm NL}}{\alpha(k,z)}\,. \end{aligned} \tag{1.19}$$

From the preceding argument, we predict that the scale-dependent $f_{\rm NL}$ bias is given by $\beta_f = 2(\partial \log n/\partial \log \Delta_\Phi)$. We will refer to this as a "weak" prediction for the bias: it cannot be used to constrain $f_{\rm NL}$ from real data, since β_f has not been expressed in terms of observable quantities.

To make further progress, we need to evaluate the derivative $(\partial \log n/\partial \log \Delta_\Phi)$, by making additional assumptions. If we assume that the halo mass function is universal, then one can calculate the derivative, obtaining $(\partial \log n/\partial \log \Delta_\Phi) = \delta_c(b_1 - 1)$, where b_1 is the Gaussian bias [62], so that:

$$\beta_f = 2\delta_c(b_1 - 1)\,. \tag{1.20}$$

We will refer to this as a "strong" prediction for the scale-dependent bias in an $f_{\rm NL}$ cosmology, since β_f has been expressed in terms of the observable quantity b_1. The strong form is essential for constraining $f_{\rm NL}$ from observations.

1.4.2 $g_{\rm NL}$ cosmology

Let us now generalize the analysis of large-scale clustering in the previous subsection to the case of a $g_{\rm NL}$ cosmology, with initial conditions given by:

$$\Phi(\boldsymbol{x}) = \Phi_G(\boldsymbol{x}) + g_{\rm NL}(\Phi_G(\boldsymbol{x})^3 - 3\langle\Phi_G^2\rangle\Phi_G(\boldsymbol{x}))\,. \tag{1.21}$$

Separating the Gaussian field into long and short wavelength pieces $\Phi_G = \Phi_l + \Phi_s$, we decompose Φ as follows:

$$\begin{aligned}\Phi(\boldsymbol{x}) &= \underbrace{\Phi_l(\boldsymbol{x}) + g_{\rm NL}(\Phi_l(\boldsymbol{x})^3 - 3\langle\Phi_l^2\rangle\Phi_l(\boldsymbol{x}))}_{\rm long} \\ &+ \Phi_s(\boldsymbol{x}) + 3g_{\rm NL}(\Phi_l(\boldsymbol{x})^2 - \langle\Phi_l^2\rangle)\Phi_s(\boldsymbol{x}) + 3g_{\rm NL}\Phi_l(\boldsymbol{x})(\Phi_s(\boldsymbol{x})^2 - \langle\Phi_s^2\rangle) \\ &+ g_{\rm NL}(\Phi_s(\boldsymbol{x})^3 - 3\langle\Phi_s^2\rangle\Phi_s(\boldsymbol{x}))\end{aligned} \tag{1.22}$$

Where the "long" part of the potential has been indicated explicitly and the rest contributes to the "short" part. As in the $f_{\rm NL}$ case, we'll consider the perturbation to the long-wavelength halo density $n_h(\boldsymbol{x})$ generated by each of these terms.

The term $3g_{\rm NL}(\Phi_l(\boldsymbol{x})^2 - \langle\Phi_l^2\rangle)\Phi_s(\boldsymbol{x})$ can be interpreted as a local modulation in the small-scale power spectrum amplitude, given by $\Delta_\Phi \to (1 + 3g_{\rm NL}(\Phi_l(\boldsymbol{x})^2 - \langle\Phi_l^2\rangle))\Delta_\Phi$. This generates a term $\Delta n_l(\boldsymbol{x}) = 3g_{\rm NL}(\Phi_l(\boldsymbol{x})^2 - \langle\Phi_l^2\rangle)(\partial n/\partial \log\Delta_\Phi)$ in the long-wavelength halo density, in close analogy with the $f_{\rm NL}$ case (the modulation is proportional to $g_{\rm NL}(\Phi_l^2 - \langle\Phi_l^2\rangle)$ in this case, rather than $f_{\rm NL}\Phi_l$).

The term $3g_{\rm NL}\Phi_l(\boldsymbol{x})(\Phi_s(\boldsymbol{x})^2 - \langle\Phi_s^2\rangle)$ can be interpreted as follows. In a local region where the long-wavelength potential takes the value Φ_l, the small-scale modes are perturbed in the same way as in an $f_{\rm NL}$ cosmology where the global value of $f_{\rm NL}$ is given by $(3g_{\rm NL}\Phi_l)$. This generates a term $\Delta n_l(\boldsymbol{x}) = 3g_{\rm NL}\Phi_l(\boldsymbol{x})(\partial n/\partial f_{\rm NL})$ in the long-wavelength halo density.

Finally, there is the usual term $\Delta n_l(\boldsymbol{x}) = \delta_l(\boldsymbol{x})(\partial n/\partial\delta_l)$ due to changes in mean background density (as in the Gaussian case).

Putting this all together, we find that the long-wavelength halo density field in a $g_{\rm NL}$ cosmology is given by:[4]

$$\begin{aligned} n_l(\boldsymbol{x}) &= \bar{n} + \frac{\partial n}{\partial \delta_l}\delta_l(\boldsymbol{x}) + 3g_{\rm NL}\frac{\partial n}{\partial \log \Delta_\Phi}(\Phi_l(\boldsymbol{x})^2 - \langle\Phi_l^2\rangle) + 3g_{\rm NL}\frac{\partial n}{\partial f_{\rm NL}}\Phi_l(\boldsymbol{x}) \\ &= \bar{n}\left(1 + b_1\delta_l(\boldsymbol{x}) + \frac{3}{2}\beta_f g_{\rm NL}(\Phi_l(\boldsymbol{x})^2 - \langle\Phi_l^2\rangle) + \beta_g g_{\rm NL}\Phi_l(\boldsymbol{x})\right) \end{aligned} \tag{1.23}$$

where b_1 and β_f were defined previously (Eqs. (1.17), (1.18)), and:

$$\beta_g = 3\frac{\partial \log n}{\partial f_{\rm NL}} \tag{1.24}$$

The large-scale halo bias $b(k) = P_{mh}(k)/P_{mm}(k)$ is given by:

$$b(k) = b_1 + \frac{\beta_g g_{\rm NL}}{\alpha(k,z)}\,. \tag{1.25}$$

Note that the $(\beta_f g_{\rm NL})$ term in Eq. (1.23) does not contribute to the bias, since the field $(\Phi_l(\boldsymbol{x})^2 - \langle\Phi_l^2\rangle)$ and the long-wavelength density field δ_l are uncorrelated (their cross correlation is a three-point function of Gaussian fields, which vanishes). This term should generate stochastic bias, but we defer a systematic study of halo stochasticity in non-Gaussian cosmologies to a future paper [22].

We have now arrived at the peak-background split prediction (1.25) for halo bias in a $g_{\rm NL}$ cosmology, which relates the scale-dependent $g_{\rm NL}$ bias to the derivative $(\partial \log n/\partial f_{\rm NL})$ of the halo mass function in an $f_{\rm NL}$ cosmology. In the terminology of the previous subsection, this is a "weak" prediction: we have shown that the problem of computing the $g_{\rm NL}$ bias is naturally related to the problem of understanding the mass function in an $f_{\rm NL}$ cosmology, but the coefficient β_g has not been expressed in terms of observable quantities.

[4] Analogously to the $f_{\rm NL}$ case, we have neglected two terms in Eq. (1.22). The term $g_{\rm NL}(\Phi_l(\boldsymbol{x})^3 - 3\langle\Phi_l^2\rangle\Phi_l(\boldsymbol{x}))$ only alters power spectra at order $\mathcal{O}(g_{\rm NL}^2)$, and we will neglect terms of this order. The term $g_{\rm NL}(\Phi_s(\boldsymbol{x})^3 - 3\langle\Phi_s^2\rangle\Phi_s(\boldsymbol{x}))$ generates kurtosis in the density field and modifies the halo mass function [44], but in a way which is independent of Φ_l and therefore does not contribute to large-scale clustering.

To obtain a "strong" prediction, we need to evaluate the derivative $(\partial \log n / \partial f_{\rm NL})$, which requires making additional assumptions. This has been done in [44], assuming a barrier crossing model for the mass function and using the Edgeworth expansion to calculate the derivative (see also [51, 43, 6, 38, 47, 14, 13]). The result is:

$$\frac{\partial \log n(M)}{\partial f_{\rm NL}} = \frac{\kappa_3(M)}{6} H_3(\nu(M)) - \frac{1}{6}\frac{d\kappa_3/dM}{d\nu/dM} H_2(\nu(M)) \tag{1.26}$$

where $\nu = \delta_c/\sigma_M$, and $H_2(x) = x^2 - 1$ and $H_3(x) = x^3 - 3x$ are Hermite polynomials. We will compare this prediction with N-body simulations in §1.6.

1.5 Barrier crossing model

In this section, we will study large-scale bias using a barrier crossing model, obtaining results which are consistent with the peak-background split formalism from the previous section. The two approaches are complementary: the barrier model has the advantage that it generates complete predictions for halo statistics (such as the mass function or bias) via an algorithmic calculational procedure, but obscures the physical intuition of the peak-background split. For completeness, the calculations in this section will be sufficiently general to include the cases of Gaussian, $f_{\rm NL}$-type, and $g_{\rm NL}$-type initial conditions.

1.5.1 Setting up the calculation

The barrier crossing model is an old, widely influential idea in cosmology, in which halos of mass $\geq M$ are identified with peaks in the smoothed linear density field [55]. Although more complex versions have been proposed, we will use the simplest version: a spherical collapse model with constant barrier height, defined formally as follows.

We model halos of mass $\geq M$ as regions where the smoothed linear density field $\delta_M(\boldsymbol{x})$ (defined in Eq. (1.5)) exceeds the threshold value δ_c, i.e. the halo number density $n_h(\boldsymbol{x})$ is

given by:

$$n_h(\boldsymbol{x}) = \frac{\rho_m}{M}\theta(\delta_M(\boldsymbol{x}) - \delta_c) \tag{1.27}$$

where θ is the step function

$$\theta(x) = \begin{cases} 0 & \text{if } x < 0 \\ 1 & \text{if } x \geq 0 \end{cases} \tag{1.28}$$

Throughout this paper, we take $\delta_c = 1.42$; this value produces somewhat improved agreement between the barrier model and simulations, compared to the Press-Schechter value $\delta_c = 1.69$.[5]

To study halo bias in this model, we define the following notation. Let $\boldsymbol{x}$, $\boldsymbol{x}'$ be two points separated by distance r, let $\delta_{\rm lin}$ denote the (unsmoothed) linear density field at $\boldsymbol{x}$, and let δ'_M denote the smoothed linear density field at $\boldsymbol{x}'$. We denote the joint PDF of these random variables by $p(\delta_{\rm lin}, \delta'_M)$, and denote the 1-variable PDF of δ'_M by $p(\delta'_M)$. We define

$$p_0 = \int_{\delta_c}^{\infty} d\delta'_M \, p(\delta'_M) \tag{1.29}$$

$$\xi_0(r) = \int d\delta_{\rm lin} \, d\delta'_M \, p(\delta_{\rm lin}, \delta'_M) \, \delta_{\rm lin}\theta(\delta'_M - \delta_c) \tag{1.30}$$

These quantities are related to the halo mass function $n(M)$ and matter-halo correlation function $\xi_{mh}(r)$, but there is one wrinkle. In the barrier crossing model, the field n_h defined in Eq. (1.27) represents the number density of halos with mass $\geq M$, whereas we want to consider a sample of halos with mass in a narrow mass range $(M, M + dM)$. Thus $n(M)$ and $\xi_{mh}(r)$ are obtained by taking derivatives as follows:

$$n(M) = -\frac{2\rho_m}{M}\left(\frac{dp_0}{dM}\right) \tag{1.31}$$

$$\xi_{mh}(r) = \frac{d\xi_0(r)/dM}{dp_0/dM} \tag{1.32}$$

[5] We experimented with using a mass-dependent barrier $\delta_c(\nu)$ chosen for consistency with a universal mass function such as Sheth-Tormen [61] or Warren [67], but found that this did not result in further improvement.

1.5.2 Mass function, halo bias, and interpretation

In principle, calculation of the halo mass function and large-scale bias in the barrier crossing model has now been reduced to evaluation of Eqs. (1.29)–(1.32). We defer details of the calculation to Appendix 1.8 and quote the final results. The halo mass function is given by:

$$\begin{aligned} n(M) &= \frac{2\rho_m}{M}\left(\frac{d\log\sigma^{-1}}{dM}\right)\frac{e^{-\nu^2/2}}{(2\pi)^{1/2}}\Bigg[\,\nu \\ &+ f_{\rm NL}\left(\kappa_3^{(1)}(M)\frac{\nu H_3(\nu)}{6} - \frac{d\kappa_3^{(1)}/dM}{d(\log\sigma^{-1})/dM}\frac{H_2(\nu)}{6}\right) \\ &+ g_{\rm NL}\left(\kappa_4^{(1)}(M)\frac{\nu H_4(\nu)}{24} - \frac{d\kappa_4^{(1)}/dM}{d(\log\sigma^{-1})/dM}\frac{H_3(\nu)}{24}\right)\Bigg] \end{aligned} \tag{1.33}$$

The halo bias $b(k) = P_{mh}(k)/P_{mm}(k)$ is given by (in the large-scale limit $k \to 0$):

$$b(k) = b_1 + b_{1f}f_{\rm NL} + b_{1g}g_{\rm NL} + \frac{\beta_f f_{\rm NL} + \beta_g g_{\rm NL}}{\alpha(k)} \tag{1.34}$$

where:

$$b_1 = 1 + \frac{\nu^2 - 1}{\delta_c} \tag{1.35}$$

$$b_{1f} = -\kappa_3^{(1)}(M)\left(\frac{\nu^3 - \nu}{2\delta_c}\right) + \frac{d\kappa_3^{(1)}/dM}{d(\log\sigma^{-1})/dM}\left(\frac{\nu + \nu^{-1}}{6\delta_c}\right) \tag{1.36}$$

$$b_{1g} = -\kappa_4^{(1)}(M)\left(\frac{\nu^4 - 3\nu^2}{6\delta_c}\right) + \frac{d\kappa_4^{(1)}/dM}{d(\log\sigma^{-1})/dM}\left(\frac{\nu^2}{12\delta_c}\right) \tag{1.37}$$

$$\beta_f = 2\nu^2 - 2 \tag{1.38}$$

$$\beta_g = \kappa_3^{(1)}(M)\frac{\nu^3 - 3\nu}{2} - \frac{d\kappa_3^{(1)}/dM}{d(\log\sigma^{-1})/dM}\left(\frac{\nu - \nu^{-1}}{2}\right) \tag{1.39}$$

Although the above expressions are the result of a purely formal calculation, we will now show that each term has a natural interpretation.

Considering first the halo mass function (1.33), we have found a Press-Schechter mass function (with $\delta_c = 1.42$) in the Gaussian case, plus first-order corrections in $f_{\rm NL}$ and $g_{\rm NL}$

which agree with those found in [43, 44] using the Edgeworth expansion. This agreement is expected since the two calculations are based on the same barrier crossing model.

Moving on to halo bias, in the Gaussian case, we predict that $b(k)$ is constant on large scales, with value b_1 given by Eq. (1.35). The peak-background split argument suggests a general relation between the large-scale halo bias and the halo mass function which applies generally to a universal mass function of the form:

$$n(M) = \frac{\rho_m}{M} f(\nu) \frac{d \log \sigma^{-1}}{dM} \tag{1.40}$$

On large scales, the bias is predicted to be scale-independent and given by [7]:

$$b_1 = 1 - \frac{\nu}{\delta_c} \frac{d \log f}{d\nu} \tag{1.41}$$

Comparing our predictions (1.33), (1.35) for $n(M)$ and b_1, we find agreement, i.e. Eq. (1.35) for b_1 can be interpreted as the general peak-background split expression for halo bias, specialized to the Press-Schechter mass function.

More generally, the b_{1f} and b_{1g} contributions to the bias (Eqs. (1.36), (1.37)) represent shifts in the scale-independent part of the bias due to primordial non-Gaussianity. It is straightforward to check that these terms can be obtained by plugging the non-Gaussian mass function in Eq. (1.33) into the peak-background split prediction (1.41) for scale-independent bias, i.e. the b_{1f} and b_{1g} terms can be interpreted as changes to the bias which are entirely due to the mass function being perturbed in a non-Gaussian cosmology. This type of term (scale-independent bias proportional to $f_{\rm NL}$) was first found for $f_{\rm NL}$ cosmologies in [17]. Note that a scale-independent shift is unobservable in practice, and cannot be used to constrain non-Gaussianity, since the bias of a real tracer population, such as galaxies or quasars, is a free parameter.

The β_f contribution to the bias is the well-known scale-dependent bias in an $f_{\rm NL}$ cosmology. Comparing Eq. (1.38) for β_f with Eqs. (1.33), (1.35), this term can be written either as

$\beta_f = 2\partial(\log n)/\partial(\log \Delta_\Phi)$ or $\beta_f = 2\delta_c(b_1 - 1)$. (In §1.4, we referred to these as "weak" and "strong" predictions.)

The β_g contribution to the bias is the focus of this paper: scale-dependent bias in a $g_{\rm NL}$ cosmology. Eq. (1.39) gives this term in the "strong" form that was found previously (Eq. (1.26)) using the peak-background split argument. Alternately, we can write this term in the "weak" form $\beta_g = 3\partial(\log n)/\partial f_{\rm NL}$ using Eq. (1.33).

In summary, we have found that the complete expression for large-scale halo bias in the barrier crossing model (Eq. (1.34)) agrees perfectly with the peak-background split calculation from §1.4. The bias contains a scale-independent part $(b_1 + b_{1f} f_{\rm NL} + b_{1g} g_{\rm NL})$ which can be obtained from the halo mass function, via the general relation (1.41). The scale-independent bias depends on $f_{\rm NL}$ and $g_{\rm NL}$, because the halo mass function depends on these parameters. The bias also contains a scale-dependent part $(\beta_f f_{\rm NL} + \beta_g g_{\rm NL})/\alpha(k)$ whose coefficients can be calculated explicitly and agree with the peak-background split predictions.

1.5.3 Comparison with previous work

It is interesting to compare the above calculations with the results of [16] (see also [25]), where β_g was calculated using the MLB formula [49], which gives N-point functions of halos as an asymptotic series in ν. The scale-dependent $g_{\rm NL}$ bias was found to be (in our notation):

$$\beta_g^{\rm MLB} = \kappa_3^{(1)}(M)\frac{\delta_c \nu (b_1 - 1)}{2} \tag{1.42}$$

When this prediction was compared to N-body simulations, it was found to be a poor fit.

Comparing $\beta_g^{\rm MLB}$ with our calculation (1.39) for β_g, it is seen that the two agree in the high-mass limit $\nu \to \infty$, but disagree in subleading terms. This is expected since the MLB formula is based on the same barrier crossing model that we have used, but it is an asymptotic result, whereas we have done an exact calculation (to first order in $f_{\rm NL}$, $g_{\rm NL}$). For realistic halo masses, the "subleading" terms neglected in the MLB formula are of order

one (to quantify this better, β_g and $\beta_g^{\rm MLB}$ agree to 10% only when the halo bias $b_1 \geq 15$), so in practice the two predictions are quite different.

Recently, ref. [15] argued that the barrier crossing model cannot generate correct predictions for general non-Gaussian initial conditions such as the $g_{\rm NL}$ model, but we found the opposite conclusion: brute-force calculation in the barrier crossing model, collecting all terms of order $\mathcal{O}(g_{\rm NL})$, agrees precisely (i.e. to all orders in $1/\nu$) with the peak-background split. It seems intuitively plausible that two must be consistent, since the peak-background split argument depends only on the assumption that halo formation is determined by the local density field, and the barrier crossing model is a concrete example of a model in which this assumption is satisfied.

1.6 Results from N-body simulations

In the last two sections, we have obtained complete analytic predictions for large-scale bias in a $g_{\rm NL}$ cosmology, finding agreement between the peak-background split formalism (§1.4) and a barrier crossing model based on spherical collapse (§1.5).

To compare these predictions with simulation, we performed collisionless N-body simulations using the GADGET-2 TreePM code [64]. Simulations were done using periodic box size $R_{\rm box} = 1600\ h^{-1}$ Mpc, particle count $N_p = 1024^3$, and force softening length $R_s = 0.05(R_{\rm box}/N_p^{1/3})$. With these parameters and the fiducial cosmology from §1.2, the particle mass is $m_p = 2.92 \times 10^{11}\ h^{-1}\ M_\odot$.

We generate initial conditions by simulating a Gaussian primordial potential Φ, and applying $f_{\rm NL}$ or $g_{\rm NL}$ corrections by straightforward use of Eq. (1.1). We linearly evolve to redshift $z_{\rm ini} = 100$ using the transfer function[6] from CAMB [40], and obtain initial particle

[6]One subtlety here: straightforward use of CAMB's transfer function at redshift 100 leads to inconsistencies since CAMB includes radiation (which is not negligible at $z = 100$) in its expansion history, while GADGET does not. For this reason we use CAMB's linear transfer function at low redshift and extrapolate back to $z = 100$ using the growth function in an $\Omega_{\rm rad} = 0$ universe.

positions at this redshift using the Zeldovich approximation [69]. (At $z_{\rm ini} = 100$, transient effects due to use of this approximation should be negligible [10].)

After running the N-body simulation, we group particles into halos using an MPI parallelized implementation of the friends-of-friends algorithm [23] with link length $L_{\rm FOF} = 0.2 R_{\rm box} N_p^{-1/3}$. For a halo containing $N_{\rm FOF}$ particles, we assign a halo position given by the mean of the individual particle positions. We estimate halo bias $b(k) = P_{mh}(k)/P_{mm}(k)$ using the procedure described in Appendix A of [63]. The statistical error $\Delta b(k)$ obtained using this procedure is smaller than the error that would be obtained assuming uncorrelated estimates of the power spectra P_{mm} and P_{mh}, since shared sample variance is taken into account.

Results in this paper are based on 4 simulations with Gaussian initial conditions, 5 simulations with $g_{\rm NL} = \pm 2 \times 10^6$, and 3 simulations with $f_{\rm NL} = \pm 250$ (for a total of 20 simulations).

1.6.1 Fitting the functional form $b(k) = b_1 + \beta_g g_{\rm NL}/\alpha(k)$

We now compare our analytic prediction for $b(k)$ to simulation in several steps, corresponding to increasingly strong versions of the prediction.

First, consider the weakest possible question: our analytic prediction for the bias is of the functional form

$$b(k) = b_1 + \beta_g \frac{g_{\rm NL}}{\alpha(k)} \tag{1.43}$$

Is this is a good fit to simulation, if we treat the coefficients b_1 and β_g as free parameters? (We will compare our analytic prediction for β_g to simulation in the next subsection; for now we are just testing whether the functional form (1.43) is correct.)

In Fig. 1.1, we show some example fits of this form, for redshift $z = 0.5$ and halo mass range $1.15 \le M \le 1.83 \times 10^{14}\ h^{-1}\ M_\odot$. Each fit was performed using bias estimates from 4 independent simulations with $L_{\rm box} = 1600\ h^{-1}$ Mpc and wavenumbers $k \le 0.04\ h$ Mpc^{-1}.

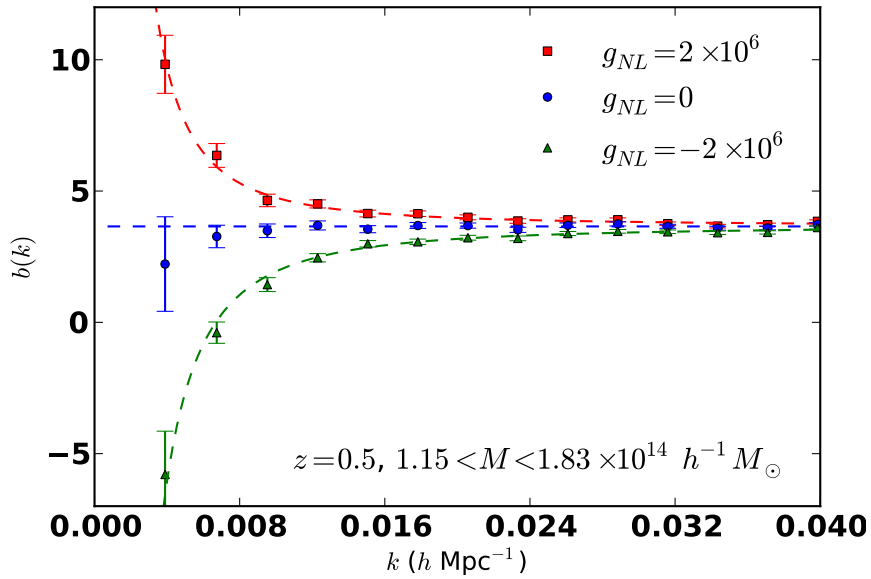

Figure 1.1: An example to illustrate that halo bias in a $g_{\rm NL}$ cosmology takes the functional form form $b(k) = b_1 + \beta_g g_{\rm NL}/\alpha(k)$. This figure corresponds to redshift $z = 0.5$ and halo mass range $1.15 \leq M \leq 1.83 \times 10^{14}\ h^{-1}\ M_\odot$, but we find the same functional form for all redshifts and halo masses.

We find good χ^2 values for the fits, with recovered parameters:

$$\begin{aligned} b_1 &= 3.653 \pm 0.026 && \text{for } g_{\rm NL} = 0 \\ (b_1, 10^3\beta_g) &= (3.575 \pm 0.038, 0.581 \pm 0.056) && \text{for } g_{\rm NL} = 2\times10^6 \\ (b_1, 10^3\beta_g) &= (3.824 \pm 0.039, 0.935 \pm 0.060) && \text{for } g_{\rm NL} = -2\times10^6 \end{aligned} \tag{1.44}$$

We note that the recovered bias parameters (1.44) in this example show that both b_1 and β_g are $g_{\rm NL}$-dependent. In the barrier crossing model, we made a prediction for the $g_{\rm NL}$ dependence of b_1 (Eq. (1.37)). We find good agreement between this prediction and our simulations. Note that in practice, the $g_{\rm NL}$ dependence of b_1 is unobservable since for a real tracer population, the halo occupation distribution is not known precisely and b_1 must be treated as a free parameter to be determined from data.

The observed $g_{\rm NL}$ dependence of β_g corresponds to scale-dependent bias of order $\mathcal{O}(g_{\rm NL}^2)$ or higher (note that β_g is defined in such a way that constant β_g corresponds to scale-dependent bias which is linear in $g_{\rm NL}$). This complicates comparison with our analytic

predictions, since we have only calculated the bias to order $\mathcal{O}(g_{\rm NL})$. We address this by estimating β_g by averaging the estimates obtained from simulations with $g_{\rm NL} = \pm 2 \times 10^6$, thus removing contributions to $b(k)$ which are proportional to $g_{\rm NL}^2$. Note that this does not remove $\mathcal{O}(g_{\rm NL}^3)$ contributions to the bias, but we have checked that such contributions are negligible for $g_{\rm NL} = \pm 2 \times 10^6$, by comparing with simulations with halved step size.

Repeating this fitting procedure for redshifts $z \in \{2, 1, 0.5, 0\}$ and a range of halo masses (the precise set of halo mass bins used is shown in Fig. 1.2 below), we find χ^2 values which are consistent with their expected distribution, i.e. we find that the functional form (1.43) is a good fit to the simulations for a wide range of redshifts and halo masses. For this reason, in subsequent sections, we will "compress" the estimates of $b(k)$ in each simulation (as shown in Fig. 1.1) to two numbers (b_1 and β_g), with statistical errors given by the fitting procedure.

1.6.2 Comparison with analytic predictions

Now that we have established the functional form $b(k) = b_1 + \beta_g g_{\rm NL}/\alpha(k)$ of the bias, and a procedure for estimating β_g from simulation as a function of redshift and halo mass, we would like to compare with our analytic predictions for β_g.

First, consider the "weak" form of the prediction ($\beta_g = 3(\partial \log n/\partial f_{\rm NL})$) obtained from the peak-background split argument. We can test this prediction by estimating the derivative $(\partial \log n/\partial f_{\rm NL})$ directly from simulations, by taking finite differences of $\log(n)$ in simulations with $f_{\rm NL} = \pm 250$. (We checked convergence in the step size.) We find that the prediction holds perfectly (within the statistical errors of the simulations) for all redshifts and halo masses (Fig. 1.2).

Second, consider the "strong" Edgeworth prediction (Eq. (1.39)), in which an explicit formula for β_g is given. In this case, we find reasonable agreement at high mass ($M \gtrsim 10^{14}$ h^{-1} $M_\odot$), but the prediction breaks down at low halo mass (Fig. 1.2).

Our interpretation is as follows. The peak-background split prediction $\beta_g = 3(\partial \log n/\partial f_{\rm NL})$ is a universal relation between bias in a $g_{\rm NL}$ cosmology and the mass function in an $f_{\rm NL}$

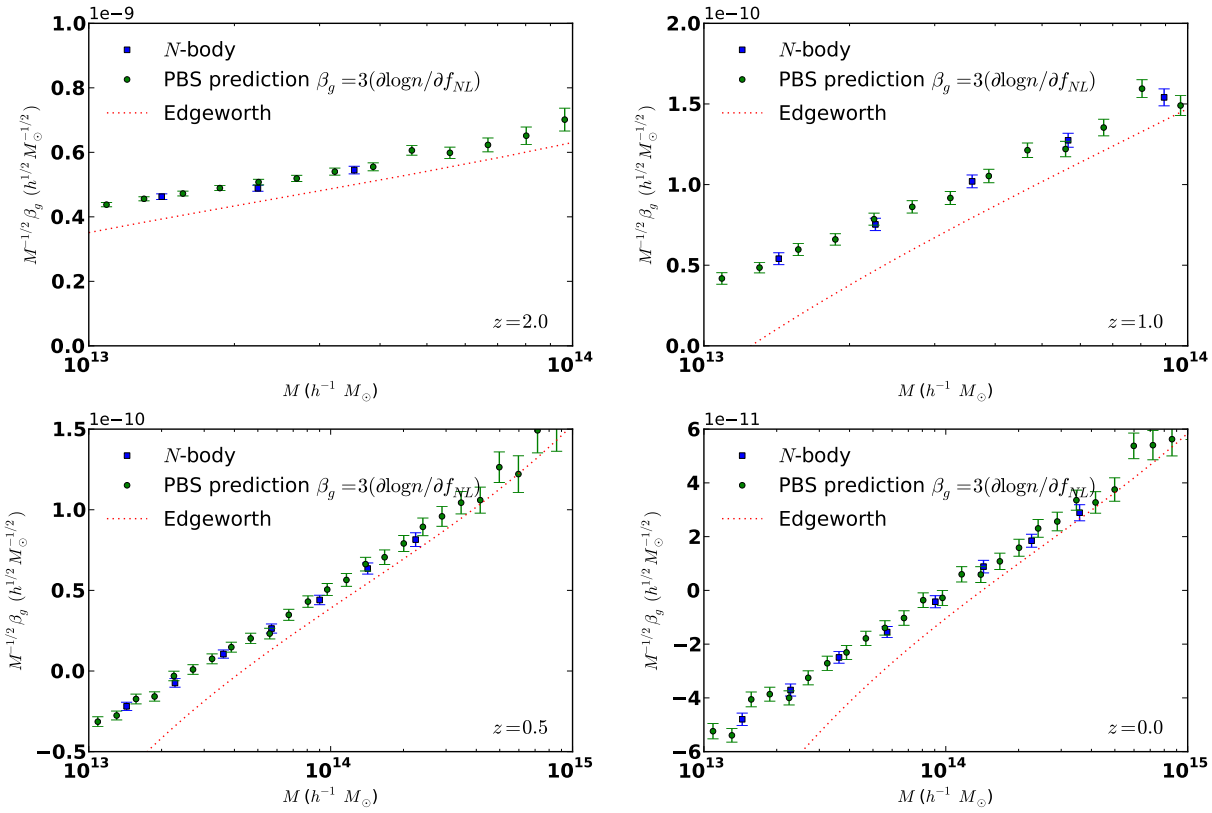

Figure 1.2: Comparison of the "weak" and "strong" predictions for the scale-dependent bias in a $g_{\rm NL}$ cosmology. **Blue squares:** Direct estimates of the bias, extracted from simulations with $g_{\rm NL} = \pm 2 \times 10^6$ as described in §1.6.1. **Green circles:** "Weak" analytic prediction for the bias ($\beta_g = 3(\partial \log n / \partial f_{\rm NL})$) from the peak-background split formalism, showing perfect agreement. The estimates of $(\partial \log n / \partial f_{\rm NL})$ shown in the figure were obtained directly from simulations with $f_{\rm NL} = \pm 250$. **Red dotted curve:** Edgeworth prediction for the bias (Eq. (1.39)). Good agreement is seen at high mass, but at low masses Edgeworth underpredicts $3(d \log n / df_{\rm NL})$. We will find an improvement in §1.6.3.

cosmology. Although "weak" in the sense that it does not supply a closed-form expression for β_g, the derivation makes few assumptions, and one expects it to be exact. In order to constrain $g_{\rm NL}$ from real data, we need a "strong" prediction which expresses β_g in closed form, using only observable quantities (i.e. the analog of the Dalal et al formula $\beta_f = 2\delta_c(b_1 - 1)$ for an $f_{\rm NL}$ cosmology). Using the Edgeworth expansion, one can make such a prediction in the context of the barrier crossing model (Eq. (1.39)), and obtain rough agreement with simulations, but the level of agreement is not really good enough for doing precision cosmology. Therefore, we next propose a slightly modified version of the Edgeworth prediction.

1.6.3 A simple universal formula for the bias in a $g_{\rm NL}$ cosmology

We would like to slightly modify the Edgeworth prediction (1.39) for β_g so that it agrees better with N-body simulations. It is also convenient to have a prediction in which β_g is given as a function of observable quantities: Gaussian bias b_1 (rather than halo mass, which is unobservable) and redshift z.

We start by rewriting the Edgeworth prediction (1.39) for β_g in terms of variables (b_1, z). The following fitting functions for κ_3 and $d\kappa_3/d\log(\sigma^{-1})$ are convenient:

$$\kappa_3 = 0.000329(1 + 0.09z)b_1^{-0.09} \tag{1.45}$$

$$\frac{d\kappa_3}{d\log\sigma^{-1}} = -0.000061(1 + 0.22z)b_1^{-0.25} \tag{1.46}$$

For purposes of this subsection, we *define* the quantity ν to be given in terms of b_1 and z by:

$$\nu = [\delta_c(b_1 - 1) + 1]^{1/2} \qquad (\text{where } \delta_c = 1.42) \tag{1.47}$$

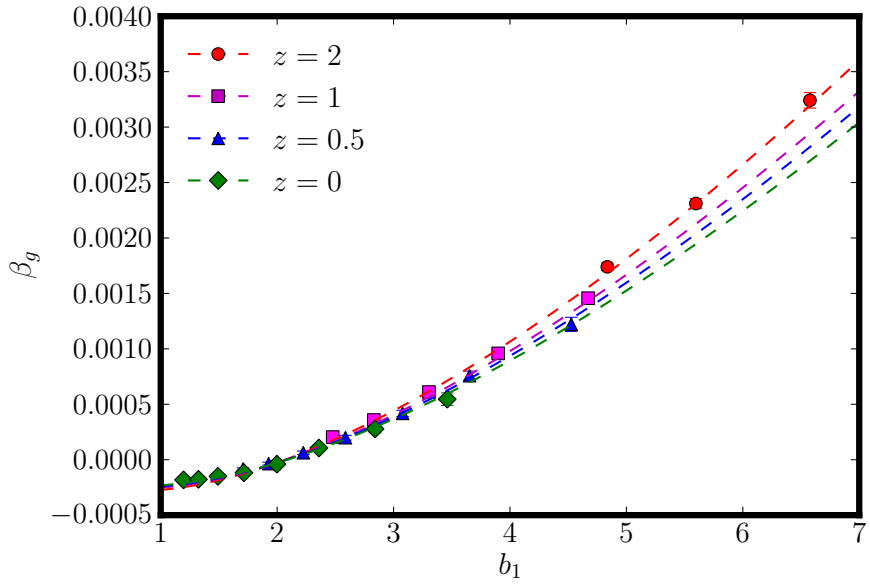

Figure 1.3: Scale-dependent $g_{\rm NL}$ bias coefficient β_g as a function of redshift z and halo bias b_1, showing excellent agreement between our final analytic result (Eq. (1.49), dashed curves) and N-body simulations (error bars).

The Edgeworth prediction for β_g can be written in the following form:

$$\beta_g^{\rm Edge.} = \kappa_3 \left[-1 + \frac{3}{2}(\nu-1)^2 + \frac{1}{2}(\nu-1)^3 \right] - \frac{d\kappa_3}{d\log\sigma^{-1}} \left(\frac{\nu - \nu^{-1}}{2} \right) \tag{1.48}$$

Empirically, we find that if we tweak the Edgeworth prediction by changing the coefficients of the polynomial in brackets as follows:

$$\beta_g = \kappa_3 \left[-0.7 + 1.4(\nu-1)^2 + 0.6(\nu-1)^3 \right] - \frac{d\kappa_3}{d\log\sigma^{-1}} \left(\frac{\nu - \nu^{-1}}{2} \right) \tag{1.49}$$

then we obtain good agreement with simulations (Fig. 1.3). The expression (1.49) for β_g (with quantities κ_3, $d\kappa_3/d\log\sigma^{-1}$, ν defined by Eqs. (1.45)–(1.47)) is one of the main results of this paper and is our observational "bottom line" when constraining $g_{\rm NL}$ from real data.

We have motivated our "tweak" to the Edgeworth prediction as essentially a fitting function for the ν dependence (although it is worth noting that the z dependence is correctly predicted by the barrier crossing model). A speculative interpretation of this tweak, which

we will defer for future work, is as follows. In the barrier crossing model, the second-order halo bias is given by $b_2 = (\nu^3 - 3\nu)/(\delta_c \sigma_M)$. It is tempting to conjecture that the expression in brackets in Eq. (1.49) is generally equal to $(\delta_c \sigma_M b_2)$, and interpret our "tweak" to the Edgeworth prediction (1.48) as perturbing the relation between b_1 and b_2, relative to the barrier crossing model. This opens up the possibility of directly measuring the second-order bias and determining β_g directly. To study the viability of this idea, one would need to compare β_g in simulation to some other estimate of second-order halo bias, such as the halo bispectrum in the squeezed limit.

1.6.4 An important caveat

There is an important caveat when using Eq. (1.49), or indeed any fitting function for the $g_{\rm NL}$ bias, to constrain $g_{\rm NL}$ from real data. It is tempting to compute β_g by simply plugging the observed bias b_1 and redshift z into Eq. (1.49). (Since the z-dependence is very mild, a rough estimate for the redshift suffices.) However, we have only shown that this procedure is correct in the limit of a narrow bin in halo mass and redshift, and a real tracer population will be a weighted average over M and z.

For example, consider the case in which the "tracers" are the dark matter particles themselves, i.e. each halo is weighted in proportion to its mass (assuming all mass is in halos). This tracer population has bias $b_1 = 1$ (for the trivial reason that we are back to the dark matter field), so straightforward use of Eq. (1.49) would suggest that $\beta_g \approx -0.00025$. (This value would make the low-k power spectrum a reasonably sensitive probe of $g_{\rm NL}$.) In fact, the true β_g of this tracer is zero, since the matter power spectrum $P_{mm}(k)$ does not contain a term proportional to $g_{\rm NL}/\alpha(k)$. This example shows that the true $g_{\rm NL}$ bias of a tracer population can differ significantly from the value obtained by straightforward

use of Eq. (1.49). In general, the $g_{\rm NL}$ bias will depend on the full HOD (halo occupation distribution) of the tracer population, not only on the Gaussian bias b_1.[7]

One popular approach to modeling the HOD is to assume that halos below some minimum mass $M_{\rm min}$ do not host tracers, whereas the mean number of tracers in a halo of mass $M \geq M_{\rm min}$ is proportional to the total mass M. For reference, we give a fitting function for the $g_{\rm NL}$ bias for this HOD:

$$\beta_g = \kappa_3 \Big[-0.4(\nu-1) + 1.5(\nu-1)^2 + 0.6(\nu-1)^3 \Big] \tag{1.50}$$

where for purposes of this equation, κ_3 and ν are defined as functions of the observables b_1 and z by Eqs. (1.45), (1.47) above.

Eq. (1.50) applies to a mass-weighted population of halos above $M_{\rm min}$, whereas Eq. (1.49) applies to a population which is narrowly selected in mass. The two agree for $b_1 \gtrsim 2.5$, suggesting that HOD dependence is small in practice for highly biased samples, but disagree qualitatively for $b_1 \lesssim 2.5$. For example, the $g_{\rm NL}$ bias β_g changes sign at $b_1 \approx 2.1$ for the narrowly selected sample (Eq. (1.49)), whereas β_g is always positive for the mass-weighted sample (Eq. (1.50)).

Our perspective is that, in order to obtain $g_{\rm NL}$ constraints which are robust to HOD modeling uncertainty, one should use highly biased samples ($b_1 \gtrsim 2.5$), where this uncertainty will be minimized. Samples which are not highly biased do not give robust constraints; for example, a tracer population with $b_1 = 1.8$ can have a $g_{\rm NL}$ bias β_g which is negative, zero, or positive, depending on the HOD.

For highly biased samples, it is useful to make the following observation: the $g_{\rm NL}$ bias $\beta_g^{\rm fit}$ which is obtained from straightforward use of Eq. (1.49) is always less than the true $g_{\rm NL}$ bias $\beta_g^{\rm true}$.[8] This follows from positivity of the second derivative $d^2\beta_g/db_1^2$. It follows that a

[7] Note that there is no analogous caveat in the $f_{\rm NL}$ case. Because the relation $\beta_f = 2\delta_c(b_1 - 1)$ is linear, it applies to both a tracer population which is narrowly selected in (M, z) and to a population which is an arbitrary weighted average over (M, z).

[8] This statement assumes that the probability that a halo hosts a tracer is a function only of the mass and redshift. If the probability depends strongly on additional variables such as merger history, triaxiality,

$g_{\rm NL}$ constraint obtained using $\beta_g^{\rm fit}$ is always valid, but slightly overestimates the statistical error that could be obtained if $\beta_g^{\rm true}$ were known. This effectively treats HOD uncertainty as an extra source of systematic error.

1.7 Discussion

We have computed large-scale halo bias for non-Gaussian initial conditions, using two analytic frameworks: the peak-background split formalism (§1.4) and a barrier crossing model (§1.5), finding agreement between the two. Although our emphasis has been on the constant-$f_{\rm NL}$ and constant-$g_{\rm NL}$ models, our calculational machinery should apply to more general non-Gaussian initial conditions.

The peak-background split formalism is simpler and also suggests a simple physical picture of non-Gaussian cosmologies on large scales. In an $f_{\rm NL}$ cosmology, the amplitude Δ_Φ of the initial fluctuations is not spatially constant, but is proportional to $(1 + 2f_{\rm NL}\Phi_l)$. Thus, Δ_Φ has fluctuations on large scales which are 100% correlated with the long-wavelength potential, generating halo bias of the form $(\beta_f f_{\rm NL}/\alpha(k))$. In a $g_{\rm NL}$ cosmology, the small-scale skewness is nonzero and proportional to $(g_{\rm NL}\Phi_l)$, leading to halo bias of the form $(\beta_g g_{\rm NL}/\alpha(k))$. The peak-background split argument is very useful for generating universal relations such as $\beta_g = 3\partial(\log n)/\partial f_{\rm NL}$, which are "weak" in the sense that the RHS has not been expressed in terms of observable quantities, but have the advantage of being exact (as can be seen by comparing the two sets of errorbars in Fig. 1.2).

The barrier crossing model generates all terms in the large-scale bias, including terms such as b_{1f} and b_{1g} which are easy to miss, by a purely algorithmic calculational procedure. In addition, the barrier crossing model generates "strong" forms of the bias coefficients (e.g. the Edgeworth expression (1.39) for β_g), which are closed-form expressions in M and z. However,

etc. then this will generate additional contributions to β_g, in analogy to the $f_{\rm NL}$ case [62, 57]. In principle, selection biases to β_g can be addressed by folding the selection into the mass function when computing $\partial(\log n)/\partial f_{\rm NL}$, but detailed study is beyond the scope of this paper.

these expressions are not exact because the barrier crossing model is approximation to the true process of halo formation.

To obtain a "bottom line" expression for the scale-dependent $g_{\rm NL}$ bias β_g in terms of redshift z and Gaussian bias z, we found it necessary to tweak slightly the b_1 dependence of the Edgeworth prediction, arriving at the expression (1.49) which agrees very well with simulations. The caveat is that Eq. (1.49) applies only to a halo population which has been selected in a narrow halo mass and redshift range. In principle, one can calculate β_g for a tracer population by multiplying by the halo occupation distribution and integrating over mass and redshift. In practice, the HOD is not known precisely and we have argued in §1.6.4 that the best approach is to only use highly biased populations ($b \gtrsim 2.5$) for constraining $g_{\rm NL}$. Since β_g is a rapidly increasing function of b_1, this strategy makes sense both from the perspective of minimizing statistical errors, and systematic errors due to HOD uncertainty. In data analysis, it may be useful to impose cuts which increase the mean halo bias at the expense of reducing the number of tracers. Another advantage of subdividing tracer populations is that this may permit $f_{\rm NL}$ and $g_{\rm NL}$ to be constrained simultaneously (with a single tracer population, the two are degenerate).

Acknowledgements

We thank Neal Dalal, Vincent Desjacques, Chris Hirata, Donghui Jeong, Brant Robertson, Fabian Schmidt, Neelima Sehgal, David Spergel and Matias Zaldarriaga for helpful discussions. K. M. S. is supported by a Lyman Spitzer fellowship in the Department of Astrophysical Sciences at Princeton University. M. L. is supported as a Friends of the Institute for Advanced Study Member and by the NSF though AST-0807444. S. F. is supported by the Martin Schwarzschild Fund in Astronomy at Princeton University. Simulations in this paper were performed at the TIGRESS high performance computer center at Princeton University which is jointly supported by the Princeton Institute for Computational Science and Engineering and the Princeton University Office of Information Technology.

1.8 Appendix: Barrier model calculations

In this appendix, we give details of the calculation of the halo mass function and large-scale bias (Eqs. (1.33)–(1.39)) in the barrier crossing model, to first order in $f_{\rm NL}$, $g_{\rm NL}$.

First, consider evaluation of the integrals in Eqs. (1.29), (1.30). Primordial non-Gaussianity enters the calculation by perturbing the PDFs which appear from Gaussian distributions. This perturbation can be written down explicitly using the Edgeworth expansion, which represents the PDF as a power series in cumulants. The Edgeworth expansion for the 1-variable PDF $p(\delta'_M)$ is:

$$\begin{aligned} p(\delta'_M) &= \exp\left(\sum_{n\geq 3}\frac{(-1)^n}{n!}\kappa_n(M)\sigma_M^n\frac{\partial^n}{\partial\delta'^n_M}\right)\frac{1}{(2\pi)^{1/2}\sigma_M}e^{-\delta'^2_M/(2\sigma^2_M)} \\ &= \frac{1}{(2\pi)^{1/2}\sigma_M}e^{-\delta'^2_M/(2\sigma^2_M)}\left(1+\frac{\kappa_3(M)}{6}H_3(\nu)+\frac{\kappa_4(M)}{24}H_4(\nu)+\cdots\right) \\ &= \frac{1}{(2\pi)^{1/2}\sigma_M}e^{-\delta'^2_M/(2\sigma^2_M)}\left(1+f_{\rm NL}\frac{\kappa_3^{(1)}(M)}{6}H_3(\nu)+g_{\rm NL}\frac{\kappa_4^{(1)}(M)}{24}H_4(\nu)+\cdots\right) \end{aligned} \tag{1.51}$$

where we have kept terms of first order in $f_{\rm NL}$, $g_{\rm NL}$. We can now compute p_0 by plugging into the definition (1.29):

$$p_0 = \frac{1}{2}{\rm erfc}\left(\frac{\nu}{\sqrt{2}}\right)+f_{\rm NL}\frac{\kappa_3^{(1)}(M)}{6}\frac{e^{-\nu^2/2}}{(2\pi)^{1/2}}H_2(\nu)+g_{\rm NL}\frac{\kappa_4^{(1)}(M)}{24}\frac{e^{-\nu^2/2}}{(2\pi)^{1/2}}H_3(\nu) \tag{1.52}$$

Armed with this expression, it is easy to compute $n(M) = -2\rho_m/M(dp_0/dM)$, obtaining the form of the mass function in Eq. (1.33).

Moving on to the 2-variable PDF $p(\delta_{\rm lin},\delta'_M)$, the Edgeworth expansion is:

$$\begin{aligned} p(\delta_{\rm lin},\delta'_M) &= \exp\left(\sigma_{\rm lin}\sigma_M\kappa_{1,1}\frac{\partial^2}{\partial\delta_{\rm lin}\,\partial\delta'_M}+\sum_{\substack{m,n\\ m+n\geq 3}}\frac{(-1)^{m+n}}{m!n!}\sigma_{\rm lin}^m\sigma_M^n\kappa_{m,n}\frac{\partial^{m+n}}{\partial\delta_{\rm lin}^m\partial\delta'^n_M}\right) \\ &\quad\times\frac{1}{2\pi\sigma_{\rm lin}\sigma_M}\exp\left(-\frac{\delta^2_{\rm lin}}{2\sigma^2_{\rm lin}}-\frac{\delta'^2_M}{2\sigma^2_M}\right) \end{aligned} \tag{1.53}$$

where $\sigma_{\rm lin} = \langle \delta_{\rm lin}^2 \rangle^{1/2}$ and the cumulant $\kappa_{m,n}$ is defined by:[9]

$$\kappa_{m,n}(M,r) = \frac{\langle (\delta_{\rm lin})^m (\delta'_M)^n \rangle_{\rm conn}}{\sigma_{\rm lin}^m \sigma_M^n} \tag{1.54}$$

Note that the cumulant $\kappa_n(M)$ defined previously in Eq. (1.7) is equal to $\kappa_{0,n}(M,r)$.

Keeping the first few terms in the Edgeworth expansion:[10]

$$\begin{aligned} p(\delta_{\rm lin}, \delta'_M) &= \frac{1}{2\pi\sigma_{\rm lin}\sigma_M} \exp\left(-\frac{\delta_{\rm lin}^2}{2\sigma_{\rm lin}^2} - \frac{\delta_M'^2}{2\sigma_M^2}\right) \\ &\quad \times \left(1 + \frac{\kappa_{1,1}(M,r)}{\sigma_{\rm lin}} \delta_{\rm lin}\left(\frac{\delta'_M}{\sigma_M}\right) + \frac{\kappa_{1,2}(M,r)}{2\sigma_{\rm lin}} \delta_{\rm lin} H_2\left(\frac{\delta'_M}{\sigma_M}\right)\right. \\ &\quad + \frac{\kappa_{1,3}(M,r)}{6\sigma_{\rm lin}} \delta_{\rm lin} H_3\left(\frac{\delta'_M}{\sigma_M}\right) + \frac{\kappa_{1,1}(M,r)\kappa_{0,3}(M)}{6\sigma_{\rm lin}} \delta_{\rm lin} H_4\left(\frac{\delta'_M}{\sigma_M}\right) \\ &\quad \left. + \frac{\kappa_{1,1}(M,r)\kappa_{0,4}(M)}{24\sigma_{\rm lin}} \delta_{\rm lin} H_5\left(\frac{\delta'_M}{\sigma_M}\right) + \cdots\right) \end{aligned} \tag{1.55}$$

we compute $\xi_0(r)$ by integrating Eq. (1.30) term by term, obtaining:

$$\begin{aligned} \xi_0(r) &= \frac{\sigma_{\rm lin} e^{-\nu^2/2}}{(2\pi)^{1/2}} \left(\kappa_{1,1}(M,r) + \frac{\kappa_{1,2}(M,r)}{2}\nu + \frac{\kappa_{1,3}(M,r)}{6} H_2(\nu)\right. \\ &\quad \left. + \frac{\kappa_{1,1}(M,r)\kappa_3(M)}{6} H_3(\nu) + \frac{\kappa_{1,1}(M,r)\kappa_4(M)}{24} H_4(\nu)\right) \end{aligned} \tag{1.56}$$

To make further progress, we convert the correlation function to a power spectrum $P_0(k) = \int d^3\boldsymbol{r}\, e^{i\boldsymbol{k}\cdot\boldsymbol{r}} \xi_0(r)$, and keep only the leading behavior of each term in the long-wavelength

[9] A technical point: $\sigma_{\rm lin}$ is formally infinite, but it will cancel from the final results in Eqs. (1.35)–(1.39). One could make $\sigma_{\rm lin}$ finite by introducing a smoothing scale R for the matter field, and take the limit $R \to 0$ at the end of the calculation.

[10] The choice of terms to keep was dictated by the following considerations. Only terms with precisely one $\delta_{\rm lin}$ derivative will give nonzero contributions to the integral $\int_{-\infty}^{\infty} d\delta_{\rm lin}\, \delta_{\rm lin} p(\delta_{\rm lin}, \delta'_M)$ appearing in $\xi_{mh}(r)$, so we have only kept these terms. (Terms with two or more derivatives would contribute to the halo-halo correlation function $\xi_{hh}(r)$, so they may be relevant for halo stochasticity.) We have also omitted terms whose leading contribution is second-order or higher in $f_{\rm NL}$ and $g_{\rm NL}$.

limit $k \to 0$.

$$\begin{aligned}\int d^3\boldsymbol{r}\, e^{i\boldsymbol{k}\cdot\boldsymbol{r}}\kappa_{1,2}(M,r) &= \frac{1}{\sigma_{\rm lin}\sigma_M^2}\int\frac{d^3\boldsymbol{q}\,d^3\boldsymbol{q}'}{(2\pi)^6}W_M(q)W_M(q')\left\langle\delta(\boldsymbol{k})\delta(\boldsymbol{q})\delta(-\boldsymbol{q}')\right\rangle \\ &\to \frac{4f_{\rm NL}}{\sigma_{\rm lin}}\frac{P(k)}{\alpha(k)} \end{aligned} \tag{1.57}$$

$$\begin{aligned}\int d^3\boldsymbol{r}\, e^{i\boldsymbol{k}\cdot\boldsymbol{r}}\kappa_{1,3}(M,r) &= \frac{1}{\sigma_{\rm lin}\sigma_M^3}\int\frac{d^3\boldsymbol{q}\,d^3\boldsymbol{q}'\,d^3\boldsymbol{q}''}{(2\pi)^9}W_M(q)W_M(q')W_M(q'') \\ &\qquad\times\left\langle\delta(\boldsymbol{k})\delta(\boldsymbol{q})\delta(\boldsymbol{q}')\delta(-\boldsymbol{q}'')\right\rangle_{\rm conn} \\ &\to \frac{18g_{\rm NL}P(k)}{\sigma_{\rm lin}\sigma_M^3\alpha(k)}\int\frac{d^3\boldsymbol{q}\,d^3\boldsymbol{q}'}{(2\pi)^6}W_M(q)W_M(q')W_M(|\boldsymbol{q}+\boldsymbol{q}'|) \\ &\qquad\times\frac{P(q)P(q')\alpha(|\boldsymbol{q}+\boldsymbol{q}'|)}{\alpha(q)\alpha(q')} \\ &= \frac{3g_{\rm NL}}{\sigma_{\rm lin}}\kappa_3^{(1)}(M)\left(\frac{P(k)}{\alpha(k)}\right) \end{aligned} \tag{1.58}$$

where "$\to$" denotes the $k \to 0$ limit, and we have used Eq. (1.10) to simplify the last line. Putting this together, we find the following expression for $P_0(k)$ in the $k \to 0$ limit:

$$\begin{aligned}P_0(k) &= \frac{e^{-\nu^2/2}}{(2\pi)^{1/2}}\left[\frac{P(k)}{\sigma_M}\left(1 + f_{\rm NL}\frac{\kappa_3^{(1)}(M)}{6}H_3(\nu) + g_{\rm NL}\frac{\kappa_4^{(1)}(M)}{24}H_4(\nu)\right)\right. \\ &\qquad\left. +2\nu f_{\rm NL}\frac{P(k)}{\alpha(k)} + \kappa_3^{(1)}(M)\frac{H_2(\nu)}{2}g_{\rm NL}\frac{P(k)}{\alpha(k)}\right] \end{aligned} \tag{1.59}$$

The halo bias in a narrow mass range is given by the derivative:

$$b(k) = \frac{dP_0(k)/dM}{(dp_0/dM)P(k)} + 1 \tag{1.60}$$

where the "+1" converts Lagrangian to Eulerian bias. Plugging in the forms of p_0, P_0 in Eqs. (1.52), (1.59), a long but straightforward calculation now gives the halo bias in the form given in the text (Eqs. (1.34)–(1.39)).

Bibliography

[1] Andreas Albrecht and Paul J. Steinhardt. Cosmology for Grand Unified Theories with Radiatively Induced Symmetry Breaking. *Phys. Rev. Lett.*, 48:1220–1223, 1982.

[2] James M. Bardeen, Paul J. Steinhardt, and Michael S. Turner. Spontaneous Creation of Almost Scale - Free Density Perturbations in an Inflationary Universe. *Phys. Rev.*, D28:679, 1983.

[3] Evgeny I. Buchbinder, Justin Khoury, and Burt A. Ovrut. Non-Gaussianities in New Ekpyrotic Cosmology. *Phys. Rev. Lett.*, 100:171302, 2008.

[4] Christian T. Byrnes and Gianmassimo Tasinato. Non-Gaussianity beyond slow roll in multi-field inflation. *JCAP*, 0908:016, 2009.

[5] Pravabati Chingangbam and Qing-Guo Huang. The Curvature Perturbation in the Axion-type Curvaton Model. *JCAP*, 0904:031, 2009.

[6] Sirichai Chongchitnan and Joseph Silk. A Study of High-Order Non-Gaussianity with Applications to Massive Clusters and Large Voids. *Astrophys.J.*, 724:285–295, 2010.

[7] Shaun Cole and Nick Kaiser. Biased clustering in the cold dark matter cosmogony. *Mon. Not. Roy. Astron. Soc.*, 237:1127–1146, 1989.

[8] Paolo Creminelli and Leonardo Senatore. A smooth bouncing cosmology with scale invariant spectrum. *JCAP*, 0711:010, 2007.

[9] Paolo Creminelli and Matias Zaldarriaga. Single field consistency relation for the 3-point function. *JCAP*, 0410:006, 2004.

[10] M. Crocce, S. Pueblas, and R. Scoccimarro. Transients from Initial Conditions in Cosmological Simulations. *Mon. Not. Roy. Astron. Soc.*, 373:369–381, 2006.

[11] Carlos Cunha, Dragan Huterer, and Olivier Dore. Primordial non-Gaussianity from the covariance of galaxy cluster counts. *Phys. Rev.*, D82:023004, 2010.

[12] Neal Dalal, Olivier Dore, Dragan Huterer, and Alexander Shirokov. The imprints of primordial non-gaussianities on large- scale structure: scale dependent bias and abundance of virialized objects. *Phys. Rev.*, D77:123514, 2008.

[13] Guido D'Amico, Marcello Musso, Jorge Norena, and Aseem Paranjape. An Improved Calculation of the Non-Gaussian Halo Mass Function. *JCAP*, 2, 001, 2011.

[14] Andrea De Simone, Michele Maggiore, and Antonio Riotto. Excursion Set Theory for generic moving barriers and non- Gaussian initial conditions, *Mon. Not. Roy. Astron. Soc.*, 412, 2587, 2011.

[15] Vincent Desjacques, Donghui Jeong, and Fabian Schmidt. Non-Gaussian Halo Bias Re-examined: Mass-dependent Amplitude from the Peak-Background Split and Thresholding. *Phys. Rev.*, D84, 063512, 2011.

[16] Vincent Desjacques and Uros Seljak. Signature of primordial non-Gaussianity of ϕ^3-type in the mass function and bias of dark matter haloes. *Phys. Rev.*, D81:023006, 2010.

[17] Vincent Desjacques, Uros Seljak, and Ilian Iliev. Scale-dependent bias induced by local non-Gaussianity: A comparison to N-body simulations, *Mon. Not. Roy. Astron. Soc.*, 396, 85, 2009.

[18] J. Dunkley et al. Five-Year Wilkinson Microwave Anisotropy Probe (WMAP) Observations: Likelihoods and Parameters from the WMAP data. *Astrophys. J. Suppl.*, 180:306–329, 2009.

[19] Gia Dvali, Andrei Gruzinov, and Matias Zaldarriaga. A new mechanism for generating density perturbations from inflation. *Phys. Rev.*, D69:023505, 2004.

[20] Kari Enqvist and Tomo Takahashi. Signatures of Non-Gaussianity in the Curvaton Model. *JCAP*, 0809:012, 2008.

[21] J. R. Fergusson, D. M. Regan, and E. P. S. Shellard. Optimal Trispectrum Estimators and WMAP Constraints. arXiv:1012.6039, 2010.

[22] Daniel Baumann, Simone Ferraro, Daniel Green, and Kendrick M. Smith. Stochastic bias from non-Gaussian initial conditions, *JCAP*, 5, 001, 2013.

[23] Carlos S. Frenk, Simon D. M. White, Marc Davis, and George Efstathiou. The formation of dark halos in a universe dominated by cold dark matter. *Astrophys. J.*, 327:507–525, 1988.

[24] Alejandro Gangui, Francesco Lucchin, Sabino Matarrese, and Silvia Mollerach. The Three point correlation function of the cosmic microwave background in inflationary models. *Astrophys. J.*, 430:447–457, 1994.

[25] Tommaso Giannantonio and Cristiano Porciani. Structure formation from non-Gaussian initial conditions: multivariate biasing, statistics, and comparison with N- body simulations. *Phys. Rev.*, D81:063530, 2010.

[26] M. Grossi, K. Dolag, E. Branchini, S. Matarrese, and L. Moscardini. Evolution of Massive Haloes in non-Gaussian Scenarios. *Mon. Not. Roy. Astron. Soc.*, 382:1261, 2007.

[27] Alan H. Guth. The Inflationary Universe: A Possible Solution to the Horizon and Flatness Problems. *Phys. Rev.*, D23:347–356, 1981.

[28] Alan H. Guth and S. Y. Pi. Fluctuations in the New Inflationary Universe. *Phys. Rev. Lett.*, 49:1110–1113, 1982.

[29] Nico Hamaus, Uros Seljak, and Vincent Desjacques. Optimal Constraints on Local Primordial Non-Gaussianity from the Two-Point Statistics of Large-Scale Structure. *Phys. Rev.*, D84, 083509, 2011.

[30] S. W. Hawking. The Development of Irregularities in a Single Bubble Inflationary Universe. *Phys. Lett.*, B115:295, 1982.

[31] Qing-Guo Huang. Curvaton with Polynomial Potential. *JCAP*, 0811:005, 2008.

[32] Qing-Guo Huang. A geometric description of the non-Gaussianity generated at the end of multi-field inflation. *JCAP*, 0906:035, 2009.

[33] Kazuhide Ichikawa, Teruaki Suyama, Tomo Takahashi, and Masahide Yamaguchi. Non-Gaussianity, Spectral Index and Tensor Modes in Mixed Inflaton and Curvaton Models. *Phys. Rev.*, D78:023513, 2008.

[34] Richard Kessler et al. First-year Sloan Digital Sky Survey-II (SDSS-II) Supernova Results: Hubble Diagram and Cosmological Parameters. *Astrophys. J. Suppl.*, 185:32–84, 2009.

[35] Lev Kofman. Probing string theory with modulated cosmological fluctuations. arXiv:astro-ph/0303614, 2003.

[36] E. Komatsu et al. Seven-Year Wilkinson Microwave Anisotropy Probe (WMAP) Observations: Cosmological Interpretation. *Astrophys. J. Suppl.*, 192:18, 2011.

[37] Eiichiro Komatsu and David N. Spergel. Acoustic signatures in the primary microwave background bispectrum. *Phys. Rev.*, D63:063002, 2001.

[38] Tsz Yan Lam and Ravi K. Sheth. Halo abundances in the f_{nl} model. *Mon. Not. Roy. Astron. Soc.*, 398, 2143, 2009.

[39] Jean-Luc Lehners and Paul J. Steinhardt. Non-Gaussian Density Fluctuations from Entropically Generated Curvature Perturbations in Ekpyrotic Models. *Phys. Rev.*, D77:063533, 2008.

[40] Antony Lewis, Anthony Challinor, and Anthony Lasenby. Efficient Computation of CMB anisotropies in closed FRW models. *Astrophys. J.*, 538:473–476, 2000.

[41] Andrei D. Linde. Chaotic Inflation. *Phys. Lett.*, B129:177–181, 1983.

[42] Andrei D. Linde and Viatcheslav F. Mukhanov. Nongaussian isocurvature perturbations from inflation. *Phys. Rev.*, D56:535–539, 1997.

[43] Marilena LoVerde, Amber Miller, Sarah Shandera, and Licia Verde. Effects of Scale-Dependent Non-Gaussianity on Cosmological Structures. *JCAP*, 0804:014, 2008.

[44] Marilena LoVerde and Kendrick M. Smith. The Non-Gaussian Halo Mass Function with f_{NL}, g_{NL} and τ_{NL}, *JCAP* 08, 003, 2011.

[45] David H. Lyth, Carlo Ungarelli, and David Wands. The primordial density perturbation in the curvaton scenario. *Phys. Rev.*, D67:023503, 2003.

[46] David H. Lyth and David Wands. Generating the curvature perturbation without an inflaton. *Phys. Lett.*, B524:5–14, 2002.

[47] Michele Maggiore and Antonio Riotto. The halo mass function from the excursion set method. III. First principle derivation for non-Gaussian theories. *Astrophys. J.*, 717, 526, 2009.

[48] Juan Martin Maldacena. Non-Gaussian features of primordial fluctuations in single field inflationary models. *JHEP*, 05:013, 2003.

[49] Sabino Matarrese, Francesco Lucchin, and Silvio A. Bonometto. A Path Integral Approach to Large Scale Matter Distribution Originated by Non-Gaussian Fluctuations. *Astrophys. J.*, 310:L21–l26, 1986.

[50] Sabino Matarrese and Licia Verde. The effect of primordial non-Gaussianity on halo bias. *Astrophys. J.*, 677:L77, 2008.

[51] Sabino Matarrese, Licia Verde, and Raul Jimenez. The abundance of high-redshift objects as a probe of non- Gaussian initial conditions. *Astrophys. J.*, 541:10, 2000.

[52] Takemi Okamoto and Wayne Hu. The Angular Trispectra of CMB Temperature and Polarization. *Phys. Rev.*, D66:063008, 2002.

[53] Will J. Percival et al. Baryon Acoustic Oscillations in the Sloan Digital Sky Survey Data Release 7 Galaxy Sample. *Mon. Not. Roy. Astron. Soc.*, 401:2148–2168, 2010.

[54] Annalisa Pillepich, Cristiano Porciani, and Oliver Hahn. Universal halo mass function and scale-dependent bias from N-body simulations with non-Gaussian initial conditions. *Mon. Not. Roy. Astron. Soc.*, 402, 191, 2010.

[55] William H. Press and Paul Schechter. Formation of galaxies and clusters of galaxies by selfsimilar gravitational condensation. *Astrophys. J.*, 187:425–438, 1974.

[56] Beth A. Reid et al. Cosmological Constraints from the Clustering of the Sloan Digital Sky Survey DR7 Luminous Red Galaxies. *Mon. Not. Roy. Astron. Soc.*, 404:60–85, 2010.

[57] Beth A. Reid, Licia Verde, Klaus Dolag, Sabino Matarrese, and Lauro Moscardini. Non-Gaussian halo assembly bias. *JCAP*, 1007:013, 2010.

[58] Adam G. Riess et al. A 3% Solution: Determination of the Hubble Constant with the Hubble Space Telescope and Wide Field Camera 3. *Astrophys. J.*, 730:119, 2011.

[59] D. S. Salopek and J. R. Bond. Nonlinear evolution of long wavelength metric fluctuations in inflationary models. *Phys. Rev.*, D42:3936–3962, 1990.

[60] Misao Sasaki, Jussi Valiviita, and David Wands. Non-gaussianity of the primordial perturbation in the curvaton model. *Phys. Rev.*, D74:103003, 2006.

[61] Ravi K. Sheth and Giuseppe Tormen. Large scale bias and the peak background split. *Mon. Not. Roy. Astron. Soc.*, 308:119, 1999.

[62] Anze Slosar, Christopher Hirata, Uros Seljak, Shirley Ho, and Nikhil Padmanabhan. Constraints on local primordial non-Gaussianity from large scale structure. *JCAP*, 0808:031, 2008.

[63] Kendrick M. Smith and Marilena LoVerde. Local stochastic non-Gaussianity and N-body simulations. *JCAP*, 11, 009, 2011.

[64] Volker Springel. The cosmological simulation code GADGET-2. *Mon. Not. Roy. Astron. Soc.*, 364:1105–1134, 2005.

[65] Alexei A. Starobinsky. Dynamics of Phase Transition in the New Inflationary Universe Scenario and Generation of Perturbations. *Phys. Lett.*, B117:175–178, 1982.

[66] A. Vikhlinin et al. Chandra Cluster Cosmology Project III: Cosmological Parameter Constraints. *Astrophys. J.*, 692:1060–1074, 2009.

[67] Michael S. Warren, Kevork Abazajian, Daniel E. Holz, and Luis Teodoro. Precision Determination of the Mass Function of Dark Matter Halos. *Astrophys. J.*, 646:881–885, 2006.

[68] Jun-Qing Xia, Carlo Baccigalupi, Sabino Matarrese, Licia Verde, and Matteo Viel. Constraints on Primordial Non-Gaussianity from Large Scale Structure Probes. *JCAP*, 8, 033, 2011.

[69] Ya. B. Zeldovich. Gravitational instability: An Approximate theory for large density perturbations. *Astron. Astrophys.*, 5:84–89, 1970.

Chapter 2

Stochastic Bias from Non-Gaussian Initial Conditions

2.1 Abstract

In this chapter we show that a stochastic form of scale-dependent halo bias arises in multi-source inflationary models, where multiple fields determine the initial curvature perturbation. We derive this effect for general non-Gaussian initial conditions and study various examples, such as curvaton models and quasi-single field inflation. We present a general formula for both the stochastic and the non-stochastic parts of the halo bias, in terms of the N-point cumulants of the curvature perturbation at the end of inflation. At lowest order, the stochasticity arises if the collapsed limit of the four-point function is boosted relative to the square of the three-point function in the squeezed limit. We derive all our results in two ways, using the barrier crossing formalism and the peak-background split method. In the next chapter, which was published as a companion paper [1], we prove that these two approaches are mathematically equivalent.

2.2 Introduction

A central goal of modern cosmology is to uncover the physics that generated the primordial density perturbations and thereby seeded the large-scale structures (LSS) we see around us. The coherent nature of the cosmic microwave background (CMB) anisotropies suggests that the fluctuations were created at very early times, possibly during a period of inflation [2].

One of the few observational probes that allows us access to the physics of that epoch is primordial non-Gaussianity [3]. At present, the best constraints on non-Gaussianity are coming from the CMB (e.g. [4]), but LSS is emerging as a promising complementary observable (e.g. [5, 6]). Historically, the usefulness of LSS as a tool for early universe cosmology has been viewed with some suspicion, since non-linear evolution can itself produce significant non-Gaussianity even if the initial conditions were perfectly Gaussian. Disentangling any primordial non-Gaussianity from these late time effects always seemed like a messy business. This attitude has changed somewhat when it was discovered that non-Gaussian initial conditions lead to a *scale-dependent* clustering of galaxies on large scales [7, 8]. In particular, it was shown that non-linear mode coupling induces a modulation of the local short-scale power $\sigma_8(\boldsymbol{x})$ by the long-wavelength gravitational potential $\Phi(\boldsymbol{x})$. This results in a biasing of halos (or galaxies) that is proportional to Φ rather than the dark matter density δ (or $\nabla^2\Phi$). Crucially, the appearance of Φ rather than δ in the halo bias implies a specific form of scale-dependence that cannot be created dynamically (i.e. by late time processes). This is the main reason that halo bias is such a robust probe of the initial conditions.

Figure 2.1: The squeezed limit of the three-point function, $k_1 \to 0$, gives the dominant contribution to the scale-dependent halo bias. A stochastic form of scale-dependent halo bias arises if the four-point function is large in the collapsed limit, $k_{12} \equiv |\boldsymbol{k}_1 + \boldsymbol{k}_2| \to 0$.

In this chapter, we study *stochastic* halo bias on large scales. The term 'stochastic' here refers to the fact that the halo over-density is not 100% correlated to the matter over-density

on large scales, i.e. the halo-halo power spectrum $P_{\rm hh}(k)$ is boosted relative to the matter-halo power spectrum $P_{\rm mh}(k)$. Formally, this means that

$$P_{\rm hh}(k) > b^2(k) P_{\rm mm}(k) + \frac{1}{n_{\rm h}} \ , \tag{2.1}$$

where $b(k) \equiv P_{\rm mh}(k)/P_{\rm mm}(k)$ is the halo bias, and $n_{\rm h}$ is the halo number density. Large-scale stochastic bias arises in non-Gaussian models when the small-scale power $\sigma_8(\boldsymbol{x})$ varies from point to point, but in a way that isn't completely correlated with the local value of $\Phi(\boldsymbol{x})$ and its derivatives. This is most easily demonstrated in models with multiple fields, where the small-scale power may depend on fields that do not contribute to the (linearized) gravitational potential. Our goal in this chapter is to provide an understanding of the origin of stochastic bias in a model-independent way. In the absence of significant isocurvature perturbations, all the relevant information must be encoded in the correlation functions of gravitational potential Φ. It will be useful to define

$$\hat{f}_{\rm NL} \equiv \frac{1}{4} \lim_{k_1 \to 0} \frac{\xi_\Phi^{(3)}(\boldsymbol{k}_1, \boldsymbol{k}_2, \boldsymbol{k}_3)}{P_1 P_2} \ , \tag{2.2}$$

$$\hat{\tau}_{\rm NL} \equiv \frac{9}{100} \lim_{k_{12} \to 0} \frac{\xi_\Phi^{(4)}(\boldsymbol{k}_1, \boldsymbol{k}_2, \boldsymbol{k}_3, \boldsymbol{k}_4)}{P_1 P_3 P_{12}} \ , \tag{2.3}$$

where $\langle \Phi_{\boldsymbol{k}_1} \cdots \Phi_{\boldsymbol{k}_N} \rangle_{\rm c} \equiv (2\pi)^3 \xi_\Phi^{(N)}(\boldsymbol{k}_1, \cdots, \boldsymbol{k}_n)\, \delta_{\rm D}(\boldsymbol{k}_1 + \cdots + \boldsymbol{k}_n)$ and $P_i \equiv \xi_\Phi^{(2)}(k_i)$. This parametrizes the amplitude of the three-point function in the *squeezed limit*, $k_1 \ll \min\{k_2, k_3\}$, and the amplitude of the four-point function in the *collapsed limit*, $k_{12} \equiv |\boldsymbol{k}_1 + \boldsymbol{k}_2| \ll \min\{k_i\}$. As we will show, stochastic bias arises if the 'collapsed four-point function' is *not* equal to the square of the 'squeezed three-point function', i.e. if $\hat{\tau}_{\rm NL} \neq (\frac{6}{5}\hat{f}_{\rm NL})^2$. There exists a well-known theoretical constraint on the relative size of $\hat{\tau}_{\rm NL}$ and $(\frac{6}{5}\hat{f}_{\rm NL})^2$. If only a single field (which may or may not be the inflaton) generates the primordial curvature perturbation and its non-Gaussianity, then $\hat{\tau}_{\rm NL} = (\frac{6}{5}\hat{f}_{\rm NL})^2$ [9] and the biasing is non-stochastic. On the other hand, if multiple coupled fields generate the

non-Gaussianity, then $\hat{\tau}_{\rm NL}$ can be larger[1] than $(\frac{6}{5}\hat{f}_{\rm NL})^2$ [16, 17] and the biasing will be stochastic. We will discuss classes of inflationary theories that predict precisely this kind of observational signature [18, 19, 20]. This provides the opportunity of using scale-dependent stochastic bias[2] as a probe of any early universe physics associated with a boosted collapsed four-point function—just like the non-stochastic scale-dependent bias is a powerful probe of the squeezed three-point function.

More generally, we find that the large-scale non-stochastic bias can be written as a sum over N-point functions $\xi_\Phi^{(N)}(\boldsymbol{k}_1, \cdots, \boldsymbol{k}_N)$ evaluated in the squeezed limit $k_1 \ll \min\{k_2, \cdots, k_N\}$.[3] The stochastic bias, on the other hand, involves a double sum over $(M+N)$-point functions $\xi_\Phi^{(M+N)}(\boldsymbol{k}_1, \cdots, \boldsymbol{k}_{M+N})$ evaluated in the collapsed limit $|\boldsymbol{k}_1 + \cdots + \boldsymbol{k}_M| \ll \min\{k_i\}$. Stochastic bias arises if any collapsed $(M+N)$-point function is boosted relative to the product of the corresponding squeezed $(M+1)$-point and $(N+1)$-point functions. In all physically interesting cases that we are aware of, this effect is due to the collapsed four-point function being boosted relative to the square of the three-point function (i.e. the case $M = N = 2$). Therefore, we will generally interpret stochastic bias as a probe of the collapsed four-point function. The main result of this chapter is a general pair of formulas, eqs. (2.36) and (2.46), for the non-stochastic and stochastic parts of the bias, for completely general non-Gaussian initial conditions parametrized by the N-point cumulants $\xi_\Phi^{(N)}(\boldsymbol{k}_1, \cdots, \boldsymbol{k}_N)$.

The outline of the chapter is as follows: We will begin, in Section 2.3, with a qualitative explanation of scale-dependent stochastic bias. In Section 2.4, we will show how our

[1] No matter how the fluctuations were created, the parameters have to satisfy the Suyama-Yamaguchi inequality $\hat{\tau}_{\rm NL} \geq (\frac{6}{5}\hat{f}_{\rm NL})^2$ [10] (see also [11, 12, 13, 14, 15]). This is easy to understand: we can think of $\hat{f}_{\rm NL}$ as a measure of the large-scale correlation between the potential Φ and the locally measured small-scale power, $\hat{f}_{\rm NL} \sim \langle \Phi_\ell \Phi_s^2 \rangle / \langle \Phi_\ell^2 \rangle \langle \Phi_s^2 \rangle$. On the other hand, $\hat{\tau}_{\rm NL}$ is a measure of the large-scale variance in the small-scale power, $\hat{\tau}_{\rm NL} \sim \langle \Phi_s^2 \Phi_s^2 \rangle_{\rm c} / \langle \Phi_\ell^2 \rangle \langle \Phi_s^2 \rangle^2$. The inequality $\hat{\tau}_{\rm NL} \geq (\frac{6}{5}\hat{f}_{\rm NL})^2$ then arises simply as the condition that the correlation coefficient between the small-scale power and Φ must be between -1 and 1.

[2] We should note that in this chapter we are interested in large-scale stochastic bias. On small scales, non-linear evolution and astrophysical processes can create local stochasticity, which is not relevant in our study.

[3] More precisely, k_1 is fixed to the large scale k where we are computing the bias, and $k_2, \cdots, k_N$ are integrated over a broad range of scales near the halo collapse scale $k_{\rm h} \sim \rho_{\rm m}^{1/3} M^{-1/3}$.

intuitive understanding is borne out in the barrier crossing model of structure formation. In Section 2.5, we will illustrate these results with explicit examples. In each case, we also derive our predictions in the peak-background split formalism. In a companion paper [1], we prove the mathematical equivalence of barrier crossing and peak-background split. We present our conclusions in Section 2.6. Finally, Appendix 2.7 discusses the convergence of the Edgeworth expansion for local non-Gaussianity.

2.3 Stochastic Bias

Galaxies reside in dark matter halos. For Gaussian initial conditions and at long wavelengths, the fluctuations in the density of halos $\delta_{\rm h}$ can be expressed as an expansion in the linear matter density field δ. At linear order, the two are simply related by a numerical factor—the bias b_g—i.e. $\delta_{\rm h} = b_g\delta$. This simple bias relation gets modified for non-Gaussian initial conditions, due to a coupling between short and long-wavelength modes. The short modes determine the collapse of dark matter halos, while long modes modulate the density on large scales, effectively raising or lowering the threshold for the formation of collapsed objects. A non-zero three-point function affects the variance of the short modes, leading to a dependence of the number density of halos on the amplitude of the long modes. For local non-Gaussianity[4] this leads to a dependence of the halo density on the long-wavelength gravitational potential Φ rather than the matter density $\delta \propto \nabla^2\Phi$. This leads to a characteristic *scale-dependence* in the bias relation, $\Delta b \propto k^{-2}$ [7]. It is this scale-dependence that allows us to trust the large-scale bias as a probe of initial conditions. Crucially, the dependence of the halo density on Φ is not something that could be mimicked by local dynamics. Dynamical processes don't care about the local value of the potential, but are only sensitive to tidal forces which are proportional to $\nabla^2\Phi$ and $\dot{\Phi}$ (essentially this is a consequence of the equivalence principle). Any dependence of the small-scale power on Φ itself can therefore only

[4]In real space, local non-Gaussianity is parametrized as $\Phi(\boldsymbol{x}) = \phi(\boldsymbol{x}) + f_{\rm NL}(\phi^2(\boldsymbol{x}) - \langle\phi^2\rangle)$, where ϕ is Gaussian.

come from the initial conditions. This is what makes scale-dependent bias such a promising probe of early universe physics, despite all the astrophysical uncertainties associated with galaxy formation.

Stochastic bias arises whenever the density of halos is not 100% correlated with the potential Φ or its derivatives. In order to develop some intuition, we now give a schematic derivation of the effect. In the next section, we will upgrade this to a more formal analysis in the barrier crossing approach. If we assume that the primordial perturbations are adiabatic, then the formation of halos can only depend on local physics of the fluctuations. Nevertheless, long-wavelength variations of the number of halos may depend, not only on the local value of the linear density field, but on all of its local correlation functions. Assuming only locality, we may therefore write the local halo number density as

$$n_{\rm h}(\boldsymbol{x}) = \bar{n}_{\rm h}(\delta(\boldsymbol{x}); [\delta^n](\boldsymbol{x})) \ , \tag{2.4}$$

where [...] denotes an average over a small region of characteristic size ℓ that is centered around $\boldsymbol{x}$. Long-wavelength fluctuations in the number of halos can then be understood as a Taylor expansion,

$$\delta_{\rm h}(\boldsymbol{x}) \equiv \frac{\delta n_{\rm h}}{\bar{n}_{\rm h}} = b_g \delta(\boldsymbol{x}) + \beta[\delta^2](\boldsymbol{x}) + \cdots \ , \tag{2.5}$$

where b_g is the Gaussian bias and

$$\beta \equiv \frac{\partial \ln n_{\rm h}}{\partial[\delta^2]} \ . \tag{2.6}$$

It is easy to see (e.g. by splitting all fields into long and short modes), that for local non-Gaussianity the short-scale power is modulated by the gravitational potential, $[\delta^2] \approx [\delta^2]_g \, (1 + 4 f_{\rm NL} \Phi(\boldsymbol{x}))$. This is the origin of scale-dependent bias in local non-Gaussianity.

Using the expansion (2.5), we can also evaluate correlation functions between two spatially separated points $\boldsymbol{x}$ and $\boldsymbol{x}'$. We use a prime to indicate that fields are evaluated at $\boldsymbol{x}'$, while fields without a prime are evaluated at $\boldsymbol{x}$. The matter-halo correlation, in a large

region of size $L \gg \ell$, then is

$$\frac{\langle \delta_{\rm h} \delta' \rangle}{\langle \delta \delta' \rangle} = b_g + \beta \frac{\langle [\delta^2] \delta' \rangle}{\langle \delta \delta' \rangle} + \cdots \ , \tag{2.7}$$

while the halo-halo correlation is

$$\frac{\langle \delta_{\rm h} {\delta_{\rm h}}' \rangle}{\langle \delta \delta' \rangle} = b_g^2 + 2 b_g \beta \frac{\langle [\delta^2] \delta' \rangle}{\langle \delta \delta' \rangle} + \beta^2 \frac{\langle [\delta^2] [\delta^2]' \rangle}{\langle \delta \delta' \rangle} + \cdots \ . \tag{2.8}$$

This leads to the possibility that the bias inferred from $\langle \delta_{\rm h} \delta \rangle$ is not equal to the bias inferred from $\langle \delta_{\rm h} {\delta_{\rm h}}' \rangle$. We characterize this so-called stochasticity of the halo bias by the following parameter[5]

$$r \equiv \frac{\langle \delta_{\rm h} {\delta_{\rm h}}' \rangle}{\langle \delta \delta' \rangle} - \left(\frac{\langle \delta_{\rm h} \delta' \rangle}{\langle \delta \delta' \rangle} \right)^2 \ . \tag{2.9}$$

Using eqs. (2.7) and (2.8), we find

$$r = \beta^2 \left[\frac{\langle [\delta^2] [\delta^2]' \rangle}{\langle \delta \delta' \rangle} - \left(\frac{\langle [\delta^2] \delta' \rangle}{\langle \delta \delta' \rangle} \right)^2 \right] + \cdots \ . \tag{2.10}$$

This simple argument gives reliable intuition for the origin of stochasticity. Specifically, we see that if a local variation in the amplitude of $[\delta^2](\boldsymbol{x})$ is uncorrelated with $\delta(\boldsymbol{x}')$, then there is no extra contribution to the bias in eq. (2.7). Nevertheless, the halo-halo correlation function in eq. (2.8) can still be modified by long-wavelength variations in $[\delta^2](\boldsymbol{x})$. Moreover, the result (2.10) makes it clear that stochasticity arises from a non-trivial four-point function of the primordial potential. In fact, the real space correlation function $\langle [\delta^2](\boldsymbol{x}) [\delta^2](\boldsymbol{x}') \rangle$ relates to the collapsed limit of the four-point function in Fourier space, i.e. $\lim_{|\boldsymbol{k}_1 + \boldsymbol{k}_2| \to 0} \langle \Phi_{\boldsymbol{k}_1} \Phi_{\boldsymbol{k}_2} \Phi_{\boldsymbol{k}_3} \Phi_{\boldsymbol{k}_4} \rangle$.

[5] In practice, we also have to subtract shot noise contributions from $\langle \delta_{\rm h} {\delta_{\rm h}}' \rangle$ and $\langle \delta_{\rm h} \delta' \rangle$—see §2.4.3. Note that other definitions of the stochasticity coefficient can be chosen. A natural alternative would be to define $\tilde{r} = \langle \delta_{\rm h} \delta' \rangle / (\langle \delta_{\rm h} {\delta_{\rm h}}' \rangle \langle \delta \delta' \rangle)^{1/2} - 1$. In both definitions $r = 0$ means that the matter and halo fields are 100% correlated.

2.4 Predictions from Barrier Crossing

In this section, we give a formal derivation of stochastic bias using the classic barrier crossing method of Press and Schechter [21]. Our goal is to obtain an expression for the stochasticity coefficient (2.9) in terms of the cumulants of the smoothed density field. These in turn can be related to N-point functions of the primordial potential and hence contain information about the initial conditions.

2.4.1 Definitions and Notation

We begin with some basic definitions and a description of our notation. Let $\hat{\delta}(\boldsymbol{x}, z)$ denote the linear density field (to be distinguished by the hat from the non-linear density field δ). The linearized Poisson equation relates $\hat{\delta}$ to the primordial potential Φ,

$$\hat{\delta}_{\boldsymbol{k}}(z) = \alpha(k, z)\Phi_{\boldsymbol{k}} \ , \tag{2.11}$$

where

$$\alpha(k, z) \equiv \frac{2}{3}\frac{k^2}{\Omega_m H_0^2}\, T(k)D(z) \ . \tag{2.12}$$

Here, $T(k)$ is the matter transfer function normalized such that $T(k) \to 1$ as $k \to 0$ and $D(z)$ is the linear growth factor (as function of redshift z), normalized so that $D(z) = (1+z)^{-1}$ in matter domination. For notational simplicity, we will from now on suppress the redshift argument from all quantities. We use $\delta_M(\boldsymbol{x})$ for the linear field smoothed with a top-hat window function with radius[6] $R_M \equiv (3M/4\pi\bar{\rho}_{\rm m})^{1/3}$, so that

$$\delta_M(\boldsymbol{x}) = \int_{\boldsymbol{k}} e^{-i\boldsymbol{k}\cdot\boldsymbol{x}}\, W_M(k)\hat{\delta}_{\boldsymbol{k}} = \int_{\boldsymbol{k}} e^{-i\boldsymbol{k}\cdot\boldsymbol{x}}\, \alpha_M(k)\Phi_{\boldsymbol{k}} \ , \tag{2.13}$$

[6]The smoothing scale R_M corresponds to the comoving size of halos of mass M in Lagrangian space.

where $\int_{\boldsymbol{k}}(\,\cdot\,) \equiv \int \frac{\mathrm{d}^3\boldsymbol{k}}{(2\pi)^3}(\,\cdot\,)$,

$$W_M(k) \equiv 3\,\frac{\sin(kR_M) - kR_M\cos(kR_M)}{(kR_M)^3}\ , \tag{2.14}$$

and $\alpha_M(k) \equiv W_M(k)\alpha(k)$. Let $\sigma_M = \langle\delta_M^2\rangle^{1/2}$ be the rms amplitude of the smoothed density field, and $\kappa_n(M)$ be its n-th non-Gaussian cumulant,

$$\kappa_n(M) = \frac{\langle\delta_M^n\rangle_{\rm c}}{\sigma_M^n}\ , \tag{2.15}$$

where the subscript 'c' indicates the use of a connected correlation function. Since δ_M and σ_M are defined via linear theory, $\kappa_n(M)$ is independent of redshift. Similar definitions apply to the unsmoothed field $\hat{\delta}$, in which case we denote the variance and cumulants by $\hat{\sigma}$ and $\kappa_{\hat{n}}$.

Ultimately, we will be interested in two-point clustering statistics. Let $\boldsymbol{x}$ and $\boldsymbol{x}'$ be two points separated by a distance $r \equiv |\boldsymbol{x} - \boldsymbol{x}'|$. Moreover, let a prime indicate that the field is evaluated at $\boldsymbol{x}'$, e.g. $\delta'_M \equiv \delta_M(\boldsymbol{x}')$. Fields without a prime are evaluated at $\boldsymbol{x}$. The joint cumulants are then defined by

$$\kappa_{\hat{m},n}(r,M) \equiv \frac{\langle\hat{\delta}^m(\delta'_M)^n\rangle_{\rm c}}{\hat{\sigma}^m\sigma_M^n}\ , \tag{2.16}$$

$$\kappa_{m,n}(r,M,\bar{M}) \equiv \frac{\langle(\delta_M)^m(\delta'_{\bar{M}})^n\rangle_{\rm c}}{\sigma_M^m\sigma_{\bar{M}}^n}\ . \tag{2.17}$$

These cumulants can be related to N-point functions of the gravitational potential,

$$\langle\Phi_{\boldsymbol{k}_1}\Phi_{\boldsymbol{k}_2}\cdots\Phi_{\boldsymbol{k}_N}\rangle_{\rm c} = (2\pi)^3\delta_{\rm D}(\boldsymbol{k}_{12\ldots N})\,\xi_\Phi^{(N)}(\boldsymbol{k}_1,\boldsymbol{k}_2,\ldots,\boldsymbol{k}_N)\ , \tag{2.18}$$

where $\boldsymbol{k}_{12\ldots N} \equiv \boldsymbol{k}_1 + \boldsymbol{k}_2 + \cdots + \boldsymbol{k}_N$.

2.4.2 Edgeworth Expansions

The probability density functions (PDFs) of weakly non-Gaussian random variables have well-defined Edgeworth expansions (for a review see e.g. [22]). Consider first the variables δ_M and δ'_M. It will be convenient to define the rescaled fields

$$\nu \equiv \frac{\delta_M}{\sigma_M} \qquad \text{and} \qquad \nu' \equiv \frac{\delta'_M}{\sigma_M} \ , \tag{2.19}$$

with $\langle\nu\rangle = \langle\nu'\rangle = 0$ and $\langle\nu^2\rangle = \langle(\nu')^2\rangle = 1$. The cumulants in eqs. (2.15) and (2.17) then become $\kappa_n = \langle\nu^n\rangle_{\rm c}$ and $\kappa_{m,n} = \langle\nu^m(\nu')^n\rangle_{\rm c}$. The Edgeworth expansion for the marginal PDF is

$$p(\nu) = \exp\left(\sum_{n\geq 3}\frac{(-1)^n}{n!}\kappa_n\frac{\partial^n}{\partial\nu^n}\right)p_g(\nu) \ , \qquad \text{where} \quad p_g(\nu) \equiv \frac{1}{\sqrt{2\pi}}e^{-\frac{1}{2}\nu^2} \ . \tag{2.20}$$

The first few terms can be written as

$$p(\nu) \ = \ \left(1 + \frac{\kappa_3}{3!}H_3(\nu) + \frac{\kappa_4}{4!}H_4(\nu) + \cdots\right)p_g(\nu) \ , \tag{2.21}$$

where the functions $H_n(\nu)$ are Hermite polynomials

$$H_n(\nu) \equiv (-1)^n e^{\frac{1}{2}\nu^2}\frac{d^n}{d\nu^n}e^{-\frac{1}{2}\nu^2} \ . \tag{2.22}$$

Similarly, the Edgeworth expansion for the joint PDF is

$$p(\nu,\nu') = \exp\left(\kappa_{1,1}\frac{\partial^2}{\partial\nu\partial\nu'} + \sum_{m+n\geq 3}\frac{(-1)^{m+n}}{m!n!}\kappa_{m,n}\frac{\partial^{m+n}}{\partial\nu^m\partial(\nu')^n}\right)p_g(\nu)p_g(\nu') \ . \tag{2.23}$$

In Appendix 2.7, we discuss the convergence properties of this expansion. In the next section, we will use it to compute halo-halo correlations.

The matter-halo case is completely analogous: to construct the joint PDF of the variables $\hat{\delta}$ and δ'_M, we define rescaled variables $\hat{\nu} = \hat{\delta}/\hat{\sigma}$ and $\nu' = \delta'_M/\sigma_M$. The joint PDF $p(\hat{\nu}, \nu')$ is then given by the Edgeworth series (2.23) with the cumulant $\kappa_{m,n}$ replaced by $\kappa_{\hat{m},n}$.

2.4.3 Barrier Crossing

In the simplest version of the barrier crossing formalism [21], halos of mass $\geq M$ are identified with regions where the *linearly* evolved smoothed density field exceeds a constant threshold value δ_c for collapse. The halo number density $n_{\rm h}(\boldsymbol{x})$ is then given by

$$n_{\rm h}(\boldsymbol{x}) = 2\,\frac{\bar{\rho}_{\rm m}}{M}\,\Theta(\delta_M(\boldsymbol{x}) - \delta_c)\ , \tag{2.24}$$

with Θ the Heaviside step function. It has been shown numerically that $\delta_c \approx 1.42$ produces good results [23], but for our analytical calculations we don't need to specify a particular value for δ_c. The fraction of space occupied by regions above the collapse threshold is

$$f(M) = \int_{\nu_c}^{\infty} [{\rm d}\nu]\ p(\nu)\ , \tag{2.25}$$

where $\nu_c(M) \equiv \delta_c/\sigma_M$. Using the Edgeworth expansion (2.21), we find[7]

$$f(M) = \frac{1}{2}\,{\rm erfc}\left(\frac{\nu_c}{\sqrt{2}}\right) + p_g(\nu_c)\left[\frac{\kappa_3(M)}{3!}H_2(\nu_c) + \frac{\kappa_4(M)}{4!}H_3(\nu_c) + \cdots\right]\ . \tag{2.26}$$

When interpreting calculations in the barrier crossing model, it must be kept in mind that eq. (2.24) for $n_{\rm h}(\boldsymbol{x})$ is the number density of halos in *Lagrangian* space. Our convention throughout this paper is that the power spectra $P_{\rm mh}(k)$ and $P_{\rm hh}(k)$ are always computed in Lagrangian space. In particular, b_g denotes the Lagrangian bias. The relevant quantity to compare to observations or simulations is the *Eulerian* bias which, to lowest order, is given by $b_g^{\rm E} = 1 + b_g$.

[7] In our notation the halo mass function is $dn_{\rm h}/dM = -\bar{\rho}_{\rm m}/M(df/dM)$.

The barrier crossing model also neglects shot noise contributions which arise from the finite halo number density $n_{\rm h}$. Throughout this paper, $P_{\rm hh}$ always denotes the halo-halo power spectrum after subtracting the shot noise contribution $1/n_{\rm h}$. (There are also shot noise, or one-halo, contributions to the matter-halo power spectrum $P_{\rm mh}$, which are usually negligible, but are a leading source of stochastic bias in the Gaussian case [24, 25].)

Matter-Halo Correlations

The correlation between the halo field at $\boldsymbol{x}'$ and the dark matter field at $\boldsymbol{x}$ is given by

$$\hat{\xi}(r, M) \;=\; \frac{M}{2\bar{\rho}_{\rm m}} \int_{-\infty}^{\infty} [{\rm d}\hat{\delta}] \int_{-\infty}^{\infty} [{\rm d}\delta'_M]\, \hat{\delta}(\boldsymbol{x})\, n_{\rm h}(\boldsymbol{x}')\, p(\hat{\delta}, \delta'_M) \;. \tag{2.27}$$

In the rescaled variables $\hat{\nu} \equiv \hat{\delta}(\boldsymbol{x})/\hat{\sigma}$ and $\nu' \equiv \delta_M(\boldsymbol{x}')/\sigma_M$, this becomes

$$\hat{\xi}(r, M) \;=\; \hat{\sigma} \int_{-\infty}^{\infty} [{\rm d}\hat{\nu}] \int_{\nu_c}^{\infty} [{\rm d}\nu']\, \hat{\nu}\, p(\hat{\nu}, \nu') \;. \tag{2.28}$$

It will be convenient to work in momentum space via $\hat{\xi}(k, M) = \int {\rm d}^3\boldsymbol{r}\, e^{i\boldsymbol{k}\cdot\boldsymbol{r}} \hat{\xi}(r, M)$. To describe the correlations of halos in the mass bin $[M, M + {\rm d}M]$, we take derivatives with respect to M. The matter-halo power spectrum is then given by

$$P_{\rm mh}(k, M) = \frac{d\hat{\xi}(k, M)}{dM} \left(\frac{df(M)}{dM}\right)^{-1} \;. \tag{2.29}$$

To compute the correlation function (2.28), we substitute the Edgeworth expansion (2.23) for $p(\hat{\nu}, \nu')$. Only terms with exactly one $\hat{\nu}$-derivative survive the integration, and we therefore find

$$\hat{\xi}(k, M) = \hat{\sigma}\, p_g(\nu_c) \left[\kappa_{\hat{1},1} + \frac{H_1(\nu_c)}{2!}\kappa_{\hat{1},2} + \frac{H_2(\nu_c)}{3!}\kappa_{\hat{1},3} + \frac{H_3(\nu_c)}{3!}\kappa_{\hat{1},1} \star \kappa_3 + \cdots\right] \;, \tag{2.30}$$

where $\star$ denotes a convolution. We see that the matter-halo correlations, or equivalently the non-stochastic part of the halo bias, only depend on the following cumulants

$$\kappa_{\hat{1},n}(k,M) = \hat{\sigma}^{-1}\sigma_M^{-n}\left(\prod_{i=1}^{n}\int_{\boldsymbol{q}_i}\alpha_M(q_i)\right)\alpha(k)\langle\Phi_{\boldsymbol{k}}\Phi_{\boldsymbol{q}_1}\cdots\Phi_{\boldsymbol{q}_n}\rangle_{\rm c}\ . \tag{2.31}$$

Moreover, we note that the large-scale limit, $\lim_{k\to 0}\kappa_{\hat{1},n}(k,M)$, is determined by the squeezed limit of the primordial $(n+1)$-point function [26],

$$\lim_{k\to 0}\xi_\Phi^{(n+1)}(\boldsymbol{k},\boldsymbol{q}_1,\cdots,\boldsymbol{q}_n)\ . \tag{2.32}$$

The explicit form of the cumulants $\kappa_{\hat{1},n\geq 2}$ depends on the type of non-Gaussianity. We compute some examples in Section 2.5.

Keeping only linear terms[8] in eq. (2.30), we get

$$\hat{\xi}(k,M) = p_g(\nu_c)(\kappa_{\hat{1},1}\hat{\sigma}\sigma_M)\left[\frac{1}{\sigma_M}+\sum_{n=2}^{\infty}\frac{H_{n-1}(\nu_c)}{n!}\,f_{\hat{1},n}+\cdots\right]\ , \tag{2.33}$$

where we defined

$$f_{\hat{1},n}(k,M) \equiv \frac{\kappa_{\hat{1},n}(k,M)}{\kappa_{\hat{1},1}(k,M)\,\sigma_M}\ . \tag{2.34}$$

It was convenient to factor out the Gaussian term $\kappa_{\hat{1},1}\hat{\sigma}\sigma_M$, since at long wavelengths it becomes the matter power spectrum

$$\kappa_{\hat{1},1}\,\hat{\sigma}\sigma_M = \int_{\boldsymbol{q}}\alpha(k)\alpha_M(q)\langle\Phi_{\boldsymbol{k}}\Phi_{\boldsymbol{q}}\rangle = W_M(k)P_{\rm mm}(k)\ \xrightarrow{k\to 0}\ P_{\rm mm}(k)\ . \tag{2.35}$$

Evaluating eq. (2.29), we find

$$P_{\rm mh}(k)\ \xrightarrow{k\to 0}\ P_{\rm mm}(k)\left[b_g+\sum_{n=2}^{\infty}\left(\beta_n+\tilde{\beta}_n\frac{d}{d\ln\sigma_M}\right)f_{\hat{1},n}+\cdots\right]\ , \tag{2.36}$$

[8] In Appendix 2.7, we explain that the lowest order cumulants usually dominate and that products of cumulants are suppressed.

where

$$b_g \equiv \frac{1}{\sigma_M}\frac{\nu_c^2-1}{\nu_c} \quad , \quad \beta_n \equiv \frac{H_n(\nu_c)}{n!} \quad \text{and} \quad \tilde{\beta}_n \equiv \frac{H_{n-1}(\nu_c)}{n!\,\nu_c} \; . \tag{2.37}$$

The ellipses in eq. (2.36) stand for terms that are non-linear in the cumulants. For local non-Gaussianity, the derivative terms $df_{\hat{1},n}/d\ln\sigma_M$ will be negligible, but in principle, we can keep them (and sometimes we have to).

Our expression (2.36) agrees with the general formula for the non-stochastic bias given in [26]; however, ref. [26] implicitly found that non-Gaussianity cannot generate large-scale stochastic bias. In the next section, we will find the opposite conclusion. The disagreement is easy to understand: Ref. [26] claims after their eq. (40) that contributions to $P_{\rm hh}$ from cumulants $\kappa_{m,n}$ with $m,n \geq 2$ must approach a constant as $k \to 0$. This is not true for general non-Gaussian initial conditions and exceptions to that statement are precisely what causes the effects discuss in this paper.

Halo-Halo Correlations

Next, we consider the correlation between the halo fields at $\boldsymbol{x}$ and $\boldsymbol{x}'$,

$$\xi(r,M,\bar{M}) \;=\; \frac{M\bar{M}}{4\bar{\rho}_{\rm m}^2}\int_{-\infty}^{\infty}[{\rm d}\delta_M]\int_{-\infty}^{\infty}[{\rm d}\delta'_{\bar{M}}]\,n_{\rm h}(\boldsymbol{x})n_{\rm h}(\boldsymbol{x}')\,p(\delta_M,\delta'_{\bar{M}}) \; . \tag{2.38}$$

In the rescaled variables $\nu \equiv \delta_M(\boldsymbol{x})/\sigma_M$ and $\nu' \equiv \delta_{\bar{M}}(\boldsymbol{x}')/\sigma_{\bar{M}}$, this becomes

$$\xi(r,M,\bar{M}) \;=\; \int_{\nu_c}^{\infty}[{\rm d}\nu]\int_{\bar{\nu}_c}^{\infty}[{\rm d}\nu']\;p(\nu,\nu') \; . \tag{2.39}$$

Notice that, in principle, we have allowed for two distinct mass thresholds, M and $\bar{M}$. The power spectrum of halos in the mass bins $[M, M+{\rm d}M]$ and $[\bar{M}, \bar{M}+{\rm d}\bar{M}]$ then is

$$P_{\rm h\bar{h}}(k) = \frac{d^2\xi(k,M,\bar{M})}{dMd\bar{M}}\left(\frac{df(M)}{dM}\frac{df(\bar{M})}{d\bar{M}}\right)^{-1} \; . \tag{2.40}$$

For simplicity, we will restrict the following presentation to correlations of equal mass halos, $M = \bar{M}$. The power spectrum for a narrow mass bin around M is then given by

$$P_{\rm hh}(k) = \left.\frac{d^2\xi(k, M, \bar{M})}{dM d\bar{M}}\right|_{\bar{M}=M} \left(\frac{df(M)}{dM}\right)^{-2} . \tag{2.41}$$

To compute the correlation function (2.39), we substitute the Edgeworth expansion (2.23) for $p(\nu, \nu')$,

$$\begin{aligned}\xi(k, M, \bar{M}) = p_g(\nu_c) p_g(\bar{\nu}_c) \Bigg[& \kappa_{1,1} + \frac{1}{2}\big(\kappa_{2,1} H_1(\nu_c) + \kappa_{1,2} H_1(\bar{\nu}_c)\big) \\ & + \frac{1}{6}\big(\kappa_{3,1} H_2(\nu_c) + \kappa_{1,3} H_2(\bar{\nu}_c)\big) + \frac{1}{4}\kappa_{2,2} H_1(\nu_c) H_1(\bar{\nu}_c) + \frac{1}{2}\kappa_{1,1} \star \kappa_{1,1} + \cdots \Bigg] .\end{aligned} \tag{2.42}$$

The form of higher-order cumulants, such as $\kappa_{1,2}$, $\kappa_{1,3}$ and $\kappa_{2,2}$, again depends on the type of non-Gaussianity. We compute some examples in Section 2.5.

Keeping only the terms linear in $\kappa_{m,n}$ (this approximation will be justified in Appendix 2.7) in eq. (2.42), we find

$$\begin{aligned}\xi(k, M, \bar{M}) \;=\; & p_g(\nu_c) p_g(\bar{\nu}_c) (\kappa_{1,1} \sigma_M \sigma_{\bar{M}}) \Bigg[\frac{1}{\sigma_M \sigma_{\bar{M}}} \\ & + \sum_{n=2}^{\infty} \left(\frac{1}{\sigma_M} \frac{H_{n-1}(\bar{\nu}_c)}{n!} f_{1,n} + \frac{1}{\sigma_{\bar{M}}} \frac{H_{n-1}(\nu_c)}{n!} f_{n,1} \right) \\ & + \sum_{m=2}^{\infty} \sum_{n=2}^{\infty} \frac{H_{m-1}(\nu_c)}{m!} \frac{H_{n-1}(\bar{\nu}_c)}{n!} f_{m,n} \;+\; \cdots \Bigg] ,\end{aligned} \tag{2.43}$$

where

$$f_{1,n}(k, M, \bar{M}) \equiv \frac{\kappa_{1,n}(k, M, \bar{M})}{\kappa_{1,1}(k, M, \bar{M}) \sigma_{\bar{M}}} \qquad \text{for } n \geq 1 , \tag{2.44}$$

$$f_{m,n}(k, M, \bar{M}) \equiv \frac{\kappa_{m,n}(k, M, \bar{M})}{\kappa_{1,1}(k, M, \bar{M}) \sigma_M \sigma_{\bar{M}}} \qquad \text{for } m, n \geq 2 . \tag{2.45}$$

We again factored out the Gaussian contribution, $\kappa_{1,1}\,\sigma_M\sigma_{\bar{M}} \xrightarrow{k\to 0} P_{\rm mm}(k)$. Note that $f_{1,n} = f_{\hat{1},n}$ in the large scale limit $k \ll R_M^{-1}$, where $f_{\hat{1},n}$ was defined in eq. (2.34). Substituting (2.43) into (2.41), we get

$$P_{\rm hh}(k) \xrightarrow{k\to 0} P_{\rm mm}(k)\left[b_g^2 + 2b_g\sum_{n=2}^{\infty}\left(\beta_n + \tilde{\beta}_n\frac{\partial}{\partial\ln\sigma_M}\right)f_{1,n} + \sum_{m=2}^{\infty}\sum_{n=2}^{\infty}\left(\beta_m + \tilde{\beta}_n\frac{\partial}{\partial\ln\sigma_M}\right)\left(\beta_m + \tilde{\beta}_n\frac{\partial}{\partial\ln\sigma_{\bar{M}}}\right)f_{m,n} + \cdots\right] . \quad (2.46)$$

Note that, while in the end we always take $M = \bar{M}$ in this paper, M and $\bar{M}$ are independent variables when calculating partial derivatives of $f_{m,n}(M,\bar{M})$.

2.4.4 Stochastic Halo Bias

We now combine the above results to evaluate the stochasticity coefficient

$$r \equiv \frac{P_{\rm hh}}{P_{\rm mm}} - \left(\frac{P_{\rm mh}}{P_{\rm mm}}\right)^2 , \quad (2.47)$$

where, as usual, it is understood that shot noise is subtracted from $P_{\rm hh}$ and $P_{\rm mh}$. Substituting eqs. (2.36) and (2.46), we find

$$r \xrightarrow{k\to 0} \sum_{m=2}^{\infty}\sum_{n=2}^{\infty}\left(\beta_m + \tilde{\beta}_m\frac{\partial}{\partial\ln\sigma_M}\right)\left(\beta_n + \tilde{\beta}_n\frac{\partial}{\partial\ln\sigma_{\bar{M}}}\right)f_{m,n} - \left[\sum_{n=2}^{\infty}\left(\beta_n + \tilde{\beta}_n\frac{\partial}{\partial\ln\sigma_M}\right)f_{n,1}\right]^2 . \quad (2.48)$$

We note that cumulants $\kappa_{m,n}(k)$ with $m,n \geq 2$ contribute to the halo-halo power spectrum but not the matter-halo power spectrum (2.36), so stochastic halo bias is sourced by these cumulants. These cumulants can be written in terms of the $(m+n)$-point functions of the

gravitational potential,

$$\kappa_{m,n}(k,M,\bar{M}) \xrightarrow{k\to 0} \frac{1}{\sigma_M^m \sigma_{\bar{M}}^n}\left(\prod_{i=1}^{m-1}\int_{\boldsymbol{q}_i}\alpha_M(q_i)\right)\left(\prod_{j=1}^{n-1}\int_{\boldsymbol{q}'_j}\alpha_{\bar{M}}(q'_j)\right)\alpha_M(q)\,\alpha_{\bar{M}}(q') \\ \times\,\xi_\Phi^{(m+n)}\left(\boldsymbol{q}_1,\cdots,\boldsymbol{q}_{m-1},-\boldsymbol{q}+\boldsymbol{k},\boldsymbol{q}'_1,\cdots,\boldsymbol{q}'_{n-1},-\boldsymbol{q}'-\boldsymbol{k}\right)\ , \qquad (2.49)$$

where $\boldsymbol{q}\equiv\sum_{i=1}^{m-1}\boldsymbol{q}_i$ and $\boldsymbol{q}'\equiv\sum_{j=1}^{n-1}\boldsymbol{q}'_j$. We see that, in general, large-scale stochastic bias arises whenever an $(m+n)$-point function $\xi_\Phi^{(m+n)}(\boldsymbol{k}_1,\cdots,\boldsymbol{k}_{m+n})$ is boosted in the collapsed limit $|\sum_{i=1}^m\boldsymbol{k}_i|\to 0$, relative to the product of the corresponding squeezed $(m+1)$-point and $(n+1)$-point functions. In the next section, we will compute eq. (2.48) for a few interesting examples. In most cases, we will get stochastic bias from the case $m=n=2$, i.e. a collapsed four-point function $\lim_{|\boldsymbol{k}_1+\boldsymbol{k}_2|\to 0}\xi_\Phi^{(4)}(\boldsymbol{k}_1,\boldsymbol{k}_2,\boldsymbol{k}_3,\boldsymbol{k}_4)$ which is larger than the square of the squeezed three-point function $\lim_{k_1\to 0}\xi_\Phi^{(3)}(\boldsymbol{k}_1,\boldsymbol{k}_2,\boldsymbol{k}_3)$.

2.5 Examples

In this section, we discuss several physical mechanisms that lead to stochastic halo bias. For each example, we will derive the result in two different ways:

1) using a peak-background split (PBS) method;

2) using the barrier crossing analysis of the previous section.

We demonstrate explicitly that both approaches lead to the same answers.

2.5.1 $\tau_{\rm NL}$ Cosmology

A simple phenomenological way to get a boosted collapsed limit for the four-point function is the following generalization of the local ansatz to multiple fields

$$\Phi = A_i\phi_i + B_{ij}\left(\phi_i\phi_j - \langle\phi_i\phi_j\rangle\right) \ , \tag{2.50}$$

with the Einstein summation convention understood. This structure arises, for example, in the curvaton model of [18] (see also [25]),

$$\Phi = \phi + \psi + f_{\rm NL}(1+\Pi)^2\left(\psi^2 - \langle\psi^2\rangle\right) \ , \qquad \text{where} \quad \frac{P_\phi}{P_\psi} \equiv \Pi \ . \tag{2.51}$$

Here, ϕ and ψ are uncorrelated Gaussian random fields with power spectra that are proportional to each other. The three- and four-point functions take the local form

$$\xi^{(3)}_\Phi(\boldsymbol{k}_1,\boldsymbol{k}_2,\boldsymbol{k}_3) \ = \ f_{\rm NL}\big[P_1P_2 + 5\,\text{perms.}\big] + \mathcal{O}(f^3_{\rm NL}) \ , \tag{2.52}$$

$$\xi^{(4)}_\Phi(\boldsymbol{k}_1,\boldsymbol{k}_2,\boldsymbol{k}_3,\boldsymbol{k}_4) \ = \ 2\left(\tfrac{5}{6}\right)^2\tau_{\rm NL}\big[P_1P_2P_{13} + 23\,\text{perms.}\big] + \mathcal{O}(\tau^2_{\rm NL}) \ , \tag{2.53}$$

where we have defined $P_i \equiv P_\Phi(k_i)$ and $P_{ij} \equiv P_\Phi(|\boldsymbol{k}_i + \boldsymbol{k}_j|)$. However, unlike the single-field local ansatz, now $\tau_{\rm NL}$ need not be equal to $\left(\frac{6}{5}f_{\rm NL}\right)^2$. Instead, the ansatz (2.51) implies $\tau_{\rm NL} \equiv$

$\left(\frac{6}{5}f_{\rm NL}\right)^2(1+\Pi)$, in agreement with the Suyama-Yamaguchi inequality, $\tau_{\rm NL} \geq \left(\frac{6}{5}f_{\rm NL}\right)^2$ [10] (see also [11, 12, 13, 14, 15]). The following limits will be useful in computing the cumulants required in the barrier crossing calculation:

$$\lim_{k_1\to 0}\xi_\Phi^{(3)}(\boldsymbol{k}_1,\boldsymbol{k}_2,\boldsymbol{k}_3) = 4f_{\rm NL}P_1P_2 \ , \tag{2.54}$$

$$\lim_{k_1\to 0}\xi_\Phi^{(4)}(\boldsymbol{k}_1,\boldsymbol{k}_2,\boldsymbol{k}_3,\boldsymbol{k}_4) = 8\left(\tfrac{5}{6}\right)^2\tau_{\rm NL}\,P_1\big[P_2P_3+P_2P_4+P_3P_4\big] \ , \tag{2.55}$$

$$\lim_{k_{12}\to 0}\xi_\Phi^{(4)}(\boldsymbol{k}_1,\boldsymbol{k}_2,\boldsymbol{k}_3,\boldsymbol{k}_4) = 16\left(\tfrac{5}{6}\right)^2\tau_{\rm NL}\,P_{12}P_1P_3 \ . \tag{2.56}$$

However, before we discuss the explicit barrier crossing result, we present an alternative derivation using the peak-background split approach.

Peak-Background Split

PBS is a heuristic procedure for predicting the large-scale clustering statistics of dark matter halos. All fields are split into long and short modes—i.e. the Gaussian fields in eq. (2.51) are written as $\phi = \phi_s+\phi_\ell$ and $\psi = \psi_s+\psi_\ell$. The short scales ($\lesssim R_M \lesssim 10$ Mpc$/h$) determine halo formation, while the long scales ($\gtrsim 100$ Mpc$/h$) are the ones on which we want to measure the clustering of halos. Long modes are therefore always much larger than the Lagrangian size of the halos that we consider, i.e. $R_M k_\ell \ll 1$. The precise split into long and short modes isn't important for physical observables, as long as it satisfies the above constraints.

The long-wavelength modes alter the statistical properties of the small-scale fluctuations. For instance, to lowest order, the locally measured small-scale power is $\sigma = \bar\sigma\,[1+2f_{\rm NL}(1+\Pi)\psi_\ell]$, and the locally measured halo number density is

$$n_{\rm h}(\boldsymbol{x}) = \bar n_{\rm h}\left(\delta_c-\delta_\ell\,;\bar\sigma\,[1+2f_{\rm NL}(1+\Pi)\psi_\ell]\right) \ . \tag{2.57}$$

Taylor expanding this expression, we get

$$\delta_{\rm h} \equiv \frac{\delta n_{\rm h}}{\bar{n}_{\rm h}} = b_g \delta_\ell + \beta_f (1+\Pi) f_{\rm NL} \psi_\ell \quad , \tag{2.58}$$

where

$$b_g \equiv \frac{\partial \ln n_{\rm h}}{\partial \delta_\ell} \quad \text{and} \quad \beta_f \equiv 2 \frac{\partial \ln n_{\rm h}}{\partial \ln \sigma} \ . \tag{2.59}$$

Hence, we find

$$P_{\rm mh} = \left(b_g + \beta_f \frac{f_{\rm NL}}{\alpha(k)} \right) P_{\rm mm} \ , \tag{2.60}$$

and

$$P_{\rm hh} = \left(b_g^2 + 2 b_g \beta_f \frac{f_{\rm NL}}{\alpha(k)} + \beta_f^2 \frac{\left(\frac{5}{6}\right)^2 \tau_{\rm NL}}{\alpha^2(k)} \right) P_{\rm mm} \ . \tag{2.61}$$

This leads to large-scale halo stochasticity of the form

$$r = \left(\left(\tfrac{5}{6}\right)^2 \tau_{\rm NL} - f_{\rm NL}^2 \right) \frac{\beta_f^2}{\alpha^2(k)} \ . \tag{2.62}$$

As $\Pi \to 0$, this reduces to the classic $f_{\rm NL}$ model, with $\tau_{\rm NL} = \left(\frac{6}{5} f_{\rm NL}\right)^2$ and hence no stochasticity.

Barrier Crossing

Next, we show that eq. (2.62) can be reproduced precisely from the barrier crossing analysis of the previous section. In Appendix 2.7, we show that only the lowest-order cumulants will be significant. Here, we calculate the relevant cumulants explicitly: Using eq. (2.54), we get

$$f_{1,2} = f_{\hat{1},2} \ \xrightarrow{k \to 0} \ 4 \, \frac{f_{\rm NL}}{\alpha(k)} \ . \tag{2.63}$$

The order-of-magnitude estimates in Appendix 2.7 suggest that this will be the dominant contribution. In particular, we expect, $f_{1,2} > f_{1,3}$. We can confirm this explicitly. Using

eq. (2.55), we get

$$f_{1,3} = f_{\hat{1},3} \xrightarrow{k\to 0} 4\,\frac{\left(\frac{5}{6}\right)^2 \tau_{\rm NL}}{\alpha(k)} \cdot \kappa_3^{(f_{\rm NL}=1)} \ , \tag{2.64}$$

where

$$\kappa_3^{(f_{\rm NL}=1)}(M) \equiv \frac{6}{\sigma_M^3} \int_{\boldsymbol{q}_1} \int_{\boldsymbol{q}_2} \alpha_M(q_1)\alpha_M(q_2)\alpha_M(q_{12})P_\Phi(q_1)P_\Phi(q_2) \ . \tag{2.65}$$

Since $\kappa_3^{(f_{\rm NL}=1)}$ is of order Δ_Φ, we see that the condition $f_{1,3} \ll f_{1,2}$ is equivalent to $f_{\rm NL}(1+\Pi)\Delta_\Phi \ll 1$. This latter condition is always satisfied if all fields are weakly coupled.[9]

Finally, using eq. (2.56), we get

$$f_{2,2} \xrightarrow{k\to 0} 16\,\frac{\left(\frac{5}{6}\right)^2 \tau_{\rm NL}}{\alpha^2(k)} \ . \tag{2.67}$$

Substituting the above into eq. (2.48) gives

$$r = \left(\left(\tfrac{5}{6}\right)^2 \tau_{\rm NL} - f_{\rm NL}^2\right) \frac{\beta_f^2}{\alpha^2(k)} \ , \tag{2.68}$$

where we have used the relation $\beta_f = 4\beta_2 = 2(\nu_c - 1)$, which can be derived by evaluating the derivative $\beta_f = 2\partial \ln n_{\rm h}/\partial \ln \sigma$ in the barrier crossing model [27]. Comparing with eq. (2.62), we find that barrier crossing and peak-background split give consistent answers.

[9] In more detail, to show that $f_{\rm NL}(1+\Pi)\Delta_\Phi \ll 1$, we argue as follows. Assuming that the field ψ is not strongly coupled, the dimensionless non-Gaussianity parameter $f_{\rm NL}^{(\psi)}\Delta_\psi = f_{\rm NL}(1+\Pi)^{3/2}\Delta_\Phi$ must be $\lesssim 1$. Therefore

$$f_{\rm NL}(1+\Pi)\Delta_\Phi = \Big[f_{\rm NL}\Delta_\Phi\Big]^{1/3} \cdot \Big[f_{\rm NL}(1+\Pi)^{3/2}\Delta_\Phi\Big]^{2/3} \lesssim [10^{-3}]^{1/3} \cdot [1] = 10^{-1} \ , \tag{2.66}$$

where the bound on the first factor is the current observational bound $f_{\rm NL} \lesssim 10^2$.

2.5.2 $g_{\rm NL}$ Cosmology

As our next example, we consider a cubic form of local non-Gaussianity.[10] In this case, the non-Gaussian potential is parametrized by the expansion

$$\Phi = \phi + g_{\rm NL}\left(\phi^3 - 3\langle\phi^2\rangle\phi\right) \ . \tag{2.69}$$

The power spectrum of the non-Gaussian field is

$$P_\Phi(k) = P_\phi(k) + g_{\rm NL}^2 P_{\phi^3}(k) \ , \tag{2.70}$$

where

$$P_{\phi^3}(k) \equiv 6\int_{\boldsymbol{q}_1}\int_{\boldsymbol{q}_2} P_\phi(q_1)P_\phi(q_2)P_\phi(|\boldsymbol{k}-\boldsymbol{q}_1-\boldsymbol{q}_2|) \ . \tag{2.71}$$

We note that for scale-invariant initial conditions, $(k^3/2\pi^2)P_\phi(k) = \Delta_\phi^2$, the power spectrum P_{ϕ^3} is infrared divergent. If the IR divergence is regulated by putting the fields in a finite box with length L, then the power spectrum diverges as

$$P_{\phi^3}(k) \ \sim \ 18\,\Delta_\phi^4 \ln^2(kL) P_\phi(k) \ . \tag{2.72}$$

On large scales, the matter power spectrum therefore is

$$P_{\rm mm}(k) \simeq \alpha^2(k)P_\Phi(k) = P_g(k)\left(1 + 18\,g_{\rm NL}^2\Delta_\phi^4\ln^2(kL)\right) \ , \tag{2.73}$$

where we defined $P_g(k) \equiv \alpha^2(k)P_\phi(k)$. Current observational constraints imply that $|g_{\rm NL}\Delta_\phi^2| \ll 1$. To obtain answers to zeroth or first order in $g_{\rm NL}\Delta_\phi^2$, it suffices to set $P_{\rm mm} \simeq P_g$.

[10] We should say from the outset that the large-scale stochasticity in the $g_{\rm NL}$ model will be too small to be observationally relevant. Although the non-stochastic and stochastic contributions to $P_{\rm hh}(k)$ will turn out to be parametrically identical ($\sim g_{\rm NL}^2\Delta_\Phi^2 P_\Phi(k)$), the non-stochastic contribution is typically larger by a constant factor $\approx 10^4$. Nevertheless, the $g_{\rm NL}$ example provides an interesting check of our formalism.

For the barrier crossing analysis, we require the following higher-order correlation functions

$$\xi_\Phi^{(4)[\rm tree]}(\boldsymbol{k}_1,\boldsymbol{k}_2,\boldsymbol{k}_3,\boldsymbol{k}_4) = g_{\rm NL}\big[P_1P_2P_3 + 23\,\text{perms.}\big] + \mathcal{O}(g_{\rm NL}^2)\ , \tag{2.74}$$

$$\xi_\Phi^{(4)[\rm loop]}(\boldsymbol{k}_1,\boldsymbol{k}_2,\boldsymbol{k}_3,\boldsymbol{k}_4) = 9\,g_{\rm NL}^2\big[P_1P_2P_{\phi^2}(k_{13}) + 11\,\text{perms.}\big]\ , \tag{2.75}$$

$$\xi_\Phi^{(6)}(\boldsymbol{k}_1,\boldsymbol{k}_2,\boldsymbol{k}_3,\boldsymbol{k}_4,\boldsymbol{k}_5,\boldsymbol{k}_6) = 36\,g_{\rm NL}^2\big[P_1P_2P_3P_4P_{125} + 89\,\text{perms.}\big]\ , \tag{2.76}$$

where $k_{ij} = |\boldsymbol{k}_i + \boldsymbol{k}_j|$, $P_i = P_\phi(k_i)$, $P_{ijk} = P_\phi(|\boldsymbol{k}_i + \boldsymbol{k}_j + \boldsymbol{k}_k|)$, and

$$P_{\phi^2}(k) \equiv 2\int_{\boldsymbol{q}} P_\phi(q)P_\phi(|\boldsymbol{k}-\boldsymbol{q}|) \ \sim\ 4\Delta_\phi^2\ln(kL)P_\phi(k)\ . \tag{2.77}$$

Note that odd-point correlation functions $\xi_\Phi^{(2N+1)}$ are zero due to the $\Phi \to -\Phi$ symmetry. Next, we will derive the stochastic halo bias both in peak-background split and in barrier crossing.

Peak-Background Split

The PBS analysis proceeds as before. Splitting the Gaussian potential into long and short modes, $\phi = \phi_\ell + \phi_s$, we find that the locally measured small-scale power is $\sigma = \bar\sigma\,[1 + 3g_{\rm NL}\,(\phi_\ell^2 - \langle\phi_\ell^2\rangle)]$. Moreover, the locally measured value of $f_{\rm NL}$ is $f_{\rm NL}^{\rm eff} = 3g_{\rm NL}\phi_\ell$ [28]. The halo number density therefore is

$$n_{\rm h}(\boldsymbol{x}) = \bar n_{\rm h}\left(\delta_c - \delta_\ell\,;\bar\sigma\left[1 + 3g_{\rm NL}\left(\phi_\ell^2 - \langle\phi_\ell^2\rangle\right)\right];f_{\rm NL}^{\rm eff}\right)\ , \tag{2.78}$$

where $\delta_\ell \simeq \alpha(k_\ell)\phi_\ell$. Taylor expanding this expression, we find

$$\delta_{\rm h} = b_g\delta_\ell + \tfrac{3}{2}\beta_f g_{\rm NL}\left(\phi_\ell^2 - \langle\phi_\ell^2\rangle\right) + \beta_g g_{\rm NL}\phi_\ell\ , \tag{2.79}$$

where b_g and β_f are the same as in (2.59), and

$$\beta_g \equiv 3\frac{\partial \ln n_{\rm h}}{\partial f_{\rm NL}} \ . \tag{2.80}$$

It follows that

$$P_{\rm mh} = b_g P_{\rm mm} + \beta_g g_{\rm NL} P_{{\rm m}\phi} = \left(b_g + \beta_g \frac{g_{\rm NL}}{\alpha(k)}\right) P_{\rm mm} \ , \tag{2.81}$$

and

$$P_{\rm hh} = \left(b_g + \beta_g \frac{g_{\rm NL}}{\alpha(k)}\right)^2 P_{\rm mm} + \frac{9}{4}\beta_f^2 g_{\rm NL}^2 P_{\phi^2} \ . \tag{2.82}$$

This implies a large-scale halo stochasticity of the form

$$r = \frac{9}{4}\beta_f^2 g_{\rm NL}^2 \frac{P_{\phi^2}}{P_{\rm mm}} \ . \tag{2.83}$$

Barrier Crossing

We now show that the same result is obtained from barrier crossing. In Appendix 2.7, we argue that only the first few cumulants need to be taken into account. It is straightforward to compute them explicitly. From eqs. (2.74) and (2.76), we get

$$f_{1,3}(k) \ \xrightarrow{k\to 0} \ \frac{3 g_{\rm NL}}{\alpha(k)}\,\kappa_3^{(f_{\rm NL}=1)} \qquad \text{and} \qquad f_{3,3}(k) = [f_{1,3}(k)]^2 \ . \tag{2.84}$$

This only contributes to the non-stochastic bias. However, since $f_{\hat{1},2} = 0$, stochastic bias arises from $f_{2,2}$. First, we note that the tree-level four-point function (2.74) leads to a very small and scale-independent contribution to $f_{2,2}$:

$$f_{2,2}^{[\rm tree]}(k, M, \bar{M}) \ \xrightarrow{k\to 0} \ \frac{12\, g_{\rm NL}}{P_{\rm mm}(k)}\left(\frac{1}{\sigma_M^2}\int_{\boldsymbol{q}} \alpha_M^2(q) P_\phi^2(q) + \frac{1}{\sigma_{\bar{M}}^2}\int_{\boldsymbol{q}} \alpha_{\bar{M}}^2(q) P_\phi^2(q)\right) \ . \tag{2.85}$$

Plugging into eq. (2.48) and noting that $\beta_2 = \frac{1}{4}\beta_f$ and $\tilde{\beta}_2 = \frac{1}{2}$, we get a small scale-dependent contribution to the large-scale stochastic bias

$$r_{[\text{tree}]} = \frac{3}{2}\frac{g_{\text{NL}}}{P_{\text{mm}}(k)}\left(\beta_f^2 + 2\beta_f\right)\left(\frac{1}{\sigma_M^2}\int_{\boldsymbol{q}} \alpha_M^2(q) P_\phi^2(q)\right) \ . \tag{2.86}$$

In practice, this contribution to the large-scale stochasticity can't be used as a probe of initial conditions, since a contribution to r with $r \propto 1/k$ (or equivalently a contribution to $P_{\text{hh}}(k)$ which approaches a constant as $k \to 0$) is degenerate with other sources of stochasticity such as second-order Gaussian bias. Finally, the one-loop four-point function (2.75) leads to the following contribution to $f_{2,2}$:

$$f_{2,2}^{[\text{loop}]}(k) \ \xrightarrow{k\to 0} \ 36\, g_{\text{NL}}^2 \cdot \frac{P_{\phi^2}(k)}{P_{\text{mm}}(k)} \ . \tag{2.87}$$

The corresponding stochasticity parameter is

$$r_{[\text{loop}]} = \frac{9}{4}\beta_f^2 g_{\text{NL}}^2 \frac{P_{\phi^2}(k)}{P_{\text{mm}}(k)} \propto \frac{1}{k^4} \ , \tag{2.88}$$

in agreement with the PBS predictions (2.83).

2.5.3 Quasi-Single-Field Inflation

Our last example is quasi-single field inflation (QSFI) [19]. These models involve extra massive scalar degrees of freedom during inflation. In the simplest examples, a single scalar field σ of mass[11] $m^2 \leq \frac{9}{4}H^2$ mixes with the fluctuation of the inflaton[12] $\delta\phi$. The mixing communicates non-Gaussianity from the hidden (isocurvature) sector to the observable (adiabatic) sector. As we now show, it also leads to a significant stochasticity in the halo bias.

[11] We note that extra scalars with masses close to the Hubble scale H are a natural prediction of supersymmetric theories of inflation (see [20] for further discussion).

[12] Recall that $\delta\phi$ in spatially flat gauge is proportional to the curvature perturbation, $\zeta \equiv -\frac{H}{\dot{\phi}}\delta\phi$.

Boosted Four-Point Function

Again, we need the squeezed and collapsed limits of the primordial correlation functions[13] [19, 20, 14]:

$$\lim_{k_1\to 0}\xi_\Phi^{(3)}(\boldsymbol{k}_1,\boldsymbol{k}_2,\boldsymbol{k}_3)=4f_{\rm NL}\left(\frac{k_1}{k_2}\right)^{\Delta}P_1P_2\ , \tag{2.89}$$

$$\lim_{k_{12}\to 0}\xi_\Phi^{(4)}(\boldsymbol{k}_1,\boldsymbol{k}_2,\boldsymbol{k}_3,\boldsymbol{k}_4)=\ 16\left(\tfrac{5}{6}\right)^2\tau_{\rm NL}\left(\frac{k_{12}^2}{k_1k_3}\right)^{\Delta}P_1P_3P_{12}\ , \tag{2.90}$$

where we defined the parameter

$$\Delta\equiv\frac{3}{2}-\sqrt{\frac{9}{4}-\frac{m^2}{H^2}}\ . \tag{2.91}$$

The non-trivial momentum scaling of eqs. (2.89) and (2.90) is a remarkable signature of extra Hubble mass scalars during inflation [19, 20, 29, 30]. Moreover, if the mixing between σ and ϕ (or ζ) is parametrized by a small dimensionless number $\varepsilon<1$, then

$$\tau_{\rm NL}\sim\varepsilon^{-2}\left(\tfrac{6}{5}f_{\rm NL}\right)^2\ >\ \left(\tfrac{6}{5}f_{\rm NL}\right)^2\ . \tag{2.92}$$

The enhancement of $\tau_{\rm NL}$ arises because the trispectrum is generated by the exchange of the σ-field which is only weakly coupled to ζ. The size of the four-point function $\langle\zeta^4\rangle$ can be estimated from the square of the three-point function $\langle\zeta^2\sigma\rangle$ at horizon crossing,

$$\langle\zeta^4\rangle\sim\langle\zeta^2\sigma\rangle^2\sim\varepsilon^{-2}\,\frac{\langle\zeta^3\rangle^2}{\langle\zeta^2\rangle}\ . \tag{2.93}$$

The boost of $\tau_{\rm NL}$ is the result of the small correlation between the curvature fluctuation and the massive field, $\varepsilon\ll 1$. The precise dependence of $f_{\rm NL}$ and $\tau_{\rm NL}$ on the fundamental parameters of the QSFI Lagrangian can be found in [14].

[13] See [20] for an intuitive explanation of the scalings in eqs. (2.89) and (2.90).

Barrier Crossing

In QSFI, the higher-order N-point functions are suppressed by factors of the power spectrum, just as in our previous examples. The dominant contributions to the large-scale structure signal therefore arise from the squeezed limit of the three-point function and the collapsed limit of the four-point function. The relevant cumulants are

$$\kappa_{\hat{1},2}(k) \xrightarrow{k\to 0} \frac{4f_{\rm NL}}{\hat{\sigma}}(kR_M)^{\Delta}\,\frac{P_{\rm mm}(k)}{\alpha(k)}\,\frac{\Sigma_M^2(\Delta)}{\sigma_M^2}\ , \tag{2.94}$$

and

$$\kappa_{2,2}(k) \xrightarrow{k\to 0} 16\left(\tfrac{5}{6}\right)^2\tau_{\rm NL}(k^2R_MR_{\bar{M}})^{\Delta}\,\frac{P_{\rm mm}(k)}{\alpha^2(k)}\,\frac{\Sigma_M^2(\Delta)}{\sigma_M^2}\frac{\Sigma_{\bar{M}}^2(\Delta)}{\sigma_{\bar{M}}^2}\ . \tag{2.95}$$

Here, we have defined

$$\Sigma_M^2(\Delta) \equiv \int \frac{{\rm d}^3k_s}{(2\pi)^3}\,W_M^2(k_s)(k_sR_M)^{-\Delta}P_{\rm mm}(k_s)\ , \tag{2.96}$$

where the integration variable, k_s, is one of the short momenta and R_M is the smoothing scale defined by eq. (2.14). By definition, $\Sigma_M(0)=\sigma_M$. In the limit $\Delta\to 0$, we recover the results of the $\tau_{\rm NL}$ model. Therefore, we find

$$f_{\hat{1},2} = 4f_{\rm NL}\,\frac{(kR_M)^{\Delta}}{\alpha(k)}\,\frac{\Sigma_M^2(\Delta)}{\sigma_M^2} \qquad \text{and} \qquad f_{2,2} = \frac{\tau_{\rm NL}}{(\frac{6}{5}f_{\rm NL})^2}\,f_{\hat{1},2}(M)f_{\hat{1},2}(\bar{M})\ . \tag{2.97}$$

To obtain the large-scale stochasticity, we substitute the cumulants into eq. (2.48),

$$r \;=\; \left(\beta_2+\tilde{\beta}_2\frac{\partial}{\partial\ln\sigma_M}\right)\left(\beta_2+\tilde{\beta}_2\frac{\partial}{\partial\ln\sigma_{\bar{M}}}\right)f_{2,2} \;-\; \left[\left(\beta_2+\tilde{\beta}_2\frac{\partial}{\partial\ln\sigma_M}\right)f_{\hat{1},2}\right]^2\ . \tag{2.98}$$

Because the cumulants depend explicitly on R_M, we have to be concerned that the derivatives with respect to σ_M may this time not be negligible. Indeed, numerical evaluation of the integral shows significant σ_M dependence of $f_{\hat{1},2}$ (see fig. 2.2). Keeping the derivative terms,

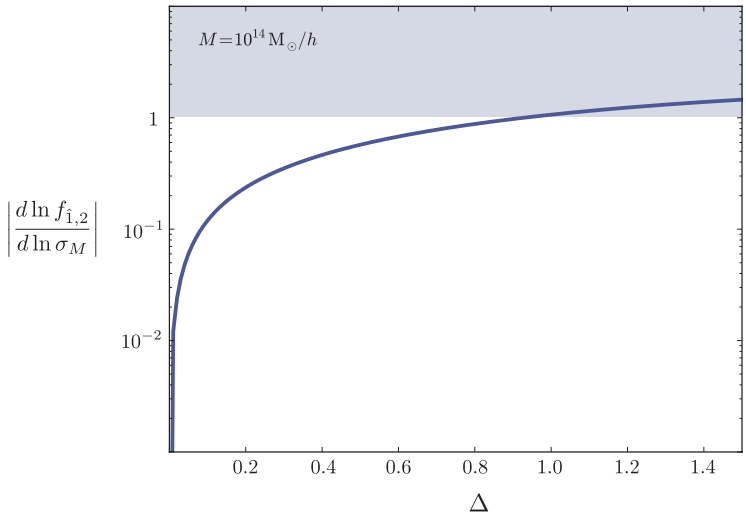

Figure 2.2: Numerical evaluation of eqs. (2.96) and (2.97). For $\Delta \gtrsim 1.0$, the cumulant $f_{\hat{1},2}$ depends significantly on the halo mass scale M. This is in contrast to local non-Gaussianity, which corresponds to the limit $\Delta \to 0$.

we get

$$\begin{aligned} r &= \left(\left(\tfrac{5}{6}\right)^2 \tau_{\rm NL} - f_{\rm NL}^2\right) \frac{k^{2\Delta}}{\alpha^2(k)} \left[\left(\beta_f + 2\,\frac{d}{d\ln\sigma_M}\right) \frac{R_M^\Delta\,\Sigma_M^2(\Delta)}{\sigma_M^2}\right]^2 \\ &\propto \frac{\left(\frac{5}{6}\right)^2 \tau_{\rm NL} - f_{\rm NL}^2}{k^{4-2\Delta}}\,. \end{aligned} \tag{2.99}$$

The characteristic momentum scaling of eq. (2.99) and the natural boost of $\tau_{\rm NL}$ makes halo stochasticity an interesting probe of quasi-single-field inflation.

2.6 Conclusions

What was the number of light degrees of freedom during inflation? And, what were their interactions? The great virtue of primordial non-Gaussianity is that it is sensitive to these basic questions about the physics of inflation. In particular, it is well-known that the squeezed limit of the primordial three-point function,

$$\lim_{k_1 \to 0} \langle \Phi_{\boldsymbol{k}_1} \Phi_{\boldsymbol{k}_2} \Phi_{\boldsymbol{k}_3} \rangle \ , \tag{2.100}$$

can only be large if more than one light field was dynamically relevant during inflation [31, 32]. Remarkably, this statement is independent of the details of the Lagrangian for the inflaton field and its initial conditions. Measurements of the squeezed limit therefore have the potential to rule out all models of single-field inflation [31, 32]. Moreover, the precise scaling in the squeezed limit is sensitive to the details of the mass spectrum [19, 14], allowing a test of extra Hubble mass fields, such as those generically expected in supersymmetric theories [20]. Having a large three-point function in the squeezed limit modulates the two-point function of halos and therefore leads to scale-dependent bias [7]. In the future, this effect may well be our most sensitive probe of the squeezed limit.

In this paper, we have discussed a *stochastic* form of scale-dependent halo bias. This effect arises if the collapsed limit of the primordial four-point function,

$$\lim_{k_{12} \to 0} \langle \Phi_{\boldsymbol{k}_1} \Phi_{\boldsymbol{k}_2} \Phi_{\boldsymbol{k}_3} \Phi_{\boldsymbol{k}_4} \rangle_{\rm c} \ , \tag{2.101}$$

is larger than the square of the squeezed limit of the three-point function. More generally, stochastic bias arises whenever a suitable collapsed limit of an $(M+N)$-point function is larger than the product of the associated squeezed $(M+1)$-point and $(N+1)$-point functions, where $M, N \geq 2$. The key tool for obtaining this result, and a main result of this paper, is a pair of formulas, eqs. (2.36) and (2.46), for the matter-halo and halo-halo power spectra

in a general non-Gaussian model parametrized by the N-point functions of the primordial potential.

In non-Gaussian models which generate significant stochastic halo bias, the results of this paper are important even at a qualitative level. As a concrete example, it should be possible to measure $f_{\rm NL}$ and $\tau_{\rm NL}$ independently using stochastic bias. This can be done either by measuring multiple tracer populations and directly estimating large-scale stochasticity (which has the advantage of eliminating sample variance), or from a single tracer population by measuring $P_{\rm hh}(k)$ and using the functional form

$$P_{\rm hh}(k) = b_g^2 \left(1 + f_{\rm NL}\frac{2\delta_c}{\alpha(k)} + \tau_{\rm NL}\frac{(\frac{5}{6})^2\delta_c^2}{\alpha^2(k)}\right) \tag{2.102}$$

to fit for b_g, $f_{\rm NL}$ and $\tau_{\rm NL}$ independently.

Recently, ref. [36] showed that if only non-stochastic bias is considered, the leading contribution from $\tau_{\rm NL}$ is small (in our language, this corresponds to the $\mathcal{O}(\tau_{\rm NL})$ contribution to $\kappa_{1,3}$) and it is difficult to separate $f_{\rm NL}$ and $\tau_{\rm NL}$, so stochastic bias has an important qualitative effect. As another example, in quasi-single field inflation, the stochastic bias is larger than the non-stochastic bias by a large factor (parametrically ε^{-2}), leading to a similarly large enhancement in signal-to-noise when stochastic bias is considered. We defer quantitative forecasts incorporating stochastic bias for future work.

In general, there is no stochastic bias if only a single field (which may or may not be the inflaton) generates the primordial curvature perturbation and its non-Gaussianity [16]. Measuring stochastic halo bias would therefore teach us about the effective number of degrees of freedom that generated the primordial fluctuations and its higher-order correlations. In particular, stochasticity is sensitive to what we may call "hidden sector non-Gaussianity", i.e. situations in which two fields generate the curvature perturbation, but only one (hidden) field is responsible for its non-Gaussianity. In this paper, we have derived this effect for general non-Gaussian initial conditions. We have also applied our formalism to a number

of explicit examples, such as curvaton models [18] and quasi-single field inflation [19]. We have shown that halo bias, in principle, gives us information about the soft limits of both the primordial three-point function and the four-point function. It is therefore a valuable tool in the quest to uncover the physics that created the initial perturbations.

Acknowledgments

We thank Valentin Assassi, Eugene Lim, Marilena LoVerde, Marcel Schmittfull, David Spergel and Matias Zaldarriaga for helpful discussions. D.B. gratefully acknowledges support from a Starting Grant of the European Research Council (ERC STG grant 279617). S.F. acknowledges support from a fellowship at the Department of Astrophysical Sciences of Princeton University. The research of D.G. is supported by the DOE under grant number DE-FG02-90ER40542 and the Martin A. and Helen Chooljian Membership at the Institute for Advanced Study. K.M.S. was supported by a Lyman Spitzer fellowship in the Department of Astrophysical Sciences at Princeton University. Research at Perimeter Institute is supported by the Government of Canada through Industry Canada and by the Province of Ontario through the Ministry of Research & Innovation.

2.7 Appendix: Convergence of the Edgeworth Expansion

In this appendix, we discuss the convergence properties of the Edgeworth expansion for local non-Gaussianity. In particular, we will estimate the relative size of the cumulants $\kappa_{n,m}(k, M)$ for general n and $m > 0$ in the large-scale limit $k \to 0$. For further discussion see e.g. [33, 34, 35]. The results in this appendix are used in the main text in several places: to justify the approximation that non-linear terms in the Edgeworth expansion are negligible in eqs. (2.33) and (2.43), and to justify keeping only certain cumulants in the $\tau_{\rm NL}$ model (§2.5.1) and the $g_{\rm NL}$ model (§2.5.2).

2.7.1 $\tau_{\rm NL}$ Cosmology

We first consider the $\tau_{\rm NL}$ model of §2.5.1.

Linear terms.—The leading contribution in the $k \to 0$ limit arises from the following contribution to the connected correlation function

$$\kappa_{n,m} \simeq \mathcal{A}_{n,m} \int \langle \overbrace{\psi_1(\psi\psi)_2} \cdots \overbrace{(\psi\psi)_n \mid (\psi\psi)_{n+1}} \cdots \overbrace{(\psi\psi)_{n+m-1}\psi_{n+m}} \rangle'_{\rm c} \, {\rm d}\mathbf{K} \,, \qquad (2.103)$$

where ${\rm d}\mathbf{K} \equiv \prod_i \frac{{\rm d}^3\boldsymbol{k}_i}{(2\pi)^3}\, \alpha_M(k_i)$ and $(\psi\psi)_i$ denotes an auto-convolution evaluated at $\boldsymbol{k}_i$. The prime on the correlation function denotes that we have dropped an overall momentum conserving delta-function. The amplitude of the cumulant is given by

$$\mathcal{A}_{n,m} \equiv c_{n,m}(1+\Pi)^{2(n+m-2)} f_{\rm NL}^{n+m-2} \,, \qquad \text{where} \qquad c_{n,m} \equiv \frac{n!m!\, 2^{n+m-2}}{\sigma_M^n \sigma_{\bar{M}}^m} \,. \qquad (2.104)$$

We arrived at eq. (2.103) by using the definition of Φ in eq. (2.51) and expanding out terms to produce a connected correlation function. The numerical factor $c_{n,m}$ in the amplitude (2.104) arises from the sum over equivalent contractions of the fields. The vertical line in

(2.103) separates the first n terms from the last m. Each contraction gives a factor of P_ψ, and the contraction crossing the vertical line carries momentum k, giving a factor of $P_\psi(k)$ that can be taken out of the integral. The power spectrum $P_\psi(k)$ diverges as $k \to 0$ and gives the largest[14] contribution to $\kappa_{n,m}$. The remaining integral over d$\mathbf{K}$ will typically be dominated by the non-linear scale $k_{\rm nl}$, where $k_{\rm nl}^3 P_{\rm mm}(k_{\rm nl}) \sim \alpha_M^2(k_{\rm nl})\Delta_\Phi^2 \sim 1$. Therefore, we may estimate the integral using $\alpha_M \sim \Delta_\Phi^{-1}$, to get

$$\kappa_{1,m} \;\simeq\; c_{1,m}\,(1+\Pi)^{m-2}\; f_{\rm NL}^{m-1}\;\Delta_\Phi^{m-2}\cdot\frac{P_{\rm mm}(k)}{\alpha(k)} \qquad \text{for} \;\; m>1\;, \tag{2.105}$$

$$\kappa_{n,m} \;\simeq\; c_{n,m}\,(1+\Pi)^{n+m-3}\; f_{\rm NL}^{n+m-2}\;\Delta_\Phi^{n+m-4}\cdot\frac{P_{\rm mm}(k)}{\alpha^2(k)} \qquad \text{for} \;\; n \text{ and } m>1\;. \tag{2.106}$$

The factor $n!m!$ appearing in $c_{n,m}$ is canceled explicitly in the Edgeworth expansion (2.23), and as shown in §2.5.1, the condition $f_{\rm NL}(1+\Pi)\Delta_\Phi \ll 1$ is always satisfied. This implies that higher-order cumulants are subdominant relative to lower-order ones, and hence the only terms we have to keep in the $\tau_{\rm NL}$ model are $\kappa_{1,1}$, $\kappa_{1,2}=\kappa_{2,1}$ and $\kappa_{2,2}$.

Non-linear terms.—When expanding the exponential in the Edgeworth expansion (2.23) we also encounter non-linear terms such as $\kappa_{n,m}^P(\boldsymbol{x})$. First, we will show that, for n and/or $m>1$, these terms are suppressed by the near-Gaussianity of the primordial perturbations. We distinguish two cases:

- When $n>1$ and $m>1$, we take powers of the contributions in (2.106), to find

$$\kappa_{n,m}^P \;\sim\; \Big[c_{n,m}\,(1+\Pi)^{n+m-3}\,f_{\rm NL}^{n+m-2}\,\Delta_\Phi^{n+m-4}\Big]^P\cdot\frac{P_{\rm mm}(k)}{\alpha^2(k)}\cdot\Delta_\Phi^{2(P-1)}\ln^{P-1}(kL)\;, \tag{2.107}$$

  where L is an infrared cutoff. This can be written as

$$\kappa_{n,m}^P \;\sim\; \kappa_{n,m}\cdot c_{n,m}^P\big[f_{\rm NL}(1+\Pi)\Delta_\Phi\big]^{(P-1)(n+m-2)}(1+\Pi)^{-P}\ln^{P-1}(kL)\;. \tag{2.108}$$

[14]Subleading contributions arise when both linear ψ terms appear on the same side. In such cases, two contractions cross the vertical line, and the resulting cumulant is finite in the $k\to 0$ limit.

Using $f_{\rm NL}(1+\Pi)\Delta_\Phi \ll 1$ and $(1+\Pi) > 1$, we see that $\kappa^P_{n,m}$ is suppressed relative to $\kappa_{n,m}$ for $n, m > 1$.

- When $n = 1$ and $m > 1$, the situation is slightly different. If we take higher powers of the results in (2.105), we find for $P > 1$,

$$\begin{aligned}\kappa^P_{1,m} &\sim c^P_{1,m}\left[(1+\Pi)^{m-2} f^{m-1}_{\rm NL}\,\Delta^{m-2}_\Phi\right]^P \Delta^{P-1}_\Phi P_{\rm mm}(k_{\rm nl}) \\ &\sim \kappa_{1,m}\cdot c^{P-1}_{1,m}\left[f_{\rm NL}(1+\Pi)\Delta_\Phi\right]^{(P-1)(m-1)}(1+\Pi)^{-P}\alpha(k)\cdot\frac{P_{\rm mm}(k_{\rm nl})}{P_{\rm mm}(k)}\ . \end{aligned} \tag{2.109}$$

  Again, as we increase the power P, the contribution is suppressed. However, there is a clear difference between $P = 1$ and $P > 1$. Nevertheless, in the limit $k \to 0$, $[P_{\rm mm}(k)/\alpha(k)]^{-1} \propto k$ so that these contributions vanish relative to $\kappa_{1,m}$.

Next, we consider products of the Gaussian piece, $\kappa^P_{1,1}$. We find for $P > 1$,

$$\begin{aligned}\kappa^P_{1,1} &\sim P^P_{\rm mm}(k_{\rm eq})\cdot(k_{\rm eq})^{3P-3} \\ &\sim \kappa_{1,1}\,\frac{P_{\rm mm}(k_{\rm eq})}{P_{\rm mm}(k)}\,\Delta^{P-1}_{\rm m}(k_{\rm eq})\ . \end{aligned} \tag{2.110}$$

Here, $\kappa_{1,1}$ receives its largest contribution from the peak of the linear matter power spectrum $\Delta^2_{\rm m}(k) = k^3\hat{P}_{\rm m}(k)$ which occurs at $k = k_{\rm eq}$, the scale set by matter-radiation equality. Because $\Delta_{\rm m}(k_{\rm eq}) < 1$ at that scale, the modes are still linear and higher powers of $\kappa_{1,1}$ will be suppressed. However, in the limit $k \to 0$, $\kappa_{1,1}$ vanishes, while $\kappa^P_{1,1}$ is finite for $P > 1$. This gives a small constant contribution to the halo power spectrum $P_{\rm hh}$ which is a free parameter in practice (we discussed this in the context of the $g_{\rm NL}$ model in §2.5.2).

Finally, we look at terms of the form $\kappa^P_{n,m}\kappa^Q_{n',m'}$. We may bound these contributions by using the above estimates with the convolution $\kappa^P_{n,m}\star\kappa^Q_{n',m'} = \int_{\boldsymbol{q}}\kappa^P_{m,n}(|\boldsymbol{q}|)\kappa^Q_{n',m'}(|\boldsymbol{k}-\boldsymbol{q}|)$. For $n, m > 1$, the convolution will be dominated by the IR, and we find

$$\kappa^P_{n,m}\star\kappa^Q_{n',m'} \sim \kappa^P_{n,m}(k)\kappa^Q_{n',m'}(k)\,\frac{\alpha^2(k)\ln(kL)}{P_{\rm mm}(k)}\ . \tag{2.111}$$

For $m = m' = 1$, the convolution is dominated by physics at the non-linear scale, so we may simply multiply (2.109) and/or (2.110) to find

$$\kappa^P_{n,1} \star \kappa^Q_{n',1} \;\sim\; \kappa^P_{n,1}(k)\kappa^Q_{n',1}(k)\, k^3_{\rm nl} \; . \tag{2.112}$$

As a result, convolutions of different cumulants will be suppressed by $f_{\rm NL}(1+\Pi)\Delta_\Phi \ll 1$.

2.7.2 $g_{\rm NL}$ Cosmology

Similar arguments apply to the $g_{\rm NL}$ model of §2.5.2.

Linear terms.—First, we note that $\kappa_{n,m} = 0$, unless $n+m$ is even. Moreover, only for both n and m odd do we get a scale-dependent tree-level contribution to the cumulant. (In the main text, we discuss the important special case $\kappa_{2,2}$.) Schematically, we can write $\kappa_{n,m} \sim g^\beta_{\rm NL}\, \Delta^\gamma_\Phi$. At tree level, we then find

$$\kappa_{1,m} \;\sim\; g_{\rm NL}^{\frac{m-1}{2}}\, \Delta_\Phi^{m-2} \cdot \frac{P_{\rm mm}(k)}{\alpha(k)} \qquad \text{for} \;\; m \text{ odd} \; , \tag{2.113}$$

$$\kappa_{n,m} \;\sim\; g_{\rm NL}^{\frac{n+m}{2}-1}\, \Delta_\Phi^{m+n-4} \cdot \frac{P_{\rm mm}(k)}{\alpha^2(k)} \qquad \text{for} \;\; n, m \text{ odd and} > 1 \; . \tag{2.114}$$

Since current observational constraints imply $|g_{\rm NL}\Delta^2_\Phi| \ll 1$, the only tree-level terms that we need to keep are $\kappa_{1,1}$, $\kappa_{1,3} = \kappa_{3,1}$ and $\kappa_{3,3}$. As we discuss in the main text, there is also an interesting loop contribution to $\kappa_{2,2}$.

Non-linear terms.—As in the $\tau_{\rm NL}$ model, products of cumulants of the form $\kappa^P_{n,m}$ will be suppressed due to the near-Gaussianity of the perturbations. The contributions of higher powers of $\kappa_{n,m}$ is nearly identical in both cases:

- When $n > 1$ and $m > 1$, we take powers of the contributions in (2.114), to find

$$\begin{aligned}\kappa_{n,m}^P &\sim \left[g_{\rm NL}^{\frac{n+m}{2}-1} \Delta_\Phi^{m+n-4} \right]^P \cdot \frac{P_{\rm mm}(k)}{\alpha^2(k)} \cdot \Delta_\Phi^{2(P-1)} \ln^{P-1}(kL) \\ &\sim \kappa_{n,m} \left[g_{\rm NL} \Delta_\Phi^2 \right]^{(P-1)(\frac{n+m-2}{2})} \ln^{P-1}(kL) \ . \end{aligned} \tag{2.115}$$

  Clearly, if $g_{\rm NL}\Delta_\Phi^2 \ll 1$, then the higher powers of $\kappa_{n,m}$ are suppressed (if we assume that the log is small).

- When $n = 1$ and $m > 1$, we take higher powers of the results in (2.113), to find for $P > 1$

$$\begin{aligned}\kappa_{1,m}^P &\sim \left[g_{\rm NL}^{\frac{m-1}{2}} \Delta_\Phi^{m-2} \right]^P \Delta_\Phi^{P-1} P_{\rm mm}(k_{\rm nl}) \\ &\sim \kappa_{1,m} \left[g_{\rm NL} \Delta_\Phi^2 \right]^{(P-1)(\frac{m-1}{2})} \alpha(k) \cdot \frac{P_{\rm mm}(k_{\rm nl})}{P_{\rm mm}(k)} \ . \end{aligned} \tag{2.116}$$

  Again, we find that $P > 1$ contributions are suppressed by powers of $g_{\rm NL}\Delta_\Phi^2 \ll 1$. As in the $\tau_{\rm NL}$ model, we find that $P = 1$ has a different scaling with k from $P > 1$.

It should be clear that other cumulants behave in the same way as in the $\tau_{\rm NL}$ model and will be suppressed by factors of $g_{\rm NL}\Delta_\Phi^2$.

Bibliography

[1] S. Ferraro, K. Smith, D. Green, and D. Baumann, "On the Equivalence of Barrier Crossing, Peak-Background Split, and Local Biasing", *to appear*.

[2] A. Guth, "The Inflationary Universe: A Possible Solution To The Horizon And Flatness Problems," Phys. Rev. D **23**, 347 (1981); • A. Linde, "A New Inflationary Universe Scenario: A Possible Solution Of The Horizon, Flatness, Homogeneity, Isotropy And Primordial Monopole Problems," Phys. Lett. B **108**, 389 (1982); • A. Albrecht and P. Steinhardt, "Cosmology For Grand Unified Theories With Radiatively Induced Symmetry Breaking," Phys. Rev. Lett. **48**, 1220 (1982);
• for a review see D. Baumann, "TASI Lectures on Inflation," [arXiv:0907.5424 [hep-th]].

[3] E. Komatsu et al., "Non-Gaussianity as a Probe of the Physics of the Primordial Universe and the Astrophysics of the Low Redshift Universe," arXiv:0902.4759 [astro-ph.CO].

[4] E. Komatsu, "Hunting for Primordial Non-Gaussianity in the Cosmic Microwave Background," Class. Quant. Grav. **27**, 124010 (2010).

[5] V. Desjacques and U. Seljak, "Primordial Non-Gaussianity in the Large-Scale Structure of the Universe," [arXiv:1006.4763 [astro-ph.CO]].

[6] M. Liguori, E. Sefusatti, J. Fergusson, and E. P. S. Shellard, "Primordial Non-Gaussianity and Bispectrum Measurements in the Cosmic Microwave Background and Large-Scale Structure," Adv. Astron. **2010**, 980523 (2010).

[7] N. Dalal, O. Dore, D. Huterer, and A. Shirokov, "The Imprints of Primordial Non-Gaussianities on Large-Scale Structure: Scale-Dependent Bias and Abundance of Virialized Objects," Phys. Rev. **D77**, 123514 (2008).

[8] S. Matarrese and L. Verde, "The Effect of Primordial Non-Gaussianity on Halo Bias," Astrophys. J. **677**, L77 (2008).

[9] C. Byrnes, M. Sasaki, and D. Wands, "The Primordial Trispectrum from Inflation," Phys. Rev. D **74**, 123519 (2006).

[10] T. Suyama and M. Yamaguchi, "Non-Gaussianity in the Modulated Reheating Scenario," Phys. Rev. D **77**, 023505 (2008).

[11] N. Sugiyama, E. Komatsu, and T. Futamase, "Non-Gaussianity Consistency Relation for Multi-Field Inflation," Phys. Rev. Lett. **106**, 251301 (2011).

[12] A. Lewis, 'The Real Shape of Non-Gaussianities," JCAP **1110**, 026 (2011).

[13] K. Smith, M. LoVerde, and M. Zaldarriaga, "A Universal Bound on N-point Correlations from Inflation," Phys. Rev. Lett. **107**, 191301 (2011).

[14] V. Assassi, D. Baumann, and D. Green, "On Soft Limits of Inflationary Correlation Functions," arXiv:1204.4207 [hep-th].

[15] A. Kehagias and A. Riotto, "Operator Product Expansion of Inflationary Correlators and Conformal Symmetry of de Sitter," arXiv:1205.1523 [hep-th].

[16] T. Suyama, T. Takahashi, M. Yamaguchi, and S. Yokoyama, "On Classification of Models of Large Local-Type Non-Gaussianity," JCAP **1012**, 030 (2010).

[17] C. Byrnes, S. Nurmi, G. Tasinato, and D. Wands, "Inhomogeneous Non-Gaussianity," JCAP **1203** (2012) 012.

[18] D. Tseliakhovich, C. Hirata, and A. Slosar, "Non-Gaussianity and Large-Scale Structure in a Two-Field Inflationary Model," Phys. Rev. **D82**, 043531 (2010).

[19] X. Chen and Y. Wang, "Quasi-Single-Field Inflation and Non-Gaussianities," JCAP **1004**, 027 (2010).

[20] D. Baumann and D. Green, "Signatures of Supersymmetry from the Early Universe," Phys. Rev. D **85**, 103520 (2012).

[21] W. Press and P. Schechter, "Formation of Galaxies and Clusters of Galaxies by Self-Similar Gravitational Condensation," Astrophys. J. **187**, 425 (1974).

[22] F. Bernardeau, S. Colombi, E. Gaztanaga, and R. Scoccimarro, "Large-Scale Structure of the Universe and Cosmological Perturbation Theory," Phys. Rept. **367**, 1 (2002).

[23] M. Grossi, L. Verde, C. Carbone, K. Dolag, E. Branchini, F. Iannuzzi, S. Matarrese, and L. Moscardini, "Large-Scale Non-Gaussian Mass Function and Halo Bias: Tests on N-body Simulations," Mon. Not. Roy. Astron. Soc. **398**, 321 (2009).

[24] N. Hamaus, U. Seljak, V. Desjacques, R. Smith, and T. Baldauf, "Minimizing the Stochasticity of Halos in Large-Scale Structure Surveys," Phys. Rev. D **82**, 043515 (2010).

[25] K. Smith and M. LoVerde, "Local Stochastic Non-Gaussianity and N-body Simulations," JCAP **1111**, 009 (2011).

[26] V. Desjacques, D. Jeong, and F. Schmidt, "Non-Gaussian Halo Bias Re-examined: Mass-Dependent Amplitude from the Peak-Background Split and Thresholding," Phys. Rev. D **84**, 063512 (2011).

[27] A. Slosar, C. Hirata, U. Seljak, S. Ho, and N. Padmanabhan, "Constraints on Local Primordial Non-Gaussianity from Large-Scale Structure," JCAP **0808**, 031 (2008).

[28] K. Smith, S. Ferraro, and M. LoVerde, "Halo Clustering and $g_{\rm NL}$-type Primordial non-Gaussianity," JCAP **1203**, 032 (2012).

[29] E. Sefusatti, J. Fergusson, X. Chen, and E. P. S. Shellard, "Effects and Detectability of Quasi-Single Field Inflation in the Large-Scale Structure and Cosmic Microwave Background," arXiv:1204.6318 [astro-ph.CO].

[30] J. Norena, L. Verde, G. Barenboim, and C. Bosch, "Prospects for Constraining the Shape of Non-Gaussianity with the Scale-Dependent Bias," arXiv:1204.6324 [astro-ph.CO].

[31] J. Maldacena, "Non-Gaussian Features of Primordial Fluctuations in Single-Field Inflationary Models," JHEP **0305**, 013 (2003).

[32] P. Creminelli and M. Zaldarriaga, "Single-Field Consistency Relation for the Three-Point Function," JCAP **0410**, 006 (2004).

[33] M. LoVerde, A. Miller, S. Shandera, and L. Verde, "Effects of Scale-Dependent Non-Gaussianity on Cosmological Structures," JCAP **0804**, 014 (2008).

[34] S. Shandera, "The Structure of Correlation Functions in Single-Field Inflation," Phys. Rev. D **79**, 123518 (2009).

[35] N. Barnaby and S. Shandera, "Feeding your Inflaton: Non-Gaussian Signatures of Interaction Structure," JCAP **1201**, 034 (2012).

[36] M. Biagetti, V. Desjacques, and A. Riotto, "Testing Multi-Field Inflation with Galaxy Bias," arXiv:1208.1616 [astro-ph.CO].

Chapter 3

On the Correspondence between Barrier Crossing, Peak-Background Split, and Local Biasing

3.1 Abstract

Several, apparently distinct, formalisms exist in the literature for predicting the clustering of dark matter halos. It has been noticed on a case-by-case basis that the predictions of these different methods agree in specific examples, but the precise correspondence remains unclear. In this chapter, we provide a simple mathematical relationship between barrier crossing, peak-background split, and local biasing.

3.2 Introduction

The large-scale clustering of dark matter halos has become an important probe of primordial cosmology. In particular, non-Gaussianity in the initial conditions would leave an imprint in the scale-dependence of the halo bias [9, 17], sometimes of stochastic type [24, 4]. Several, apparently distinct, methods are commonly used to compute these effects. So far, these

methods have been considered to be independent, even though they give the same results when applied to specific examples [10, 4]. In this paper, we will show that the barrier crossing (BC) model, the peak-background split (PBS) method and the local biasing (LB) approach are, in fact, mathematically closely related.

Barrier crossing is the classic model of structure formation dating back to the pioneering work of Press and Schechter [18]. In its simplest formulation, it identifies halos as regions of the linearly evolved density field above some critical density δ_c. The clustering properties of halos can then be calculated as an Edgeworth expansion in the cumulants of the probability density of the primordial density fluctuations, which in turn can be expressed in terms of N-point functions of the potential [15, 10, 23, 4].

Peak-background split is a method for calculating the influence of long-wavelength fluctuations (larger than the halo size) on the locally measured statistical properties. It has been widely used in cosmology [3, 8] and its usefulness in dealing with non-Gaussian initial conditions has been first pointed out in [9]. In the most common implementation, the non-Gaussian field is defined as a non-linear function of auxiliary Gaussian fields, which are split into short-wavelength and long-wavelength components. By modulating the statistics of the short modes, the long modes affect the clustering statistics. In this paper, we will generalize the PBS approach so that it can be applied to arbitrary non-Gaussian initial conditions, parametrized by arbitrary N-point functions of the primordial potential. This will require introducing additional fields $\rho_2, \rho_3, \cdots$, which measure the local power spectrum amplitude, skewness, etc.

Local biasing [11, 20, 12, 2, 19] refers to the idea of expressing the halo density field $\delta_{\rm h}$ as a function the local dark matter density (smoothed on some scale) and expanding in powers of the density contrast δ,

$$\delta_{\rm h}(\boldsymbol{x}) = b_1\delta(\boldsymbol{x}) + b_2\delta^2(\boldsymbol{x}) + b_3\delta^3(\boldsymbol{x}) + \cdots \ . \tag{3.1}$$

Correlation functions can then be computed straightforwardly in terms of the coefficients in the expansion. Several variations of this formalism exist in literature (for example some use an expansion in the non-linear dark matter density, while others use the linearly evolved density). In this work, we will demonstrate the equivalence between barrier crossing and a particular variant of local biasing, in which the expansion is in the linearly evolved and non-Gaussian dark matter density contrast.

In a companion paper [4] (included here as Chapter 2), we derived the clustering statistics for specific non-Gaussian models, both in the peak-background split formalism and in the barrier crossing model. We showed for each example that both approaches give consistent results. The goal of this paper is to prove that this agreement isn't accidental, but follows from a mathematical relationship between both methods.

The outline of the chapter is as follows. After defining our notation in Section 3.3, we introduce our main technical tool in Section 3.4: a series expansion for the halo field $\delta_{\rm h}$ in the barrier crossing model. We review some examples of non-Gaussian models and show how the series expansion is used for efficiently calculating halo power spectra. In Section 3.5, we use the series expansion to provide a mathematical relationship the barrier crossing model, the peak-background split method, and the local biasing formalism. We conclude with brief comments in Section 3.6. An appendix collects some elementary properties of Hermite polynomials.

3.3 Preliminaries and Notation

Non-Gaussian initial conditions can be parameterized by the connected N-point functions $\xi_\Phi^{(N)}$ of the primordial gravitational potential Φ. In Fourier space, these are defined as

$$\langle \Phi_{\boldsymbol{k}_1} \Phi_{\boldsymbol{k}_2} \cdots \Phi_{\boldsymbol{k}_N} \rangle_{\rm c} = (2\pi)^3 \delta_{\rm D}(\boldsymbol{k}_{12\ldots N})\, \xi_\Phi^{(N)}(\boldsymbol{k}_1, \boldsymbol{k}_2, \ldots, \boldsymbol{k}_N) \ , \tag{3.2}$$

where $\boldsymbol{k}_{12\ldots N} \equiv \boldsymbol{k}_1 + \boldsymbol{k}_2 + \cdots + \boldsymbol{k}_N$. The primordial potential is related to the linearly evolved matter density contrast via Poisson's equation

$$\delta_{\boldsymbol{k}}(z) = \alpha(k,z)\Phi_{\boldsymbol{k}} \ , \tag{3.3}$$

where

$$\alpha(k,z) \equiv \frac{2k^2 T(k) D(z)}{3\Omega_m H_0^2} \ . \tag{3.4}$$

Here, $T(k)$ is the matter transfer function normalized such that $T(k) \to 1$ as $k \to 0$ and $D(z)$ is the linear growth factor (as function of redshift z), normalized so that $D(z) = (1+z)^{-1}$ in matter domination. For notational simplicity, we will from now on suppress the redshift argument from all quantities. The field $\delta_M(\boldsymbol{x})$ denotes the linear density contrast smoothed with a top-hat filter of radius $R_M = (3M/4\pi\bar{\rho}_{\rm m})^{1/3}$. In Fourier space,

$$\delta_M(\boldsymbol{k}) = W_M(k)\delta_{\boldsymbol{k}} \ , \tag{3.5}$$

where $W_M(k)$ is the Fourier transform of the top-hat filter,

$$W_M(k) \equiv 3\,\frac{\sin(kR_M) - kR_M\cos(kR_M)}{(kR_M)^3} \ . \tag{3.6}$$

We also define $\sigma_M \equiv \langle \delta_M^2 \rangle^{1/2}$ and $\alpha_M(k) \equiv W_M(k)\alpha(k)$.

The main quantity of interest, in this paper, is the halo density contrast in Lagrangian space

$$\delta_{\rm h}(\boldsymbol{x}) \equiv \frac{n_{\rm h}(\boldsymbol{x}) - \langle n_{\rm h}\rangle}{\langle n_{\rm h}\rangle} \ , \tag{3.7}$$

where $n_{\rm h}(\boldsymbol{x})$ is the halo number density. To lowest order, $\delta_{\rm h}$ is related to the halo over-density in Eulerian space via $\delta_{\rm h}^{\rm E} = \delta_{\rm h} + \delta$. We will determine the large-scale behavior of the matter-halo and halo-halo power spectra $P_{\rm mh}(k) \equiv \langle \delta\delta_{\rm h}\rangle(k)$ and $P_{\rm hh}(k) \equiv \langle \delta_{\rm h}\delta_{\rm h}\rangle(k)$. We define $P_{\rm hh}(k)$ to be the halo power spectrum after the shot noise contribution $1/n_{\rm h}$ has

been subtracted, where $n_{\rm h}$ is the halo number density. Analogously, we define $P_{\rm mh}(k)$ to be the matter-halo power spectrum after subtracting the 1-halo term (in practice, this term is usually negligibly small). We define the (Lagrangian) halo bias as

$$b(k) \equiv \frac{P_{\rm mh}(k)}{P_{\rm mm}(k)} \ . \tag{3.8}$$

This is related to the Eulerian bias via $b_{\rm E} = b + 1$. A stochastic form of halo bias arises whenever the density of halos isn't 100% correlated with the dark matter density [4]. In that case, the bias inferred from $P_{\rm hh}$ will be different from the bias inferred from $P_{\rm mh}$, i.e.

$$\frac{P_{\rm hh}(k)}{P_{\rm mm}(k)} \ \neq \ \left(\frac{P_{\rm mh}(k)}{P_{\rm mm}(k)}\right)^2 \ . \tag{3.9}$$

3.4 A Series Representation of Barrier Crossing

In this section, we introduce the barrier crossing formalism and quote results from our companion paper [4]. We also introduce a series representation of barrier crossing, which will be our main tool to prove the equivalence to local biasing and peak-background split in Section 3.5.

3.4.1 Review of Barrier Crossing

In the simplest version of the barrier crossing model [18], halos of mass $\geq M$ are modeled as regions of space in which the smoothed density field δ_M exceeds the collapse threshold δ_c, i.e. the halo number density $n_{\rm h}(\boldsymbol{x})$ is given by

$$n_{\rm h}^{MW}(\boldsymbol{x}) \propto \Theta(\delta_M(\boldsymbol{x}) - \delta_c) \ , \tag{3.10}$$

where Θ is the Heaviside step function. Eq. (3.10) models the abundance of a *mass-weighted* sample of halos whose mass exceeds some minimum value M.[1] We will also consider the case of a halo sample defined by a narrow mass bin, which is obtained from the mass-weighted case by differentiating with respect to M, i.e.

$$n_{\rm h}^N(\boldsymbol{x}) \propto \frac{\partial}{\partial M}\Theta(\delta_M(\boldsymbol{x}) - \delta_c) \ . \tag{3.11}$$

Throughout the paper, we will refer to these two types of halo samples as "mass-weighted samples" (MW) and "narrow samples" (N).

The barrier crossing model allows us to compute the statistics of halo-halo and halo-matter correlations. To discuss correlations between quantities at two points $\boldsymbol{x}$ and $\boldsymbol{x}'$, it is useful to define $\delta_M = \delta_M(\boldsymbol{x}), \delta'_M = \delta_M(\boldsymbol{x}')$ and $r = |\boldsymbol{x} - \boldsymbol{x}'|$. The joint cumulants of the density fields are then[2]

$$\kappa_{\hat{m},n}(r, M) \ \equiv \ \frac{\langle \delta^m (\delta'_M)^n \rangle_{\rm c}}{\sigma^m \sigma_M^n} \ , \tag{3.12}$$

$$\kappa_{m,n}(r, M, \bar{M}) \ \equiv \ \frac{\langle (\delta_M)^m (\delta'_{\bar{M}})^n \rangle_{\rm c}}{\sigma_M^m \sigma_{\bar{M}}^n} \ . \tag{3.13}$$

The hat on $\kappa_{\hat{m},n}$ denotes the use of the unsmoothed density field δ. In the limit $k \to 0$, we find $\kappa_{\hat{1},1}(k) \to P_{\rm mm}(k)/(\sigma\sigma_M)$ and $\kappa_{1,1}(k) \to P_{\rm mm}(k)/(\sigma_M\sigma_{\bar{M}})$. This motivates the following

[1]This type of sample is often assumed when fitting models to observations of luminous tracers such as galaxies or quasars. In the absence of detailed knowledge of the halo occupation distribution (HOD), a simple choice is to assume that halos below some minimum mass M are unpopulated with tracers, whereas the expected number of tracers in a halo of mass $\geq M$ is proportional to the halo mass.

[2]Note that the variance of the unsmoothed linear density contrast $\sigma^2 = \langle \delta^2 \rangle$ is formally infinite, but cancels in the definition (3.14) of the quantity $f_{\hat{1},n}$ which will appear in our final expressions.

definitions

$$f_{\hat{1},n}(k,M) \equiv \frac{\kappa_{\hat{1},n}(k,M)}{\kappa_{\hat{1},1}(k,M)\,\sigma_M} \qquad \text{for } n \geq 1 \ , \tag{3.14}$$

$$f_{1,n}(k,M,\bar{M}) \equiv \frac{\kappa_{1,n}(k,M,\bar{M})}{\kappa_{1,1}(k,M,\bar{M})\sigma_{\bar{M}}} \qquad \text{for } n \geq 1 \ , \tag{3.15}$$

$$f_{m,n}(k,M,\bar{M}) \equiv \frac{\kappa_{m,n}(k,M,\bar{M})}{\kappa_{1,1}(k,M,\bar{M})\sigma_M\sigma_{\bar{M}}} \qquad \text{for } m,n \geq 2 \ . \tag{3.16}$$

Using the function $\alpha(k,z)$ defined in (3.3), it is straightforward to relate the above cumulants to the primordial correlation functions $\xi_\Phi^{(N)}$ defined in (3.2).

In [4], we showed how the matter-halo and halo-halo power spectra are computed in the barrier crossing model using the Edgeworth expansion for the joint probability density function $p(\delta_M, \delta'_M)$. (We refer the reader to that paper for detailed derivations and further discussion.) The result can be expressed in terms of the cumulants $f_{\hat{1},n}$ and $f_{m,n}$. Taking the limit $k \to 0$ for the case of a mass-weighted sample with $M = \bar{M}$, we find

$$P_{\rm mh}(k,M) = P_{\rm mm}(k)\left(b_g^{MW}(M) + \sum_{n\geq 2} \alpha_n(M) f_{\hat{1},n}(k,M) \right) \ , \tag{3.17a}$$

$$P_{\rm hh}(k,M) = P_{\rm mm}(k)\Bigg(b_g^{MW}(M)^2 + 2b_g^{MW}(M) \sum_{n\geq 2} \alpha_n(M) f_{1,n}(k,M,M) + \sum_{m,n\geq 2} \alpha_m(M)\alpha_n(M) f_{m,n}(k,M,M) \Bigg) \ , \tag{3.17b}$$

where the coefficients α_n (not to be confused with the α of eq. (3.3)) are defined in terms of Hermite polynomials (see Appendix 3.7),

$$\alpha_n(M) \equiv \sqrt{\frac{2}{\pi}} \frac{e^{-\nu_c^2/2}}{\mathrm{erfc}(\frac{1}{\sqrt{2}}\nu_c)} \frac{H_{n-1}(\nu_c)}{n!} \ , \quad \text{with} \quad \nu_c(M) \equiv \frac{\delta_c}{\sigma_M} \ . \tag{3.18}$$

We also defined the Gaussian bias as

$$b_g^{MW}(M) \equiv \frac{\alpha_1(M)}{\sigma_M} \ . \tag{3.19}$$

Note that $b_g^{MW}(M)$ is the Press-Schechter bias for the mass-weighted halo sample. In writing (3.17), we have dropped "nonlinear" terms in the Edgeworth expansion, i.e. terms involving products $(\kappa_{m_1 n_1}\kappa_{m_2 n_2}\cdots\kappa_{m_p n_p})$ with $p > 1$.

Similarly, for the case of a halo sample defined by a narrow mass bin, we have

$$P_{\rm mh}(k,M) = P_{\rm mm}(k)\left(b_g^N(M) + \sum_{n\geq 2}\mathcal{D}_n(M) f_{\hat{1},n}(k,M)\right) \ , \tag{3.20a}$$

$$P_{\rm hh}(k,M) = P_{\rm mm}(k)\Bigg(b_g^N(M)^2 + 2b_g^N(M)\sum_{n\geq 2}\mathcal{D}_n(M) f_{1,n}(k,M,\bar{M})\Big|_{M=\bar{M}} + \sum_{m,n\geq 2}\mathcal{D}_m(M)\mathcal{D}_n(\bar{M}) f_{m,n}(k,M,\bar{M})\Big|_{M=\bar{M}}\Bigg) \ , \tag{3.20b}$$

where we have defined the differential operator

$$\mathcal{D}_n(M) \equiv \beta_n(M) + \tilde{\beta}_n(M)\frac{\partial}{\partial \ln \sigma_M} \ , \tag{3.21}$$

as well as the functions

$$b_g^N(M) \equiv \frac{1}{\sigma_M}\frac{\nu_c^2 - 1}{\nu_c} \quad , \quad \beta_n(M) \equiv \frac{H_n(\nu_c)}{n!} \quad \text{and} \quad \tilde{\beta}_n(M) \equiv \frac{H_{n-1}(\nu_c)}{n!\,\nu_c} \ . \tag{3.22}$$

Note that $b_g^N(M)$ is the Press-Schechter bias of a halo sample defined by a narrow mass bin. In eq. (3.20b) for $P_{\rm hh}$, we have assumed $M = \bar{M}$ for simplicity, but the variables M and $\bar{M}$ should be treated as independent for purposes of taking derivatives.

3.4.2 Hermite Polynomial Expansion

In this section, we will develop an alternative (to the Edgeworth expansion) algebraic framework for analyzing clustering in the barrier crossing model. First, consider the case of a

mass-weighted halo sample, where the halo field is modeled as a step function

$$n_{\rm h}^M W(\boldsymbol{x}) \propto \Theta\left(\nu(\boldsymbol{x}) - \nu_c\right) \ , \quad \text{where} \quad \nu(\boldsymbol{x}) \equiv \frac{\delta_M(\boldsymbol{x})}{\sigma_M} \ . \tag{3.23}$$

Since the Hermite polynomials $H_n(\nu)$ are a complete basis, any function of ν can be written as a linear combination of Hermite polynomials. In particular, we can write the Heaviside step function $\Theta(\nu - \nu_c)$ as

$$\Theta(\nu - \nu_c) = \sum_{n=0}^{\infty} a_n(\nu_c)\, H_n(\nu) \ , \tag{3.24}$$

where

$$a_n(\nu_c) = \frac{1}{n!}\int_{-\infty}^{\infty} {\rm d}\nu \ \Theta(\nu - \nu_c)\, \frac{e^{-\nu^2/2}}{\sqrt{2\pi}}\, H_n(\nu) = \begin{cases} \frac{1}{2}{\rm erfc}(\frac{1}{\sqrt{2}}\nu_c) & n = 0 \\ \frac{1}{n!}\frac{1}{\sqrt{2\pi}} e^{-\nu_c^2/2}\, H_{n-1}(\nu_c) & n \geq 1 \end{cases} \ . \tag{3.25}$$

Plugging this series expansion into eq. (3.23), and normalizing the halo field to the fractional overdensity $\delta_{\rm h}$, we get

$$\begin{aligned} \delta_{\rm h}(\boldsymbol{x}) &= \sum_{n\geq 1} \frac{a_n(\nu_c)}{a_0(\nu_c)} H_n\left(\frac{\delta_M(\boldsymbol{x})}{\sigma_M}\right) \\ &= b_g^{MW}(M)\delta_M(\boldsymbol{x}) + \sum_{n\geq 2} \alpha_n(M)\rho_n(\boldsymbol{x}) \ , \quad \text{[mass-weighted sample]} \end{aligned} \tag{3.26}$$

where $\alpha_n(M)$ and $b_g^{MW}(M)$ were introduced in eqs. (3.18) and (3.19), respectively. The fields ρ_n are defined as

$$\rho_n(\boldsymbol{x}) \equiv H_n\left(\frac{\delta_M(\boldsymbol{x})}{\sigma_M}\right) \ . \tag{3.27}$$

On large scales, the field $\rho_2 = \delta_M^2/\sigma_M^2 - 1$ tracks long-wavelength variations in the locally measured small-scale power, and for non-Gaussian initial conditions the power spectrum $P_{\rho_2\rho_2}(k)$ may acquire extra large-scale contributions. Analogously, the field $\rho_3 = \delta_M^3/\sigma_M^3 -$

$3\delta_M/\sigma_M$ tracks long-wavelength variations in the locally measured small-scale skewness, and so on for higher ρ_n.

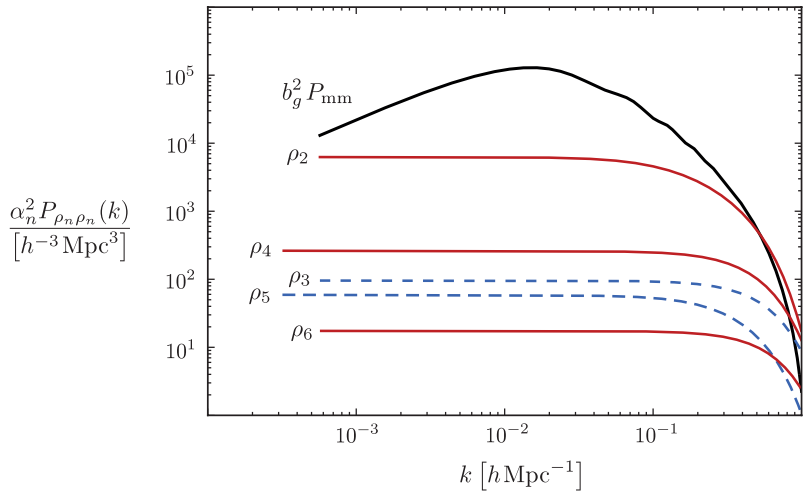

Figure 3.1: Convergence of the series representation (3.26) at low k, illustrated by comparing terms in the halo-halo power spectrum $P_{\mathrm{hh}}(k) = b_g^2(M)P_{\mathrm{mm}}(k) + \sum_{n=2}^{\infty} \alpha_n^2(M)P_{\rho_n\rho_n}(k)$ in a Gaussian cosmology. (Note that for Gaussian initial conditions, cross power spectra $P_{\rho_m\rho_n}(k)$ with $m \neq n$ are zero.) We have taken $z = 0$ and a mass-weighted sample of halos with mass $M \geq 2 \times 10^{13}\ h^{-1}\ M_\odot$.

We emphasize that the series representation (3.26) is mathematically equivalent to the barrier crossing model, since it is obtained by simply substituting the convergent Hermite series (3.24) into the barrier crossing expression (3.23) for n_{h}. The series representation converges for all values of $\boldsymbol{x}$, but its usefulness depends on how rapidly it converges, i.e. how many terms we need to get a good approximation. For example, to compute the halo field $\delta_{\mathrm{h}}(\boldsymbol{x})$ at a single point $\boldsymbol{x}$ in real space, many terms are needed (of order 100) and the series representation is not useful. On the other hand, the Fourier transformed series representation $\delta_{\mathrm{h}}(\boldsymbol{k}) = b_g^{MW}\delta_M + \sum_{n=2}^{\infty} \alpha_n \rho_n(\boldsymbol{k})$ converges rapidly on large scales (i.e. $k \ll k_{\mathrm{nl}}$), as shown in fig. 3.1, and the series representation is very convenient. (The series converges for all k, but only converges rapidly for $k \ll k_{\mathrm{nl}}$.)

The preceding expressions have all applied to the case of a mass-weighted halo sample. For the case of a halo sample defined by a narrow mass bin, the halo field is modeled as

$$\begin{aligned} n_{\rm h}^N(\boldsymbol{x}) &\propto \frac{\partial}{\partial \ln \sigma_M} \Theta\left(\frac{\delta_M(\boldsymbol{x})}{\sigma_M} - \nu_c\right) \\ &= \frac{\partial}{\partial \ln \sigma_M} \sum_{n\geq 0} a_n(\nu_c) H_n\left(\frac{\delta_M(\boldsymbol{x})}{\sigma_M}\right) \\ &= \sum_{n\geq 0} \left((n+1)\nu_c\, a_{n+1}(\nu_c) + a_n(\nu_c)\frac{\partial}{\partial \ln \sigma_M}\right) H_n\left(\frac{\delta_M(\boldsymbol{x})}{\sigma_M}\right) . \end{aligned} \tag{3.28}$$

Normalizing $n_{\rm h}$ to the fractional halo overdensity $\delta_{\rm h}$, we get

$$\begin{aligned} \delta_{\rm h}(\boldsymbol{x}) &= \sum_{n\geq 1} \left((n+1)\frac{a_{n+1}(\nu_c)}{a_1(\nu_c)} + \frac{a_n(\nu_c)}{\nu_c a_1(\nu_c)}\frac{\partial}{\partial \ln \sigma_M}\right) H_n\left(\frac{\delta_M(\boldsymbol{x})}{\sigma_M}\right) \\ &= \left(\frac{\nu_c^2 - 1}{\nu_c \sigma_M}\right)\delta_M(x) + \frac{1}{\nu_c \sigma_M}\frac{\partial \delta_M(\boldsymbol{x})}{\partial \ln \sigma_M} \\ &\qquad + \sum_{n\geq 2}\left(\frac{1}{n!}H_n(\nu_c) + \frac{1}{n!}\frac{H_{n-1}(\nu_c)}{\nu_c}\frac{\partial}{\partial \ln \sigma_M}\right) H_n\left(\frac{\delta_M(\boldsymbol{x})}{\sigma_M}\right) . \end{aligned} \tag{3.29}$$

We drop the term containing $\partial \delta_M / \partial \ln \sigma_M$, since this term vanishes on large scales, $k \ll R_M^{-1}$, and write the result using the notation $b_g, \beta_n, \tilde{\beta}_n$ defined in eq. (3.22):

$$\delta_{\rm h}(\boldsymbol{x}) = b_g^N(M)\delta_M(\boldsymbol{x}) + \sum_{n=2}^{\infty}\left(\beta_n(M) + \tilde{\beta}_n(M)\frac{\partial}{\partial \ln \sigma_M}\right)\rho_n(\boldsymbol{x}) . \qquad \text{[narrow sample]} \tag{3.30}$$

As a check on our formalism, we can verify that the matter-halo and halo-halo power spectra obtained from the series (3.26) agree with the results obtained previously in [4] using the Edgeworth expansion. We first write the power spectrum $P_{\delta\rho_n}(k)$ in terms of the correlation function (3.2),

$$P_{\delta\rho_n}(k) = \frac{\alpha(k)}{\sigma_M^n}\left(\prod_{i=1}^{n-1}\int_{\boldsymbol{q}_i}\alpha_M(q_i)\right)\alpha_M(-|\boldsymbol{k}+\boldsymbol{q}|) \times \xi_\Phi^{(n+1)}(\boldsymbol{k}, \boldsymbol{q}_1, \cdots, \boldsymbol{q}_{n-1}, -\boldsymbol{k}-\boldsymbol{q}) , \tag{3.31}$$

where we have defined $\int_{\boldsymbol{q}_i}(\,\cdot\,) \equiv \int \frac{\mathrm{d}^3\boldsymbol{q}_i}{(2\pi)^3}(\,\cdot\,)$ and $\boldsymbol{q} \equiv \sum_{i=1}^{n-1}\boldsymbol{q}_i$. Similarly, we can express $P_{\rho_m\rho_n}(k)$ as[3]

$$\begin{aligned} P_{\rho_m\rho_n}(k) &= \frac{1}{\sigma_M^m\sigma_{\bar{M}}^n}\left(\prod_{i=1}^{m-1}\int_{\boldsymbol{q}_i'}\alpha_M(q_i')\right)\left(\prod_{j=1}^{n-1}\int_{\boldsymbol{q}_j}\alpha_{\bar{M}}(q_j)\right)\alpha_M(q')\alpha_{\bar{M}}(q) \\ &\quad\times\,\xi_\Phi^{(m+n)}(\boldsymbol{q}_1',\cdots,\boldsymbol{q}_{m-1}',-\boldsymbol{q}'+\boldsymbol{k},\boldsymbol{q}_1,\cdots,\boldsymbol{q}_{n-1},-\boldsymbol{q}-\boldsymbol{k})\;, \end{aligned} \tag{3.32}$$

where $\boldsymbol{q}' \equiv \sum_{i=1}^{m-1}\boldsymbol{q}_i'$. Using the notation $f_{\hat{1},n}$ and $f_{m,n}$ defined in eqs. (3.14) and (3.16), and taking the limit $k \to 0$, we find

$$P_{\delta\rho_n}(k) = f_{\hat{1},n}(k,M)\,P_{\mathrm{mm}}(k)\;, \tag{3.33}$$

$$P_{\rho_m\rho_n}(k) = f_{m,n}(k,M,\bar{M})\,P_{\mathrm{mm}}(k)\;. \tag{3.34}$$

For the case of the mass-weighted halo sample, the series representation (3.26) therefore gives the following matter-halo and halo-halo power spectra

$$P_{\mathrm{mh}}(k,M) = P_{\mathrm{mm}}(k)\left(\sum_{n\geq 1}\alpha_n(M)f_{\hat{1},n}(k,M)\right)\;, \tag{3.35a}$$

$$P_{\mathrm{hh}}(k,M,\bar{M}) = P_{\mathrm{mm}}(k)\left(\sum_{m,n\geq 1}\alpha_m(M)\alpha_n(\bar{M})f_{m,n}(k,M,\bar{M})\right)\;, \tag{3.35b}$$

in agreement with the Edgeworth calculation (3.17). The case of the narrow mass bin can be verified similarly.

[3]We have made an approximation here: by using *connected* correlation functions in eqs. (3.31) and (3.32), we have neglected some contributions to the power spectra $P_{\delta\rho_n}$ and $P_{\rho_m\rho_n}$. More precisely, we have neglected disconnected terms whose factorization contains multiple higher cumulants (i.e. $\kappa_{m,n}$ with $m+n \geq 3$), and also some contributions to $P_{\rho_m\rho_n}(k)$ which approach a constant as $k \to 0$. (Note that subleading terms in the Hermite polynomial $\rho_n = (\delta_M/\sigma_M)^n - n(n-1)(\delta_M/\sigma_M)^{n-2}/2 + \cdots$ cancel the largest disconnected contributions to the power spectra in eqs. (3.31) and (3.32).) The derivation in [4] of eq. (3.17) contains equivalent approximations, which is why we will shortly find agreement with the results of [4]. In principle, one can avoid making any approximations by including disconnected contributions when calculating power spectra $P_{\delta\rho_n}$ and $P_{\rho_m\rho_n}$. However, in Appendix A of [4], we showed that these approximations are always valid in the observationally relevant regime where the initial perturbations are close to Gaussian.

Eqs. (3.26) and (3.30) are the main results of this section and give a series representation for the halo field in the barrier crossing model, for the cases of a mass-weighted halo sample and a narrow mass bin respectively. Using the series representation, we will give a simple, conceptual proof of the close correspondence of the barrier model, the peak-background split, and local biasing in Section 3.5. However, it is useful to first build intuition by considering a few example non-Gaussian models.

3.4.3 Examples

For a given non-Gaussian model, one can analyze large-scale clustering by keeping a small set of terms in the series expansion of $\delta_{\rm h}$ (either eq. (3.26) or (3.30) for a mass-weighted sample or narrow mass bin, respectively), and computing the necessary power spectra $P_{\rho_m \rho_n}(k)$ on large scales. This is a computationally convenient way to compute the non-Gaussian clustering signal, and allows the signal to be interpreted physically as arising from large-scale variations in locally measured quantities such as small-scale power and skewness, as we will see in the context of some example models.

$\tau_{\rm NL}$ Cosmology

Consider a non-Gaussian model in which the initial Newtonian potential is given by

$$\Phi(\boldsymbol{x}) = \phi(\boldsymbol{x}) + f_{\rm NL}\left(\phi^2(\boldsymbol{x}) - \langle\phi^2\rangle\right) \ , \tag{3.36}$$

where ϕ is a Gaussian field. We will refer to this as the "$f_{\rm NL}$ model" (or local model). This type of non-Gaussianity arises somewhat generically in multi-field models of the early universe, e.g. modulated reheating models [25], curvaton models [14, 16], or multi-field ekpyrotic scenarios [13, 6]. In this section, we will study a generalization of the $f_{\rm NL}$ model which we will call the "$\tau_{\rm NL}$ model". This type of non-Gaussianity arises in "multi-source" models, i.e. models in which quantum mechanical perturbations in multiple fields determine the ini-

tial adiabatic curvature perturbation [24, 7, 5, 1]. The non-Gaussian potential Φ is given in terms of two uncorrelated Gaussian fields ϕ and ψ, with power spectra that are proportional to each other

$$\Phi(\boldsymbol{x}) = \phi(\boldsymbol{x}) + \psi(\boldsymbol{x}) + f_{\rm NL}(1+\Pi)^2 \left(\psi^2(\boldsymbol{x}) - \langle\psi^2\rangle\right) \ , \tag{3.37}$$

where $f_{\rm NL}$ and $\Pi = P_\phi(k)/P_\psi(k)$ are free parameters. It is easy to compute the three- and four-point functions,

$$\xi_\Phi^{(3)} = f_{\rm NL}\big[P_1P_2 + 5\,\text{perms.}\big] + \mathcal{O}(f_{\rm NL}^3) \ , \tag{3.38}$$

$$\xi_\Phi^{(4)} = 2\left(\tfrac{5}{6}\right)^2 \tau_{\rm NL}\big[P_1P_2P_{13} + 23\,\text{perms.}\big] + \mathcal{O}(\tau_{\rm NL}^2) \ , \tag{3.39}$$

where we have defined $\tau_{\rm NL} = (\frac{6}{5}f_{\rm NL})^2(1+\Pi)$, $P_i \equiv P_\Phi(k_i)$, and $P_{ij} \equiv P_\Phi(|\boldsymbol{k}_i + \boldsymbol{k}_j|)$. It is conventional to parametrize this model with variables $\{f_{\rm NL}, \tau_{\rm NL}\}$, which correspond to the amplitudes of the 3-point and 4-point functions, rather than the variables $\{f_{\rm NL}, \Pi\}$. The $f_{\rm NL}$ model (with $\Pi = 0$ so that ψ contributes but not ϕ) corresponds to the special case $\tau_{\rm NL} = (\frac{6}{5}f_{\rm NL})^2$.

To compute halo clustering in the $\tau_{\rm NL}$ model, we keep the first two terms in the series expansion for $\delta_{\rm h}$ (eqs. (3.26) and (3.30)), obtaining:

$$\delta_{\rm h} = \begin{cases} b_g^{MW}\delta_M + \alpha_2\rho_2 \ , & \text{[mass-weighted sample]} \\ b_g^N\delta_M + \left(\beta_2(M) + \tilde{\beta}_2(M)\frac{\partial}{\partial\ln\sigma_M}\right)\rho_2 \ . & \text{[narrow sample]} \end{cases} \tag{3.40}$$

Using eqs. (3.38) and (3.39) in eqs. (3.31) and (3.32), we obtain the following power spectra in the $k \to 0$ limit:

$$P_{\delta\rho_2}(k) = 4f_{\rm NL}\frac{P_{\rm mm}(k)}{\alpha(k)} \ , \tag{3.41}$$

$$P_{\rho_2\rho_2}(k) = 16\left(\tfrac{5}{6}\right)^2\tau_{\rm NL}\frac{P_{\rm mm}(k)}{\alpha^2(k)} \ . \tag{3.42}$$

Putting everything together, we find

$$P_{\rm mh}(k) = \left(b_g + f_{\rm NL}\frac{\beta_f}{\alpha(k)}\right) P_{\rm mm}(k) \ , \tag{3.43a}$$

$$P_{\rm hh}(k) = \left(b_g^2 + 2b_g f_{\rm NL}\frac{\beta_f}{\alpha(k)} + \left(\tfrac{5}{6}\right)^2 \tau_{\rm NL}\frac{\beta_f^2}{\alpha^2(k)}\right) P_{\rm mm}(k) \ . \tag{3.43b}$$

where we have defined the non-Gaussian bias parameter

$$\beta_f = \begin{cases} 4\alpha_2(M) \ , & \text{[mass-weighted sample]} \\ 4\beta_2(M) \ . & \text{[narrow sample]} \end{cases} \tag{3.44}$$

In both the mass-weighted and narrow mass bin cases, the non-Gaussian and Gaussian parts of the bias are related by $\beta_f = 2\delta_c b_g$. Note that in the narrow mass bin case, there is a derivative term in $\delta_{\rm h}$ (the term $\partial\rho_2/\partial \ln \sigma_M$ in eq. (3.40)), but this ends up giving zero contribution to the power spectra $P_{\rm mh}$ and $P_{\rm hh}$, since the power spectra $P_{\delta\rho_2}$ and $P_{\rho_2\rho_2}$ are independent of M in the $\tau_{\rm NL}$ model.

Our calculation of the clustering power spectra (3.43) agrees with previous calculations in the literature (e.g. [24, 4]) but the series representation gives some physical intuition: the large-scale non-Gaussian clustering is due to large-scale fluctuations in the field ρ_2, which we interpret as long-wavelength variations in the locally measured small-scale power. If $\tau_{\rm NL} = (\frac{6}{5}f_{\rm NL})^2$, then long-wavelength variations in ρ_2 are 100% correlated to the matter density δ on large scales, and the non-Gaussian halo bias is non-stochastic. If $\tau_{\rm NL} > (\frac{6}{5}f_{\rm NL})^2$, then ρ_2 and δ are not 100% correlated, leading to stochastic bias.

$g_{\rm NL}$ Cosmology

The $g_{\rm NL}$ model is a non-Gaussian model in which the initial potential Φ is given in terms of a single Gaussian field ϕ by:

$$\Phi(\boldsymbol{x}) = \phi(\boldsymbol{x}) + g_{\rm NL}\left(\phi^3(\boldsymbol{x}) - 3\langle\phi^2\rangle\phi(\boldsymbol{x})\right) \ . \tag{3.45}$$

We keep the first three terms in the series expansion for $\delta_{\rm h}$, obtaining:

$$\delta_{\rm h} = \begin{cases} b_g^{MW}\delta_M + \alpha_2\rho_2 + \alpha_3\rho_3 \ , & \text{[mass-weighted sample]} \\ b_g^N\delta_M + \left(\beta_2(M) + \tilde{\beta}_2(M)\frac{\partial}{\partial\ln\sigma_M}\right)\rho_2 & \\ \qquad + \left(\beta_3(M) + \tilde{\beta}_3(M)\frac{\partial}{\partial\ln\sigma_M}\right)\rho_3 \ . & \text{[narrow sample]} \end{cases} \tag{3.46}$$

To compute power spectra we will need the following cumulants in the $g_{\rm NL}$ model:

$$\xi_\Phi^{(4)[\rm tree]} = g_{\rm NL}\big[P_1P_2P_3 + 23\,\text{perms.}\big] + \mathcal{O}(g_{\rm NL}^2) \ , \tag{3.47}$$

$$\xi_\Phi^{(4)[\rm loop]} = 9g_{\rm NL}^2\big[P_1P_2P_{\phi^2}(k_{13}) + 11\,\text{perms.}\big] \ , \tag{3.48}$$

$$\xi_\Phi^{(6)} = 36g_{\rm NL}^2\big[P_1P_2P_3P_4P_{125} + 89\,\text{perms.}\big] \ . \tag{3.49}$$

Here, we have defined $P_{ijk} = P_\phi(|\boldsymbol{k}_i + \boldsymbol{k}_j + \boldsymbol{k}_k|)$ and

$$P_{\phi^2}(k) \equiv 2\int_{\boldsymbol{q}} P_\phi(q)P_\phi(|\boldsymbol{k}-\boldsymbol{q}|) \ \sim \ 4\Delta_\phi^2\ln(kL)P_\phi(k) \ , \tag{3.50}$$

where $\Delta_\phi^2 \equiv (k^3/2\pi^2)P_\phi(k)$ and we have regulated the infrared divergence by putting the field in a finite box of size L. Note that the power spectra $P_{\delta\rho_2}$ and $P_{\rho_2\rho_3}$ are zero (since there is a $\Phi \to -\Phi$ symmetry). The remaining power spectra can be calculated by substituting eqs. (3.47), (3.48) and (3.49) into eqs. (3.31) and (3.32). In the limit $k \to 0$, this gives

$$P_{\delta\rho_3}(k) = 3g_{\rm NL}\frac{P_{\rm mm}(k)}{\alpha(k)}\kappa_3^{(f_{\rm NL}=1)} \ , \tag{3.51}$$

$$P_{\rho_2\rho_2}(k) = \frac{24g_{\rm NL}}{\sigma_M^2}\left(\int_{\boldsymbol{q}}\alpha_M^2(q)P_\phi^2(q)\right) + 36g_{\rm NL}^2P_{\phi^2}(k) \ , \tag{3.52}$$

$$P_{\rho_3\rho_3}(k) = 9g_{\rm NL}^2\frac{P_{\rm mm}(k)}{\alpha^2(k)}\left(\kappa_3^{(f_{\rm NL}=1)}\right)^2 \ . \tag{3.53}$$

Here, $\kappa_3^{(f_{\rm NL}=1)}$ denotes the dimensionless skewness parameter $\kappa_3 = \langle\delta_M^3(\boldsymbol{x})\rangle_{\rm c}/\sigma_M^3$ in the local model with $f_{\rm NL} = 1$. Note that we use the tree-level cumulant $\xi_\Phi^{(4)[\rm tree]}$ when computing $P_{\delta\rho_3}$,

but use both the tree-level cumulant and the one-loop cumulant $\xi_\Phi^{(4)[\text{loop}]}$ when computing $P_{\rho_2\rho_2}$. Although the $\mathcal{O}(g_{\rm NL}^2)$ one-loop cumulant is generally smaller than the $\mathcal{O}(g_{\rm NL})$ tree-level cumulant, the one-loop cumulant dominates in the $|\boldsymbol{k}_1+\boldsymbol{k}_2|\to 0$ limit which is relevant for $P_{\rho_2\rho_2}$.

Putting the above calculations together, we find:[4]

$$P_{\rm mh}(k) = \left(b_g + g_{\rm NL}\frac{\beta_g}{\alpha(k)}\right) P_{\rm mm}(k)\ , \tag{3.54a}$$

$$P_{\rm hh}(k) = \left(b_g + g_{\rm NL}\frac{\beta_g}{\alpha(k)}\right)^2 P_{\rm mm}(k) + \frac{9}{4}\beta_f^2 g_{\rm NL}^2 P_{\phi^2}(k)\ , \tag{3.54b}$$

where β_f was defined in eq. (3.44) and we have defined

$$\beta_g = \begin{cases} 3\,\alpha_3(M)\kappa_3^{(f_{\rm NL}=1)}\ , & \text{[mass-weighted sample]} \\ 3\Big(\beta_2(M) + \tilde{\beta}_2(M)\frac{\partial}{\partial \ln\sigma_M}\Big)\,\kappa_3^{(f_{\rm NL}=1)}\ . & \text{[narrow sample]} \end{cases} \tag{3.55}$$

Note that in the narrow mass bin case, there are derivative terms in $\delta_{\rm h}$ (eq. (3.46)), and their contributions to $P_{\rm mh}$ and $P_{\rm hh}$ are non-zero (unlike the previously considered $\tau_{\rm NL}$ model), because the power spectra $P_{\rho_m\rho_n}$ in eqs. (3.51)–(3.53) depend on halo mass via the mass-dependent quantity $\kappa_3^{(f_{\rm NL}=1)}$.

These expressions for $P_{\rm mh}$ and $P_{\rm hh}$ agree with previous calculations in the literature based on the Edgeworth expansion [10, 23, 4]. Our series expansion gives some physical intuition as follows. The non-Gaussian contribution to $P_{\rm mh}$ comes from the power spectrum $P_{\delta\rho_3}$, and can therefore be interpreted as arising from long-wavelength variations in the locally measured small-scale skewness ρ_3. On large scales, the non-Gaussian fluctuations in ρ_3 are 100% correlated to the density field, and therefore the associated halo bias is non-stochastic. The leading contribution to stochastic bias comes from the power spectrum $P_{\rho_2\rho_2}$ and can

[4]We have neglected contributions to $P_{\rm hh}(k)$ which approach a constant as $k\to 0$; such contributions are unobservable in practice since they are degenerate with other contributions such as second-order halo bias.

be interpreted as long-wavelength variations in small-scale power which are uncorrelated to the density field.

3.5 Proof of the Correspondence

In the previous section, we showed that the barrier crossing model can be formulated as a series representation:

$$\delta_{\rm h}(\boldsymbol{x}) = \begin{cases} b_g^{MW}\delta_M(\boldsymbol{x}) + \sum_{n\geq 2}\alpha_n(M)\rho_n(\boldsymbol{x}) \ , & \text{[mass-weighted sample]} \\ b_g^{N}\delta_M(\boldsymbol{x}) + \sum_{n\geq 2}\left(\beta_n(M) + \tilde{\beta}_n(M)\frac{\partial}{\partial \ln\sigma_M}\right)\rho_n(\boldsymbol{x}) \ . & \text{[narrow sample]} \end{cases} \tag{3.56}$$

In this section, we will use this result to prove that barrier crossing is mathematically related to local biasing (§3.5.1) and peak-background split (§3.5.2), and in particular they give equivalent results.

3.5.1 Local Biasing

"Local biasing" refers to any model of halo clustering in which the halo field is represented as a local function of the dark matter density, e.g. a power series

$$\delta_{\rm h}(\boldsymbol{x}) = b_1\delta(\boldsymbol{x}) + b_2\delta^2(\boldsymbol{x}) + b_3\delta^3(\boldsymbol{x}) + \cdots \ . \tag{3.57}$$

Several versions of local biasing exist in the literature (e.g. [11, 20, 12, 2]). We notice that the series on the right-hand side of (3.56) is a type of local biasing expansion, since the ρ_n fields are local functions of the smoothed density field δ_M. Therefore, our series representation proves that the barrier crossing model is mathematically equivalent to a specific version of the local biasing formalism.[5]

[5]In [10], the authors have argued that the barrier crossing model can be written as a local expansion in terms of 'renormalized' bias parameters (see Section III.B and III.C). We note that a local Hermite expansion is well defined and will automatically generate the correct bias coefficients in the Gaussian or weakly non-Gaussian case, without need for renormalization. See Section II.D of [22] for further discussion.

In this section, we would like to elaborate on the connection between our series representation and the usual way of thinking about local biasing, and comment on the differences with other versions of the formalism.

First, the density field δ_M which appears in the series representation is the non-Gaussian and *linearly evolved* density field, smoothed on the mass scale M. In particular, there is no need to introduce a new smoothing scale which is distinct from the halo scale, as done in some versions of local biasing. We do not include non-linear evolution in δ_M since the standard barrier crossing model is based on thresholding the linear density field.

Second, we do not need to introduce explicit dependence of the halo over-density $\delta_{\rm h}$ on the long-wavelength potential Φ_ℓ in a non-Gaussian cosmology. In some versions of local biasing, $\delta_{\rm h}$ is expanded in both δ_ℓ and Φ_ℓ, in order to keep the relation local. In our version, the Φ_ℓ dependence happens automatically, since $\delta_{\rm h}$ depends on higher cumulants $\rho_2, \rho_3, \cdots$, and these cumulants can be correlated with Φ_ℓ in a non-Gaussian model. To see how this happens in detail, consider the $f_{\rm NL}$ model. Inspection of the power spectra in eqs. (3.41) and (3.42) shows (taking $\tau_{\rm NL} = (\frac{6}{5} f_{\rm NL})^2$) that ρ_2 is 100% correlated with the field $\Phi_\ell = \alpha_M^{-1}(k)\delta_M$ as $k \to 0$. More precisely, $\rho_2 \to 4 f_{\rm NL}\Phi_\ell$ on large scales. Making this substitution in eq. (3.56), we get $\delta_{\rm h} = b_g\delta_\ell + f_{\rm NL}\beta_f\Phi_\ell + \cdots$ and recover the usual result.

This example shows that including explicit Φ_ℓ dependence in the local expansion of $\delta_{\rm h}$ is not necessary (in fact, including it our model would "double-count" the non-Gaussian clustering), if higher powers of the density field are included in the expansion. In the $f_{\rm NL}$ model, the modulation to the locally measured power ρ_2 is directly proportional to Φ_ℓ. More generally, the expansion should be in all of the non-negligible cumulants $\rho_2, \rho_3, \cdots$.

It is also interesting to consider the $\tau_{\rm NL}$ model in the case $\tau_{\rm NL} > (\frac{6}{5} f_{\rm NL})^2$. Here, the locally measured small-scale power ρ_2 has excess power on large scales which is not 100% correlated with Φ_ℓ, leading to stochastic bias [4]. This qualitative behavior is correctly captured by a local biasing model of the form $\delta_{\rm h} = b_g\delta_\ell + \alpha_2\rho_2$, but not by a local biasing model of the form $\delta_{\rm h} = b_g\delta_\ell + b_2\Phi_\ell$.

In the narrow mass bin case, our series expansion includes derivative terms of the form $\partial\rho_n/\partial \ln \sigma_M$. To our knowledge, derivative terms have not been been proposed in any version of local biasing which has appeared in the literature. In the barrier crossing model, derivative terms appear naturally for a narrowly selected halo sample, since this case is obtained from the mass-weighted case (which does not contain derivative terms) by differentiating with respect to halo mass.

Finally, even in the mass-weighted case, there is a difference between the Hermite polynomial expansion

$$\delta_{\rm h}(\boldsymbol{x}) = b_g^{MW}\delta_M(\boldsymbol{x}) + \sum_{n\geq 2}\alpha_n(M)\,H_n\left(\frac{\delta_M(\boldsymbol{x})}{\sigma_M}\right) \tag{3.58}$$

and a power series expansion of the form

$$\delta_{\rm h}(\boldsymbol{x}) = b_1\delta_M(\boldsymbol{x}) + b_2\delta_M^2(\boldsymbol{x}) + b_3\delta_M^3(\boldsymbol{x}) + \cdots\ . \tag{3.59}$$

At first sight, the two may appear equivalent: if both series are truncated at the same order N, then we can rearrange coefficients to transform either series into the other (since both just parametrize an arbitrary degree-N polynomial). However, when we write the power series expansion (3.59), we are assuming that the values of the low-order coefficients $b_1, b_2, \cdots$ are independent of the order N at which the series is truncated. This means for example that in a Gaussian cosmology, the matter-halo power spectrum $P_{\rm mh}(k) = (b_1 + 3\sigma_M^2 b_3 + 15\sigma_M^4 b_5 + \cdots)P_{\rm mm}(k)$ depends on where the series is truncated. In contrast, the Hermite expansion (3.58) is more stable: $P_{\rm mh}(k)$ is always equal to $b_g^{MW}P_{\rm mm}(k)$, regardless of how many terms are retained in the series. Note that the barrier crossing model has a convergent Hermite polynomial expansion (3.24), but cannot be sensibly expanded as a power series in δ_M, since the Heaviside step function $\Theta(\delta_M/\sigma_M - \delta_c)$ is not an analytic function of δ_M.

In summary, the barrier crossing model is mathematically equivalent to a specific version of the local biasing formalism in which the following choices have been made: we linearly evolve the density field and smooth it at mass scale M; we include higher cumulants $\rho_2, \rho_3, \cdots$

in the density field, but not additional fields such as the potential Φ_ℓ; derivative terms appear in the narrow mass bin case; and we use a Hermite polynomial expansion in δ_M/σ_M rather than the power series expansion. Other variants of the local biasing formalism exist in the literature, and we are not claiming that our choices are optimal (in the sense of producing best agreement with simulations); the purpose of this section was simply to point out which set of choices is equivalent to the barrier crossing model.

3.5.2 Peak-Background Split

The "peak-background split" is a formalism for modeling halo clustering on large scales, in which one relates large-scale modes of the halo density field $\delta_{\rm h}$ to large-scale modes of fields whose power spectra can be calculated directly. For example, the PBS formalism was applied to an $f_{\rm NL}$ cosmology in [21]. On large scales, $k \ll R_M^{-1}$, one can argue that the halo density is related to the linear density field δ and the Newtonian potential Φ by

$$\delta_{\rm h}(\boldsymbol{k}) = b_g \delta(\boldsymbol{k}) + f_{\rm NL}\beta_f \Phi(\boldsymbol{k}) \ , \tag{3.60}$$

where b_g is the usual Gaussian bias, and $\beta_f = 2\partial \ln n_{\rm h}/\partial \ln \sigma_8$. Using this expression, it is easy to show that the large-scale bias is given by $b(k) = b_g + f_{\rm NL}\beta_f/\alpha(k)$, and is non-stochastic. For additional examples of the PBS formalism applied to non-Gaussian models, see [24, 23, 4]. In this section, we will show how the PBS formalism generalizes to an arbitrary non-Gaussian model, and give a simple proof that this generalization is equivalent to the barrier crossing model. We will work out in detail the case of a mass-weighted halo sample; the narrow mass bin case follows by differentiating with respect to M.

There is one technical point that we would like to make explicit. We want to generalize the peak-background split formalism so that it applies to an arbitrary non-Gaussian model, parametrized by the N-point correlation functions of the initial Newtonian potential Φ. As an example, consider the $\tau_{\rm NL}$ model from §3.4.3, with constituent fields ϕ, ψ. The PBS

analysis of this model has been worked out in [24, 4] and requires keeping track of the long-wavelength parts ϕ_ℓ, ψ_ℓ of both fields, in order to correctly predict non-Gaussian stochastic bias on large scales. (Intuitively, multiple fields are needed because we need to keep track of long-wavelength density fluctuations and long-wavelength variations in the locally measured small-scale power, and the two are not 100% correlated in the $\tau_{\rm NL}$ model.) This raises a conceptual puzzle: how would we get stochastic bias if we were just given correlation functions of the single field Φ, rather than a description of the $\tau_{\rm NL}$ model involving multiple constituent fields? As we will now see, we must extend the PBS formalism by introducing additional fields which correspond to the locally measured small-scale power, small-scale skewness, kurtosis, etc. These fields are precisely the quantities $\rho_2, \rho_3, \cdots$ which appeared earlier in our series expansion in §3.4. This will allow us to connect the PBS formalism with the barrier crossing model (and in fact prove that the two are mathematically equivalent).

Consider a large subvolume of the universe containing many halos, but over which the long mode is reasonably constant, and let $(\,\cdot\,)_\ell$ denote a spatial average over the subvolume. Let us assume that the halo number density $(n_{\rm h})_\ell$ in the subvolume is a function of the one-point PDF of the underlying dark matter field δ_M (when linearly evolved and smoothed on the halo scale). For weakly non-Gaussian fields, the one-point PDF in each subvolume can be characterized completely by its mean $(\delta_M)_\ell$, variance $(\sigma_M^2)_\ell$, and higher cumulants $(\kappa_n)_\ell = (\langle \delta_M^n \rangle_{\rm c}/\sigma_M^n)_\ell$ for $n \geq 3$. Therefore we can write $(n_{\rm h})_\ell \equiv \bar{n}_{\rm h}((\delta_M)_\ell, (\sigma_M^2)_\ell, \{(\kappa_n)_\ell\})$. Taylor expanding to *first order* in these parameters, we get

$$(n_{\rm h})_\ell = \bar{n}_{\rm h} \left(1 + \frac{\partial \ln n_{\rm h}}{\partial (\delta_M)_\ell} (\delta_M)_\ell + \frac{\partial \ln n_{\rm h}}{\partial (\sigma_M^2)_\ell} \big((\sigma_M^2)_\ell - \sigma_M^2 \big) + \sum_{n=3}^{\infty} \frac{\partial \ln n_{\rm h}}{\partial (\kappa_n)_\ell} (\kappa_n)_\ell \right) . \qquad (3.61)$$

Here, we have used the notation $(\sigma_M^2)_\ell$ to denote the variance of δ_M restricted to the subvolume, and σ_M^2 to denote the global variance. To make contact with our previous notation, note

that $\big((\sigma_M^2)_\ell - \sigma_M^2\big) = \sigma_M^2(\rho_2)_\ell$ and $(\kappa_n)_\ell = (\rho_n)_\ell$.[6] Making these substitutions in eq. (3.61), we get

$$(\delta_{\rm h})_\ell = \frac{\partial \ln n_{\rm h}}{\partial(\delta_M)_\ell}(\delta_M)_\ell + \sigma_M^2 \frac{\partial \ln n_{\rm h}}{\partial(\sigma_M^2)_\ell}\,(\rho_2)_\ell + \sum_{n=3}^{\infty} \frac{\partial \ln n_{\rm h}}{\partial(\kappa_n)_\ell}\,(\rho_n)_\ell\ . \tag{3.62}$$

Since this equation applies when taking the subvolume average $(\,\cdot\,)_\ell$ over any large subvolume, it also applies to any large-scale Fourier mode:

$$\delta_{\rm h}(\boldsymbol{k}) \ \xrightarrow{k\to 0}\ \frac{\partial \ln n_{\rm h}}{\partial \delta_M}\delta_M(\boldsymbol{k}) + \sigma_M^2 \frac{\partial \ln n_{\rm h}}{\partial \sigma_M^2}\,\rho_2(\boldsymbol{k}) + \sum_{n=3}^{\infty} \frac{\partial \ln n_{\rm h}}{\partial \kappa_n}\,\rho_n(\boldsymbol{k})\ . \tag{3.63}$$

Let us compare this expression with our series representation of $\delta_{\rm h}$ in the barrier crossing model:

$$\delta_{\rm h}(\boldsymbol{k}) = b_g^{MW}\delta_M(\boldsymbol{k}) + \sum_{n\geq 2} \alpha_n(M)\rho_n(\boldsymbol{k})\ . \tag{3.64}$$

The form of the two series representations is the same, but the coefficients appear to be different. In the barrier crossing model, we have the following explicit formula for the coefficient $\alpha_n(M)$ of the n-th term in the series:

$$\alpha_n(M) = \sqrt{\frac{2}{\pi}}\,\frac{e^{-\nu_c^2/2}}{\mathrm{erfc}(\frac{1}{\sqrt{2}}\nu_c)}\,\frac{H_{n-1}(\nu_c)}{n!}\ , \tag{3.65}$$

whereas in the PBS derivation, α_n is given by a suitable derivative of the halo mass function:

$$\alpha_2 = \sigma_M^2 \frac{\partial \ln n_{\rm h}}{\partial \sigma_M^2} \quad \text{and} \quad \alpha_n = \frac{\partial \ln n_{\rm h}}{\partial \kappa_n} \ \text{ for } n \geq 3\ . \tag{3.66}$$

If we assume a Press-Schechter mass function, then one can evaluate the mass function derivatives in the above equation using the machinery from [15]. The result agrees precisely with the explicit formula (3.65). Therefore, the barrier crossing model and the generalized PBS formalism with fields $\rho_2, \rho_3, \cdots$ are formally equivalent, but only under the assumption

[6] The identity $(\rho_n)_\ell = (\kappa_n)_\ell$ holds for $n \leq 5$, but has non-linear corrections for $n \geq 6$. For example, $(\rho_6)_\ell = (\kappa_6)_\ell + 10(\kappa_3)_\ell^2$. We have neglected these non-linear corrections since eq. (3.61) is an expansion to first order anyway.

of a Press-Schechter mass function (note that this assumption is "built in" to the barrier crossing model).

If we relax the assumption of a Press-Schechter mass function, then the barrier crossing model and the generalized PBS formalism can both be written as series expansions with the same general form, but make different predictions for the coefficients $\alpha_n(M)$. One can ask which prediction agrees better with N-body simulations. In [23], the two predictions for α_3 were compared with simulations in the context of the $g_{\rm NL}$ model. It was found that the PBS prediction (3.66) is exact (within the $\approx 1\%$ statistical error of the simulations) if both the bias and the mass function derivative $(\partial \ln n_{\rm h}/\partial\kappa_3)$ are evaluated numerically from the simulations. The barrier crossing prediction (3.65) is an approximation: although it is based on an exact calculation within the barrier crossing model, this model is an approximation to the true dynamics of an N-body simulation. The approximation works reasonably well for large halo mass but breaks down for low masses, motivating the use of fitting functions for practical data analysis. It is natural to conjecture that the same qualitative statements will be true for the α_n coefficients with $n > 3$, but we have not attempted to verify this with simulations. (Note that no fitting function is necessary for α_2, since the relation $\beta_f \approx 2\delta_c b_g$ holds to $\approx 10\%$ accuracy in N-body simulations.)

In summary, the barrier crossing model is closely related to the PBS formalism, appropriately generalized to an arbitrary non-Gaussian cosmology by introducing additional fields $\rho_2, \rho_3, \cdots$, plus the additional assumption of a Press-Schechter mass function. The barrier crossing model is analytically tractable (e.g. one can derive closed-form expressions for the coefficients $\alpha_n(M)$ and $\beta_n(M)$), and usually a reasonable approximation, making it very useful for analytic studies or forecasts. However, for data analysis, it may be necessary to go beyond the Press-Schechter approximation by replacing the closed-form expressions for coefficients such as $\alpha_n(M)$ with their PBS counterparts measured from simulations.

3.6 Conclusions

In this paper, we have demonstrated the precise mathematical relationship between barrier crossing, peak-background split and local biasing. We first introduced a Hermite polynomial expansion of the halo density contrast $\delta_{\rm h}$ in the barrier crossing model: eqs. (3.26) and (3.30). We showed that this allows a computationally efficient way to calculate the clustering power spectra $P_{\rm mh}$ and $P_{\rm hh}$. Moreover, the series expansion makes the formal equivalence of the various halo modeling formalisms very transparent. First, it automatically takes the form of a local biasing model, in which the non-Gaussian and linearly evolved density contrast is expanded in Hermite polynomials. Second, it provides a very natural connection between barrier crossing and peak-background split. To make this relationship manifest, we generalized the PBS formalism so that it can be applied to the most general set of non-Gaussian initial conditions, parametrized by the N-point functions of the primordial potential. This extension of PBS involves additional fields which correspond to the locally measured small-scale power, small-scale skewness, kurtosis, etc. Mapping those fields to fields in the Hermite polynomial expansion of the barrier crossing model, we showed the close relationship between PBS and BC. Finally, although in this paper we have concentrated on computing power spectra, our series expansion should also be useful for analyzing the effects of primordial non-Gaussianity on other clustering statistics, such as the halo bispectrum [2].

Acknowledgments

We thank Marilena LoVerde, Marcel Schmittfull, David Spergel and Matias Zaldarriaga for helpful discussions. S.F. acknowledges support from a fellowship at the Department of Astrophysical Sciences of Princeton University. K.M.S. was supported by a Lyman Spitzer fellowship in the Department of Astrophysical Sciences at Princeton University. Research at Perimeter Institute is supported by the Government of Canada through Industry Canada and by the Province of Ontario through the Ministry of Research & Innovation. The research of D.G. is supported by the DOE under grant number DE-FG02-90ER40542 and the Martin

A. and Helen Chooljian Membership at the Institute for Advanced Study. D.B. gratefully acknowledges support from a Starting Grant of the European Research Council (ERC STG grant 279617).

3.7 Appendix: convention on Hermite Polynomials

In this paper, we have used the *probabilists'* definition of Hermite Polynomials

$$H_n(\nu) = (-1)^n e^{\nu^2/2} \frac{d^n}{d\nu^n} e^{-\nu^2/2} \ , \tag{3.67}$$

satisfying the recursion relation

$$H_{n+1}(\nu) = \nu H_n(\nu) - H_n'(\nu) \tag{3.68}$$

and the orthogonality condition

$$\int_{-\infty}^{\infty} \mathrm{d}\nu \, \frac{1}{\sqrt{2\pi}} e^{-\nu^2/2} \, H_m(\nu) H_n(\nu) = m! \, \delta_{mn} \ . \tag{3.69}$$

For reference, we list some of the low-order Hermite polynomials

$$H_0(\nu) = 1 \ , \tag{3.70}$$

$$H_1(\nu) = \nu \ , \tag{3.71}$$

$$H_2(\nu) = \nu^2 - 1 \ , \tag{3.72}$$

$$H_3(\nu) = \nu^3 - 3\nu \ , \tag{3.73}$$

$$H_4(\nu) = \nu^4 - 6\nu^2 + 3 \ . \tag{3.74}$$

We have made use of the following integral

$$\frac{1}{n!}\int_{\nu_c}^{\infty} \mathrm{d}\nu\, \frac{1}{\sqrt{2\pi}} e^{-\nu^2/2}\, H_n(\nu) = \begin{cases} \frac{1}{2}\mathrm{erfc}(\frac{1}{\sqrt{2}}\nu_c) & n = 0 \\ \frac{1}{n!}\frac{1}{\sqrt{2\pi}} e^{-\nu_c^2/2}\, H_{n-1}(\nu_c) & n \geq 1 \end{cases} . \tag{3.75}$$

Bibliography

[1] Assassi V., Baumann D., Green D., 2012, JCAP, 1211, 047

[2] Baldauf T., Seljak U., Senatore L., 2011, JCAP, 1104, 006

[3] Bardeen J. M., Bond J., Kaiser N., Szalay A., 1986, Astrophys.J., 304, 15

[4] Baumann D., Ferraro S., Green D., Smith K. M., 2012

[5] Baumann D., Green D., 2012, Phys.Rev., D85, 103520

[6] Buchbinder E. I., Khoury J., Ovrut B. A., 2007, Phys.Rev., D76, 123503

[7] Chen X., Wang Y., 2010, JCAP, 1004, 027

[8] Cole S., Kaiser N., 1989, Mon.Not.Roy.Astron.Soc., 237, 1127

[9] Dalal N., Dore O., Huterer D., Shirokov A., 2008, Phys.Rev., D77, 123514

[10] Desjacques V., Jeong D., Schmidt F., 2011, Phys.Rev., D84, 063512

[11] Fry J. N., Gaztanaga E., 1993, Astrophys.J., 413, 447

[12] Giannantonio T., Porciani C., 2010, Phys.Rev., D81, 063530

[13] Lehners J.-L., McFadden P., Turok N., Steinhardt P. J., 2007, Phys.Rev., D76, 103501

[14] Linde A. D., Mukhanov V. F., 1997, Phys.Rev., D56, 535

[15] LoVerde M., Miller A., Shandera S., Verde L., 2008, JCAP, 0804, 014

[16] Lyth D. H., Wands D., 2002, Phys.Lett., B524, 5

[17] Matarrese S., Verde L., 2008, Astrophys.J., 677, L77

[18] Press W. H., Schechter P., 1974, Astrophys.J., 187, 425

[19] Scoccimarro R., Hui L., Manera M., Chan K. C., 2012, Phys.Rev., D85, 083002

[20] Sefusatti E., 2009, Phys.Rev., D80, 123002

[21] Slosar A., Hirata C., Seljak U., Ho S., Padmanabhan N., 2008, JCAP, 0808, 031

[22] Schmidt F., Jeong D., Desjacques, V., [arXiv:1212.0868]

[23] Smith K. M., Ferraro S., LoVerde M., 2012, JCAP, 1203, 032

[24] Tseliakhovich D., Hirata C., Slosar A., 2010, Phys.Rev., D82, 043531

[25] Zaldarriaga M., 2004, Phys.Rev., D69, 043508

Chapter 4

Using Large Scale Structure to measure $f_{\rm NL}$, $g_{\rm NL}$ and $\tau_{\rm NL}$

4.1 Abstract

Primordial non-Gaussianity of local type is known to produce a scale-dependent contribution to the galaxy bias. Several classes of multi-field inflationary models predict non-Gaussian bias which is *stochastic*, in the sense that dark matter and halos don't trace each other perfectly on large scales. In this work, we forecast the ability of next-generation Large Scale Structure surveys to constrain common types of primordial non-Gaussianity like $f_{\rm NL}$, $g_{\rm NL}$ and $\tau_{\rm NL}$ using halo bias, including stochastic contributions. We provide fitting functions for statistical errors on these parameters which can be used for rapid forecasting or survey optimization. A next-generation survey with volume $V = 25h^{-3}{\rm Gpc}^3$, median redshift $z = 0.7$ and mean bias $b_g = 2.5$, can achieve $\sigma(f_{\rm NL}) = 6$, $\sigma(g_{\rm NL}) = 10^5$ and $\sigma(\tau_{\rm NL}) = 10^3$ if no mass information is available. If halo masses are available, we show that optimally weighting the halo field in order to reduce sample variance can achieve $\sigma(f_{\rm NL}) = 1.5$, $\sigma(g_{\rm NL}) = 10^4$ and $\sigma(\tau_{\rm NL}) = 100$ if halos with mass down to $M_{\rm min} = 10^{11}\ h^{-1}M_\odot$ are resolved, outperforming Planck by a factor of 4 on $f_{\rm NL}$ and nearly an order of magnitude on $g_{\rm NL}$ and $\tau_{\rm NL}$. Finally, we study the

effect of photometric redshift errors and discuss degeneracies between different non-Gaussian parameters, as well as the impact of marginalizing Gaussian bias and shot noise.

4.2 Introduction

The study of the statistical properties of the primordial fluctuations beyond the power spectrum has enormous constraining power on inflationary models. While single field slow roll inflation predicts Gaussian fluctuations [51, 52], for which all of the information lies in the primordial power spectrum, a wealth of alternative models (in particular multifield models) can produce detectable non-Gaussianity.

At the time of writing the best constraints come from measurements of the *Cosmic Microwave Background* radiation (CMB) [2, 1]. However these measurements are already close to being cosmic-variance limited since the CMB is produced on a two dimensional surface, and small scales are suppressed by Silk damping (although future measurements of E-mode polarization may improve statistical errors by a factor $\approx \sqrt{2}$).

With the ability of extracting 3D information and smaller scale modes, Large Scale Structure (LSS) has the potential of soon reaching and improving CMB constraints. The simplest forms of primordial local non-Gaussianity have been shown to leave a very distinctive imprint in the halo power spectrum, in the form of a scale-dependent bias proportional to k^{-2} [24, 25]. This has been recently generalized [42, 6, 5] to arbitrary inflationary models. In some multifield models, non-Gaussian halo bias can be *stochastic*: the halo and matter fields are not 100% correlated on large scales [37, 6, 41]. This is an important observational signature which can be used to discriminate between models which do and do not predict stochastic bias.

Analysis of existing LSS datasets yield constraints that are comparable to the ones from WMAP [31, 28, 32, 13, 43, 47, 46, 48], with almost all of them being limited by spurious large-scale power due to systematics (extinction, stellar contamination, imperfect calibration, etc.

[26, 27]). Recently developed techniques such as mode projection and extensions [26, 28, 29, 30] or weights method [31, 32] are very promising ways to reduce the impact of systematics.

The k^{-2} scaling makes the signal largest on the very largest scales, which are affected by cosmic variance. In [7, 8, 17], it was observed that cosmic variance may be partially cancelled by splitting the sample in bins of different halo mass, and taking a linear combination of halo fields such that the Gaussian bias terms ($b_g\delta_m$) nearly cancel, but non-Gaussian bias terms of the form ($b_{NG}\delta_m/k^2$) do not cancel. A related idea for reducing statistical errors, proposed in [18, 19], is to reduce *Poisson* variance by taking a different linear combination of mass bins (essentially mass weighting) whose Poisson variance is lower than the naive ($1/n$) expectation due to mass conservation.

Previous work [9, 12, 16, 8, 11, 14, 15, 10, 45] has used the Fisher matrix formalism to forecast constraints on primordial non-Gaussianity through halo bias. Here we revisit the Fisher matrix calculation and provide analytically motivated fitting functions that are intended to be convenient for rapid forecasting or survey optimization. We study some issues which are observationally relevant like the impact of marginalizing Gaussian bias and shot noise, and the impact of photometric redshift errors. We then extend the multi-tracer method of [8, 11, 14, 49] to include the effects of stochastic bias and to distinguish $f_{\rm NL}$ from $g_{\rm NL}$, which are completely degenerate when only a single tracer population is available. Finally, we discuss separating the non-Gaussian parameters $f_{\rm NL}$, $g_{\rm NL}$, and $\tau_{\rm NL}$, clarifying results in the literature and giving quantitative forecasts.

This chapter is organized as follows: In Section 4.3 we introduce our notation and formalism, as well as discuss possible consequences of the recent claims of the BICEP2 collaboration about the amplitude of primordial tensor modes. The single-tracer case is treated analytically and numerically in detail in Section 4.4, while in Section 4.5, we discuss the effect of marginalization and redshift errors on our forecasts. In Section 4.6 we show how constraints can be improved by using mass information. The (partial) degeneracy between models is discussed in Section 4.7, followed by discussion and conclusions in Section 4.8.

4.3 Definitions and notation

4.3.1 Primordial non-Gaussianity and Large Scale Structure

The statistical properties of the primordial potential $\Phi(\boldsymbol{k}) = (3/5)\zeta(\boldsymbol{k})$ can be completely characterized by its N-point connected correlation function, which we will denote by $\xi_\Phi^{(N)}$:

$$\langle \Phi(\boldsymbol{k}_1)\Phi(\boldsymbol{k}_2)\cdots\Phi(\boldsymbol{k}_N)\rangle_{\rm c} = (2\pi)^3\delta_{\rm D}(\boldsymbol{k}_1+\boldsymbol{k}_2+\cdots+\boldsymbol{k}_N)\,\xi_\Phi^{(N)}(\boldsymbol{k}_1,\boldsymbol{k}_2,\ldots,\boldsymbol{k}_N)\ , \tag{4.1}$$

It is customary to define the potential power spectrum $P_\Phi(k) = \xi_\Phi^{(2)}(\boldsymbol{k},-\boldsymbol{k})$ and the dimensionless power spectrum $\Delta^2_\Phi(k) = k^3P_\Phi(k)/2\pi^2$.

We shall consider a model with primordial bispectrum and trispectrum parametrized by two parameters $f_{\rm NL}$ and $\tau_{\rm NL}$, which here we will assume to be independent[1]

$$\xi_\Phi^{(3)}(k_1,k_2,k_3) = f_{\rm NL}\big[P_\Phi(k_1)P_\Phi(k_2) + 5\,\text{perms.}\big], \tag{4.2}$$

$$\xi_\Phi^{(4)}(k_1,k_2,k_3,k_4) = 2\left(\tfrac{5}{6}\right)^2\tau_{\rm NL}\big[P_\Phi(k_1)P_\Phi(k_2)P_\Phi(|\boldsymbol{k}_1+\boldsymbol{k}_3|) + 23\,\text{perms.}\big]\ , \tag{4.3}$$

This can be realized for example in the curvaton model [36, 6, 37], in which the non-Gaussian gravitational potential Φ is expressed in terms of two uncorrelated Gaussian fields ϕ and ψ, with power spectra that are proportional to each other

$$\Phi(\boldsymbol{x}) = \phi(\boldsymbol{x}) + \psi(\boldsymbol{x}) + f_{\rm NL}(1+\Pi)^2\,\left(\psi^2(\boldsymbol{x}) - \langle\psi^2\rangle\right)\ , \tag{4.4}$$

where $f_{\rm NL}$ and $\Pi = P_\phi(k)/P_\psi(k)$ are free parameters. In this case, we can check that $\tau_{\rm NL} = (\frac{6}{5}f_{\rm NL})^2(1+\Pi)$, so that $f_{\rm NL}$ and $\tau_{\rm NL}$ are independent parameters.

The matter overdensity $\delta_m(\boldsymbol{k},z)$ is related to the primordial potential $\Phi(\boldsymbol{k})$ through the Poisson equation,

$$\delta_m(\boldsymbol{k},z) = \alpha(k,z)\Phi(\boldsymbol{k})\ . \tag{4.5}$$

[1] It can be shown on general grounds that they have to satisfy the Suyama-Yamaguchi [34, 35] inequality $\tau_{\rm NL} \geq (\frac{6}{5}f_{\rm NL})^2$. Specific theories of inflation will predict particular relations between $f_{\rm NL}$ and $\tau_{\rm NL}$.

Here we have defined $\alpha(k,z)$ by

$$\alpha(k,z) = \frac{2k^2 T(k)}{3\Omega_m H_0^2} D(z) \tag{4.6}$$

where $D(z)$ is the linear growth function normalized so that $D(z) = 1/(1+z)$ in matter domination (so that $D(z) \approx 0.76$ at $z = 0$) and $T(k)$ is the transfer function normalized to 1 at low k.

It can be shown that in presence of non-zero $f_{\rm NL}$ or $\tau_{\rm NL}$, the halo matter and halo-halo power spectra acquire a scale dependent bias on large scales [42, 6, 37]:

$$P_{mh}(k,z) = \left(b_g + f_{\rm NL}\frac{\beta_f}{\alpha(k,z)}\right) P_{mm}(k,z) \tag{4.7}$$

$$P_{hh}(k,z) = \left(b_g^2 + 2b_g f_{\rm NL}\frac{\beta_f}{\alpha(k,z)} + \frac{25}{36}\tau_{\rm NL}\frac{\beta_f^2}{\alpha(k,z)^2}\right) P_{mm}(k,z) + \frac{1}{n_{\rm eff}} \tag{4.8}$$

Here, b_g is the Eulerian halo bias, and β_f is a non-Gaussian bias parameter which can be expressed exactly as a derivative of the tracer density n with respect to the power spectrum amplitude: $\beta_f = 2\partial \ln n / \partial \ln \Delta_\Phi$. Throughout this paper, we will use the alternate expression $\beta_f = 2\delta_c(b_g - 1)$, which is exact in a barrier crossing model with barrier height δ_c and is a good ($\approx 10\%$ accurate) fit to N-body simulations. We will take $\delta_c = 1.42$, as appropriate for the Sheth-Tormen [33] halo mass function. The $1/n_{\rm eff}$ term enters as a Poisson shot noise term in P_{hh} due to the discrete nature of tracers. The value of $n_{\rm eff}$ is only approximately equal to the number density of tracers n and marginalization over a constant contribution to P_{hh} will be discussed in Section 4.4.

We note that if $\tau_{\rm NL} > (\frac{6}{5} f_{\rm NL})^2$, then Eq. (4.8) implies that halo and matter fields are not 100% correlated on large scales even in the absence of shot noise. This phenomenon is known as '*stochastic bias*'.

Another model that we will study is one that is cubic in the potential:

$$\Phi(\boldsymbol{x}) = \phi(\boldsymbol{x}) + g_{\rm NL}\left(\phi^3(\boldsymbol{x}) - 3\langle\phi^2\rangle\phi(\boldsymbol{x})\right) \ . \tag{4.9}$$

Here it is easy to show [44, 42, 6, 5] that for low k:

$$P_{mh}(k,z) = \left(b_g + g_{\rm NL}\frac{\beta_g}{\alpha(k,z)}\right) P_{mm}(k,z) \ , \tag{4.10}$$

$$P_{hh}(k,z) = \left(b_g + g_{\rm NL}\frac{\beta_g}{\alpha(k,z)}\right)^2 P_{mm}(k,z) + \frac{1}{n_{\rm eff}} \ , \tag{4.11}$$

where $\beta_g = 3\partial \ln n/\partial f_{\rm NL}$ is the derivative of the tracer density with respect to $f_{\rm NL}$. In this case, the barrier crossing model prediction for β_g does not agree well with N-body simulations, and for numerical work we use fitting functions for β_g from Section 5.3 of [44].

Currently the best limits on $f_{\rm NL}$ and $\tau_{\rm NL}$ are from the Planck satellite [1], which constrains (local) $f_{\rm NL} = 2.7 \pm 5.8$ and $\tau_{\rm NL} < 2800$ (95% CL). Regarding $g_{\rm NL}$, an independent analysis of WMAP9 data has found $g_{\rm NL} = (-3.3 \pm 2.2) \times 10^5$ [23], while the Planck Fisher matrix forecast is $\sigma(g_{\rm NL}) = 6.7 \times 10^4$ [23].

Throughout the paper we will assume a flat ΛCDM model as our fiducial cosmology with parameters from the Planck (2013) data release: $\Omega_m h^2 = 0.14$, $\Omega_\Lambda = 0.69$, $h = 0.68$, $\ln(10^{10} A_s) = 3.09$, $\tau = 0.09$ and $n_s = 0.96$.

4.3.2 Fisher Matrix analysis

The Fisher information matrix for a multivariate random variable π which depends on parameters $\{\theta_\alpha\} = \{f_{\rm NL}, \tau_{\rm NL}, g_{\rm NL}\}$ through the conditional likelihood $\mathcal{L}(\pi|\theta_\alpha)$ is given by

$$F_{\alpha\beta} = -\left\langle \frac{\partial^2 \ln \mathcal{L}(\pi|\theta)}{\partial\theta_\alpha \, \partial\theta_\beta} \right\rangle \tag{4.12}$$

where the expectation value is taken over random realizations of π for a fixed fiducial set of parameters θ_α.

We specialize Eq. (4.12) to the case where $\pi = (\delta_1(\boldsymbol{k}), \cdots, \delta_N(\boldsymbol{k}))$ represents all k-modes of a set of Gaussian fields δ_i, and the N-by-N covariance matrix $C_{ij}(k) = P_{\delta_i\delta_j}(k)$ depends

on the parameters θ_α. In this case, we have:

$$\log \mathcal{L}(\delta_i|\theta_\alpha) = \sum_{\boldsymbol{k}} \left(-\frac{1}{2}\mathrm{Tr}\log C(k) - \frac{1}{2}\delta_i(\boldsymbol{k})C^{-1}_{ij}(k)\delta_j(\boldsymbol{k}) \right) \tag{4.13}$$

which leads to the Fisher matrix:

$$F_{\alpha\beta} = \sum_{\boldsymbol{k}} \frac{1}{2}\mathrm{Tr}\left[C^{-1}\ \frac{\partial C}{\partial\theta_\alpha}\ C^{-1}\ \frac{\partial C}{\partial\theta_\beta} \right] \tag{4.14}$$

and every term is evaluated around the fiducial cosmology (usually $f_{\rm NL} = \tau_{\rm NL} = g_{\rm NL} = 0$). The (marginalized) error on θ_α is given by $\sigma_\alpha = (F^{-1})^{1/2}_{\alpha\alpha}$ (no sum), while the error on θ_α fixing all other parameters to their fiducial values is $\sigma_\alpha = (F_{\alpha\alpha})^{-1/2}$ (again no sum). Similarly, the covariances are given by $\mathrm{Cov}(\hat{\theta}_\alpha, \hat{\theta}_\beta) = (F^{-1})_{\alpha\beta}$.

For a 3D Large Scale Structure survey with volume V, we replace the mode sum $\sum_{\boldsymbol{k}}$ by:

$$\sum_{\boldsymbol{k}} \longrightarrow V \int \frac{d^3\boldsymbol{k}}{(2\pi)^3} = V \int_{k_{\rm min}}^{k_{\rm max}} \frac{dk\ k^2}{2\pi^2} \tag{4.15}$$

where $k_{\rm min} = 2\pi/V^{1/3}$ is the fundamental mode and $k_{\rm max}$ will be specified in context.

In the single-tracer case where the random variable is the halo overdensity δ_h, the fiducial covariance is the 1-by-1 matrix $C(k) = b_g^2 P_{mm}(k) + 1/n$ and the derivative terms are (assuming that $1/n_{\rm eff}$ is approximately independent of the non-gaussian parameters):

$$\frac{\partial C}{\partial f_{\rm NL}} = 2b_g \frac{\beta_f}{\alpha(k,z)} P_{mm}\ , \quad \frac{\partial C}{\partial \tau_{\rm NL}} = \left(\frac{5}{6}\right)^2 \frac{\beta_f^2}{\alpha(k,z)^2} P_{mm}\ , \quad \frac{\partial C}{\partial g_{\rm NL}} = 2b_g \frac{\beta_g}{\alpha(k,z)} P_{mm} \tag{4.16}$$

4.3.3 A comment on tensor modes

Recent advances in sensitivity of CMB polarization experiments have allowed the detection of B-modes at degree angular scale by the BICEP2 collaboration [3]. If the amplitude of the signal is entirely attributed to primordial tensor modes[2], it would correspond to a tensor-to-

[2]At the time of writing, it is unclear what fraction of the signal is due to galactic foregrounds [53, 54].

scalar ratio $r = 0.2^{+0.07}_{-0.05}$. In this section, we comment on the implications of a detection of r on local primordial non-Gaussianity.

For simplicity, assume that the inflaton produces Gaussian scalar curvature perturbation $\zeta_{inf} = (5/3)\phi$, and that there is a second 'curvaton' field contributing to the scalar perturbations by an amount ζ_{cur}, but that is not driving inflation and is allowed to generate large non-Gaussianity.

If the inflaton and curvaton are uncorrelated, the total scalar perturbation is $\Delta^2_{\zeta,tot} = \Delta^2_{\zeta,inf} + \Delta^2_{\zeta,cur}$. By definition of r this is:

$$\Delta^2_{\zeta,tot} = \frac{\Delta^2_t}{r} = \frac{8}{r}\left(\frac{H_I}{2\pi}\right)^2 \tag{4.17}$$

Here $\Delta^2_t = 8(H_I/2\pi)^2$ is the tensor power spectrum and H_I is the Hubble parameter during inflation. The portion produced by the inflaton is

$$\Delta^2_{\zeta,inf} = \frac{1}{2\epsilon}\left(\frac{H_I}{2\pi}\right)^2 \tag{4.18}$$

where $\epsilon = -\dot{H}_I/H_I^2$ is one of the slow roll parameters. This means that the fraction of the scalar power generated by the inflaton is

$$Q^2 \equiv \frac{\Delta^2_{\zeta,inf}}{\Delta^2_{\zeta,tot}} = \frac{r}{16\epsilon} \tag{4.19}$$

Since slow-roll inflation requires $\epsilon \ll 1$, or more typically $\epsilon \sim 0.01$, a detection of $r \sim 10^{-2}$ or larger would imply that Q^2 is not $\ll 1$, i.e. a sizable fraction of the scalar perturbations must be produced by the inflaton (see also [4]). Detectable non-Gaussianity is still possible in this model, but requires (modest) tuning, since the power spectra of ζ_{inf} and ζ_{cur} must be comparable. A sharper conclusion we can draw is that $\tau_{\rm NL}$ cannot be close to its minimal value $(\frac{6}{5}f_{\rm NL})^2$, since

$$\tau_{\rm NL} = \left(\frac{6}{5}f_{\rm NL}\right)^2 \frac{1}{1-Q^2} \tag{4.20}$$

in this model. Rephrasing, if $r \gtrsim 10^{-2}$, an appreciable fraction of the non-Gaussian halo bias must be stochastic.

4.4 Single tracer forecasts

In this Section, we forecast $f_{\rm NL}$ and $\tau_{\rm NL}$ constraints obtained without use of multi-tracer techniques. The survey will be characterized by $(V, z, b_g, 1/n, k_{\rm max})$, where b_g represents the mean (number weighted) bias of the sample. Our model for $P_{hh}(k)$ is the following:

$$P_{hh}(k,z) = \left(b_g^2 + 2 b_g f_{\rm NL} \frac{\beta_f}{\alpha(k,z)} + \frac{25}{36} \tau_{\rm NL} \frac{\beta_f^2}{\alpha(k,z)^2} \right) P_{mm}(k,z) + \frac{1}{n} \quad , \tag{4.21}$$

where we have taken the fiducial value of $n_{\rm eff}$ to be n. First of all we note that $f_{\rm NL}$ and $\tau_{\rm NL}$ are not (completely) degenerate in P_{hh}, since they generate a different scale dependence, so it's possible to distinguish them even with a single tracer population. We defer further discussion about correlations between parameters to Section 4.7.

From here we can calculate a 4-by-4 Fisher matrix whose rows correspond to the parameters $(f_{\rm NL}, \tau_{\rm NL}, b_g, 1/n_{\rm eff})$, and compute statistical errors on each parameter, with various choices for which other parameters are marginalized.

4.4.1 Some definitions

Since the Φ power spectrum is nearly scale invariant, we can write $k^3 P_\Phi(k) = A_\Phi I(k)$, where $I(k) \equiv (k/k_0)^{n_s - 1}$. The dimensionless coefficient A_Φ is given in terms of the primordial curvature perturbation amplitude by $A_\Phi = (18\pi^2/25)\Delta_\zeta^2(k_0)$. For our fiducial cosmology based parameters from the Planck 2013 release, we find $A_\Phi \approx 1.56 \times 10^{-8}$, measured at $k_0 = 0.05$ Mpc^{-1}.

We define $k_{\rm eq}$, the scale of matter-radiation equality, to be (aH) evaluated at $a = \Omega_r/\Omega_m$. Numerically, $k_{\rm eq} \approx 0.0154h$ Mpc^{-1}.

We will express our final results in terms of a comoving distance $R_0(z)$ and comoving tracer number density $n_0(z)$ defined by:

$$\begin{aligned} R_0(z)^2 &= \frac{2D(z)}{3\Omega_m H_0^2} = \frac{\alpha(k,z)}{k^2 T(k)} \\ n_0(z) &= (A_\Phi R_0(z)^4 k_{\rm eq})^{-1} \end{aligned} \tag{4.22}$$

The length $R_0(z)$ is equal to the comoving Hubble length $1/(aH)$, times some z-dependent factors of order unity. A survey with tracer density n is sample variance limited at the Hubble scale if $(n/n_0) \gg k_{\rm eq} R_0 \approx 50$, and Poisson limited on all scales if $(n/n_0) \ll 1$. Numerically, $R_0(z) = 3214\ h^{-1}$ Mpc and $n_0(z) = 3.87 \times 10^{-5}\ h^3\ {\rm Mpc}^{-3}$ at $z = 0.7$.

4.4.2 Factoring the Fisher matrix

Let $F_{\alpha\beta}$ denote the 4-by-4 Fisher matrix with parameters $(f_{\rm NL}, \tau_{\rm NL}, b_g, 1/n)$. In this Section, we will show that F *and its inverse* can be factored in the form

$$\Big(\text{Simple function of } \{V, b_g, z\}\Big) \times \Big(\text{Complicated function of } \Big\{k_{\rm min}, k_{\rm max}, \frac{b_g^2 n}{n_0(z)}\Big\}\Big) \tag{4.23}$$

This simplifies attempts to find a fitting function, since we can fit the two factors separately. Since the inverse Fisher matrix also factors, this simplification also works for bias-marginalized statistical errors.

To derive the factorization (4.23), write the Fisher matrix as:

$$F_{\alpha\beta} = \frac{V}{2} \int \frac{d^3\boldsymbol{k}}{(2\pi)^3} \frac{(\partial_\alpha P_{hh}(k,z))(\partial_\beta P_{hh}(k,z))}{P_{hh}(k,z)^2} \tag{4.24}$$

Now rewrite the halo-halo power spectrum in the form:

$$P_{hh}(k,z) = b_g^2 A_\Phi R_0(z)^4 \left(kT(k)^2 I(k) + k_{\rm eq} \frac{n_0(z)}{b_g^2 n} \right) \tag{4.25}$$

and note that the parameter derivative $\partial_\alpha P_{hh}(k,z)$ can be factored as $f_\alpha(z)g_\alpha(k)$, where α denotes any of the parameters $\{f_{\rm NL}, \tau_{\rm NL}, b_g, 1/n\}$, and the quantities f, g are defined by:

$$f_\alpha(z) = \begin{pmatrix} 4\delta_c b_g(b_g-1)A_\Phi R_0(z)^2 \\ \frac{25}{36}4\delta_c^2(b_g-1)^2 A_\Phi \\ 2b_g A_\Phi R_0(z)^4 \\ 1 \end{pmatrix} \qquad g_\alpha(k) = \begin{pmatrix} k^{-1}T(k)I(k) \\ k^{-3}I(k) \\ kT(k)^2 I(k) \\ 1 \end{pmatrix} \tag{4.26}$$

We plug the above expressions into the Fisher matrix (4.24) to obtain:

$$F_{\alpha\beta} = \frac{V}{2}\frac{f_\alpha(z)f_\beta(z)}{b_g^4 A_\Phi^2 R_0(z)^8}F'_{\alpha\beta} \qquad F^{-1}_{\alpha\beta} = \frac{2}{V}\frac{b_g^4 A_\Phi^2 R_0(z)^8}{f_\alpha(z)f_\beta(z)}F'^{-1}_{\alpha\beta} \tag{4.27}$$

where we have defined

$$F'_{\alpha\beta} = \int \frac{d^3\boldsymbol{k}}{(2\pi)^3}\frac{g_\alpha(k)g_\beta(k)}{[kT(k)^2I(k) + k_{\rm eq}n_0(z)/(b_g^2 n)]^2} \tag{4.28}$$

Since $F'_{\alpha\beta}$ and its inverse only depend on $\{k_{\rm min}, k_{\rm max}, b_g^2 n/n_0(z)\}$, we have now derived the factorization (4.23).

It will be convenient to specialize the above factorization to the cases $\alpha = \beta = f_{\rm NL}$ and $\alpha = \beta = \tau_{\rm NL}$. If we do not marginalize either b_g or $1/n$ (and set $\tau_{\rm NL} = 0$ when forecasting $f_{\rm NL}$ and vice versa), the statistical errors on $f_{\rm NL}$ and $\tau_{\rm NL}$ are given by:

$$\begin{aligned} \sigma(f_{\rm NL}) &= \frac{\sqrt{2}}{4\delta_c}\frac{b_g}{b_g-1}R_0(z)^2 V^{-1/2}(F'_{f_{\rm NL}})^{-1/2} \\ \sigma(\tau_{\rm NL}) &= \left(\frac{6}{5}\right)^2\frac{\sqrt{2}}{4\delta_c^2}\left(\frac{b_g}{b_g-1}\right)^2 R_0(z)^4 V^{-1/2}(F'_{\tau_{\rm NL}})^{-1/2} \end{aligned} \tag{4.29}$$

where:

$$\begin{aligned} F'_{f_{\rm NL}} &= \int \frac{d^3\boldsymbol{k}}{(2\pi)^3} \left(\frac{k^{-1}T(k)I(k)}{kT(k)^2 I(k) + k_{\rm eq} n_0(z)/(b_g^2 n)} \right)^2 \\ F'_{\tau_{\rm NL}} &= \int \frac{d^3\boldsymbol{k}}{(2\pi)^3} \left(\frac{k^{-3}I(k)}{kT(k)^2 I(k) + k_{\rm eq} n_0(z)/(b_g^2 n)} \right)^2 \end{aligned} \tag{4.30}$$

To marginalize over b_g and/or $1/n$, we would replace matrix elements of F' in Eq. (4.29) by matrix elements of an appropriate inverse Fisher matrix.

4.4.3 Sample Variance and Poisson limits; qualitative behavior

As an illustration of the factorization in the previous Section, let's derive approximate expressions for $\sigma(f_{\rm NL}), \sigma(\tau_{\rm NL})$ in the sample variance dominated limit $n/n_0(z) \gg k_{\rm eq} R_0(z)$ and Poisson dominated limit $n/n_0(z) \ll 1$, without bias marginalization (and setting $n_s = 1$ for this subsection). First we take limits of Eq. (4.29), obtaining:

$$\begin{aligned} F'_{f_{\rm NL}} &\to \frac{1}{2\pi^2} k_{\rm min}^{-1} && \text{(SVD)} \\ &\to \frac{Z}{2\pi^2} k_{\rm eq}^{-1} \left(\frac{b_g^2 n}{n_0(z)} \right)^2 && \text{(PD)} \\ F'_{\tau_{\rm NL}} &\to \frac{1}{10\pi^2} k_{\rm min}^{-5} && \text{(SVD)} \\ &\to \frac{1}{6\pi^2} k_{\rm min}^{-3} k_{\rm eq}^{-2} \left(\frac{b_g^2 n}{n_0(z)} \right)^2 && \text{(PD)} \end{aligned} \tag{4.31}$$

where we have defined the dimensionless number $Z = k_{\rm eq}^{-1} \int dk\, T(k)^2$, and SVD and PD stand for 'Sample Variance Dominated' and 'Poisson Dominated' respectively. Plugging into Eq. (4.29) to get parameter errors, and taking $k_{\rm min} = 2\pi/V^{1/3}$, we get the following approximate limits:

$$
\begin{aligned}
\sigma(f_{\rm NL}) &\rightarrow 2.77\frac{b_g}{b_g-1}\left(\frac{V}{R_0(z)^3}\right)^{-2/3} && \text{(SVD)} \\
&\rightarrow 0.95\frac{b_g}{b_g-1}(k_{\rm eq}R_0(z))^{1/2}\left(\frac{V}{R_0(z)^3}\right)^{-1/2}\left(\frac{b_g^2 n}{n_0(z)}\right)^{-1} && \text{(PD)} \\
\sigma(\tau_{\rm NL}) &\rightarrow 248\left(\frac{b_g}{b_g-1}\right)^2\left(\frac{V}{R_0(z)^3}\right)^{-4/3} && \text{(SVD)} \\
&\rightarrow 30.6\left(\frac{b_g}{b_g-1}\right)^2(k_{\rm eq}R_0(z))\left(\frac{V}{R_0(z)^3}\right)^{-1}\left(\frac{b_g^2 n}{n_0(z)}\right)^{-1} && \text{(PD)} \qquad (4.32)
\end{aligned}
$$

As we expected, the statistical errors are independent of tracer density n in the sample variance limited case, while they scale as $1/n$ in the Poisson limit. This behavior becomes very clear in the numerical results shown in Figure 4.1.

We also notice the errors often depend on volume in a way which differs from the usual $V^{-1/2}$ scaling. This happens when the k-integral for the Fisher matrix element diverges at low-k, so that most of the statistical weight comes from the survey scale $k_{\rm min} = 2\pi/V^{1/3}$. This divergence always occurs for $\tau_{\rm NL}$, so the $\tau_{\rm NL}$ constraint is always dominated by the largest-scale modes in the survey (i.e. a few modes). For $f_{\rm NL}$ this depends on the level of Poisson noise; in the sample variance limit the statistical weight is dominated by the largest scale modes, but in the Poisson dominated limit the statistical weight is distributed over a range of scales between $k_{\rm min}$ and $k_{\rm eq}$.

We also note that in the Poisson dominated case, the last line of (4.32) can be rewritten:

$$
\sigma(\tau_{\rm NL}) = 30.6\left(\frac{1}{b_g-1}\right)^2(k_{\rm eq}R_0(z)^4 n_0(z))\frac{1}{nV} \qquad \text{(Poisson dominated)} \qquad (4.33)
$$

i.e. $\sigma(\tau_{\rm NL})$ only depends on n, V through the total number of tracers (nV) in the Poisson-dominated case.

The analytic results in this subsection are approximate (we have assumed $n_s = 1$ and $T(k) = 1$) and shouldn't be used in forecasting. In Figure 4.1 we show the numerical results

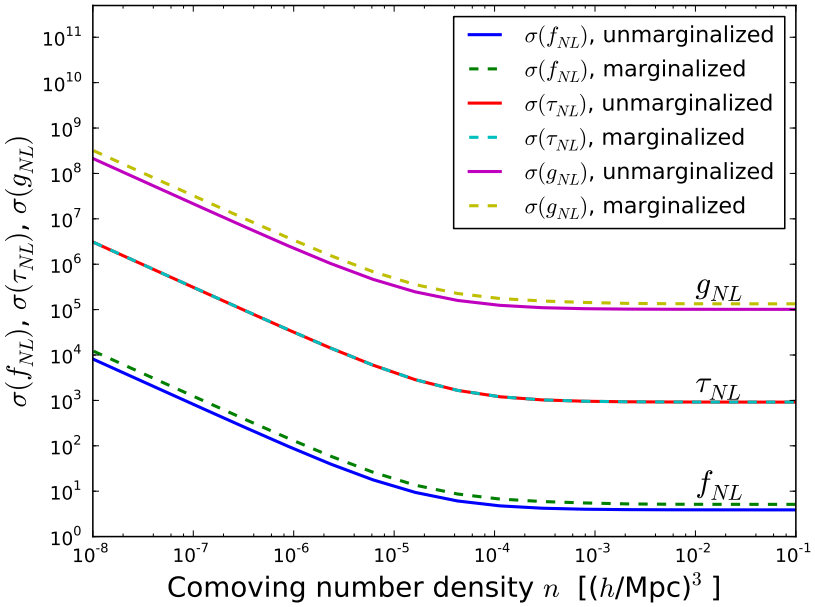

Figure 4.1: Statistical errors on $f_{\rm NL}$ (bottom) and $\tau_{\rm NL}$ (middle) and $g_{\rm NL}$ (top) for varying tracer density n, for our fiducial survey with volume $V = 25\ h^{-3}$ Gpc^3, redshift $z = 0.7$, tracer bias $b_g = 2.5$ and maximum wavenumber $k_{\rm max} = 0.1\ h$ Mpc^{-1}. The 'marginalized' case (dashed lines) refers to marginalization over Gaussian bias and a 20% Gaussian prior on $1/n_{\rm eff}$ around the fiducial value $1/n_{\rm eff} = 1/n$. When forecasting each parameter $\{f_{\rm NL}, \tau_{\rm NL}, g_{\rm NL}\}$, the other two parameters are set to zero. Constraining $g_{\rm NL}$ is discussed in Section 4.4.5, while degeneracies and their covariance are discussed in Section 4.7.

and in the next subsection we give fitting functions which work at the few percent level and include the effect of non-trivial n_s and $T(k)$.

4.4.4 Fitting functions

Motivated by the analytically discussion of the previous Section, here we present fitting functions for $\sigma(f_{\rm NL})$ and $\sigma(\tau_{\rm NL})$ as functions of (V, z, b_g, n), while fixing all of the parameters of the background cosmology to the Planck 2013 values, as explained in Section 4.3. Moreover, we take $k_{max} = 0.1h$ Mpc^{-1} throughout.

As a first step, we define the quantity

$$\Gamma(n, z) = \frac{b_g^2 n}{n_0(z)} = b_g^2 \left(\frac{n}{1.17 \times 10^{-5} h^3\ \mathrm{Mpc}^{-3}} \right) D^2(z) \tag{4.34}$$

To make our fitting functions self-contained, we note that the linear growth factor $D(z)$ is well fit by [50]:

$$D(z) \approx \frac{5}{2}\frac{\Omega_m(z)}{1+z}\left[\Omega_m(z)^{4/7} - \Omega_\Lambda(z) + \left(1+\frac{1}{2}\Omega_m(z)\right)\left(1+\frac{1}{70}\Omega_\Lambda(z)\right)\right]^{-1} \tag{4.35}$$

where $\Omega_m(z)$ and $\Omega_\Lambda(z)$ are defined by

$$\Omega_m(z) = \frac{\Omega_m(1+z)^3}{\Omega_\Lambda + \Omega_m(1+z)^3} \qquad \Omega_\Lambda(z) = \frac{\Omega_\Lambda}{\Omega_\Lambda + \Omega_m(1+z)^3} \tag{4.36}$$

Our fitting functions for $\sigma(f_{\rm NL})$ and $\sigma(\tau_{\rm NL})$ will be sums of sample variance and Poisson terms as follows:

$$\sigma(f_{\rm NL}) = \sigma_S(f_{\rm NL}) + \sigma_P(f_{\rm NL}) \qquad \sigma(\tau_{\rm NL}) = \sigma_S(\tau_{\rm NL}) + \sigma_P(\tau_{\rm NL}) \tag{4.37}$$

Note these are just fitting functions, and we are making no claims about the true variance decomposing into separate contributions. Following the analytic results of Section 4.4.3, we fit the individual terms with the functional forms:

$$\begin{aligned}
\sigma_S(f_{\rm NL}) &= \mathcal{A}_S\ D(z)\ \frac{b_g}{b_g-1}\left(\frac{V}{V_0}\right)^{-2/3+\epsilon_S+\frac{1}{2}\mu_S\ln(V/V_0)} \\
\sigma_P(f_{\rm NL}) &= \mathcal{A}_P\ D(z)\ \frac{b_g}{b_g-1}\ \Gamma^{-1}(n,z)\left(\frac{V}{V_0}\right)^{-1/2+\epsilon_P+\frac{1}{2}\mu_P\ln(V/V_0)} \\
\sigma_S(\tau_{\rm NL}) &= \mathcal{A}'_S\ D^2(z)\left(\frac{b_g}{b_g-1}\right)^2\left(\frac{V}{V_0}\right)^{-4/3+\epsilon'_S+\frac{1}{2}\mu'_S\ln(V/V_0)} \\
\sigma_P(\tau_{\rm NL}) &= \mathcal{A}'_P\ D^2(z)\left(\frac{b_g}{b_g-1}\right)^2\Gamma^{-1}(n,z)\left(\frac{V}{V_0}\right)^{-1+\epsilon'_P+\frac{1}{2}\mu'_P\ln(V/V_0)}
\end{aligned} \tag{4.38}$$

where $V_0 = 5h^{-3}$ Gpc^3 and values of the remaining parameters depend on whether we are marginalizing over bias or not. As in the previous discussion we will consider the two cases: (i) when no marginalization is performed, and (ii) when we marginalize over the gaussian bias b_g and assume a 20% Gaussian prior on the shot noise $1/n_{\rm eff}$. Best-fit parameter values

in these two cases are given by:

$$\begin{aligned}
&\text{for } f_{\rm NL}: \quad (\mathcal{A}_S, \epsilon_S, \mu_S, \mathcal{A}_P, \epsilon_P, \mu_P) = \\
&\quad = \begin{cases} (10.7,\ 0.096,\ -0.009,\ 33.7,\ -0.039,\ 0.012) & \text{if } b_g, n_{\rm eff} \text{ unmarginalized} \\ (15.9,\ 0.002,\ 0.005,\ 54.2,\ -0.102,\ 0.037) & \text{if } b_g, n_{\rm eff} \text{ marginalized} \end{cases} \\
&\text{for } \tau_{\rm NL}: \quad (\mathcal{A}'_S, \epsilon'_S, \mu'_S, \mathcal{A}'_P, \epsilon'_P, \mu'_P) = \\
&\quad = \begin{cases} (8477,\ 0.098,\ -0.037,\ 30405,\ -0.013,\ 0.000) & \text{if } b_g, n_{\rm eff} \text{ unmarginalized} \\ (8493,\ 0.089,\ -0.030,\ 30830,\ -0.035,\ 0.015) & \text{if } b_g, n_{\rm eff} \text{ marginalized} \end{cases}
\end{aligned} \tag{4.39}$$

This completes the description of our fitting functions for $\sigma(f_{\rm NL})$ and $\sigma(\tau_{\rm NL})$. With the above definitions, we find that our fitting functions are accurate to better than 10% for $0.5 \leq (V \,/\, h^{-3}\,{\rm Gpc}^3) \leq 50$ and arbitrary (b, n). (Note that $k_{\rm max} = 0.1$ has been assumed throughout; we will study the effect of varying $k_{\rm max}$ in Section 4.5.1.)

From this we read off the following: A sample variance limited survey with comoving volume $V = 25h^{-3}$ Gpc^3 and $b_g = 2.5$ has statistical errors $\sigma(f_{\rm NL}) \approx 6$ and $\sigma(\tau_{\rm NL}) \approx 1000$, comparable to Planck. Therefore, the only way to improve statistical errors beyond Planck is to measure a larger volume or to use a multi-tracer analysis, as described later.

4.4.5 Forecasts for $g_{\rm NL}$

As we have briefly mentioned in Section 4.3, the large scale bias in presence of primordial $g_{\rm NL}$ is approximately given by

$$P_{hh}(k) = \left(b_g + g_{\rm NL}\frac{\beta_g}{\alpha(k)}\right)^2 P_{mm}(k) + \frac{1}{n}\,, \tag{4.40}$$

where $\beta_g = 3\partial \ln n / \partial f_{\rm NL}$. In [44] we have found a fitting function for β_g:

$$\beta_g(\nu) \approx \kappa_3 \Big[-0.7 + 1.4(\nu-1)^2 + 0.6(\nu-1)^3 \Big] - \frac{d\kappa_3}{d\ln\sigma^{-1}} \left(\frac{\nu - \nu^{-1}}{2}\right) \quad . \tag{4.41}$$

where:

$$\nu = [\delta_c(b_g - 1) + 1]^{1/2}\,, \quad \kappa_3 = 0.000329(1 + 0.09z)\ b_g^{-0.09}\,,$$
$$\frac{d\kappa_3}{d\ln\sigma^{-1}} = -0.000061(1 + 0.22z)\ b_g^{-0.25} \tag{4.42}$$

with $\delta_c = 1.42$. Comparing Equation (4.8) for a 'pure' $f_{\rm NL}$ cosmology (i.e. one in which $\tau_{\rm NL} = \left(\frac{6}{5} f_{\rm NL}\right)^2$), with Equation (4.40), we find that the effect of $g_{\rm NL}$ on halo bias is the same as the effect of $f_{\rm NL} = (\beta_f/\beta_g) g_{\rm NL}$ and therefore they are indistinguishable with a single tracer population. In particular, if we want forecasts on the detectability of $g_{\rm NL}$ with a single tracer population assuming $f_{\rm NL} = 0$, we just write $\sigma(g_{\rm NL}) = (\beta_f/\beta_g)\sigma(f_{\rm NL}) \approx (2\delta_c(b_g - 1)/\beta_g)\sigma(f_{\rm NL})$ and use results from the previous subsection. Numerical results for our fiducial survey are shown in Figure 4.1.

As we will show in Sections 4.6 and 4.7, multiple tracer populations with different mass (or equivalently Gaussian bias), can allow us to distinguish between $f_{\rm NL}$ and $g_{\rm NL}$, thanks to the different dependence of the scale dependent correction on the Gaussian bias b_g.

4.5 General considerations when constraining $f_{\rm NL}$ from Large Scale Structure

4.5.1 How much do statistical errors degrade when marginalizing bias and Poisson noise?

When analyzing data from a real survey, the values of b_g and $n_{\rm eff}$ must be measured together with the non-Gaussian parameters, and it is important to understand the amount of information lost in doing so. In this Section, we quantify this by forecasting statistical errors on $f_{\rm NL}$ and $\tau_{\rm NL}$ when the parameters b_g and $(1/n_{\rm eff})$ are marginalized, and discuss our results as a function of $k_{\rm max}$.

We first note that $(1/n_{\rm eff})$ is only approximately equal to $(1/n)$, where n is the number density of tracers. In addition to the $(1/n)$ term expected from Poisson statistics, there are several effects which contribute constant power on large scales: non-linear galaxy bias, halo exclusion [22], tidal tensor bias [20, 21], and contributions from the HOD. Throughout this section, when we marginalize $(1/n_{\rm eff})$, we assign a Gaussian prior around the fiducial value $(1/n)$ with width equal to 20% of the value itself.

In Figure 4.2, we compare statistical errors on $f_{\rm NL}$ and $\tau_{\rm NL}$ in the cases with no marginalization, or marginalization over b_g and with a 20% prior on $n_{\rm eff}$. It is seen that marginalizing b_g can make a large difference in $\sigma(f_{\rm NL})$, e.g. in the sample variance limited case with $k_{\rm max} \gtrsim 0.1h$ Mpc^{-1}. This is because the non-Gaussian correction to the bias scales as $b_{NG}(k) \sim f_{\rm NL}/(k^2 T(k))$, with $T(k) \sim k^{-2} \ln(k/k_{eq})$ for $k \gg k_{\rm eq}$. Hence, the non-Gaussian part of the bias becomes nearly degenerate with the Gaussian bias b_g for $k \gg k_{\rm eq}$. For $\tau_{\rm NL}$, marginalization makes practically no difference and the statistical power increases very slowly going to higher k.

Based on these plots, we note that statistical errors on $f_{\rm NL}$ and $\tau_{\rm NL}$ are approximately saturated at $k_{\rm max} \sim 0.1h$ Mpc^{-1}, if Gaussian bias is properly marginalized. Therefore we take $k_{\rm max} = 0.1h$ Mpc^{-1} as our fiducial value in this paper.

4.5.2 Redshift Errors and 3D $\rightarrow$ 2D projection

Most observational constraints on non-Gaussianity reported in the literature have made use of projected angular correlation functions, rather than using redshift information. In this Section we discuss the effect of projecting three-dimensional measurements into one or more radial bins. This will quantify the information lost by 3D $\rightarrow$ 2D projection, and will also indicate how accurate photometric redshifts must be in order to avoid losing information relative to an ideal 3D survey.

We use a formalism which neglects curved-sky corrections, boundary effects, and redshift evolution, but is self-consistent given these approximations. Consider a rectangular 3D box

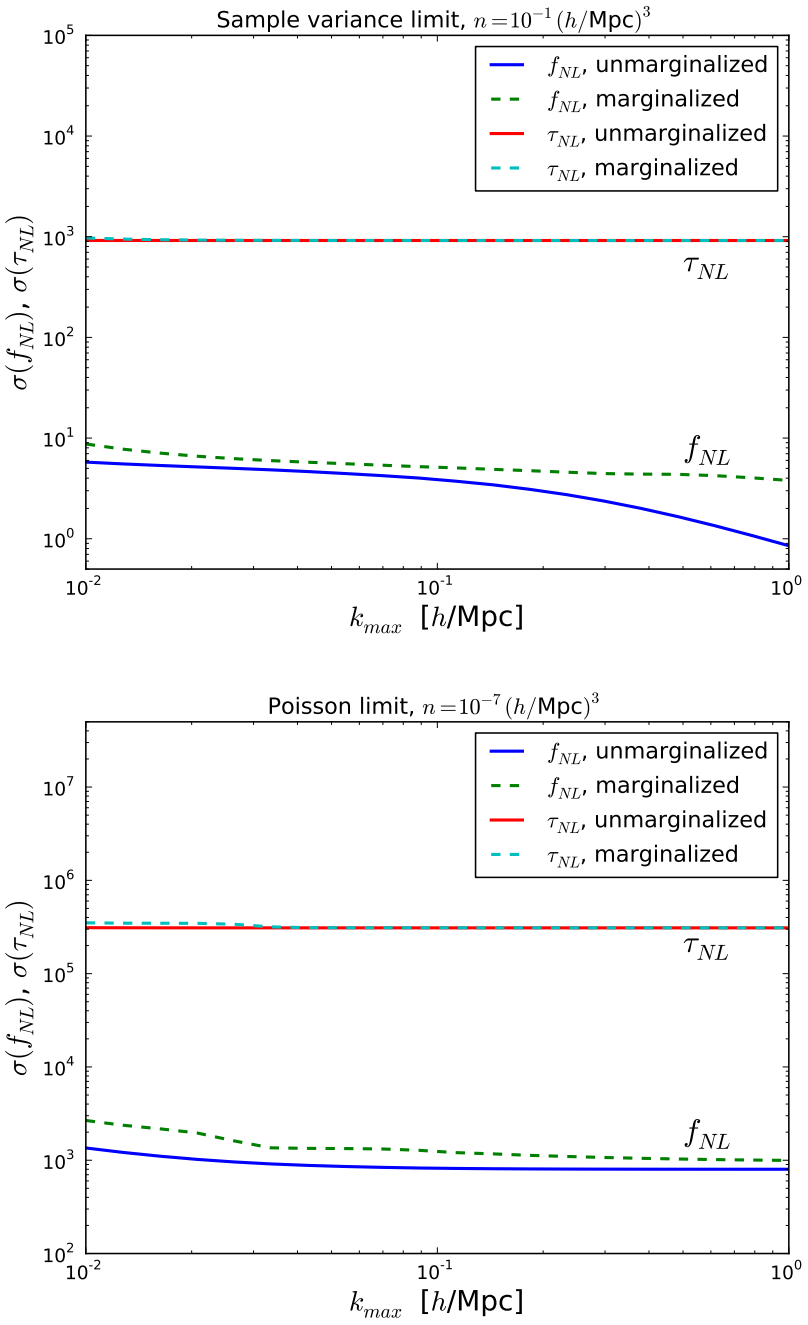

Figure 4.2: Forecasts on $f_{\rm NL}$ and $\tau_{\rm NL}$ as a function of maximum wavenumber $k_{\rm max}$ in the sample variance limited (top) and Poisson limited (bottom) regimes. Here $V = 25h^{-1}$Gpc, $z = 0.7$, and $b_g = 2.5$.

with periodic boundary conditions, and treat one of the three dimensions as the 'radial' direction, and the other two dimensions as 'transverse'. Let $A_\perp$ be the transverse area of the

box, and let $L_\parallel$ be the length of the box in the radial direction. We divide our 3D survey in N_{bins} radial slices and project the 3D halo field onto the closest slice. The case $N_{\text{bins}} = 1$ corresponds to neglecting any redshift information (i.e. a purely 2D survey), while the limit $N_{\text{bins}} \to \infty$ corresponds to an ideal 3D survey with perfect redshifts.

Suppose that the halo field in the box is a 3D field δ_{3D} with power spectrum

$$P_{hh}^{3D}(k) = \left(b_g + f_{\text{NL}} \frac{2\delta_c(b_g - 1)}{\alpha(k)}\right)^2 P_{mm}(k) + \frac{1}{n} \tag{4.43}$$

where the Gaussian bias b_g, redshift, and number density n are assumed constant throughout the box. We divide the box into N_{bins} radial bins and project the 3D halo field into N_{bins} two-dimensional fields $\delta_1, \cdots, \delta_{N_{\text{bins}}}$. We then use the 2D Fisher matrix formalism to forecast the statistical error on $\sigma(f_{\text{NL}})$, and study the dependence of $\sigma(f_{\text{NL}})$ on N_{bins}.

For Fisher forecasting, we will need to compute power spectra $P_{ij}(l)$ of the 2D fields δ_i. We will avoid using the Limber approximation since we will be interested in the limit $N_{\text{bins}} \to \infty$ in which the Limber approximation becomes arbitrarily bad (note that we are making the flat sky approximation throughout, but the flat sky and Limber approximations are independent). In real space, the 3D $\to$ 2D projection is given by

$$\delta_i(x, y) = \frac{N_{\text{bins}}}{L_\parallel} \int_{\chi_i - L_\parallel/2N_{\text{bins}}}^{\chi_i + L_\parallel/2N_{\text{bins}}} d\chi \; \delta_{3D}(x, y, \chi) \tag{4.44}$$

where (x, y) are transverse coordinates, χ is the radial coordinate, and χ_i is the central χ-value of the i-th bin. In Fourier space, the 3D $\to$ 2D projection is given by:

$$\tilde{\delta}_i(l_x, l_y) = \int_{-\infty}^{\infty} \frac{dl_\chi}{2\pi} \; \tilde{\delta}_i(l_x, l_y, l_\chi) \; \text{sinc}\left(\frac{l_\chi L_\parallel}{2N_{\text{bins}}}\right) e^{il_\chi \chi_i} \tag{4.45}$$

where (l_x, l_y) is a 2D wavevector of modulus $l = (l_x^2 + l_y^2)^{1/2}$ and $\mathrm{sinc}(x) = (\sin x)/x$. It follows that the N_{bins}-by-N_{bins} matrix of 2D projected power spectra is:

$$P_{ij}(l) = \int_{-\infty}^{\infty} \frac{dl_\chi}{2\pi}\; P_{hh}^{3D}\left(\sqrt{l^2 + l_\chi^2}\right)\; \mathrm{sinc}^2\left(\frac{l_\chi L_\parallel}{2N_{\mathrm{bins}}}\right) e^{il_\chi(\chi_i - \chi_j)} \tag{4.46}$$

We will compute 2D Fisher matrices to maximum wavenumber $l_{\mathrm{max}} = 0.1\ h\ \mathrm{Mpc}^{-1}$, but take the upper limit of the l_χ integral in Eq. (4.46) large enough that the integral converges. Note that the 2D Fisher matrix is given by

$$F_{\alpha\beta} = \frac{A_\perp}{2} \int \frac{d^2\boldsymbol{l}}{(2\pi)^2} \mathrm{Tr}\left[\boldsymbol{P}^{-1}\; \frac{\partial \boldsymbol{P}}{\partial\theta_\alpha} \boldsymbol{P}^{-1}\; \frac{\partial \boldsymbol{P}}{\partial\theta_\beta}\right] \tag{4.47}$$

with $\boldsymbol{P} = P_{ij}(l)$ given by Eq. (4.46).

In Figure 4.3 we show the dependence of $\sigma(f_{\mathrm{NL}})$ on N_{bins}, in both Poisson and sample variance limited cases. We see that completely neglecting redshift information significantly degrades the amount of information available; the statistical error on f_{NL} in a 2D analysis (i.e. $N_{\mathrm{bins}} = 1$) is larger than the 3D case by a factor close to 3. However, binning in redshift bins with with redshift spread $\Delta z \sim 0.1$ or smaller is sufficient to capture almost all of the 3D information.

We can also comment briefly on the effect of photometric redshift uncertainties. Photometric redshifts from a multi-band instrument such as LSST are several times smaller than $\Delta z \sim 0.1$, and therefore we expect that photometric redshift uncertainties should not significantly degrade statistical errors on f_{NL}. A caveat to this analysis is that a small fraction of *catastrophic* photometric redshift errors may add large-scale power; this case should be studied separately. (For a different approach to the study of photometric redshift errors and the closely related issue of redshift space distortions, see [16, 12].)

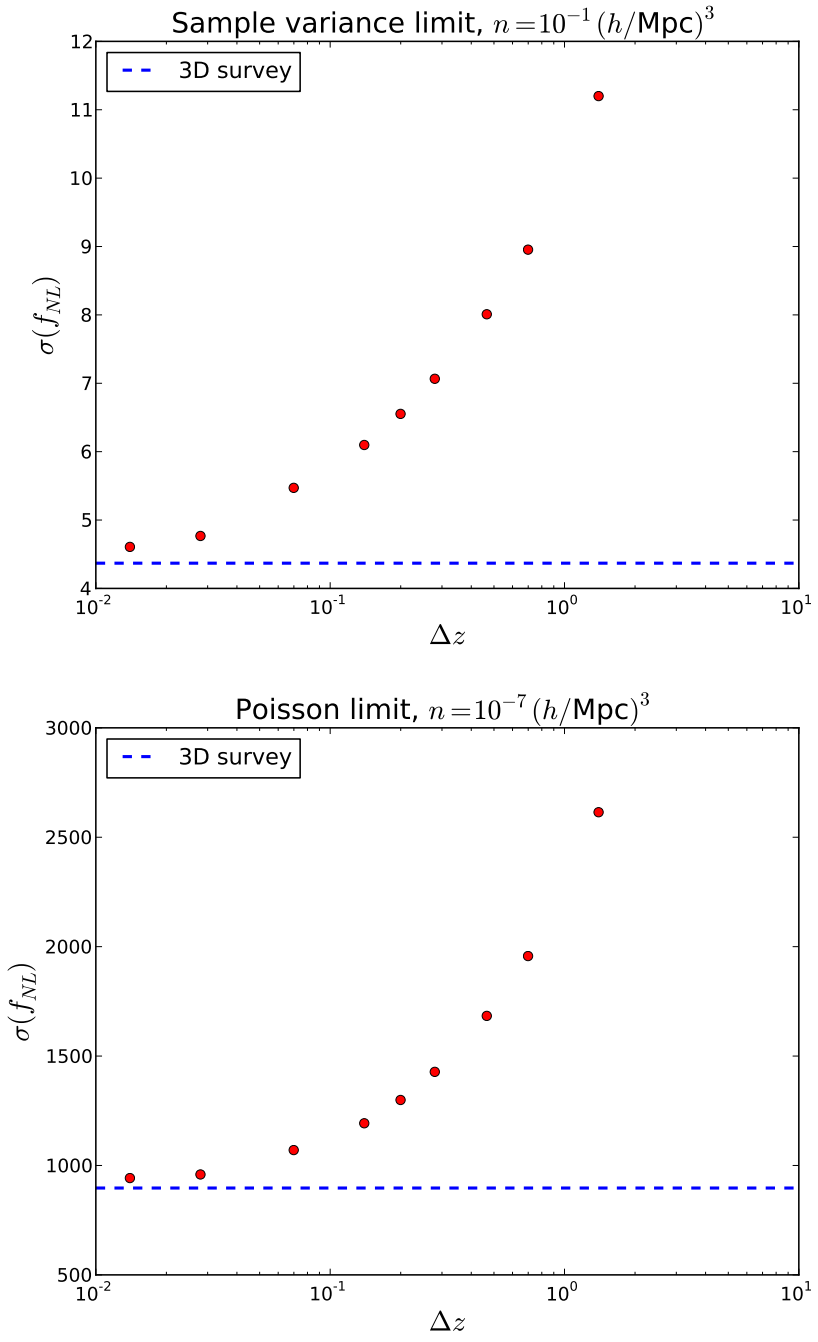

Figure 4.3: Dependence of statistical error $\sigma(f_{\rm NL})$ on redshift bin width (Δz), corresponding to (from right to left) $N_{\rm bins} = 1,\ 2,\ 3,\ 5,\ 7,\ 10,\ 20,\ 50$, and 100. The fiducial survey has volume $V = 25\ h^{-3}\ \mathrm{Gpc}^3$, redshift $z = 0.7$ and bias $b_g = 2.5$, with a cubic geometry assumed so that $A_\perp = V^{2/3}$ and $L_\parallel = V^{1/3}$. Note that the rightmost point corresponds to a 2D survey, and that the loss of information is roughly the same in the sample variance limited and Poisson limited cases.

4.6 Multi-tracer forecasts - Optimal Weighting

In this Section, we will consider multiple tracers with different Gaussian bias and show how to combine them optimally for the best constraining power on primordial non-Gaussianity. Here we will assume that all halos above some minimum mass $M_{\rm min}$ have been detected, and use the halo model prediction (with Sheth-Tormen mass function) for the number density and bias. Thus the parameters of our forecasts will be $(V, z, M_{\rm min})$.

Following the formalism of [8], we can divide the halo overdensity into $N \gg 1$ mass bins $\boldsymbol{\delta}_h = (\delta_1, \ldots, \delta_N)^T$. The number of bins will be determined by the finite mass resolution of the survey. Assuming halos to be locally biased and stochastic tracers of the underlying density field, we can write

$$\boldsymbol{\delta}_h = \boldsymbol{b}\ \delta + \boldsymbol{\epsilon} \tag{4.48}$$

where $\boldsymbol{\epsilon}$ is the residual (Poisson-like) noise field, with zero mean and uncorrelated with the matter density δ. Here b_i is the mean (number weighted) Gaussian bias of tracers in bin i:

$$b_i = \frac{\int_{M\in\text{bin }i} dM \frac{dn}{dM} b_g(M)}{\int_{M\in\text{bin }i} dM \frac{dn}{dM}} \tag{4.49}$$

The halo covariance matrix $C_{ij}(k) = \langle \delta_i^*(\boldsymbol{k})\delta_j(\boldsymbol{k})\rangle$ is

$$\boldsymbol{C}(k) = \langle \boldsymbol{\delta}_h \boldsymbol{\delta}_h^T \rangle = \boldsymbol{b}\boldsymbol{b}^T P_{mm}(k) + \boldsymbol{E} \tag{4.50}$$

where $E_{ij} = \langle \epsilon_i \epsilon_j \rangle$ is the error matrix. This has been studied analytically and with N-body simulations in several earlier papers (see for example [8, 19]). They find that $\boldsymbol{E}$ is approximately scale independent on the range of k considered, and that the dependence on $f_{\rm NL}$ is pretty weak and will be neglected here.

We will use the halo model prediction for $\boldsymbol{E}$ at low k, which has been shown to be a pretty good approximation to N-body simulations [19]:[3]

$$\begin{aligned} E_{ij} &= \langle \epsilon_i \epsilon_j \rangle = \langle (\delta_i - b_i \delta)(\delta_j - b_j \delta) \rangle \\ &= \langle \delta_i \delta_j \rangle - b_i \langle \delta_j \delta \rangle - b_j \langle \delta_i \delta \rangle + b_i b_j \langle \delta^2 \rangle \\ &= \frac{\delta_{ij}}{n_i} - b_i \frac{M_j}{\bar{\rho}} - b_j \frac{M_i}{\bar{\rho}} + b_i b_j \frac{\langle nM^2 \rangle}{\bar{\rho}^2} \end{aligned} \tag{4.51}$$

In the last line, we have taken the limit $k \to 0$ of the halo model predictions. Here we have defined

$$\langle nM^2 \rangle = \int dM \, \frac{dn}{dM} M^2 \tag{4.52}$$

Note that the two-halo contribution to E_{ij} cancels entirely. The off-diagonal components have a contribution from the one-halo term, while the on-diagonal components are a sum of the usual Poisson-like term $1/n_i$ and one-halo contribution. It is possible to construct an estimator that weighs each halo bin optimally, which is going to be a compromise between reduction of Poisson shot noise (which would correspond to pure mass weighing) and cancellation of cosmic variance. As shown in [7], the Fisher Matrix formalism already includes these effects.

In Figure 4.4, we show forecasted statistical errors $\sigma(f_{\rm NL})$, $\sigma(\tau_{\rm NL})$ and $\sigma(g_{\rm NL})$ from optimal weighting, for varying minimum halo mass $M_{\rm min}$. For high $M_{\rm min}$ we are in the Poisson limited regime and the constraints from halo bias are not competitive with those from Planck. As $M_{\rm min}$ decreases, the statistical errors decrease rapidly, then plateau near $M_{\rm min} \sim 5 \times 10^{13}$ $h^{-1} M_\odot$, then decrease more slowly.

This "sample variance plateau" region can be interpreted as the range of $M_{\rm min}$ where the tracer density is high enough to be sample variance limited, but not high enough that sample variance cancellation is effective. The sample variance plateau is important when thinking

[3] We find that our forecasts for $\sigma(f_{\rm NL}), \sigma(g_{\rm NL}), \sigma(\tau_{\rm NL})$ in this section are nearly unchanged if we use the Poisson approximation $E_{ij} \approx \delta_{ij}/n_i$ to Eq. (4.51), except for a $\sim 10\%$ increase in the errors on the sample variance plateau.

about survey optimization. Once a survey is deep enough to reach the sample variance plateau, further improvements in survey depth do not significantly improve constraints on primordial non-Gaussianity, unless the improvement is large enough ($\gtrsim 3$ magnitudes) to go past the plateau. Pushing to lower $M_{\rm min} \lesssim 4 \times 10^{12} h^{-1} M_\odot$, cancellation of sample variance becomes effective with a moderate effect on $f_{\rm NL}$ or $g_{\rm NL}$, and a much larger one on $\tau_{\rm NL}$, since for the latter case, most of the signal-to-noise comes from the very largest scales, which are the ones that are most affected by cosmic variance.

From Figure 4.4, we see that a future generation with $V = 25\ h^{-3}\ {\rm Gpc}^3$ is competitive with Planck if resolving halos down to $M_{\rm min} \sim 10^{14} h^{-1} M_\odot$. In order to significantly improve over Planck, either an increase in volume or a multi-tracer analysis with $M_{\rm min} \lesssim 10^{13} h^{-1} M_\odot$ are needed.

4.7 Separating $f_{\rm NL}$, $g_{\rm NL}$, $\tau_{\rm NL}$

So far, we have studied statistical errors on the parameters $f_{\rm NL}, g_{\rm NL}, \tau_{\rm NL}$ individually, i.e. we forecast the statistical error on each parameter assuming that the other two parameters are zero[4]. In this Section, we ask the question: to what extent can the parameters $f_{\rm NL}, g_{\rm NL}, \tau_{\rm NL}$ be constrained jointly?

4.7.1 Single tracer

Considering the single-tracer case first, it is clear that $f_{\rm NL}$ and $g_{\rm NL}$ are completely degenerate, since the clustering signature produced by $f_{\rm NL} \neq 0$ is identical to the signature produced by $g_{\rm NL} = (\beta_f/\beta_g) f_{\rm NL}$. On the other hand, there is some scope for separating $f_{\rm NL}$ and $\tau_{\rm NL}$ with a single tracer, since the non-Gaussian bias has different scale dependence in the two cases ($f_{\rm NL} k^{-2} T(k)^{-1}$ versus $\tau_{\rm NL} k^{-4} T(k)^{-2}$). We can quantify this by using the Fisher matrix

[4]This assumption is not strictly consistent for the case of $f_{\rm NL}$, since $\tau_{\rm NL}$ must satisfy the inequality $\tau_{\rm NL} \geq (\frac{6}{5} f_{\rm NL})^2$ on general grounds. However, we find that $\sigma(\tau_{\rm NL}) \gg \sigma(f_{\rm NL})^2$ for all forecasts considered in this paper, which implies that assuming $\tau_{\rm NL} = 0$ when forecasting $\sigma(f_{\rm NL})$ is a good approximation to assuming the 'minimal' value $\tau_{\rm NL} = (\frac{6}{5} f_{\rm NL})^2$

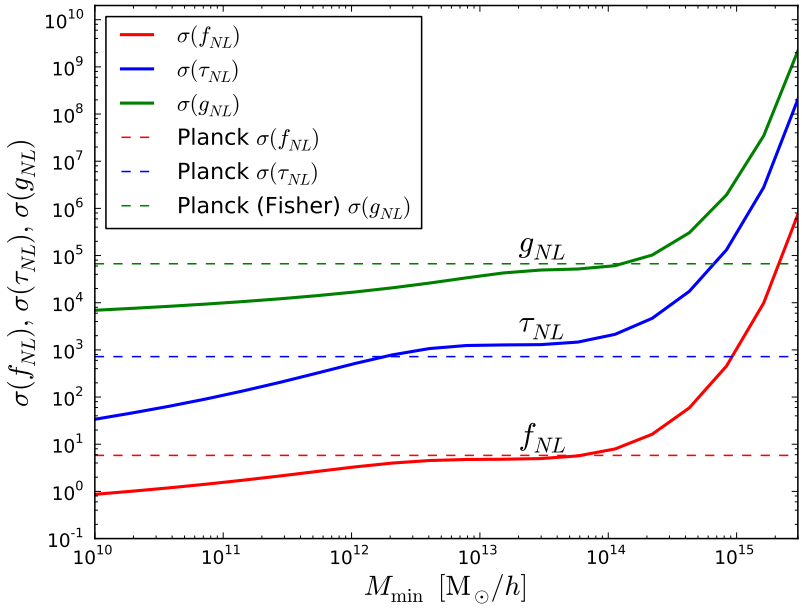

Figure 4.4: Statistical errors on $f_{\rm NL}$ (bottom solid curve), $\tau_{\rm NL}$ (middle solid curve) and $g_{\rm NL}$ (top solid curve) in a multitracer analysis, with varying $M_{\rm min}$ and $N = 50$ mass bins equally spaced on a log scale. When forecasting a given parameter $\{f_{\rm NL}, \tau_{\rm NL}, g_{\rm NL}\}$, the other two are set to zero. Here the volume is $V = 25\ h^{-3}$ Gpc^3, the redshift $z = 0.7$ and $k_{\rm max} = 0.1\ h$ Mpc^{-1}. Note the 'sample variance plateau' at $M_{\rm min} \sim 3 \times 10^{13}\ h^{-1} M_\odot$. The upper dashed line shows the Planck Fisher forecast $\sigma(g_{\rm NL}) = 6.7 \times 10^4$ from [23]. The middle dashed line is the Planck $\sigma(\tau_{\rm NL}) \approx 720$, obtained by fitting a Gaussian to the upper part of the $\tau_{\rm NL}$ posterior for $L_{\rm max} = 50$ (Figure 19 of [1]).

formalism to compute the correlation coefficient

$$\mathrm{Corr}(f_{\rm NL}, \tau_{\rm NL}) = -\frac{F_{f_{\rm NL},\tau_{\rm NL}}}{\sqrt{F_{f_{\rm NL}} F_{\tau_{\rm NL}}}} \tag{4.53}$$

where the minus sign appears because the covariance matrix is the inverse of the Fisher matrix.

An analytic calculation along the lines of Section 4.4.3 suggests that there should always be a moderate negative correlation between $f_{\rm NL}$ and $\tau_{\rm NL}$ in the single-tracer case. Figure 4.5 shows the numerical results for our fiducial survey. Note that having to marginalize over b_g and $1/n_{\rm eff}$ makes $f_{\rm NL}$ and $\tau_{\rm NL}$ more degenerate and harder to distinguish.

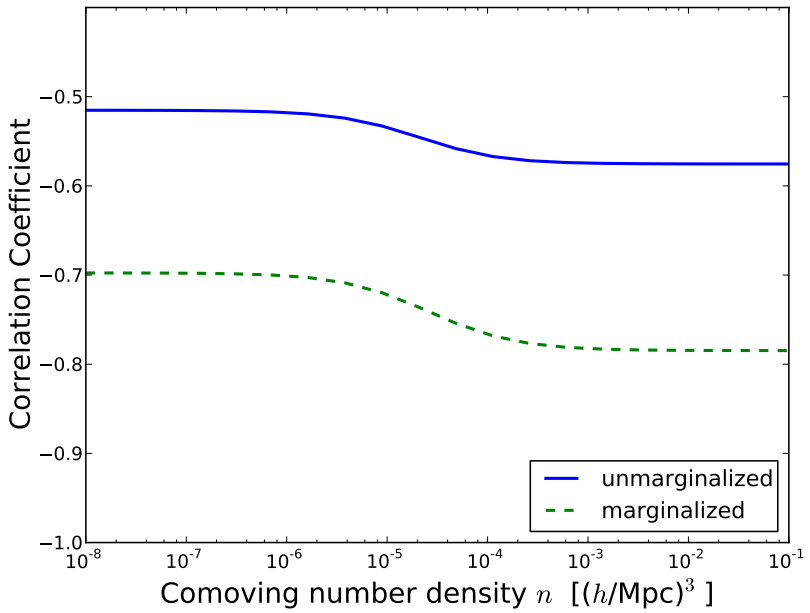

Figure 4.5: Single-tracer correlation coefficient between $f_{\rm NL}$ and $\tau_{\rm NL}$ in the unmarginalized case (top curve) and marginalizing over b_g with a 20% Gaussian prior on $1/n_{\rm eff}$ (bottom curve). The results are shown for our fiducial survey with $V = 25\ h^{-3}\ \mathrm{Gpc}^3$, $z = 0.7$ and $b_g = 2.5$.

4.7.2 Multiple tracer

The multi-tracer case is more interesting since $f_{\rm NL}$ and $g_{\rm NL}$ are no longer degenerate due to the different dependence of β_f and β_g on halo mass (or equivalently on Gaussian bias). Following Section 4.6, we assume perfect measurements of all halos above some minimum mass $M_{\rm min}$, and use the Fisher matrix formalism to compute the correlation coefficients $\mathrm{Corr}(f_{\rm NL}, \tau_{\rm NL})$ and $\mathrm{Corr}(f_{\rm NL}, g_{\rm NL})$. Numerical results are shown in Figure 4.6.

Let's consider the $f_{\rm NL} - \tau_{\rm NL}$ case first. In the region with high $M_{\rm min}$ the tracer density is low and we are deeply in the Poisson dominated regime, with correlation coefficient close to -0.5, in agreement with Figure 4.5. Decreasing $M_{\rm min}$ allows more tracers to be included and the correlation becomes more negative, as expected from the previous discussion. As soon as $M_{\rm min}$ reaches the sample variance plateau, $f_{\rm NL}$ and $\tau_{\rm NL}$ start to decorrelate, reaching nearly zero correlation at $M_{\rm min} \sim 10^{10} h^{-1} M_\odot$.

Joint constraints on $f_{\rm NL}, \tau_{\rm NL}$ were also studied in [11], who found poor prospects for distinguishing the two, and generally weak constraints on $\tau_{\rm NL}$, if the stochastic bias from $\tau_{\rm NL}$ is not included. We therefore conclude that stochastic bias is a very powerful observational probe of $\tau_{\rm NL}$.

In the $f_{\rm NL} - g_{\rm NL}$ case, the two are completely degenerate in the Poisson limit of high $M_{\rm min}$ and are therefore observationally indistinguishable using halo bias. Close to the sample variance plateau they decorrelate partially, to become highly negatively correlated again in the region of sample variance cancellation. We conclude that $f_{\rm NL}, g_{\rm NL}$ are not perfectly degenerate in a multi-tracer analysis, but are always significantly correlated (see also [10] for a detailed discussion of the degeneracy between $f_{\rm NL}$ and $g_{\rm NL}$).

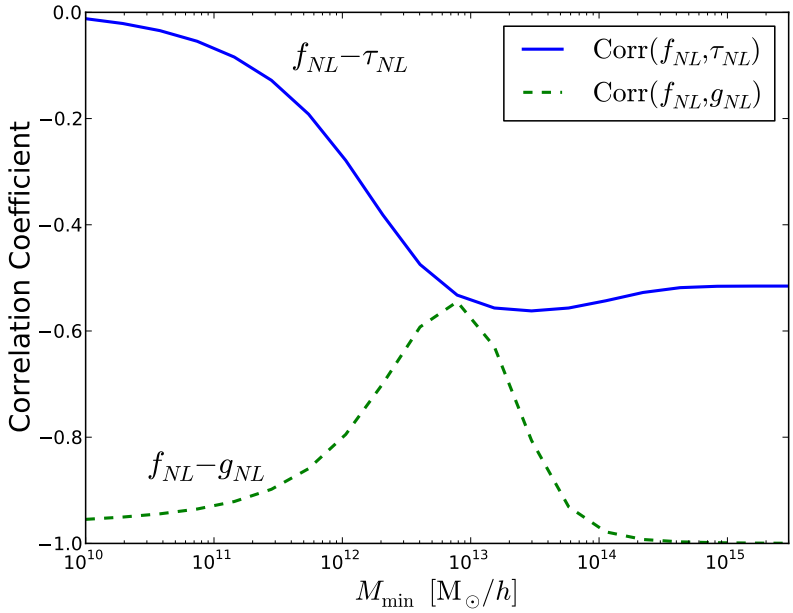

Figure 4.6: Multi-tracer correlation coefficients Corr($f_{\rm NL}, \tau_{\rm NL}$) (top curve) and Corr($f_{\rm NL}, g_{\rm NL}$) (bottom curve), for varying minimum halo mass $M_{\rm min}$.

4.8 Discussion and Conclusions

A detection of primordial non-Gaussianity would have very profound consequences for our understanding of the early Universe. Non-Gaussianity of the local type has been shown to leave an imprint on the large scale distribution of halos and galaxies in the form of a scale-dependent correction to the bias. Looking for this effect is one of the most promising ways to improve on the already tight bounds obtained by the Planck satellite.

In this work we have consider the effects of the scale-dependent bias on the power spectrum of halos and obtained forecasts applicable to upcoming Large Scale Structure surveys. Below we summarize our conclusions:

- If no mass information or other proxy for the bias of individual objects is available, a 'single tracer' analysis is used. A survey volume $V = 25h^{-3}\mathrm{Gpc}^3$, median redshift $z = 0.7$ and mean bias $b_g = 2.5$, can achieve $\sigma(f_{\rm NL}) = 6$, $\sigma(g_{\rm NL}) = 10^5$ and $\sigma(\tau_{\rm NL}) = 10^3$, if enough objects are resolved that the survey is sample variance limited.

- The statistical error on $f_{\rm NL}$ and $g_{\rm NL}$ approximately scales like $V^{-2/3}$ and $V^{-1/2}$ in sample variance or Poisson domination regimes respectively. The error on $\tau_{\rm NL}$ scales like $V^{-4/3}$ (sample variance domination) or V^{-1} (Poisson domination). In cases where the statistical error does not scale as $V^{-1/2}$, most of the statistical weight comes from the very largest scales in the survey.

- When constraining primordial non-Gaussianity from large-scale structure, it is always important to marginalize over Gaussian bias b_g (and to a lesser extent, Poisson noise $1/n_{\rm eff}$) In particular, if b_g is not marginalized in the sample variance dominated case, small increases in $k_{\rm max}$ can appear to produce a large improvement on statistical errors. This is not the case when proper bias marginalization is performed, since in this regime and for $k \gtrsim 10^{-1}h$ Mpc^{-1}, Gaussian bias and non-Gaussian corrections become nearly degenerate.

- Neglecting redshift information in large-scale structure degrades statistical errors on primordial non-Gaussianity by a factor close to 3. However, redshift uncertainties of order $\Delta z \approx 0.1$ increase the errors by ≈ 1.4 compared to the knowing the redshifts perfectly. Therefore a next generation photometric survey will be able to extract most of the information.

- A single-tracer sample variance limited survey with $V = 25h^{-3}\mathrm{Gpc}^3$ has a statistical power comparable to Planck. Improvement over CMB experiments would require either a larger volume or the use of multi-tracer techniques. If the mass or bias of individual objects is known, it is possible to combine different populations optimally in order to partially cancel sample variance and decrease the error. This mechanism becomes effective when resolving halos with $M_{\rm min} \lesssim 10^{13}h^{-1}M_\odot$. If halos down to $M_{\rm min} \sim 10^{11}h^{-1}M_\odot$ are resolved, we forecast $\sigma(f_{\rm NL}) = 1.5$, $\sigma(g_{\rm NL}) = 10^4$ and $\sigma(\tau_{\rm NL}) = 100$, improving over Planck or a single-tracer analysis by a factor of 4 for $f_{\rm NL}$ and nearly an order of magnitude for $g_{\rm NL}$ and $\tau_{\rm NL}$.

- $f_{\rm NL}$ and $\tau_{\rm NL}$ can be distinguished even with a single tracer, due to the different scale dependence of the bias on large scales (k^{-2} vs k^{-4}), but there is a significant correlation in the single tracer case. They can be decorrelated by using a multi-tracer analysis and pushing to $M_{\rm min} \lesssim 10^{13}h^{-1}M_\odot$. $f_{\rm NL}$ and $g_{\rm NL}$ are indistinguishable in the single-tracer case since the clustering signature produced by $f_{\rm NL} \neq 0$ is identical to the that produced by $g_{\rm NL} = (\beta_f/\beta_g)f_{\rm NL}$. The multi-tracer case can make use of the fact that the non-Gaussian bias depends on the Gaussian bias in different ways to distinguish the two. However, the correlation coefficient is always close to -1.

- Finally we briefly comment on survey optimization for primordial non-Gaussianity. For most cases of practical interest the 'sample variance plateau' makes it very hard to reach the regime in which sample variance cancellation becomes effective. So the most effective way of reducing the statistical errors is to increase the survey area (and

hence the total volume), unless already resolving halos with masses at the lower end of the plateau ($M_{\rm min} \sim 10^{13} h^{-1} M_\odot$ with our fiducial volume), in which case a deeper survey will also correspond to a significant improvement of statistical power.

Acknowledgements

We thank Paolo Creminelli, Marilena LoVerde, Emmanuel Schaan, Fabian Schmidt, Sarah Shandera, David Spergel, Michael Strauss and Matias Zaldarriaga for very helpful discussions and Pat McDonald for pointing out a typo to us. SF is supported by NASA ATP grant NNX12AG72G, NSF grant AST1311756, and thanks Perimeter Institute for hospitality. KMS was supported by an NSERC Discovery Grant. Research at Perimeter Institute is supported by the Government of Canada through Industry Canada and by the Province of Ontario through the Ministry of Research & Innovation.

Bibliography

[1] Planck Collaboration, "Planck 2013 Results. XXIV. Constraints on primordial non-Gaussianity", arXiv:1303.5084 (2013)

[2] WMAP Collaboration, "Nine-Year Wilkinson Microwave Anisotropy Probe (WMAP) Observations: Final Maps and Results", ApJS 208 20 (2013)

[3] BICEP2 Collaboration, "BICEP2 I: Detection Of B-mode Polarization at Degree Angular Scales", [arXiv:1403.3985]

[4] D. Lyth, "BICEP2, the curvature perturbation and supersymmetry" [arXiv:1403.7323]

[5] S. Ferraro, K. Smith, D. Green, and D. Baumann, "On the Equivalence of Barrier Crossing, Peak-Background Split, and Local Biasing", Mon. Not. Roy. Astron. Soc. **435**, 934 (2013)

[6] D. Baumann, S. Ferraro, D. Green, and K. Smith, "Stochastic Bias from Non-Gaussian Initial Conditions", JCAP **1305** 001 (2013)

[7] U. Seljak, "Extracting Primordial Non-Gaussianity without Cosmic Variance", Phys. Rev. Lett. **102**, 021302 (2009)

[8] N. Hamaus, U. Seljak, V. Desjacques, "Optimal constraints on local primordial non-Gaussianity from the two-point statistics of large-scale structure", Phys. Rev. D **84**, 083509 (2011)

[9] C. Carbone, L. Verde, S. Matarrese, "Non-Gaussian halo bias and future galaxy surveys" Astrophys. J. **684** L1-L4 (2008)

[10] N. Roth, C. Porciani, "Can we really measure $f_{\rm NL}$ from the galaxy power spectrum?" Mon. Not. Roy. Astron. Soc. **425** L81 (2012)

[11] M. Biagetti, V. Desjacques, A. Riotto, "Testing multifield inflation with halo bias" Mon. Not. Roy. Astron. Soc. **429**, 1774 (2012)

[12] T. Giannantonio, C. Porciani, J. Carron, A. Amara, A. Pillepich, "Constraining primordial non-Gaussianity with future galaxy surveys" Mon. Not. Roy. Astron. Soc. **422** 2854 (2012)

[13] T. Giannantonio, A. Ross, W. Percival et al., "Improved Primordial Non-Gaussianity Constraints from Measurements of Galaxy Clustering and the Integrated Sachs-Wolfe Effect", Phys. Rev. D **89**, 023511 (2014)

[14] L. Ferramacho, M. Santos, M. Jarvis, S. Camera, "Radio Galaxy populations and the multi-tracer technique: pushing the limits on primordial non-Gaussianity", arXiv:1402.2290

[15] A. Pillepich, C. Porciani and T. H. Reiprich, "The X-ray cluster survey with eROSITA: forecasts for cosmology, cluster physics, and primordial non-Gaussianity," Mon. Not. Roy. Astron. Soc. **422**, 44 (2012) [arXiv:1111.6587 [astro-ph.CO]].

[16] C. Cunha, D. Huterer, Olivier Doré, "Primordial non-Gaussianity from the covariance of galaxy cluster counts" Phys. Rev. D **82**, 023004 (2010)

[17] H. Gil-Marín, C. Wagner, L. Verde, R. Jimenez, A. F. Heavens, "Reducing sample variance: halo biasing, non-linearity and stochasticity", Mon. Not. Roy. Astron. Soc. **407**, 772 (2010)

[18] U. Seljak, N. Hamaus, V. Desjacques, "How to suppress the shot noise in galaxy surveys", Phys. Rev. Lett. **103** 091303 (2009)

[19] N. Hamaus, U. Seljak, V. Desjacques, R. Smith, T. Baldauf, "Minimizing the stochasticity of halos in large-scale structure surveys", Phys. Rev. D **82**, 043515 (2010)

[20] T. Baldauf, U. Seljak, V. Desjacques, P. McDonald, "Evidence for Quadratic Tidal Tensor Bias from the Halo Bispectrum", Phys. Rev. D **86** 083540 (2012)

[21] K. Chan, R. Scoccimarro, R. Sheth. "Gravity and Large-Scale Non-local Bias", Phys. Rev. D **85**, 083509 (2012)

[22] T. Baldauf, U. Seljak, R. Smith, N. Hamaus, V. Desjacques, "Halo Stochasticity from Exclusion and non-linear Clustering", Phys. Rev. D **88**, 083507 (2013)

[23] T. Sekiguchi, N. Sugiyama, "Optimal constraint on $g_{\rm NL}$ from CMB", JCAP **09** 002 (2013)

[24] N. Dalal, O. Doré, D. Huterer, and A. Shirokov, "The Imprints of Primordial Non-Gaussianities on Large-Scale Structure: Scale-Dependent Bias and Abundance of Virialized Objects," Phys. Rev. D **77**, 123514 (2008).

[25] S. Matarrese and L. Verde, "The Effect of Primordial Non-Gaussianity on Halo Bias," Astrophys. J. **677**, L77 (2008).

[26] A. Pullen, C. Hirata, "Systematic effects in large-scale angular power spectra of photometric quasars and implications for constraining primordial nongaussianity", Publications of the Astronomical Society of the Pacific, 125, 928, pp. 705-718 (2013)

[27] D. Huterer, C. E. Cunha and W. Fang, "Calibration errors unleashed: effects on cosmological parameters and requirements for large-scale structure surveys," MNRAS 432, **2945** (2013)

[28] B. Leistedt, H. Peiris, N. Roth, "Constraints on primordial non-Gaussianity from 800,000 photometric quasars", [arXiv:1405.4315]

[29] B. Leistedt, H. V. Peiris, D. J. Mortlock, A. Benoit-Lvy and A. Pontzen, "Estimating the large-scale angular power spectrum in the presence of systematics: a case study of Sloan Digital Sky Survey quasars," arXiv:1306.0005 [astro-ph.CO].

[30] B. Leistedt and H. V. Peiris, "Exploiting the full potential of photometric quasar surveys: Optimal power spectra through blind mitigation of systematics," arXiv:1404.6530 [astro-ph.CO].

[31] A. Ross et al., "The Clustering of Galaxies in SDSS-III DR9 Baryon Oscillation Spectroscopic Survey: Constraints on Primordial Non-Gaussianity", Mon. Not. Roy. Astron. Soc. **428**, 1116 (2013).

[32] D. Karagiannis, T. Shanks, N. Ross, "Search for primordial non-Gaussianity in the quasars of SDSS-III BOSS DR9", Mon. Not. Roy. Astron. Soc. **441**, 486 (2014)

[33] R. Sheth, G. Tormen, "Large scale bias and the peak background split" Mon. Not. Roy. Astron. Soc. **308**, 119 (1999)

[34] T. Suyama and M. Yamaguchi, "Non-Gaussianity in the Modulated Reheating Scenario," Phys. Rev. D **77**, 023505 (2008).

[35] K. Smith, M. LoVerde, and M. Zaldarriaga, "A Universal Bound on N-point Correlations from Inflation," Phys. Rev. Lett. **107**, 191301 (2011).

[36] D. Lyth and D. Wands "Generating the curvature perturbation without an inflaton", Phys. Lett. B 524:5-14 (2002).

[37] D. Tseliakhovich, C. Hirata, and A. Slosar, "Non-Gaussianity and Large-Scale Structure in a Two-Field Inflationary Model," Phys. Rev. **D82**, 043531 (2010).

[38]

[39] W. Press and P. Schechter, "Formation of Galaxies and Clusters of Galaxies by Self-Similar Gravitational Condensation," Astrophys. J. **187**, 425 (1974).

[40] N. Hamaus, U. Seljak, V. Desjacques, R. Smith, and T. Baldauf, "Minimizing the Stochasticity of Halos in Large-Scale Structure Surveys," Phys. Rev. D **82**, 043515 (2010).

[41] K. Smith and M. LoVerde, "Local Stochastic Non-Gaussianity and N-body Simulations," JCAP **1111**, 009 (2011).

[42] V. Desjacques, D. Jeong, and F. Schmidt, "Non-Gaussian Halo Bias Re-examined: Mass-Dependent Amplitude from the Peak-Background Split and Thresholding," Phys. Rev. D **84**, 063512 (2011).

[43] A. Slosar, C. Hirata, U. Seljak, S. Ho, and N. Padmanabhan, "Constraints on Local Primordial Non-Gaussianity from Large-Scale Structure," JCAP **0808**, 031 (2008).

[44] K. Smith, S. Ferraro, and M. LoVerde, "Halo Clustering and $g_{\rm NL}$-type Primordial non-Gaussianity," JCAP **1203**, 032 (2012).

[45] E. Sefusatti, J. Fergusson, X. Chen, and E. P. S. Shellard, "Effects and Detectability of Quasi-Single Field Inflation in the Large-Scale Structure and Cosmic Microwave Background," arXiv:1204.6318 [astro-ph.CO].

[46] J. -Q. Xia, M. Viel, C. Baccigalupi, G. De Zotti, S. Matarrese and L. Verde, "Primordial Non-Gaussianity and the NRAO VLA Sky Survey," Astrophys. J. **717**, L17 (2010)

[47] J. -Q. Xia, A. Bonaldi, C. Baccigalupi, G. De Zotti, S. Matarrese, L. Verde and M. Viel, "Constraining Primordial Non-Gaussianity with High-Redshift Probes," JCAP **1008**, 013 (2010)

[48] S. Ho, N. Agarwal, A. D. Myers, R. Lyons, A. Disbrow, H. J. Seo, A. Ross and C. Hirata *et al.*, "Sloan Digital Sky Survey III Photometric Quasar Clustering: Probing the Initial Conditions of the Universe using the Largest Volume," arXiv:1311.2597 [astro-ph.CO].

[49] D. Yamauchi, K. Takahashi and M. Oguri, "Constraining primordial non-Gaussianity via multi-tracer technique with Euclid and SKA," arXiv:1407.5453 [astro-ph.CO].

[50] S. M. Carroll, W. H. Press and E. L. Turner, "The Cosmological constant," Ann. Rev. Astron. Astrophys. **30**, 499 (1992).

[51] J. Maldacena, "Non-Gaussian Features of Primordial Fluctuations in Single-Field Inflationary Models," JHEP **0305**, 013 (2003).

[52] P. Creminelli and M. Zaldarriaga, "Single-Field Consistency Relation for the Three-Point Function," JCAP **0410**, 006 (2004).

[53] M. J. Mortonson and U. Seljak, "A joint analysis of Planck and BICEP2 B modes including dust polarization uncertainty," arXiv:1405.5857 [astro-ph.CO].

[54] R. Flauger, J. C. Hill and D. N. Spergel, "Toward an Understanding of Foreground Emission in the BICEP2 Region," arXiv:1405.7351 [astro-ph.CO].

Chapter 5

A WISE measurement of the ISW effect

5.1 Abstract

The *Integrated Sachs-Wolfe effect* (ISW) measures the decay of the gravitational potential due to cosmic acceleration and is thus a direct probe of Dark Energy. In some of the earlier studies, the amplitude of the ISW effect was found to be in tension with the predictions of the standard ΛCDM model. We measure the cross-power of galaxies and AGN from the WISE mission with CMB temperature data from WMAP9 in order to provide an independent measurement of the ISW amplitude. Cross-correlations with the recently released Planck lensing potential maps are used to calibrate the bias and contamination fraction of the sources, thus avoiding systematic effects that could be present when using auto-spectra to measure bias. We find an amplitude of the cross-power of $\mathcal{A} = 1.24 \pm 0.47$ from the galaxies and $\mathcal{A} = 0.88 \pm 0.74$ from the AGN, fully consistent with the ΛCDM prediction of $\mathcal{A} = 1$. The ISW measurement signal-to-noise ratio is 2.7 and 1.2 respectively. Comparing the amplitudes of the galaxy and AGN cross-correlations, which arise from different redshifts, we find no

evidence for redshift evolution in Dark Energy properties, consistent with a Cosmological Constant.

5.2 Introduction

The nature and the properties of Dark Energy are among the most significant unsolved problems in physics. We now believe that Dark Energy accounts for about 70% of the energy density of the Universe and is causing the cosmic expansion to accelerate. Measurements of Type Ia supernovae, Baryon Acoustic Oscillations, galaxy clusters or gravitational lensing (of the Cosmic Microwave Background, galaxies, or strongly lensed quasars) [2, 3, 4, 5, 6, 7], when combined with measurements of the Cosmic Microwave Background (CMB) anisotropies [1, 43], all provide evidence for an accelerated expansion [15] and imply a flat and Dark Energy dominated universe.

While theorists have proposed a large number of models to explain cosmic acceleration, including modifications to General Relativity on large scales [14], there exist only very few observational windows into the properties of this phenomenon.

Measurements of the *Integrated Sachs-Wolfe* effect (ISW) [16] provide a powerful method to probe Dark Energy, as this effect is sensitive to the time evolution of the gravitational potential sourced by Large Scale Structure and thus probes Einstein's equations beyond the simple Friedmann equation. The ISW effect is the distortion of the CMB temperature due to the time evolution of the gravitational potential along the line of sight: photons entering a gravitational potential well blue-shift and subsequently redshift when leaving the well. In a matter-dominated universe, the gravitational potential is time-independent on large scales, so the amount of blue- and red- shifting is the same and the photon energy is overall unchanged; Dark Energy causes an accelerated expansion, making the gravitational potential shallower with time and resulting in a net blue-shift of the photons. This effect is too small to be detected directly in the CMB spectrum [17] but it is expected to be measurable through

the correlation between the measured temperature anisotropies of the CMB and the Large Scale Structure, which acts as a tracer of the gravitational potential.

Such analyses have been carried out in earlier work (see for example [22, 21, 23, 24, 27, 34, 35, 36, 28, 20, 29, 30]), with the strongest detection to date (at the 4.5σ level) relying on the combination of many different data sets [34]. One interesting feature of several of the previous studies is that the cross-correlation signal lies systematically above (by $\sim 1-2\sigma$) the predicted value in the standard cosmological model (in which the Dark Energy is a Cosmological Constant) [34, 29, 19]. The same is true for some analyses based on stacking large clusters and voids, with the tension with ΛCDM reaching $> 3\sigma$ [24, 25, 26, 45, 46].

We perform a new ISW cross-correlation analysis using a sample of galaxies and quasars from the *Wide-field Infrared Survey Explorer* (WISE, [11]), which scanned the full sky in 4 frequency bands, ranging from 3.4 to 22 μm, and detected hundreds of millions of sources. The 3.4 μm band probes massive galaxies out to $z \sim 1$ and with a median redshift of 0.3 [31]. The large area of the survey, together with its redshift distribution and the large number of sources, makes WISE one of the best catalogs for this kind of work. An early study with the WISE preliminary release catalog found an amplitude that is 2σ above the ΛCDM prediction [29], while a subsequent work [30] using the full sky galaxy catalog found an amplitude consistent with ΛCDM, but at low significance (1σ). We use a larger sample (applying less restrictive cuts to the data) with higher median redshift and expect to detect the signal at a considerably higher significance. The Planck collaboration has recently combined the ISW measurements from WISE with several other datasets to obtain a 4.0σ measurement of the ISW amplitude [46].

Since galaxies and quasars trace the dark matter and hence the potential up to a bias factor (a proportionality factor relating tracer overdensity to mass overdensity), it is crucial to measure the bias reliably in order to be able to compare the ISW amplitude with theoretical predictions. Methods to measure the bias from the auto-correlation spectrum can be prone to systematic errors, especially for WISE maps which contain strong galactic and

instrumental signals, and can lead to incorrect conclusions about the amplitude of the ISW effect. Recent progress in the measurement of the gravitational lensing of the CMB by the *Atacama Cosmology Telescope* (ACT, [12, 42]), *South Pole Telescope* (SPT, [13, 48, 10]), POLARBEAR [8, 9] and the Planck Satellite [43, 44], allow a direct measurement of bias (lensing is sourced directly by the gravitational potential itself), by cross-correlating lensing potential maps with the tracer field. We expect this measurement to be more robust and less prone to systematic errors. This chapter is organized as follows: The ISW effect is briefly reviewed in section 5.3. Sections 5.4 and 5.5 introduce our tracer and CMB datasets, while in section 5.6 we discuss the calibration of the bias using CMB lensing. Our ISW results are presented in section 5.6.3, followed by a discussion and conclusions in section 5.8.

5.3 The ISW effect

As discussed in the introduction, the ISW effect is a secondary CMB anisotropy which is due to the time variation of the gravitational potentials along the line of sight [16] (see [47] for a recent review):

$$\begin{aligned}\left(\frac{\Delta T}{T}\right)_{ISW}(\widehat{\mathbf{n}}) &= -\int d\eta\; e^{-\tau(z)}(\dot{\Phi}+\dot{\Psi})[\eta, \widehat{\mathbf{n}}(\eta_0-\eta)] \\ &\approx -2\int d\eta\; \dot{\Phi}[\eta, \widehat{\mathbf{n}}(\eta_0-\eta)] \end{aligned} \tag{5.1}$$

where in the second line we have used the GR prediction that in absence of anisotropic stresses $\Phi = \Psi$ and have approximated the optical depth $\tau(z) \ll 1$ over the period where $\dot{\Phi} \neq 0$, so that we can take $e^{-\tau(z)} \approx 1$. Note that during matter domination, $\dot{\Phi} = 0$ and there in no ISW contribution. Since in the standard cosmological model the effect of Dark Energy is relevant only at $z \lesssim 1$, the largest contribution comes from the very largest scales. The typical low ℓ contribution to the CMB fluctuation spectrum is $\sim 100\ \mu\mathrm{K}^2$, compared

to the $\sim 1000\ \mu\mathrm{K}^2$ of the primary fluctuations, too small to be detected directly in presence of cosmic variance. This problem can be overcome by cross-correlating the observed CMB temperature with tracers of the gravitational potential, such as galaxies or quasars, that would otherwise be uncorrelated with the CMB in the absence of the ISW contribution.

We will work with the projected overdensity field of tracers (galaxies or quasars), which can be expressed in terms of the matter overdensity δ:

$$\delta_g(\widehat{\mathbf{n}}) = \int dz\ b(z)\frac{dN}{dz}\delta(\widehat{\mathbf{n}}, z) \tag{5.2}$$

Where we have assumed a (redshift dependent) linear bias model for the tracers and dN/dz is the redshift distribution normalized such that $\int dz' \frac{dN}{dz'} = 1$.

We can compute the angular cross-correlation[1]:

$$C_\ell^{Tg} = C_\ell^{\dot{\Phi}g} = 4\pi \int \frac{dk}{k}\Delta_m^2(k) K_\ell^{\dot{\Phi}}(k) K_\ell^g(k) \tag{5.3}$$

in terms of the dimensionless (linear) matter power spectrum at redshift $z = 0$, $\Delta_m^2(k) = k^3 P(k, z = 0)/2\pi^2$. Here the galaxy and ISW weight functions are given by:

$$K_\ell^g(k) = \int dz\ b(z)\frac{dN}{dz}D(z)\ j_\ell[k\chi(z)] \tag{5.4}$$

$$K_\ell^{\dot{\Phi}}(k) = \frac{3\Omega_m H_0^2}{k^2}\int dz \frac{d}{dz}((1+z)D(z))\ j_\ell[k\chi(z)] \tag{5.5}$$

where j_ℓ are the spherical Bessel functions, $D(z)$ is the linear growth factor normalized to $D(z = 0) = 1$ and $\chi(z) = \eta_0 - \eta(z)$ is the comoving distance to redshift z.

[1]Here we assume that the ISW contribution is the only component of the temperature anisotropy correlated with low-redshift tracers of the potential, so that we can write $C_\ell^{Tg} = C_\ell^{\dot{\Phi}g}$.

A simple Fisher matrix analysis gives the expected signal-to-noise ratio for a coverage fraction f_{sky},

$$\left(\frac{S}{N}\right)^2 \approx f_{sky} \sum_\ell (2\ell+1) \frac{[C_\ell^{Tg}]^2}{C_\ell^{TT} C_\ell^{gg} + [C_\ell^{Tg}]^2} \tag{5.6}$$

$$\approx f_{sky} \sum_\ell (2\ell+1) \frac{[C_\ell^{Tg}]^2}{C_\ell^{TT} C_\ell^{gg}} \tag{5.7}$$

where in the second line we have used the fact that the correlation is weak $C_\ell^{Tg} \ll \sqrt{C_\ell^{TT} C_\ell^{gg}}$. It can be shown that most of the signal-to-noise comes from $\ell \sim 20$ and $z \sim 0.4$, with a wide redshift distribution, and that the contributions from $z > 1.5$ and $\ell > 100$ are negligible [18].

Note that due to cosmic variance, there is a theoretical maximum for the signal-to-noise ratio, which we can see as follows: The correlation coefficient $r \equiv C_\ell^{\dot{\Phi}g} / \sqrt{C_\ell^{\dot{\Phi}\dot{\Phi}} C_\ell^{gg}}$ is constrained to be[2] $-1 \leq r \leq 1$, so that $[C_\ell^{Tg}]^2 = [C_\ell^{\dot{\Phi}g}]^2 \leq C_\ell^{\dot{\Phi}\dot{\Phi}} C_\ell^{gg}$. Therefore

$$\left(\frac{S}{N}\right)^2 \approx f_{sky} \sum_\ell (2\ell+1) \frac{[C_\ell^{Tg}]^2}{C_\ell^{TT} C_\ell^{gg}} \tag{5.8}$$

$$\leq f_{sky} \sum_\ell (2\ell+1) \frac{C_\ell^{\dot{\Phi}\dot{\Phi}}}{C_\ell^{TT}} \tag{5.9}$$

This can be evaluated in a given cosmological model and for ΛCDM one finds $(S/N) \lesssim 7.6\sqrt{f_{sky}}$ and about 15% more if polarization information is added [35].

5.4 WISE data

WISE scanned the entire sky in four bands at 3.4, 4.6, 12 and 22 μm (W1 to W4) and provided a much deeper dataset than other experiments at similar frequencies (such as 2MASS and IRAS). The WISE W1 and W2 bands primarily probe starlight coming from other galaxies or galactic stars, while the W3 and W4 bands are more sensitive to the thermal emission from dust grains.

[2]Here the value of C_ℓ includes the shot-noise contribution.

The WISE Source Catalog [11] contains more than 500 million sources which are detected at $S/N > 5$ in at least one band (usually W1 since it is the most sensitive). Galactic stars and quasars each account for approximately 12% of the catalog at high galactic latitude. Approximately 70% are normal star-forming galaxies, while 6% are unusually red, unidentified sources [31]. Previous work [31, 37, 38] has shown that the four WISE bands are sufficient to effectively distinguish stars and quasars from normal galaxies. The details of this color-color selection are outlined in the next subsections.

Unfortunately, parts of the WISE catalog are contaminated by moonlight: when WISE observes near the Moon (or as far as 30 deg away), stray light can affect the images and produce spurious detections. This is visible as several bright (overdense) stripes, which are perpendicular to the ecliptic equator and parallel to the WISE scan direction. The catalog's `moon_lev` flag denotes the fraction of frames that are believed to be contaminated. We discard all objects that have `moon_lev` > 4 in any band and regions with high density of such objects are added to the mask.

We also discard any source for which `cc_flags` $\neq 0$, since it is considered an artifact (diffraction spike, optical ghost, etc.).

Due to the scan strategy, the coverage depth is very inhomogeneous (the poles were scanned to much greater depth than the equator) and the selection function is mostly unknown. The median coverage in W1 is 15 exposures, with 12 exposure being the 'typical' number for points near the equator and 160 for points near the ecliptic poles. Plotting the source magnitude distribution as a function of position of the sky, we find that for high galactic latitude, the distribution is fairly uniform for W1 < 17.0. According to the WISE Explanatory Supplement[3], the catalog is 95% complete for sources with W1 < 16.6. Therefore we apply this magnitude cut to ensure good completeness and uniformity and at the same time retain the largest number of sources.

Below we outline our selection criteria for stars, galaxies and AGN:

[3]http://wise2.ipac.caltech.edu/docs/release/allsky/expsup/sec2_2.html

5.4.1 Stars

Emission from stars in the mid-IR is dominated by the Rayleigh-Jeans tail of the spectrum, meaning that the color[4] is close to zero and approximately independent of surface temperature. We use the following color cuts proposed in [37] to separate stars from galaxies and AGN: stars have W1 < 10.5, W2 $-$ W3 < 1.5 and W1 $-$ W2 < 0.4. In addition, we find that stars close to the galactic plane are effectively removed by classifying as 'star' anything with W1 $-$ W2 < 0.

Dust-poor elliptical galaxies at low redshift are hard to distinguish from stars with WISE colors alone and can therefore be misidentified and fall into this category.

5.4.2 Galaxies

Here we adopt an empirical definition of "Galaxy" as anything not classified as a star or AGN. Due to the negative k-correction in the IR, the WISE W1 band can probe galaxies out to $z \gtrsim 1$, since the W1 flux does not change significantly in the range $z \sim 0.5 - 1.5$ [31]. We use the redshift distribution of WISE galaxies as measured in [31]. In this paper, the authors cross-matched WISE sources with SDSS DR7 [32] in high galactic latitude regions and found the distribution to be fairly broad, peaking at $z \sim 0.3$ and extending all the way to $z = 1$. In order to more effectively remove galactic stars and be able to use a larger portion of the sky, we had to make the additional cut W1 $-$ W2 > 0, compared to [31]. The effect of this on the redshift distribution should be negligible, since from their color-color diagrams, the vast majority of galaxies are shown to indeed have W1 $-$ W2 > 0. To further test the effect of uncertainties in the redshift distribution, we repeat the analysis by shifting the whole distribution by $\Delta z = \pm 0.1$ (corresponding to a $\sim$30% shift in the peak z) and find that the best fit ISW amplitude is only changed by $\sim 5\%$, corresponding to about 0.1σ. We therefore conclude that it is appropriate to use the distribution as in [31] without additional corrections.

[4]Here by color we mean difference between magnitudes in two of the WISE bands.

The redshift distribution and the very large number of sources (our sample consists of approximately 50 million galaxies) make WISE nearly ideal for ISW cross-correlation.

The criterion $W1 - W2 > 0$ for galaxies ensures that the stellar contamination is small, at the cost of omitting a small number of galaxies. The remaining contamination, if uncorrelated with the CMB, affects the normalization of C_ℓ^{Tg} in the same way as it affects the cross-correlation with CMB lensing, and therefore can be calibrated out[5]. (see section 5.6). If in addition the contamination sources are clustered (like stars close to the galactic plane), they will add to the auto-power spectrum on large scales, acting as noise in the ISW measurement and thus lowering the statistical significance.

We adopt a fiducial bias model that constant with redshift for WISE selected galaxies and we measure the bias via lensing in section 5.6. To investigate the dependence of our results on the uncertainty in bias evolution, we also repeat the analysis for an evolving bias model $b^G(z) = b_0^G(1+z)$, with constant b_0^G.

Our conservative masking leaves $f_{sky} = 0.47$ and about 50 million galaxies.

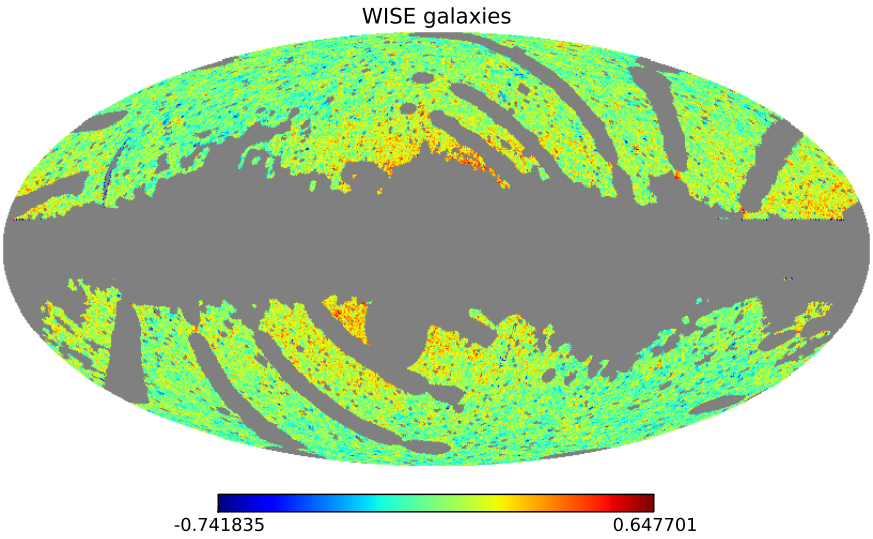

Figure 5.1: The WISE galaxy overdensity map, including the mask, displayed in grey.

[5]both C_ℓ^{Tg} and $C_\ell^{\kappa g}$ are lowered by the same multiplicative factor (1− contamination fraction). Therefore the measured bias is an 'effective bias' = real bias × (1− contamination fraction).

5.4.3 AGN

The mid-IR selection of AGN is a well-studied problem. Following [33, 38] we use the selection criteria W1 − W2 > 0.85 and W2 < 15.0. This has been shown to work well for both Type 1 and Type 2 AGN up to redshift $z \lesssim 3$ and leads to a source density of 42 deg^{-2}. Mid-IR selection is not significantly affected by dust extinction and the only potential contaminants are brown dwarfs and asymptotic giant branch stars, both of which have much smaller surface density.

We use the redshift distribution of WISE AGN that has been recently measured in [49] by cross-matching AGN on 7.9 deg^2 of the Boötes/AGES field. The authors show that it peaks at $z \sim 1.1$, with a spread $\Delta z \sim 0.6$ and further constrain the contamination fraction to be less than 15%.

We take the redshift dependence of the bias to be the one appropriate for the Type 1 QSOs, as suggested by [52]: $b^A(z) = b_0^A[0.53+0.289(1+z)^2]$, where b_0 is an overall amplitude, which we measure from the cross-correlation with CMB lensing maps.

Stellar contamination is expected to be very small, since AGN are easily distinguishable from stars using WISE bands.

Our masking leaves $f_{sky} = 0.48$ and about 910,000 AGN.

5.5 CMB data

Our CMB temperature data is obtained from the foreground reduced WMAP9 maps [1] in the Q, V and W bands (respectively at 40, 60 and 90 GHz), and the cosmological parameters taken from [1]. At the scales of interest ($\ell \lesssim 100$), the data is cosmic variance limited with negligible instrumental noise. For the CMB we apply the `KQ75y9` extended temperature analysis mask, which includes point sources detected in WMAP and has $f_{sky} \approx 0.69$. The total mask is the product of the CMB mask and the appropriate WISE mask for AGN

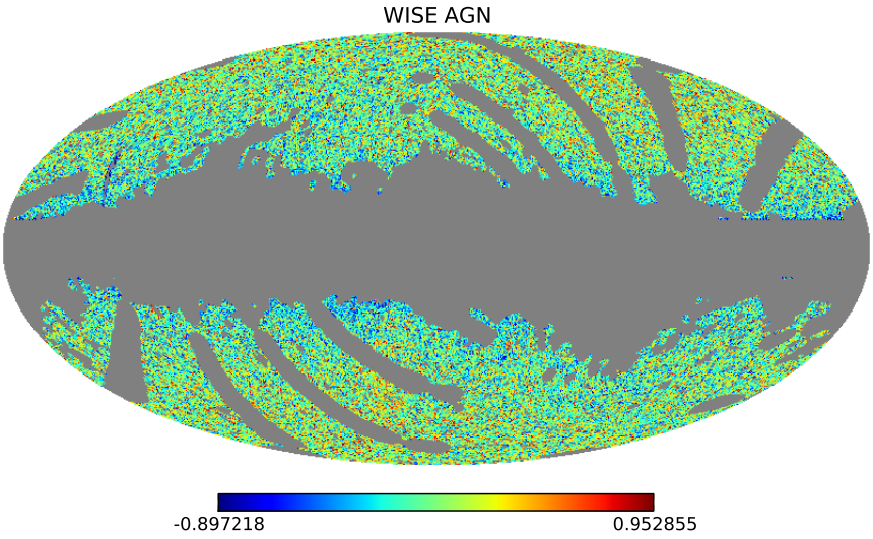

Figure 5.2: The WISE AGN overdensity map, including the mask, displayed in grey.

or galaxies. The same comprehensive mask is applied to both datasets before the cross-correlation analysis.

5.6 Lensing bias calibration

We use weak lensing of the CMB by our tracers to measure an effective bias, which takes into account the level of contamination by stars or artifacts.

5.6.1 Introduction

The observed (lensed) temperature $T(\widehat{\mathbf{n}})$ in a given direction $\widehat{\mathbf{n}}$ is a remapping of the original temperature $T_{\rm or}$ in the direction $\widehat{\mathbf{n}}+\mathbf{d}$, where $\mathbf{d}$ is the displacement field: $T(\widehat{\mathbf{n}}) = T_{\rm or}(\widehat{\mathbf{n}}+\mathbf{d})$.

It is convenient to work with the convergence field, defined as $\kappa \equiv -\nabla\cdot\mathbf{d}/2$ and which can be expressed as an integral along the line of sight [39, 40]:

$$\kappa(\widehat{\mathbf{n}}) = \int dz\ K^{\kappa}(z)\delta(\widehat{\mathbf{n}}, z) \tag{5.10}$$

In a flat universe (an assumption that we make throughout), the lensing kernel is given by:

$$K^{\kappa}(z) = \frac{3\Omega_m H_0^2}{2H(z)}(1+z)\chi(z)\frac{\chi_* - \chi(z)}{\chi_*} \tag{5.11}$$

where $\chi_* \sim 14$ Gpc is the comoving distance to the last scattering surface.

The cross-correlation between the lensing convergence and the projected density field can be calculated using the Limber approximation, which is expected to work well here, since we only use modes $\ell \gtrsim 50$:

$$C_\ell^{\kappa g} = \int dz \; \frac{H(z)}{\chi^2(z)} \; K^g(z) K^{\kappa}(z) P\left(k = \frac{\ell + 1/2}{\chi(z)}, z\right) \tag{5.12}$$

We note that the linear bias factor $b(z)$ appears in $C_\ell^{\kappa g}$ and C_ℓ^{Tg} weighed by different kernels and therefore it is important to account for the redshift dependence of b. As discussed previously, our fiducial galaxy bias is a constant with redshift, but we also investigate the model $b^G(z) = b_0^G(1+z)$, while for the AGN we take $b^A(z) = b_0^A[0.53 + 0.289(1+z)^2]$.

5.6.2 Planck lensing potential

The Planck collaboration released a map of the lensing potential ϕ_L (related to the lensing convergence by $\kappa = -\nabla^2\phi_L/2$), covering over 70% of the sky [44]. As we can see from equation (5.10), this is a direct measurement of the projected density field out to the surface of last scattering, weighted by a broad kernel which peaks at $z \sim 2$.

The correlation between WISE and the Planck lensing potential was recently investigated in [44, 49], where a $\sim 7\sigma$ detection was found for both galaxies and quasars. Here we repeat the analysis with the same maps and masks used for the ISW work.

5.6.3 Results

We use the Planck lensing potential and WISE maps at HEALPix [50] resolution $N_{side} = 512$ and measure the cross-correlation signal for $100 \leq \ell \leq 400$, correcting for the effects of the pixel window function and of the mask. Note that we use the same ℓ_{max} as in the cosmological analysis by the Planck team [44]. Including higher ℓ would probe the non-linear regime, where a constant bias model is likely to be inadequate and require corrections. Furthermore, including higher ℓ would be unnecessary from a statistical point of view, as the error on the bias is not the dominant source of uncertainty on the ISW amplitude. Lacking realistic simulated Planck lensing maps, the error bars are computed from the variance of the values in a given ℓ bin. We have however checked that they are consistent but $\sim 30 - 60\%$ larger than the theory error bars computed in the Gaussian approximation, which represent a theoretical lower bound.

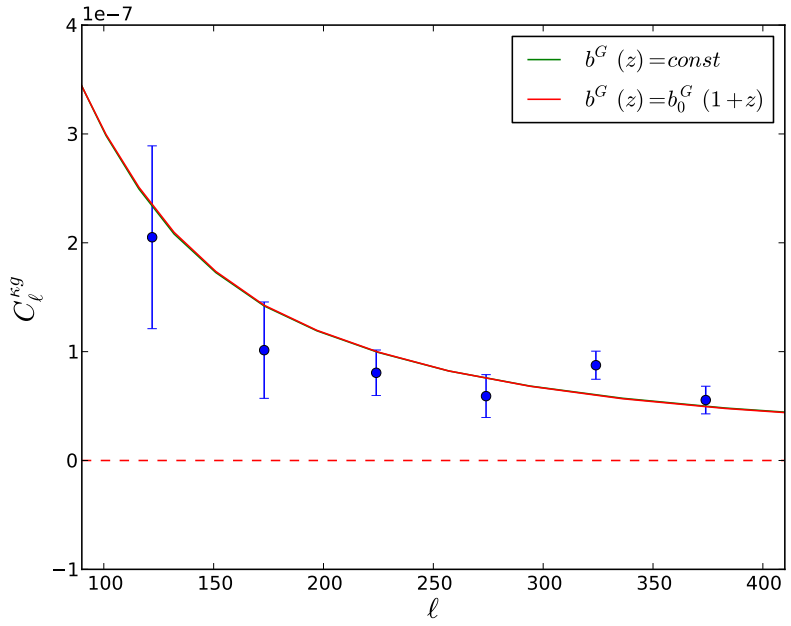

Figure 5.3: Lensing convergence-galaxy cross-correlation as a measure of the linear bias for WISE galaxies.

Figures 5.3 and 5.4 show the cross-correlation signal. For our fiducial galaxy bias model (a redshift independent constant), we find $b^G = 1.41 \pm 0.15$. This value is larger than that found

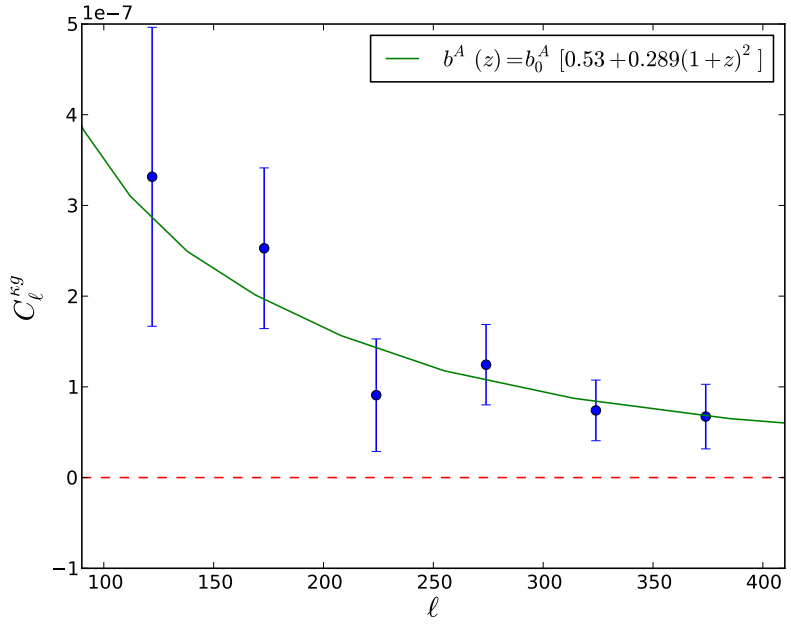

Figure 5.4: Lensing convergence-AGN cross-correlation as a measure of the linear bias for WISE AGN.

by the Planck Collaboration [44]; this difference is expected, because Planck uses a more conservative magnitude cut and hence measures bias of lower redshift, less biased sources. If instead we consider our second model $b^G(z) = b_0^G(1+z)$, we measure $b_0^G = 0.98 \pm 0.10$. We note that there is a slight dependence on ℓ_{max}, which could be due to statistical fluctuations, a failure of our linear bias model on small scales, or other effects. However, this dependence is negligible for the purpose of this paper: even in the extreme case of using $\ell_{max} = 2000$ instead of our fiducial 400, the bias we measure is higher by only 12%, translating into a change in ISW amplitude of 0.13σ.

For the AGN with bias $b^A(z) = b_0^A[0.53+0.289(1+z)^2]$, we measure $b_0^A = 1.26 \pm 0.23$. Our result is stable with respect to changes in ℓ_{max} and is only $\sim 1\sigma$ higher than the SPT result [49], $b_0^A = 0.97 \pm 0.13$. Again, this uncertainty corresponds to a shift in the ISW amplitude derived from the AGN sample of about 0.3σ and is therefore not important for the purpose of this work.

5.7 ISW results

We measure the cross-correlation of the WISE galaxy and AGN samples with the WMAP CMB temperature maps in the Q, V and W bands. We estimate the signal in 7 bins (bandpowers), equally spaced in ℓ space and spanning multipoles from 5 to 100. Since we are only interested in $\ell \leq 100$, we use maps with HEALPix $N_{side} = 128$, after correcting for the WMAP beam (different for each band) and for the pixel window function. The complex geometry of the mask induces non-trivial off diagonal correlations between bandpowers and we use the MASTER algorithm [51] to largely undo the effect of the mask and obtain an unbiased (but slightly suboptimal) estimate of the bandpowers.

To estimate the error bars and the covariance matrix, we cross-correlate the WISE galaxy and AGN samples[6] with 5000 simulated CMB maps as follows: We use our fiducial cosmology CMB power spectrum and the WMAP beam transfer function to obtain 5000 simulated CMB maps (Gaussian random fields) for each band. Then noise is added to each pixel in the form of a Gaussian random variable with zero mean and standard deviation given by $\sigma = \sigma_0/\sqrt{N_{exp}}$, where σ_0 is 2.188, 3.131 or 6.544 mK, for Q, V and W bands respectively, and N_{exp} is the number of exposures of the corresponding pixel in the WMAP survey.

The Monte Carlo covariance matrices for the Q band are shown in figure 5.7 in appendix 5.9. We verify convergence by varying the number of simulations and noting consistent results. While the covariance matrix is dominated by the diagonal components, the off diagonal components are non-negligible and should be taken into account.

The cross-correlation results are shown in figures 5.5 and 5.6 and summarized in tables 5.1 and 5.2. If $\mathbf{d}$ are the measured bandpowers and $\mathbf{t}$ are the corresponding theory values, the best fit amplitude $\mathcal{A} = C_\ell^{Tg,bestfit}/C_\ell^{Tg,\Lambda CDM}$ is obtained by minimizing $\chi^2 = (\mathbf{d}-\mathbf{t})^T C^{-1}(\mathbf{d}-\mathbf{t})$, where C^{-1} is the inverse of the covariance matrix. The significance is computed as $\sqrt{\chi^2_{null} - \chi^2_{min}}$, with χ^2_{null} referring to the null hypothesis $\mathbf{t} = \mathbf{0}$ (i.e. no ISW signal). When

[6]Because of the uncertainties on the WISE selection function and noise properties, we choose to use the real data in estimating the Monte Carlo covariance matrix.

quoting the ISW amplitude, the value of the bias is fixed to the mean value found in the previous section, and uncertainties in the bias determination are very subdominant compared to the cosmic variance errors.

The null tests are performed by cross-correlation with the simulated CMB maps are shown in figure 5.8 in appendix 5.9 for each band. All of the null tests are consistent with zero signal as expected.

5.7.1 Galaxies

For WISE galaxies with constant bias, we measure an amplitude of $\mathcal{A} = 1.24 \pm 0.47$, fully consistent with the ΛCDM prediction $\mathcal{A} = 1$. The amplitudes and some basic statistical properties for each band are reported in table 5.1 and the results are shown in figure 5.5.

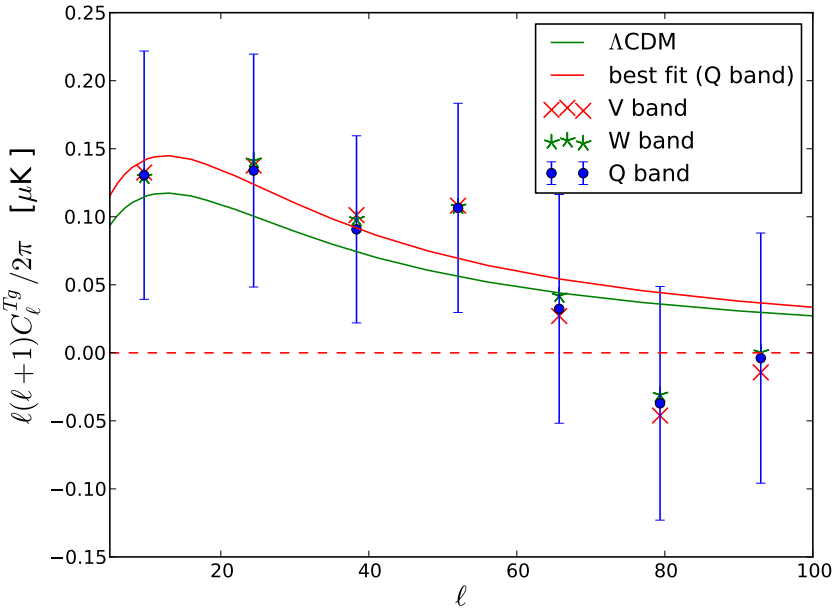

Figure 5.5: cross-correlation between WISE galaxies and WMAP temperature maps, where the ΛCDM theory curve is computed assuming a redshift independent bias. The error bands are shown only for Q band and the other error bars are within 5% of the ones shown.

The correlation signal is essentially independent of frequency over the range 40 - 90 GHz, which makes a significantly contamination by foregrounds unlikely.

Band	Amplitude $\mathcal{A}$	χ^2 / dof	p-value	S/N
Q	1.22 ± 0.47	1.42 / 6	0.04	2.6
V	1.25 ± 0.47	1.81 / 6	0.06	2.6
W	1.26 ± 0.47	1.25 / 6	0.03	2.7

Table 5.1: ISW amplitude and significance for the galaxy sample, assuming a constant bias model.

As we can see from table 5.1, the χ^2 of the best fit is slightly low, but it is expected this high or low about 6 - 12% of the time. To test the error calculation, we used the Gaussian approximation (Fisher formalism) to analytically compute the errors bars using the measured WISE auto-power spectrum, obtaining a result that is fully consistent with the Monte Carlo estimate.

To test the stability of our results with respect to changes in the mask, we repeat the cross-correlation with masks leaving $f_{sky} = 0.35, 0.40$ and 0.51, and find best fit amplitudes $\mathcal{A} = 1.10, 1.01$ and 1.10 respectively. The masks with small f_{sky} were chosen to effectively mask the stellar overdensity visible in figure 5.1 close to the galactic plane and show that the signal is not due to correlation between stellar overdensity and residual contaminants in the CMB map.

To assess the dependence of our result on uncertainties in the evolution of bias, we repeat the analysis with a model in which it evolves linearly with redshift $b^G(z) = b_0^G(1+z)$. In this case we find $\mathcal{A} = 1.54 \pm 0.59$, with again $S/N \approx 2.7$. This corresponds to a shift in amplitude of about one half sigma and therefore we can conclude that our measurement is fairly robust under uncertainties in the evolution of the bias.

5.7.2 AGN

The measured amplitude $\mathcal{A} = 0.88 \pm 0.74$ is again consistent with the ΛCDM predictions. The amplitude is stable under small changes in the mask and is frequency independent, as can be seen from table 5.2 and figure 5.6.

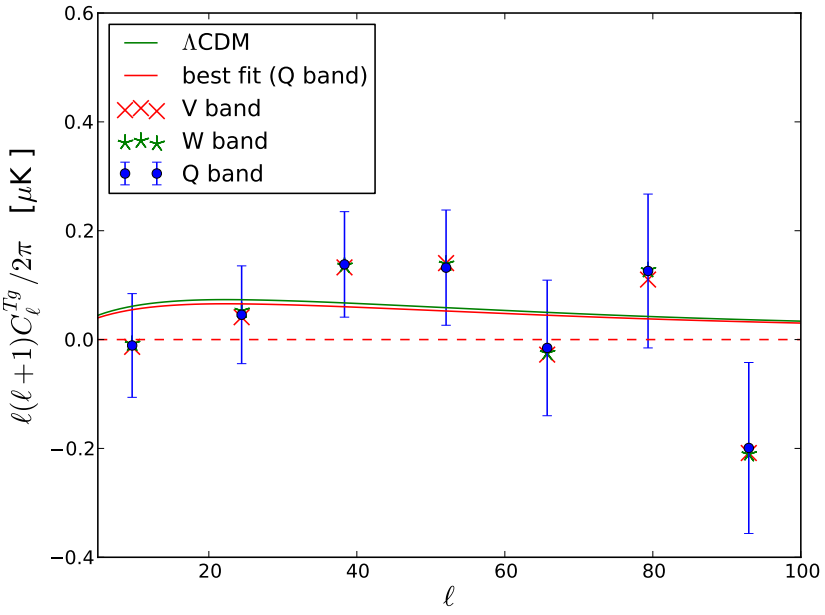

Figure 5.6: Cross-correlation between WISE AGN and WMAP temperature maps. The error bands are shown only for Q band; the other error bars are within 5% of the ones shown.

Band	Amplitude $\mathcal{A}$	χ^2 / dof	p-value	S/N
Q	0.88 ± 0.74	4.6 / 6	0.4	1.2
V	0.86 ± 0.74	4.7 / 6	0.4	1.2
W	0.91 ± 0.75	4.6 / 6	0.4	1.2

Table 5.2: ISW amplitude and significance for the AGN sample.

As the highest ℓ bin in figure 5.6 appears low, we extend our analysis to $\ell = 200$ to test that this value is simply a fluctuation. We find that the points for $100 \leq \ell \leq 200$ are consistent with the low-ℓ-fit signal curve as expected[7].

Though the AGN sample is simpler to cleanly select than the galaxy sample, the significance of the AGN sample is lower. Partially this is because the expected signal itself is smaller, as a large fraction of WISE AGN lie at $z \gtrsim 1$, where Dark Energy is unimportant. In addition, the smaller number of sources makes the sample shot-noise limited in the high ℓ bins, further reducing the significance of the measurement.

[7]in particular, the next two bandpowers in figure 6 would lie at (0.066 ± 0.134) and (0.003 ± 0.147) μK respectively.

5.8 Conclusions

Dark Energy remains one of the most elusive outstanding problems in Physics, and the ISW effect provides one of the most direct probes of its properties.

In this work we have measured the cross-correlation between the CMB temperature and both WISE galaxies and AGN. The correlation is expected to be entirely due to the ISW effect and hence absent in a Universe with no Dark Energy.

We find a positive signal which is consistent with the ΛCDM predictions, with significances of 2.7σ and 1.2σ for galaxies and AGN respectively. It can be shown that the bulk contribution to the galaxy ISW signal comes from $z \sim 0.2 - 0.6$, with a peak at $z \sim 0.3$, while the AGN, due to their fairly high median redshift, receive a fairly uniform contribution in the interval $z \sim 0.2 - 1.2$. Therefore, the AGN act as a useful probe of Dark Energy at an earlier time. We find that our results show no evidence for evolution of the Dark Energy density, as expected from a Cosmological Constant.

We use the CMB lensing potential from the Planck mission to calibrate the bias and stellar contamination of our sample, a method that has recently become available with advances in high-resolution CMB experiments. Calibration with lensing cross-correlation allows a direct measurement of the effective bias, with a smaller sensitivity to some systematic errors that can affect a measurement with the auto power spectra. Moreover, any instrumental systematic that could affect both the CMB temperature and the reconstructed lensing potential should be mitigated by using two independent experiments for the lensing and ISW analyses.

The signal we detect is fairly insensitive to the choice of mask and, more crucially, frequency independent. An imperfect foreground subtraction on the CMB side could potentially create spurious correlation with WISE, but any residual foreground contamination is expected to vary significantly over the range 40 - 90 GHz that we probe here. Therefore we conclude that any contamination, if present, is likely to be highly subdominant.

While some previous studies hinted at the possibility of a signal with amplitude higher than what expected from ΛCDM, we find no deviation from the standard cosmological model in either amplitude or redshift dependence, in agreement with some of the other previous measurements (eg [22, 35, 36, 45]). We are also in agreement with a recent analysis of the ISW effect from WISE galaxies [30] that used a somewhat smaller sample at lower redshift and measured an amplitude consistent with ΛCDM, with a significance of about 1σ.

Acknowledgements

We thank Olivier Doré, Amir Hajian, Eiichiro Komatsu, Fabian Schmidt, Kendrick Smith, Michael Strauss and Matias Zaldarriaga for very helpful discussions. Moreover we are grateful to the anonymous referees who helped improve the paper significantly. SF and DNS are supported by NASA ATP grant NNX12AG72G and NSF grant AST1311756. BDS was supported by a Miller Research Fellowship at Berkeley and by a Charlotte Elizabeth Procter Honorific Fellowship at Princeton University.

5.9 Appendix 1: Covariance matrix and null tests

Here we show plots for the Q-band covariance matrices and the null tests. For a description of the methodology, see section 5.7 in the main text.

5.10 Appendix 2: Doppler effect contamination to the ISW signal

In this appendix we discuss the magnitude of another secondary anisotropy of the CMB that preserves the black-body frequency spectrum: the Doppler (or linear kinetic Sunyaev-Zel'dovich) effect. This is caused by the Doppler shift when a CMB photon scatters off coherently moving electrons with line-of-sight velocity v_r. The fractional CMB temperature

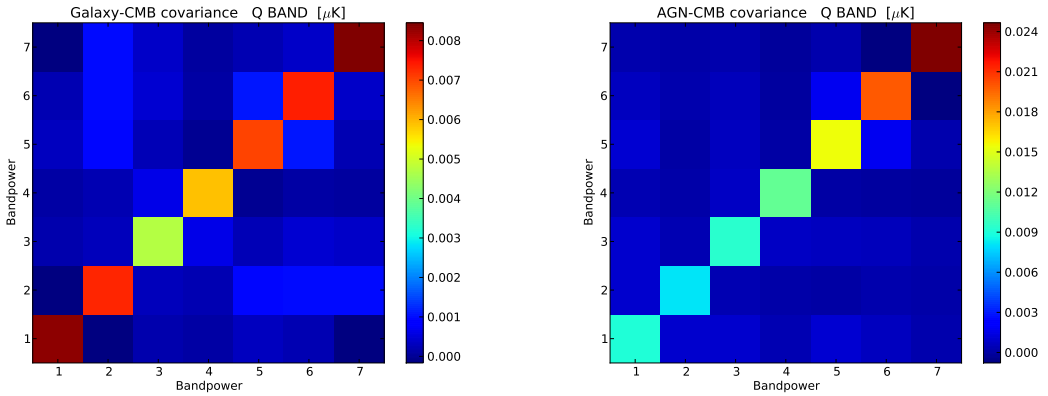

Figure 5.7: Q-band Monte Carlo covariance matrices for galaxies (left) and AGN (right). V and W band covariances are very similar and are not shown here.

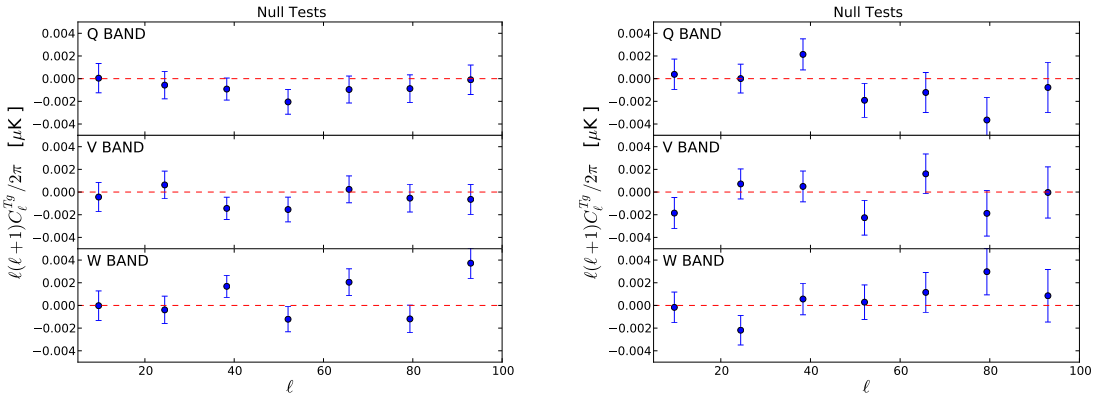

Figure 5.8: Null tests: correlation of the WISE galaxy (left) and AGN (right) maps with 5000 simulated CMB realizations. All are consistent with zero signal.

fluctuation $\Theta = \Delta T/T$ caused by the Doppler effect is given by [55, 56, 54]:

$$\Theta(\hat{\mathbf{n}}) = -\int d\eta\ \dot{\tau} e^{-\tau} v_r \tag{5.13}$$

Where the integral is taken along the line of sight. To linear order, we take $\tau(z)$ to be the average τ at redshift z. Since velocity is related to density by the continuity equation, which to linear order reads

$$\dot{\delta} + \nabla \cdot \boldsymbol{v} = 0 \quad , \tag{5.14}$$

this is an additional source of CMB-matter correlation beyond the ISW effect and is independent of frequency and therefore not distinguishable through component separation. At the power spectrum level, the Doppler effect can be calculated by including the $\dot{\tau}e^{-\tau}v_r$ term in the line-of-sight integral of [53] as a source term, considering the fact that v_r is a spin-1 quantity under rotation and therefore the projection kernel from $\boldsymbol{k}$ to ℓ involves the time derivative of the spherical Bessel functions $j'_\ell(k\chi)$, rather than $j_\ell(k\chi)$ which is used for the projection of scalars (such as density or potential). Moreover we note that Limber approximation is very inaccurate for velocities on large scales and we will use the exact equations instead.

Figure 5.9 shows that on large scales ($\ell < 100$), the Doppler contribution is comparable to the ISW amplitude.

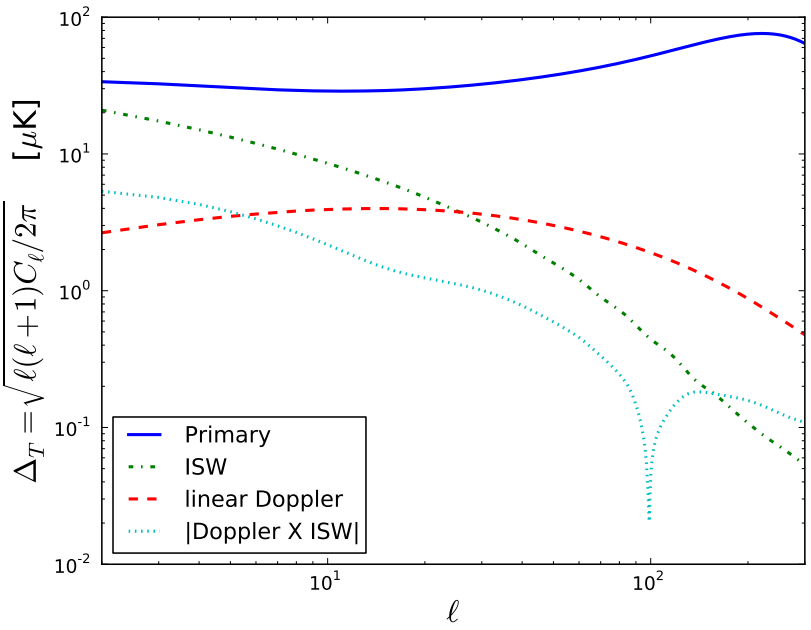

Figure 5.9: Doppler and ISW contribution from the CMB power spectrum, compared to the primary anisotropy.

5.10.1 WISE galaxies and AGN

It becomes natural to ask if the Doppler effect can be a large contaminant to the ISW measurements presented previously, since they are comparable at the power spectrum level. Firstly, as discussed in [57], the Doppler contribution has the same sign as the ISW effect: consider a matter overdensity at redshift z_*. Gas from $z > z_*$ will be infalling with a peculiar velocity pointing towards us, thus upscattering CMB photons. The contrary is true for gas at $z < z_*$, which will have a peculiar velocity pointing away from us and will thus downscatter CMB photons energy. However, since the probability of Thomson scattering (the visibility function $\dot{\tau}e^{-\tau}$) is decreasing with time, scattering at higher redshift is more likely and therefore an overdensity will be associated with a hot spot in the CMB temperature.

Figures 5.10 and 5.11 shows the result of numerical computation of the Doppler-galaxy and Doppler-AGN correlations for the WISE catalog, obtained by modifying the publicly available CAMB Sources code[8], to only include the Doppler contribution as a source function and the appropriate redshift distribution for the WISE objects.

We see that the Doppler contamination to our kSZ measurement is about 1% for WISE galaxies and 4% for WISE AGN. To explain such a small number, we must note that the vast majority of the linear Doppler signal is produced around the redshift or reionization, when the visibility function is largest. On the contrary the ISW effect arises only when the effect of Dark Energy is dominant, and most of the signal comes from $z < 1$. This explains the very weak correlation between the Doppler signal and low-redshift structure.

[8] http://camb.info/sources/

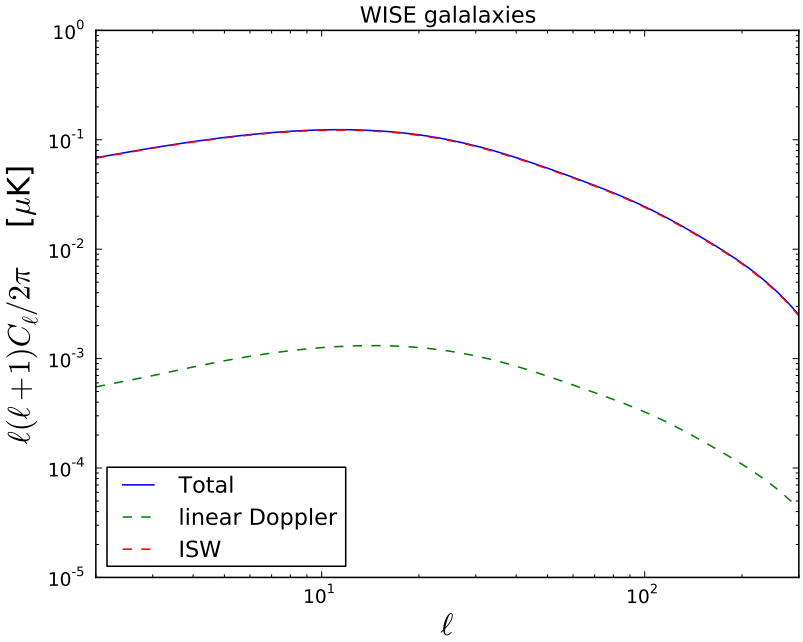

Figure 5.10: Doppler and ISW contribution to the CMB-galaxy cross correlation for WISE selected galaxies

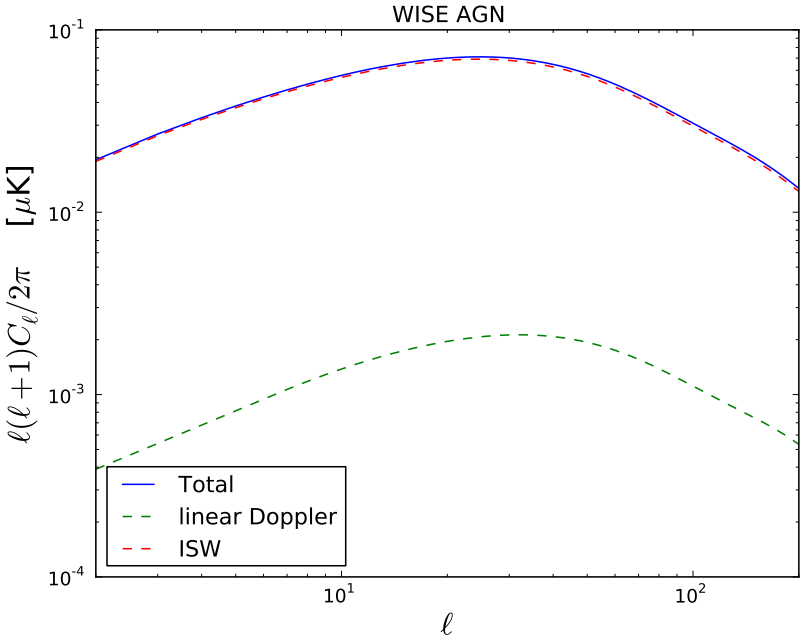

Figure 5.11: Doppler and ISW contribution to the CMB-AGN cross correlation for WISE selected AGN.

5.10.2 Anomalous signal from superclusters and supervoids

As mentioned in the introduction to this chapter, the ISW signal obtained by stacking on SDSS DR7 superclusters and supervoids is in $\sim 4\sigma$ tension with the ΛCDM expectation [24, 25, 26]. In this section we ask whether the Doppler contribution can relieve at least part of the tension.

In [24], the authors identify the 100 largest superstructures in 7500 square degrees of the SDSS LRG catalog. They are split between 50 'superclusters' and 50 'supervoids', and span a redshift range $0.4 < z < 0.75$, with a median redshift of 0.5. An aperture photometry filter[9] (AP) with 4 degrees radius is applied to the WMAP5 CMB temperature map to obtain an estimate of the ISW signal. The mean of the absolute value of the stacked ISW signal on these 100 superstructures is found to be $9.6 \pm 2.2\mu$K, compared to a prediction from ray-tracing simulations of $\sim 2\mu$K [25]. While the original analysis was performed on WMAP data, this has been subsequently confirmed by the Planck team [45, 46].

The choice of 4 degrees radius for the AP filter corresponds to the typical angular size of these structures in the sky, while the typical spatial extent is $\sim 100h^{-1}$ Mpc. Therefore we shouldn't think of these as bound structures with a well defined profile, but rather as mild hills and valleys in the potential. On these scales linear theory is expected to work remarkably well.

The exact profile of these structures is not known and ray-tracing through N-body simulations seems like the most robust approach. However here we give an approximate treatment which is expected to at least accurately predict the ratio between the ISW and Doppler signals. Since the scales of interest are in the linear regime, we can compute the expected RMS CMB fluctuations produced by ISW and Doppler effects caused by these structures, by using the usual line-of-sight integral, restricting the integration over the spatial extent of the typical structure. Note that since potential (which sources ISW) and velocity (which

[9] the filter output is defined as the mean temperature in a disk of radius θ_d, to which the mean temperature in a surrounding ring of equal area is subtracted.

sources Doppler) scale differently with the matter overdensity δ ($\Phi \propto \delta/k^2$ and $v \propto \delta/k$), the spatial extent of the structure will be slightly different in potential and velocity. For density, we assume that the window function is a spherical tophat of $100h^{-1}$ Mpc in radius and solve for a potential and velocity window function. We modify the public code CAMB[10] in order to only perform the integration of the Doppler and ISW source terms, with a given window function.

After applying the AP filter with 4 degrees radius like in the analysis on real data, we find that the Doppler contribution is only $\sim 2\%$ of the ISW signal. There is also a non-trivial cross-correlation between ISW and Doppler, and it is as large as $\sim 20\%$ of the ISW amplitude.

As a last step, we would like to see if we can reproduce the expected level of ISW and Doppler, and not only their ratio. We note that these structures are not randomly chosen, but they are the most extreme superstructures in the SDSS footprint. Therefore we should quantify how extreme these fluctuations are compared to the RMS, in other words, we would like to compute the 'significance' $\nu = \delta/\sigma$ for these structures. We will calculate this approximately in the Press-Schechter formalism and use linear theory throughout. Under the assumption of Gaussian initial conditions, we find that ν_c required to have 50 regions above ν_c in a volume equal to the volume spanned by the SDSS LRG, when smoothing the density field on $100h^{-1}$ Mpc scale is $\nu_c = 4.2$.

Figure 5.12 shows the expected ISW and Doppler signals for fixed $\nu_c = 4.2$ and as a function of AP filter size. We find the expected ISW signal to be $\sim 1.9\mu$K, in good agreement with simulation results. While this calculation is very approximate (and can be improved by using the 'peak formalism'), the ratio between Doppler and ISW is independent of ν_c.

In conclusion, the Doppler contamination to the ISW signal is of order 2% (with a 20% cross correlation between the two), and both contributions have the same sign. While this goes in the direction of easing the tension, it does not fully resolve it. To decide whether this

[10] http://camb.info

is a purely 'statistical' fluctuation or something different more data is needed and the Dark Energy Survey collaboration is currently repeating the analysis on new, non-overlapping structures with similar properties. Their results might shed new light on this intriguing discrepancy.

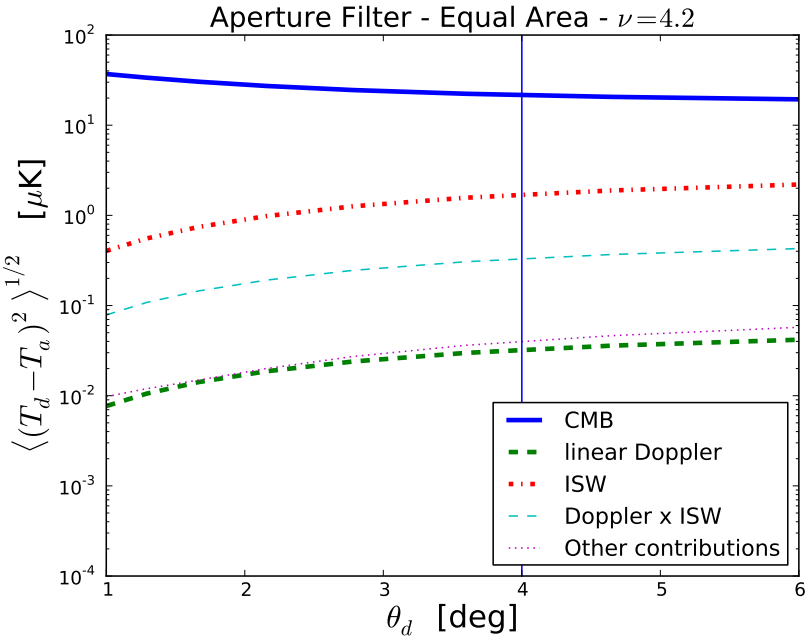

Figure 5.12: Expected Doppler and ISW signal from an Aperture Photometry filter at the location of the super-cluster/void. The plot shows RMS fluctuation of the output of the Aperture Photometry filter, multiplied by the significance $\nu_c = 4.2$, versus the filter radius θ_d (except for the primary CMB which is not multiplied by ν_c). As we can see, the primary CMB fluctuations are the main source of noise. The curve labelled 'other contributions' includes all of the other contributions that are correlated with the presence of low redshift over- or under- densities; the main contribution to this term is the ordinary Sachs-Wolfe effect due to the correlation between density at the surface of last scattering and at low redshift. The sign of the Sachs-Wolfe effect is the same as Doppler and ISW.

Bibliography

[1] C. Bennett et al., ApJS, 208, 20 (2013)

[2] M. Hicken et al., ApJ, 700, 1097 (2009)

[3] R. Kessler et al., ApJS, 185, 32 (2009)

[4] B. A. Reid et al., MNRAS, 404, 60 (2010)

[5] A. Riess et al., ApJ, 699, 539 (2009)

[6] A. Vikhlinin et al., ApJ, 692, 1060 (2009)

[7] S. Suyu et al., ApJ 766, 70 (2013).

[8] POLARBEAR Collaboration: P. Ade et al., eprint arXiv:1312.6645

[9] POLARBEAR Collaboration: P. Ade et al., eprint arXiv:1312.6646

[10] SPTpol Collaboration: D. Hanson et al., Phys. Rev. Lett. 111, 141301 (2013)

[11] E. Wright et al., ApJ, 140, 1868 (2010)

[12] D. S. Swetz et al., ApJS, 194, 41 (2011)

[13] R. Keisler et al., ApJ, 743, 28 (2011)

[14] T. Clifton et al., Physics Reports 513, 1 (2012), 1-189

[15] A. Riess et al., ApJ, 607, 665 (2004)

[16] R. Sachs and A. Wolfe, Astrophys. J. 147, 73 (1967)

[17] K. Huffenberger, U. Seljak, A. Makarov, Phys. Rev. D 70, 063002 (2004)

[18] N. Afshordi, Phys. Rev. D 70, 083536 (2004)

[19] S. Ho et al., Phys. Rev. D 78, 043519 (2008)

[20] J. Xia et al., JCAP 0909 003 (2009)

[21] P. Corasaniti, T. Giannantonio, A. Melchiorri, Phys. Rev. D, 71, 123521 (2005)

[22] R. Scranton et al., (2003) eprint astro-ph/0307335

[23] P. Fosalba, E. Gaztanaga, F. Castander, ApJL 597, L89 (2003)

[24] B Granett, M Neyrinck, I. Szapudi, ApJL 683, L99 (2008)

[25] C. Hernández-Monteagudo, R. Smith, Mon. Not. R. Astron. Soc. 435, 1094 (2013)

[26] S. Flendera, S. Hotchkissa, S. Nadathurb, JCAP 02 013 (2013)

[27] N. Padmanabhan et al., Phys. Rev. D, 72, 4, 043525 (2005)

[28] C. Hernández-Monteagudo et al., eprint arXiv:1303.4302

[29] T. Goto, I. Szapudi, B. Granett, MNRAS Letters, 422: L77L81 (2012)

[30] A. Kovács et al., MNRAS Letters, 431, L28 (2013)

[31] L. Yan et al., The Astronomical Journal, 145, 55 (2013)

[32] K. Abazajian et al. 2009, ApJS, 182, 543

[33] R. Assef et al., ApJ, 772, 26 (2013)

[34] T. Giannantonio et al., Phys. Rev. D 77, 123520 (2008)

[35] T. Giannantonio et al., Mon. Not. R. Astron. Soc. 426, 2581 (2012)

[36] T. Giannantonio et al., eprint arXiv:1303.1349

[37] T. Jarrett et al., ApJ, 735 112 (2011)

[38] D. Stern et al., ApJ, 753, 30 (2012)

[39] A. Cooray, W. Hu, ApJ, 534, 533 (2000)

[40] A. Lewis, A. Challinor, Phys. Rep., 429, 1 (2006)

[41] B. Sherwin, S. Das et al., Phys. Rev. D 86, 083006 (2012)

[42] S. Das, B. Sherwin et al., Phys. Rev. Lett. 107, 021301 (2011)

[43] Planck Collaboration paper I (2013) eprint arXiv:1303.5062

[44] Planck Collaboration paper XVII (2013) eprint arXiv:1303.5077

[45] Planck Collaboration paper XIX (2013) eprint arXiv:1303.5079

[46] Planck Collaboration paper XXI (2015) eprint arXiv:1502.01595

[47] A. Nishizawa, Prog. Theor. Exp. Phys. (2014) 06B110

[48] A. van Engelen et al., ApJ 756 142 (2012)

[49] J. Geach et al., ApJ Letters, 776, 41 (2013)

[50] K. Gorski at al., ApJ, 622, 759 (2005)

[51] E. Hivon et al., ApJ, 567, 2 (2002)

[52] S. Croom et al., MNRAS 356: 415-438 (2005)

[53] U. Seljak, & M. Zaldarriaga, (1996), ApJ, 469, 437

[54] W. Hu, & M. White (1996), A&A, 315, 33

[55] R. A. Sunyaev, & Y. B. Zel'dovich, (1972), Comments Astrophys. Space Phys., 4, 173

[56] R. A. Sunyaev, & Y. B. Zel'dovich, (1980), ARA&A, 18, 537

[57] T. Giannantonio, & R. Crittenden, (2007), MNRAS, 381, 819

Chapter 6

Prospects for kSZ detection without accurate redshift information

6.1 Introduction

In this chapter we ask the question of whether the kinetic Sunyaev-Zel'dovich (kSZ) signal can be extracted in cross-correlation, in absence of reliable redshift estimates for the tracer population (for example in the case of the WISE catalog [1]).

The kSZ effect is produced by Thomson scattering of CMB photons off of coherently moving electrons. The amplitude of the kSZ signal depends linearly on the local free electron density n_e (and is independent of temperature), and is therefore suited to probe the low density and low temperature outskirts of galaxies and cluster. The sign of the effect depends on the direction of the peculiar line-of-sight velocity of the free electrons. In particular, if a galaxy or cluster is moving towards us, it will on average up-scatter CMB photons, producing a 'hot spot' in the observed CMB map. The contrary is true for galaxies or clusters moving away from us.

The equal likelihood of positive and negative kSZ signals leads to a large cancellation in the cross-correlation of low-redshift tracers with CMB maps. In absence of redshift informa-

tion, we can't perform velocity reconstruction, or use any of the other common techniques to avoid the cancellation . To overcome this difficulty, the CMB temperature map can be squared in real space before cross-correlating with tracers. Since primary CMB fluctuations are dominant to the kSZ power spectrum at $\ell < 3000$, we apply a Wiener filter to the CMB map, before squaring it in real space. This filter downweights angular scales on which the kSZ signal is most subdominant to the primary CMB, ISW, and noise.

First suggested in [7], this cross-correlation probes the mass and line-of-sight velocity of the gas associated with galaxies used as tracers . It thus provides a method with which to find the missing baryons [2], similar to but distinct from other kSZ techniques based on momentum template reconstruction [9, 10] or pairwise velocities [6]. In particular, this method does not require redshift estimates, but just a statistical redshift distribution. Similarly, individual halo mass estimates are not required for the inference of the kSZ amplitude in this method, in contrast to the pairwise velocity or velocity reconstruction approaches.

6.2 Theory summary

The fractional CMB temperature shift induced by the kSZ effect, $\Theta^{\rm kSZ}(\hat{\mathbf{n}}) = \Delta T^{\rm kSZ}/T_{\rm CMB}(\hat{\mathbf{n}})$, in a direction $\hat{\mathbf{n}}$ on the sky is given by [3, 4, 5] (in units with $c = 1$):

$$\Theta^{\rm kSZ}(\hat{\mathbf{n}}) = -\int d\eta\ g(\eta)\ \boldsymbol{p}_e \cdot \hat{\mathbf{n}} \tag{6.1}$$

$$= -\sigma_T \int \frac{d\eta}{1+z} e^{-\tau(z)} n_e(\hat{\mathbf{n}}, \eta)\ \boldsymbol{v}_e \cdot \hat{\mathbf{n}}, \tag{6.2}$$

where σ_T is the Thomson scattering cross-section, $\eta(z)$ is the comoving distance to redshift z, τ is the optical depth to Thomson scattering, $g(\eta) = \dot{\tau} e^{-\tau}$ is the visibility function. Here n_e is the physical free electron number density, $\boldsymbol{v}_e$ is the peculiar velocity of the electrons, and we have defined the electron momentum $\boldsymbol{p}_e = (1+\delta)\boldsymbol{v}_e$. For concreteness, we will focus on

two promising low-redshift tracers: the projected WISE galaxy catalog [1] and the CFHTLS lensing convergence map [11].

The projected galaxy overdensity δ_g is defined by

$$\delta_g(\hat{\mathbf{n}}) = \int_0^{z_{\max}} dz\ W^g(z)\ \delta_m(\eta\hat{\mathbf{n}}, \eta) \tag{6.3}$$

where $z_{\max}$ is the maximum source redshift, and $W^g(z)$ is the projection kernel given by:

$$W^g(z) = b_g p_s(z) \tag{6.4}$$

Here b_g is the linear bias factor and $p_s(z) \propto dn/dz$ is the redshift distribution of source galaxies (normalized to have unit integral).

The Weak Lensing (WL) convergence field depends on the projected matter overdensity δ_m along the LOS and the lensing kernel:

$$\kappa(\hat{\mathbf{n}}) = \int_0^{z_{\max}} dz\ W^\kappa(z)\ \delta_m(\eta\hat{\mathbf{n}}, \eta) \tag{6.5}$$

where $W^\kappa(z)$ is the lensing kernel:

$$W^\kappa(z) = \frac{3\Omega_m H_0^2 \eta(z)}{2aH(z)} \int_z^{z_{\max}} dz_s\ p_s(z_s) \frac{\eta(z_s) - \eta(z)}{\eta(z_s)} \tag{6.6}$$

Since the projected density and the convergence field are closely related to each other, we will use κ and δ_g interchangeably in what follows. All equations can be transformed from one to the other by the simple exchange $W^\kappa \leftrightarrow W^g$.

As explained in the introduction, the cross-correlation between kSZ and tracers is expected to vanish on small scales because of the $\boldsymbol{v}_e \to -\boldsymbol{v}_e$ symmetry. We therefore square the temperature fluctuation map in real space before performing the cross correlation.

In order to minimize spurious contributions to the primary fluctuations and detector noise, we filter the temperature map with a filter F before squaring:

$$\Theta_f(\boldsymbol{\ell}) = F(\ell)\Theta(\boldsymbol{\ell}) \tag{6.7}$$

where

$$F(\ell) = \frac{C_\ell^{\rm kSZ}}{C_\ell^{\rm tot}} \tag{6.8}$$

And $C_\ell^{\rm tot}$ is the total fluctuation power, which includes primary CMB, kSZ, ISW and noise.

Following [7, 8], we can write the angular spectrum of the kSZ^2–δ_g (or kSZ^2–WL) cross-correlation as

$$C_\ell^{{\rm kSZ}^2\times\delta_{\rm g}} = \int_0^{z_{\rm max}} \frac{dz}{\eta^2} W^g(z) g^2(\eta) \mathcal{T}(k=\ell/\eta(z), z) \tag{6.9}$$

Where we have used the Limber approximation, and have defined the *triangle power spectrum* $\mathcal{T}$

$$\mathcal{T}(k,z) = \int \frac{d^2\boldsymbol{q}}{(2\pi)^2} F(q\eta) F(|\boldsymbol{k}+\boldsymbol{q}|\eta) B_{\delta p_{\hat{\mathbf{n}}} p_{\hat{\mathbf{n}}}}(\boldsymbol{k}, \boldsymbol{q}, -\boldsymbol{k}-\boldsymbol{q}) \tag{6.10}$$

The hybrid bispectrum $B_{\delta p_{\hat{\mathbf{n}}} p_{\hat{\mathbf{n}}}}$ is the three point function of one density contrast and two line of sight momenta, $p_{\hat{\mathbf{n}}}$. The triangle power spectrum $\mathcal{T}$ is the integral over all triangles with sides $\boldsymbol{k}$, $\boldsymbol{q}$, and $-\boldsymbol{k}-\boldsymbol{q}$, lying on planes of constant redshift.

Considering that the momentum field $\boldsymbol{p} \sim \delta\boldsymbol{v}$ on small scales, that the hybrid bispectrum $B_{\delta p_{\hat{\mathbf{n}}} p_{\hat{\mathbf{n}}}}$ contains terms of the form $\langle vv\rangle\langle\delta\delta\delta\rangle$, $\langle v\delta\rangle\langle\delta\delta v\rangle$, ..., and a connected part $\langle vv\delta\delta\delta\rangle_c$. Reference [8] argues that the former term $\langle vv\rangle\langle\delta\delta\delta\rangle$ is the dominant on small scales ($k \gg k_{eq}$) and we have verified this numerically.

On small scales we can therefore approximate the hybrid bispectrum in terms of the 3D velocity dispersion $v_{\rm rms}^2$ and the non-linear matter bispectrum $B_m^{\rm NL}$ [7, 8]:

$$B_{\delta p_{\hat{\mathbf{n}}} p_{\hat{\mathbf{n}}}} \approx \frac{1}{3} v_{\rm rms}^2 B_m^{\rm NL} \tag{6.11}$$

6.3 Possible contaminants

One drawback of this technique is that it is very sensitive to the leakage of emission from the tracers themselves to the CMB temperature map, and therefore good frequency coverage that allows effective component separation is required. The main sources of leakage are expected to be synchrotron, thermal Sunyaev-Zel'dovich (tSZ) and dust emission. Moreover, spatial changes in the spectral index of the dust or synchrotron emission can also mimic the kSZ signal. Work in progress in collaboration with Colin Hill and David Spergel shows that a multi-frequency analysis of the Planck data [12] is powerful enough to limit the contamination by foregrounds to a small fraction of the signal (see Hill, Ferraro et al, in preparation).

The contaminants that preserve the black-body spectrum of the CMB cannot however be removed by component separation. Apart from kSZ, the ISW effect and weak gravitational lensing are also frequency-independent. While the ISW (and its non-linear generalization) is expected to be negligible at $\ell > 100$, it turns out that the weak lensing contribution is large (in fact larger than the signal itself) and must be accurately modeled and removed in order to detect kSZ.

In the next section we calculate the weal lensing leakage in this cross-correlation.

6.4 Lensing leakage

Let $\Theta = \Delta T/T$ be the unlensed temperature fluctuation and $\tilde{\Theta}$ be the corresponding lensed fluctuation. We first note that in absence of filter/beam, lensing preserved the total variance, i.e. $\langle\tilde{\Theta}^2(\boldsymbol{x})\rangle = \langle\Theta^2(\boldsymbol{x})\rangle$ (essentially just looking at a different point in the sky), so that there is no lensing contribution to $\langle\tilde{\Theta}^2(\boldsymbol{x})\delta_g(\boldsymbol{y})\rangle$.

Now things are a bit different when including filter and beam. Let $\tilde{\Theta}_f(\ell) = f(\ell)\tilde{\Theta}(\ell)$, where $f(\ell) = F(\ell)b(\ell)$ is the product of a filter F and the beam function b. We want to

compute the Fourier Transform of $\langle\tilde{\Theta}_f^2(\boldsymbol{x})\delta_g(\boldsymbol{y})\rangle$:

$$\langle\tilde{\Theta}_f^2(\boldsymbol{\ell}_1)\delta_g(\boldsymbol{\ell}_2)\rangle = \tag{6.12}$$

$$= \int \frac{d^2\boldsymbol{L}}{(2\pi)^2}\langle\tilde{\Theta}_f(\boldsymbol{L})\tilde{\Theta}_f(\boldsymbol{\ell}_1-\boldsymbol{L})\delta_g(\boldsymbol{\ell}_2)\rangle \tag{6.13}$$

$$= \int \frac{d^2\boldsymbol{L}}{(2\pi)^2} f(L)f(|\boldsymbol{\ell}_1-\boldsymbol{L}|)\langle\tilde{\Theta}(\boldsymbol{L})\tilde{\Theta}(\boldsymbol{\ell}_1-\boldsymbol{L})\delta_g(\boldsymbol{\ell}_2)\rangle \tag{6.14}$$

The lensed fluctuations can be expanded in terms of the unlensed ones:

$$\tilde{\Theta}(\boldsymbol{x}) = \Theta(\boldsymbol{x}) + \nabla\psi\cdot\nabla\Theta(\boldsymbol{x}) + \frac{1}{2}\nabla^a\psi\nabla^b\psi\nabla_a\nabla_b\Theta(\boldsymbol{x}) + \dots \tag{6.15}$$

where ψ is the lensing potential, so that we can express

$$[\nabla\psi\cdot\nabla\Theta](\boldsymbol{L}) = -\int \frac{d^2\boldsymbol{L}'}{(2\pi)^2}\boldsymbol{L}'\cdot(\boldsymbol{L}-\boldsymbol{L}')\psi(\boldsymbol{L}')\Theta(\boldsymbol{L}-\boldsymbol{L}') \tag{6.16}$$

Now, in perturbation theory (up to first order in the displacement),

$$\langle\tilde{\Theta}(\boldsymbol{L})\tilde{\Theta}(\boldsymbol{\ell}_1-\boldsymbol{L})\delta_g(\boldsymbol{\ell}_2)\rangle = \langle\Theta(\boldsymbol{L})\Theta(\boldsymbol{\ell}_1-\boldsymbol{L})\delta_g(\boldsymbol{\ell}_2)\rangle \tag{6.17}$$
$$+ \langle[\nabla\psi\cdot\nabla\Theta](\boldsymbol{L})\tilde{\Theta}(\boldsymbol{\ell}_1-\boldsymbol{L})\delta_g(\boldsymbol{\ell}_2)\rangle + (\boldsymbol{L}\to\boldsymbol{\ell}_1-\boldsymbol{L}) + \dots$$

The first term is due to ISW + kSZ only, while the second and third terms should contribute equally by symmetry. Plugging in equation 6.14 and using 6.16:

$$\langle\tilde{\Theta}_f^2(\boldsymbol{\ell}_1)\delta_g(\boldsymbol{\ell}_2)\rangle = \langle\Theta_f^2(\boldsymbol{\ell}_1)\delta_g(\boldsymbol{\ell}_2)\rangle - 2\int \frac{d^2\boldsymbol{L}}{(2\pi)^2} f(L)f(|\boldsymbol{\ell}_1-\boldsymbol{L}|) \tag{6.18}$$
$$\times \int \frac{d^2\boldsymbol{L}'}{(2\pi)^2}\boldsymbol{L}'\cdot(\boldsymbol{L}-\boldsymbol{L}')\langle\psi(\boldsymbol{L}')\Theta(\boldsymbol{L}-\boldsymbol{L}')\Theta(\boldsymbol{\ell}_1-\boldsymbol{L})\delta_g(\boldsymbol{\ell}_2)\rangle$$

There is a non-zero connected trispectrum (due to ISW and subleading to the other terms), and two non-zero contractions $\langle\psi\delta_g\rangle\langle\Theta\Theta\rangle$ and $\langle\psi\Theta\rangle\langle\Theta\delta_g\rangle$, the latter again due to ISW.

Consider the first one and write:

$$\langle \psi(\boldsymbol{L}')\delta_g(\boldsymbol{\ell}_2)\rangle = (2\pi)^2\ C^{\psi\delta_g}_{\ell_2}\ \delta_D(\boldsymbol{L}'+\boldsymbol{\ell}_2) \tag{6.19}$$

$$\langle \Theta(\boldsymbol{L}-\boldsymbol{L}')\Theta(\boldsymbol{\ell}_1-\boldsymbol{L})\rangle = (2\pi)^2\ C^{TT}_{|\boldsymbol{\ell}_1-\boldsymbol{L}|}\ \delta_D(\boldsymbol{\ell}_1-\boldsymbol{L}') \tag{6.20}$$

Then the main correction due to lensing is

$$-2(2\pi)^2\delta_D(\boldsymbol{\ell}_1+\boldsymbol{\ell}_2)\int \frac{d^2\boldsymbol{L}}{(2\pi)^2} f(L)f(|\boldsymbol{L}-\boldsymbol{\ell}_1|)\ \boldsymbol{\ell}_1\cdot(\boldsymbol{L}-\boldsymbol{\ell}_1)\ C^{\psi\delta_g}_{\ell_1}\ C^{TT}_{|\boldsymbol{L}-\boldsymbol{\ell}_1|} \tag{6.21}$$

Similarly, the other contraction gives rise to

$$-2(2\pi)^2\delta_D(\boldsymbol{\ell}_1+\boldsymbol{\ell}_2)\int \frac{d^2\boldsymbol{L}}{(2\pi)^2} f(L)f(|\boldsymbol{L}-\boldsymbol{\ell}_1|)\ \boldsymbol{\ell}_1\cdot(\boldsymbol{L}-\boldsymbol{\ell}_1)\ C^{\psi T}_{\ell_1}\ C^{T\delta_g}_{|\boldsymbol{L}-\boldsymbol{\ell}_1|} \tag{6.22}$$

which is due to ISW and numerically is found to be factor of $\sim 10^4 - 10^5$ smaller than the lensing contribution on the scales considered here.

Changing variable in (6.21) to $\boldsymbol{L}' = \boldsymbol{L} - \boldsymbol{\ell}_1$:

$$\Delta C_\ell^{\mathrm{T}^2\times\mathrm{g}} \approx -2\frac{\ell\ C^{\psi\delta_g}_\ell}{(2\pi)^2}\int_0^\infty dL'\ L'^2 f(L')C^{TT}_{L'}\int_0^{2\pi} d\phi\ f(|\boldsymbol{L}'+\boldsymbol{\ell}|)\cos\phi \tag{6.23}$$

Note also that if $f(\ell) =$ constant, the lensing correction vanishes identically as expected.

6.5 Numerical results

Here we show the results from numerical integration of equation (6.9) and (6.23). The evaluation of equation (6.9) is computationally expensive and is achieved by precomputing all of the terms involving the fitting function to the non-linear bispectrum on a grid, followed by interpolation. The angular integrals in both cases involve large cancellations and a high number of integration points are required. For both the power spectrum and bispectrum

we use fitting functions that have been matched to N-body simulations ([14] for the power spectrum and [15] for the bispectrum).

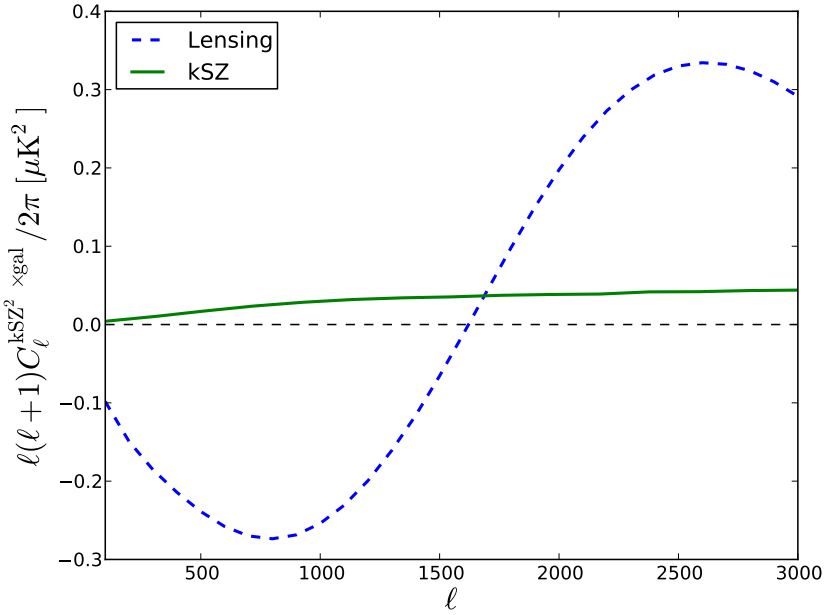

Figure 6.1: kSZ^2 and lensing contribution for WISE galaxies

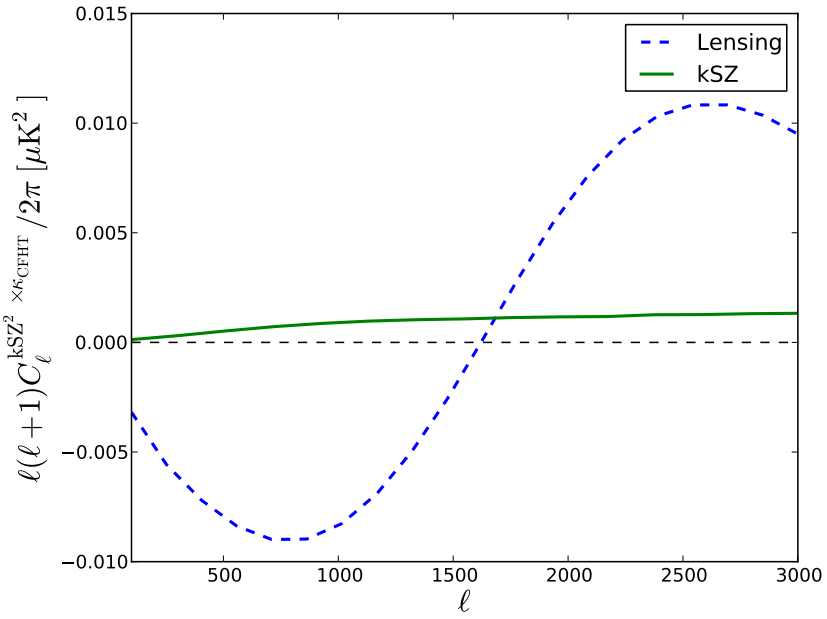

Figure 6.2: kSZ^2 and lensing contribution for CFHTLS convergence

6.6 Lensing cosmic variance

When subtracting the lensing contamination to identify the kSZ^2 signal, the amplitude of the lensing is subject to the a cosmic variance uncertainty. In the Gaussian approximation, the relative error in the lensing calculation in a bin of width $\Delta\ell$ due to cosmic variance is

$$\frac{\sigma(\Delta C_\ell^{\mathrm{T}^2\times\mathrm{g}})}{\Delta C_\ell^{\mathrm{T}^2\times\mathrm{g}}} = \sqrt{\frac{2}{f_{sky}(2\ell+1)\Delta\ell}} \tag{6.24}$$

For $\Delta\ell = 500$, we get the following relative errors ($f_{sky} = 0.00339$ and 0.5 for CFHTLS and WISE)

$\ell =$	500	1000	2000	3000
CFHTLS	3.4 %	2.4 %	1.7 %	1.4 %
WISE	0.3 %	0.2 %	0.14 %	0.11 %

Table 6.1: Fractional error on lensing amplitude due to cosmic variance for bins of $\Delta\ell = 500$.

As we will see these uncertainties are much smaller than the typical error bar on the cross-correlation and we conclude that the lensing cosmic variance is never the leading source of uncertainty in our analysis. Much larger uncertainties will be arise from our modeling of the relevant quantities (like lensing power spectrum and the bias) in the mildly non-linear regime, as well as the error in determining the bias of our tracers (usually through cross-correlation with CMB lensing maps).

6.7 Fisher forecast for kSZ^2 detection

The maximum S/N ratio can be estimated by using Fisher's formula as follows:

$$\left(\frac{S}{N}\right)^2 = f_{sky}\sum_\ell (2\ell+1)\frac{[C_\ell^{\mathrm{kSZ}^2\times\mathrm{g}}]^2}{C_\ell^{\tilde{T}^2\tilde{T}^2,f}C_\ell^{gg} + [C_\ell^{\mathrm{kSZ}^2\times\mathrm{g}}]^2} \tag{6.25}$$

and for $C_\ell^{\tilde{T}^2\tilde{T}^2,f}$ we use the Gaussian approximation:

$$C_\ell^{\tilde{T}^2\tilde{T}^2,f} \approx 2\int \frac{d^2\boldsymbol{L}}{(2\pi)^2} C_L^{\tilde{T}\tilde{T},f} C_{|\boldsymbol{L}-\boldsymbol{\ell}|}^{\tilde{T}\tilde{T},f} \tag{6.26}$$

Where $C_\ell^{\tilde{T}\tilde{T},f} = F^2(\ell)b^2(\ell)(C_\ell^{TT} + C_\ell^{\rm kSZ}) + F^2(\ell)C_\ell^{NN}$, and $F(\ell)$ is the Wiener filter, $b(\ell)$ is the beam function and C_ℓ^{NN} is the map noise.

Considering typical numbers for a Planck component separated map (5 arcmin beam and noise at the level of the Planck SMICA map), and restricting our analysis to $100 \leq \ell \leq 3000$, we get the following:

	f_{sky}	(S/N)
CFHTLS	0.0034	0.35
WISE	0.5	3.6
κ_{CMB}, no noise	0.7	1.1

Table 6.2: Forecast for the kSZ^2 cross correlation. The κ_{CMB} field corresponds to cross-correlating the square of a CMB temperature map with a CMB lensing convergence map as a tracer of low-z matter, assuming no noise in the latter.

6.8 Conclusions and future work

In conclusion, a CMB data-set like Planck should allow a statistical kSZ detection with $S/N \sim 3.6$ when combined with the WISE galaxy catalog. This is assuming that the frequency coverage of Planck is sufficient to remove the emission from the tracers in question. While none of the official Planck component separated maps is adequate due to large residual leakage of tSZ, it is possible to implement component separation methods such as the LGMCA [13] that explicitly set the tSZ residual to vanish. Preliminary work suggests that the contamination by foregrounds can be reduced to a small fraction of the statistical uncertainty on the kSZ amplitude. We have however shown that weak lensing of the CMB is a major source of contamination in this analysis, and it is not removable by component separation because it preserved the black-body spectrum of the CMB. We have calculated

the amplitude of the lensing and shown that the cosmic variance uncertainty is negligibly small when considering large fractions of the sky.

Work is in progress in collaboration with Colin Hill and David Spergel to perform this cross-correlation using Planck data and the WISE galaxy catalog. The remaining sources of theoretical uncertainty are the effects of non-linearity and redshift dependence of the galaxy bias and this is subject of current effort.

Acknowledgments

We thank Blake Sherwin, Kendrick Smith, Michael Strauss and Matias Zaldarriaga for very helpful discussion. I am supported by NSF grant AST1311756 and NASA grant NNX12AG72G.

6.9 Appendix: Comparison with simulations

Since we have made a number of approximations and relied extensively on semi-analytical fitting function for the power spectrum and bispectrum in non-linear regime, we compare our results with hydrodynamical simulations:

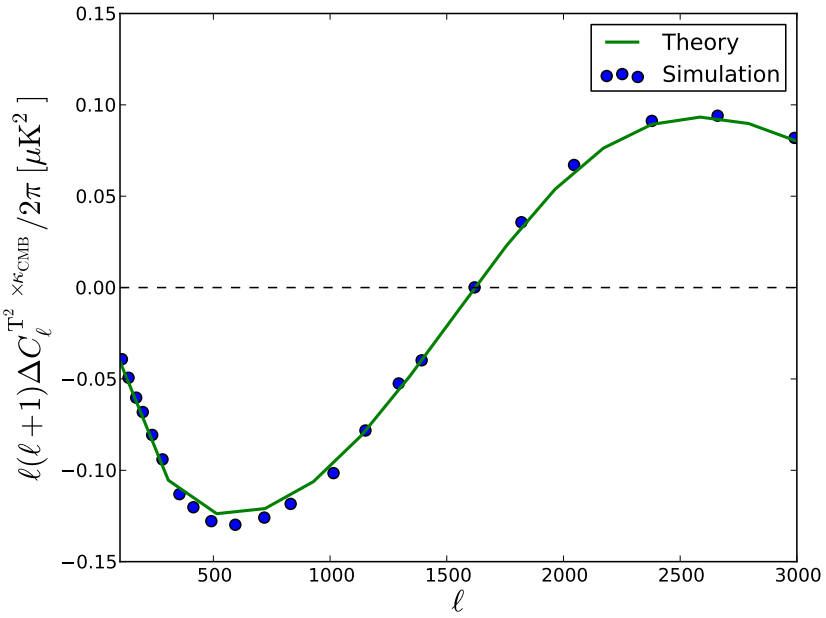

Figure 6.3: Lensing leakage in $\langle \tilde{T}_f^2\ \kappa_{CMB}\rangle$. The blue dots show the quantity measured in the simulations of Sehgal et al [16], while the solid line is first order the calculation presented in this chapter. The agreement is excellent and implies that higher order terms are subleading. Simulation data courtesy of Colin Hill - theory curve by the author.

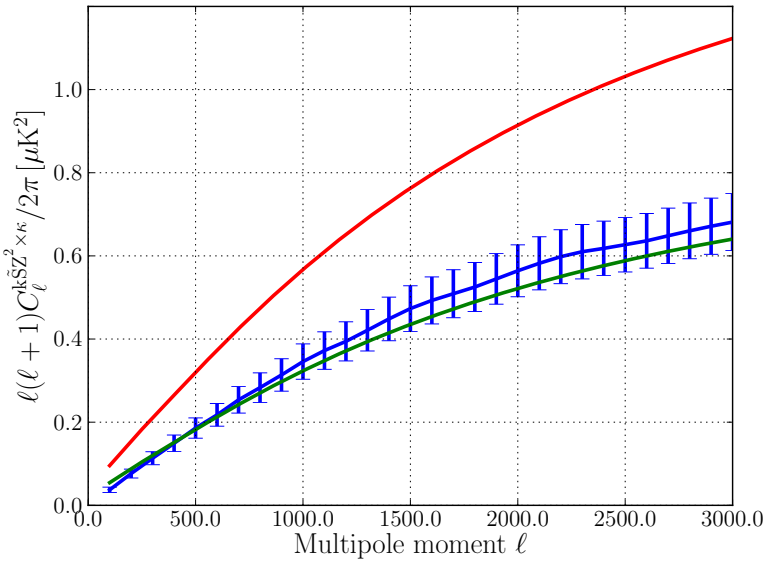

Figure 6.4: $\langle \mathrm{kSZ}^2 \times \kappa_{CFHT} \rangle$ – *unfiltered* result with $f(\ell) = 1$. The blue curve with error bars shows the result from simulations of Battaglia et al [17]. The red (top) curve shows the fiducial theory computation. The green curve shows the theory computation but with same k_{min} and k_{max} as in the simulation. This comparison shows that the simulation results are biased low due to the lack of super-box long wavelength velocity modes. This effect can be large as can be seen here. Simulation data courtesy of Nick Battaglia, theory curves by the author.

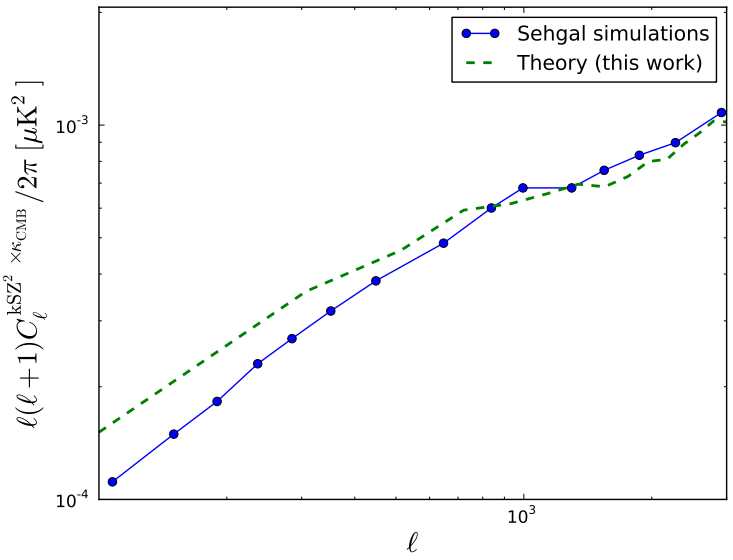

Figure 6.5: Filtered $\langle \mathrm{kSZ}^2 \times \kappa_{\mathrm{CMB}} \rangle$ from the simulations of Sehgal et al [16] and with $f(\ell)$ appropriate for Planck data. The agreement at large ℓ is excellent and the slight disagreement at low ℓ can be due to the fact that these simulations are known not to reproduce the kSZ power spectrum on large scales. Simulation data courtesy of Colin Hill - theory curve by the author.

Bibliography

[1] E. Wright et al., ApJ, 140, 1868 (2010)

[2] Fukugita, M., Hogan, C. J., & Peebles, P. J. E. 1998, ApJ, 503, 518

[3] Sunyaev, R. A., & Zel'dovich, Y. B. 1972, Comments Astrophys. Space Phys., 4, 173

[4] Sunyaev, R. A., & Zeldovich, I. B. 1980, ARA&A, 18, 537

[5] Ostriker, J. P., & Vishniac, E. T. 1986, ApJ, 306, L51

[6] Hand, N., Addison, G. E., Aubourg, E., et al. 2012, Physical Review Letters, 109, 041101

[7] Doré, O., Hennawi, J. F., & Spergel, D. N. 2004, ApJ, 606, 46

[8] DeDeo, S., Spergel, D. N., & Trac, H. 2005, arXiv:astro-ph/0511060

[9] Ho, S., Dedeo, S., & Spergel, D. 2009, arXiv:0903.2845

[10] Li, M., Angulo, R. E., White, S. D. M., & Jasche, J. 2014, MNRAS, 443, 2311

[11] Heymans, C., Van Waerbeke, L., Miller, L., et al. 2012, MNRAS, 427, 146

[12] Planck Collaboration, Adam, R., Ade, P. A. R., et al. 2015, arXiv:1502.05956

[13] Bobin, J., Sureau, F., Starck, J.-L., Rassat, A., & Paykari, P. 2014, A&A, 563, A105

[14] Takahashi, R., Sato, M., Nishimichi, T., Taruya, A., & Oguri, M. 2012, ApJ, 761, 152

[15] Gil-Marín, H., Wagner, C., Fragkoudi, F., Jimenez, R., & Verde, L. 2012, J. Cosmology Astropart. Phys., 2, 047

[16] Sehgal, N., Bode, P., Das, S., et al. 2010, ApJ, 709, 920

[17] Battaglia, N., Natarajan, A., Trac, H., Cen, R., & Loeb, A. 2013, ApJ, 776, 83